# CFD MODELLING OF DISPERSION WITHIN RANDOMLY DISTRIBUTED CYLINDER ARRAYS

A thesis submitted to the University of Sheffield in partial fulfilment of the
requirements for the degree of Doctor of Philosophy

## MAHSHID GOLZAR

Supervised by Virginia Stovin and Fred Sonnenwald

**Department of Civil & Structural Engineering,**
**The University of Sheffield**

**August 2018**

# ABSTRACT

Vegetation has a significant role in reducing the negative effects of polluted water on natural water bodies. However, a lack of understanding with respect to vegetation-flow interactions may result in poorer performance than expected. The most common vegetation types have been modelled as cylinders by many researchers both in the laboratory and numerical studies. However, experimental studies face practical issues, such as the need for expensive equipment. The quality of the velocity and scalar transport data collected from laboratory setups is also often lower than expected. On the other hand, attempts to model flow and mixing within cylinder arrays using advanced CFD models, e.g. LES, are extremely computationally expensive and cannot be used to produce comparable data to that recorded in laboratory setups.

This thesis proposes and validates the use of commercial less-computationally expensive CFD models (RSM models available in ANSYS FLUENT) as a complementary tool. This tool allows cylinder arrays to be modelled at the same scale as laboratory setups, provides high-resolution flow and turbulence data of high accuracy, and in combination with scalar transport modelling, provides estimated mixing coefficients of the same level of accuracy as those observed in laboratory studies.

The general modelling methodology is built based on the results of a series of preliminary studies. These include novel studies on estimating the advective zone length and the minimum required mixing reach length necessary to provide the desired accuracy, both presented for the first time, as well a validation of the general methodology. The developed methodology was used to produce a new high-resolution and high-accuracy dataset.

The main outcome of this thesis is a very convincing set of evidence that justifies the use of the CFD model as an alternative to traditional lab-based work. A few future studies are suggested to develop a deeper understanding of the processes that control mixing.

# ACKNOWLEDGEMENTS

I would like to deeply thank Prof. Virginia Stovin for her support, guidance and patience. I was extremely lucky to have her quick, detailed and constructive feedback throughout my PhD. A big thank you to Dr Fred Sonnenwald, who generously supported me with his exemplary computer science and patiently answered my questions when I needed immediate answers. Enormous thanks are due to Prof. Ian Guymer, who, although not officially but indeed (and in deed) supervised my work and kindly shared his vast knowledge and understanding of the subject.

The Faculty of Engineering, the University of Sheffield is gratefully acknowledged for offering me the generous full scholarship which made this journey possible.

A PhD is not only the result of the years spent working on it but also of all the previous years spent learning and understanding. Among all the previous teachers and supervisors to whom I am grateful, I am beholden the most to Prof. Salah Kouchakzadeh, whose unconditional care and support have always given me the courage and motivation to continue, progress and achieve.

Last, but not least, I would like to offer my appreciation to my friends and family, especially my parents Mina and Ehsan, whose presence and support have made this experience a wonderful adventure I shall always remember.

# CONTENTS

# LIST OF TABLES

# LIST OF FIGURES

# LIST OF APPENDICES

# NOMENCLATURE

| Name | Symbol | units |
|---|---|---|
| Advective flux in the x direction | $I_x$ | m.ppm/s |
| Area fraction occupied by wakes | $WF$ | - |
| Bed drag coefficient | $C_B$ | - |
| Bed shear | | N/m$^2$ |
| Centre to centre distance between one cylinder and its nearest neighbour | $S_{nc}$ | m |
| Channel Slope | $S$ | - |
| Concentration | $c$ | ppm |
| The cross-sectional area of the channel | $A$ | m$^2$ |
| Cylinder diameter | $d$ | m |
| Drag coefficient | $C_D$ | - |
| Drag force | $F_D$ | N |
| Flow depth | $h$ | m |
| Fluid density | $\rho$ | kg/m$^3$ |
| Frontal Cylinder area per unit volume | $a$ | 1/m |
| Longitudinal dispersion coefficient | $D_x$ | m$^2$/s |
| Longitudinal distance | $x$ | m |
| longitudinal velocity | $u$ | m/s |
| Longitudinal velocity fluctuation | $u'$ | m/s |
| Mass of the injected tracer | M | kg |
| Mechanical dispersion coefficient | $D_{mech}$ | m$^2$/s |
| molecular diffusion coefficient | $e_m$ | m$^2$/s |
| molecular diffusive flux in x direction | $J_x$ | m.ppm/s |
| Reynolds number based on cylinder diameter | $Re_d$ | - |
| Shear velocity | $u*$ | m/s |
| Solid volume fraction or density of cylinders | ø | - |
| Surface to the surface distance between one cylinder and its nearest neighbour | $S_n$ | m |
| time | $t$ | s |
| Transverse dispersion coefficient | $D_y$ | m$^2$/s |
| Transverse distance | $y$ | m |
| Transverse velocity | $v$ | m/s |
| Transverse velocity fluctuation | $v'$ | m/s |
| Turbulent kinetic energy per unit mass | $k$ | m$^2$/s$^2$ |
| Turbulence intensity | $I$ | - |
| Turbulent diffusion coefficient | $e_t$ | m$^2$/s |
| Turbulent Schmidt number | $Sc_t$ | - |
| Turbulent viscosity | $\nu_t$ | m$^2$/s |
| Vertical distance | $z$ | m |
| vertical velocity | $w$ | m/s |
| Vertical velocity fluctuation | $w'$ | m/s |
| viscous dissipation rate | $\varepsilon$ | m$^2$/s$^3$ |
| The width of the flume | $B$ | m |

# 1 INTRODUCTION

## 1.1 Background

Vegetation has a significant role to play in reducing the destructive effects of polluted water on the environment and natural water bodies. However, a lack of understanding with respect to vegetation/flow interactions may result in poorer performance than expected. Vegetation affects the hydrodynamics of the flow in several ways, such as changing the velocity, bending the streamlines, creating dead zones and exerting forces on the flow. Vegetation also affects the biochemical processes within the flow through both physical and chemical modifications. Thus, the accuracy of performance predictions can be improved by understanding these effects. This thesis contributes to a better understanding of the physical effects of the vegetation on flow and mixing in vegetated water bodies.

Form and the density of the vegetation determine the intensity of its effects on the flow and on the mixing processes. Higher densities may act as a rigid obstacle in front of the flow and lower densities may act as a sparse porous media which allows water to flow through it. Figure 1-1 shows a tracer study in a vegetated pond. It can be seen that the central patch of vegetation has caused the tracer plume to go around the pond, while the tracer can easily move through the sparse stems surrounding the perimeter of the pond. These mixing effects in combination are referred to as dispersion. *Typha latifolia*, *Phragmites australis* and *Schoenoplectus lacustris* are the most common vegetation types grown in ponds, (Shilton, 2008) a picture of each type is shown in Figure 1-2. These types of vegetation have been modelled as cylinders in a simplified representation by many researchers both in the laboratory and numerical studies e.g. Nepf et al. (1997), Serra et al. (2004), Stoesser et al. (2010) and Sonnenwald et al. (2017). Examples of laboratory experiments employing rigid cylinders to model vegetated flow are shown in Figure 1-3.

**Figure 1-1 Tracer test in a vegetated pond in Lyby, Sweden, taken by Ian Guymer**

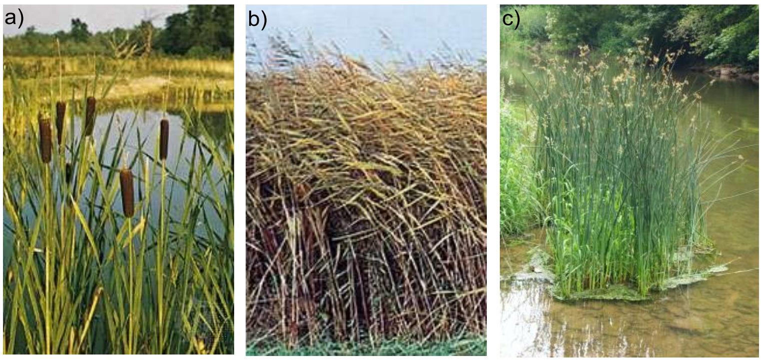

**Figure 1-2 Common vegetation types in ponds and wetlands a) *Typha latifolia* b) *Phragmites australis*, c) *Schoenoplectus lacustris, taken from Encyclopaedia Britannica and other free sources***

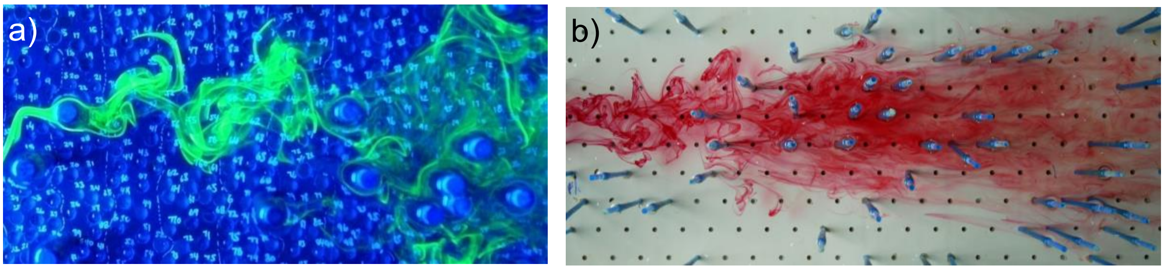

**Figure 1-3 Tracer study within artificial vegetation modelled by cylinders a) from Tanino (2008) cylinder diameter = 0.006 m, b) from a recent study in Warwick University, cylinder diameter = 0.004 m**

These studies have typically focused on identifying longitudinal or transverse dispersion coefficient to describe the within-vegetation mixing processes. Several authors (White and Nepf, 2003; Tanino and Nepf, 2008b; Sonnenwald et al. 2017) have attempted to relate these dispersion coefficients to the physical characteristics of the vegetation such as stem diameter, stem spacing and stem density. However, there is considerable scope to extend and improve understanding of the relevant processes and to produce more robust and generalized predictive relationships.

Acquiring accurate velocity and concentration data from a laboratory setup is dependent on expensive equipment, such as Laser Doppler Velocimetry (LDV) and Laser-Induced Fluorescence (LIF). Building and positioning the cylinder arrays is also very time consuming and changing the density requires heavy manual work or expensive machines. Besides the practical challenges, the quality and the resolution of data may also be limited, and it may not be possible to record all the desired parameters. Thus, a complementary method, with fewer practical challenges and the potential to provide high quality and high-resolution data, is needed. Computational Fluid Dynamics (CFD) is suggested as a complementary tool to study flow and mixing within cylinder arrays in this thesis. Another advantage of a CFD-based investigation is that both longitudinal and transverse dispersion coefficients can be derived from the same experimental data; most studies (with the exception of Sonnenwald et al. 2017) have not evaluated these two coefficients simultaneously. Both transverse and longitudinal dispersion coefficients are evaluated simultaneously in this thesis.

Two main approaches have been applied by researchers who have used CFD to represent the flow within vegetation. One is considering the bulk effects of vegetation and modelling it as a porous media e.g. Saggiori (2010); Tsavdaris et al. (2014) and Sonnenwald et al. (2017). The other approach is to model individual stems using high-level CFD models such as Large Eddy Simulation (LES) e.g. Kim and Stoesser (2011); Huai et al. (2011) and Chang and Constantinescu (2015). The porous media approach requires describing the whole patch of vegetation with a bulk drag coefficient which is not straightforward to estimate. However, the high-level CFD models are usually very computationally expensive and allow only a few stems to be modelled with current computational facilities. The approach taken within this thesis has an intermediate level of complexity which allows explicit modelling of a large number of individual stems as cylinder arrays and providing useful information and insights. The aims and objectives of the thesis are outlined in the following section.

## 1.2 Aims and Objectives

As previously mentioned, the general motivation of this thesis is to assess the suitability of CFD for quantifying the flow and mixing characterises of cylinder arrays as a complementary tool similar to the laboratory setups, i.e. a CFD laboratory which can be used in a similar way to the physical laboratories. This thesis also aims to generate new data and provide a better understanding of flow and mixing within random cylinder arrays.

The main objectives of this thesis are to:

1. Undertake a feasibility study on using commercial CFD tools, specifically ANSYS FLUENT, for modelling flow and mixing processes within random cylinder arrays;
2. Find the most suitable and efficient modelling setup to produce comparable data to those collected in previously published laboratory studies;
3. Validate the CFD modelling setup by comparing the results with previously published laboratory data;
4. Reproduce previously published laboratory experiments to review and validate the suggested theories regarding, flow, turbulence and mixing;
5. Expand and generalize the available data set on mixing within random cylinder arrays by testing different cylinder diameters and densities for transverse and longitudinal dispersion simultaneously

## 1.3 Thesis Approach

As will be explained in Chapter 2, the literature suggests the suitability of two-dimensional modelling of flow within cylinder arrays. Thus, all the models presented in this thesis were built and modelled as two-dimensional planar models. The steady pressure-based solver option available in ANSYS FLUENT was used for solving the flow equations along with the Reynolds Stress Models (RSM) closure for modelling the turbulence. After solving the flow equations, the solver was switched to the transient mode and the solute transport was modelled. A detailed explanation can be found in Chapter 3. The general methodology has been validated by reproducing previously-published laboratory experiments, Tanino and Nepf (2008b). The established modelling method has then been used to produce a new set of data to expand the existing dataset.

## 1.4 Thesis Layout

After an introduction to the thesis, presented in the current chapter, a background literature review is presented in Chapter 2. All the concepts that are used throughout the thesis, including the basic mixing concepts and the hydraulics of flow past cylinders are introduced and defined through the literature review. After a brief general review of the studies that have investigated flow within cylinder arrays, those studies with the potential to provide validation data are reviewed in detail. Laboratory studies which have investigated transverse and longitudinal mixing within random cylinder arrays are reviewed in detail, as their results are compared with the results of the models in this thesis in Chapter 3 and Chapter 4. The last category of studies reviewed in Chapter 2 are those that have used CFD in modelling flow and mixing within random cylinder arrays or within other similar setups.

The preliminary studies are presented in Chapter 3. These studies include the validation study which compares the CFD results with the results of Tanino (2008) and Tanino and Nepf (2008b). Other preliminary studies presented in Chapter 3 were conducted to define efficient and valid settings and modelling setups, such as geometry size, meshing setup and the mixing reach length. These will be used for the main models presented in Chapter 4. To the author’s knowledge, a study of finding the shortest required mixing reach length is presented here for the first time.

Chapter 4 presents the new dataset modelled in this thesis which includes 54 new data points for each transverse and longitudinal dispersion coefficient. This dataset covers a wide range of densities, three Reynolds numbers and two cylinder diameters, while all the previously published studies are limited to one single diameter and mostly to a limited range of array density. The effects of density and Reynolds number on transverse and longitudinal dispersion coefficients are investigated and a detailed comparison between the results of the current study with previously published laboratory data is provided. This comparison provides a very convincing set of evidence that justifies the use of the CFD model as an alternative to traditional laboratory setups. A few new predictive relationships are also suggested based on the new data set.

A summary of the thesis along with the list of the main conclusions is provided in Chapter 5, followed by suggestions for future work.

§3.2 has been presented as “Transverse Mixing Coefficient in Random Cylinder Arrays –A CFD Validation Study” by Golzar et al. (2017) at the 37th IAHR World Congress, 13-18 August 2017, Kuala Lumpur, Malaysia

Part of §3.3 of this thesis was originally presented as “A CFD based comparison of mixing due to regular and random cylinder arrays” by Golzar et al. (2018) at the 36th International School of Hydraulics, Jackranka, Poland, 23-26 May 2017. It was subsequently published as a book chapter in Free Surface Flows and Transport Processes in 2018

# 2 LITERATURE REVIEW

## 2.1 Introduction

All the concepts used in this thesis are introduced and explained in this chapter along with a detailed review of relevant previously published literature. The basic concepts of mixing are explained for laminar flow conditions in §2.2 and then more complex mixing processes are explained in §2.3 for turbulent flow conditions. The flow regimes and hydrodynamics of flow around cylinders are explained in §2.4 followed by an introduction to the metrics used for random cylinder arrays in the literature. Laboratory studies investigating transverse and longitudinal mixing are reviewed in §2.6.1 and §2.6.2, respectively. A brief introduction to CFD basics and the equations solved in this thesis is given in §2.7 followed by a review of the studies performed using CFD to investigate mixing within random cylinder arrays. Finally, the gaps in the literature, along with the main aims of the thesis, are outlined in §2.9.

## 2.2 Mixing in Laminar Flow

### 2.2.1 Advection

If a tracer, a soluble contaminant, is introduced to a laminar flow, two main processes contribute to its spreading, or in other words to its mixing. Advection is the result of the mainstream velocity, i.e. the tracer is carried along the channel by the current (Rutherford, 1994). As a result of the velocity profile, different particles of the tracer will move at different velocities which adds to the spread of the tracer in the longitudinal direction. This process, named differential advection, is the main contribution of advection to the mixing. The advective flux can be described as the product of the velocity and the tracer concentration, Eq. 2-1

$$I_x = uc \qquad 2\text{-}1$$

where $I_x$ is the advective flux in the $x$-direction i.e. the main flow direction, $u$ is velocity in the $x$-direction and $c$ is the tracer concentration.

### 2.2.2 Molecular Diffusion

The second process is the result of Brownian random molecular motion and is termed molecular diffusion. Molecular diffusion is considered a Fickian process, i.e. can be described by Fick's first law, Eq. 2-2,

$$J_x = -e_m \frac{\partial c}{\partial x} \qquad \text{2-2}$$

where, $J_x$ is the molecular diffusive flux in the $x$-direction, $c$ is the tracer concentration, $\frac{\partial c}{\partial x}$ is tracer concentration gradient in the $x$-direction and $e_m$ is the molecular diffusion coefficient. This law is based on an analogy between the diffusion of a solute in water with the diffusion of heat along a metal rod. Although this law is based on a hypothesis, laboratory results have confirmed it to a high degree. The molecular diffusion coefficient value is in the range of 0.5 - 2.0 × $10^{-9}$ $m^2/s$ for solutes in water (Rutherford, 1994).

To derive an equation which models the tracer concentration in laminar flow, the effects of advection and molecular diffusion should be combined, by assuming that the two processes are independent and additive. The equation can be derived by writing the conservation of mass principle for tracer into and out of a very small rectangular parcel of fluid which moves at the mean velocity and then considering the molecular diffusive fluxes into and out of the parcel. Doing so will result in Eq. 2-3,

$$\frac{\partial c}{\partial t} + u\frac{\partial c}{\partial x} + v\frac{\partial c}{\partial y} + w\frac{\partial c}{\partial z} = e_m\left(\frac{\partial^2 c}{\partial x^2} + \frac{\partial^2 c}{\partial y^2} + \frac{\partial^2 c}{\partial z^2}\right) \qquad \text{2-3}$$

where $t$ is time, $y$ is the transverse direction, $v$ is the velocity in the $y$-direction, $z$ is the vertical direction, and $w$ is velocity in the $z$-direction. This equation is known as the three-dimensional advection-diffusion equation in rectangular Cartesian coordinates. Detailed derivation of this equation can be found in Rutherford (1994). It should be borne in mind that as the molecular diffusion is a property of the fluid its value is constant in all directions. Eq. 2-3 is a linear partial differential equation thus its solutions can be superimposed, i.e. the solutions for a number of injections can be superimposed to form the final solution.

If $e_m$, $u$, $v$ and $w$ are known and considered constant then the distribution of a conservative tracer of mass $M$ released at $x = y = z = 0$ and $t = 0$ can be predicted using Eq. 2-4 at a given time, $t$.

$$c(x,y,z,t) = \frac{M}{\sqrt{4\pi e_m t}} exp\left( -\frac{(x-ut)^2 + (y-vt)^2 + (z-wt)^2}{4e_m t} \right) \tag{2-4}$$

Eq. 2-4 is a specific solution of Eq. 2-3 and can also be derived based on the random path of molecules caused by the Brownian motion of molecules (Nepf, 2008). The tracer concentration distribution predicted using Eq. 2-4 is a Gaussian, bell-shaped, curve along the $x$, $y$ and $z$-axes, thus its variance along different directions can be calculated using Eq. 2-5.

$$\sigma_x{}^2 = \sigma_y{}^2 = \sigma_z{}^2 = 2e_m t \tag{2-5}$$

This equation can be used for estimating the molecular diffusion coefficient based on the variance calculated for laboratory data. Taylor (1953) provides one of the earliest studies on mixing in laminar pipe flow. An analytical solution for solute distribution was predicted and was confirmed by laboratory experiments. The experiments were done using a 1.52 m long glass pipe of approximately $5 \times 10^{-4}$ m internal diameter and potassium permanganate as the tracer. The tracer concentration was measured by comparing the colour of the stream in the main pipe with that of known concentration solutions prepared as samples in glass comparison tubes of the same internal and external diameter. The comparison tube was moved along the main pipe until it reached a point of the same colour, so $c$, the concentration was determined as a function of the longitudinal distance, $x$. An example of the measured concentration profiles presented in Taylor (1953) is shown in Figure 2-1. The molecular diffusion coefficient for this case was reported to be around $0.8 \times 10^{-9}$ m$^2$/s. Taylor (1954) expanded the work to turbulent flows, which was used as a basis for other studies as will be discussed in future sections.

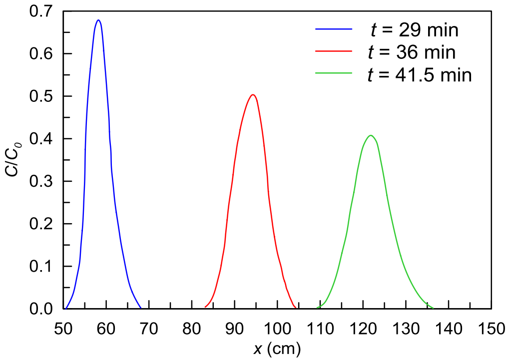

**Figure 2-1 Reproduced figure 8 from Taylor (1953), distribution of tracer at three stages of mixing, $e_m = 0.8 \times 10^{-9}$ m$^2$/s**

The molecular diffusion coefficient is a characteristic of the solvent and it depends on the temperature; though its value and effect are negligible compared to other mixing processes to be discussed in coming sections, and it is only important in laminar flows which rarely occur in real engineering and environmental applications. However, the equations which are used to describe it can be considered a basis for deriving the equations for more complex mixing processes.

## 2.3 Mixing in Turbulent Flows

As the velocity, and in turn the Reynolds number, increases, not only the spatial velocity profiles change but also the temporal velocity profiles become unsteady as a result of turbulent fluctuations. It is difficult to define a turbulent fluid motion but as a disease may be recognized by its symptoms, a turbulent flow can also be described by specific occurrences. Figure 2-2a shows the classic demonstration of Reynolds experiment in pipe flow, where the dye mixes much faster in turbulent flow. The filament of dye makes a straight streak along the centreline in laminar flow, while the streak is quickly broken up and spreads across the pipe in turbulent flow (Fischer et al., 1979).

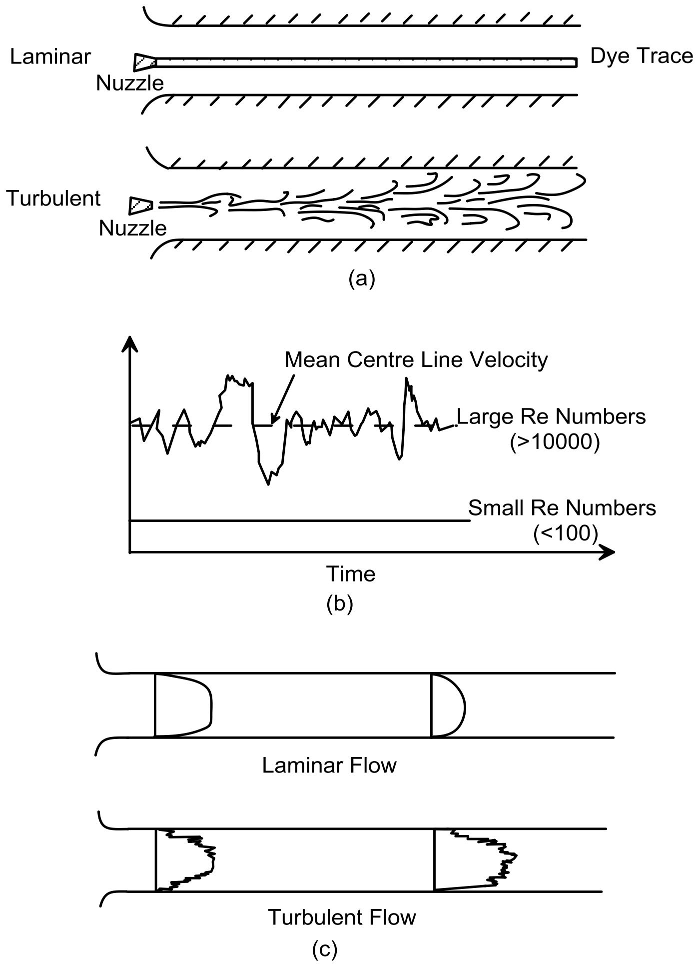

**Figure 2-2 Reproduced Figure 3-1 from Fischer et al (1979) a) Dye introduced at the upstream end of a pipe in laminar and turbulent flow, b) Record of longitudinal velocity at the centre of a pipe at a large and a small Re number, c) Deformation of a dye surface in laminar and turbulent flow**

Figure 2-2(b) shows the longitudinal velocity measured at the centreline of a pipe for both laminar and turbulent flows. Velocity stays constant in laminar steady flow while in turbulent steady flow, velocity fluctuates around the constant mean velocity.

Four different cases of spreading of a uniform line of dye introduced in a pipe with laminar and turbulent flows are shown in Figure 2-2(c). The first case shows a line of dye introduced at the entrance of a laminar flow in the pipe where the flow is not yet fully developed. It can be seen that in this case the only scale of distortion taken place in the dye plane is the thickness of the boundary layer. If the dye is introduced further downstream, where the flow is fully developed, the dye will be distorted into a parabolic shape across the pipe. Here the diameter of the pipe is the scale of distortion. The third and the fourth cases show the distortion in the dye plane at the entrance and in the mid-length of a pipe with turbulent flow. The dye plane gets distorted both by the effect of the velocity profile and also by the effect of velocity fluctuations. The latter is attributed to the turbulent eddies, which also define the turbulent scales.

### 2.3.1 Turbulent Diffusion

When a cloud of dye is introduced to the turbulent flow it gets distributed by the effect of turbulent eddies. Turbulent eddies cause the velocity, and in turn the tracer concentration, to change randomly over time and space. Thus three different averages have been defined for reporting velocity and also the tracer concentration: ensemble, time and space averages. Consider the experiment of releasing a certain mass of tracer into a turbulent flow and measuring the tracer concentration at a fixed point $x_0$, $y_0$, $z_0$, and time $t_0$ after injection. If the same experiment is repeated several times and the concentration is measured at the same point and at the same time after release, because the flow is turbulent, each concentration measurement will be different, say $c_i$ to $c_N$, $N$ being the number of experiments. Then the average of all the experiments will give an estimate of the ensemble average concentration at $x_0$, $y_0$, $z_0$, and $t_0$. In some conditions, such as a steady source of tracer, the ensemble average concentration at a fixed point can be approximated by the time average. Alternatively, in a region where the tracer is well-mixed but rapidly time-varying, the ensemble average may be approximated by the spatial average of the concentration.

Reynolds decomposition for velocity components and tracer concentration is a good start for deriving equations which describe mixing in turbulent flows. Eqs. 2-6 to 2-9 are known as Reynolds decomposition,

$$u = \overline{u} + u' \qquad \text{2-6}$$

$$v = \overline{v} + v' \qquad \text{2-7}$$

$$w = \overline{w} + w' \qquad \text{2-8}$$

$$c = \overline{c} + c' \qquad \text{2-9}$$

where over-bar shows the ensemble average and the prime shows the deviation from the average value for each quantity. It should be noted that the average of the fluctuating velocities and concentration are zero, i.e. $\overline{c'} = \overline{u'} = \overline{v'} = \overline{w'} = 0$. Substituting Eqs. 2-6 to Eq. 2-9 into Eq. 2-2 for a one dimensional case and time averaging yields:

$$\frac{\partial \bar{c}}{\partial t} + \bar{u}\frac{\partial \bar{c}}{\partial x} = e_m\left(\frac{\partial^2 c}{\partial x^2}\right) + \frac{\partial\left(-\overline{u'c'}\right)}{\partial x} \tag{2-10}$$

To utilize Eq. 2-10, a model is required for the term $\overline{u'c'}$. This term is a mass flux, as it is the product of velocity and concentration, and since both components of this term are the turbulence fluctuations, it is mass flux associated with the turbulence. An analogy between this turbulent diffusive flux and the laminar diffusive flux, i.e. Eq. 2-2 yields:

$$\overline{u'c'} = e_t \frac{\partial c}{\partial x} \tag{2-11}$$

where $e_t$ is the turbulent diffusion coefficient (eddy diffusivity). This analogy was derived by Taylor (1921) using an analytical method, known as Taylor's analysis of turbulent diffusion. "Turbulent eddies transfer both momentum and mass and experimental work shows that in many flows the rates of transfer are almost the same. This assumption is known as the Reynolds analogy." Thus turbulent diffusion has a direct relation with turbulent viscosity which is responsible for the rate of momentum transfer. Eq. 2-12 shows the relation between eddy viscosity and eddy diffusivity.

$$e_t = Sc_t \nu_t \tag{2-12}$$

where $\nu_t$ is turbulent viscosity and $Sc_t$ is the turbulent Schmidt number, a dimensionless number which must be determined experimentally. Typically in rivers $0.3 < Sc_t < 1.0$ (Rutherford, 1994). It is worth briefly mentioning that a recent study on turbulent Schmidt number, which reviewed the studies on environmental flow and investigated three modelling case studies, stated that "it is impossible to identify a universal value of $Sc_t$ valid for all the cases" Gualtieri et al. (2017). They also reported a number of studies on tracer transport which used the value of 1.0 for $Sc_t$, as well as extensive measurements in compound channel flow e.g. Arnold et al. (1989) which suggested values from 0.1 to1.0 with the vast majority of the values between 0.5 and 0.9.

Substituting Eq. 2-11 in Eq. 2-10, yields:

$$\frac{\partial \bar{c}}{\partial t}+\bar{u}\frac{\partial \bar{c}}{\partial x}=e_t\left(\frac{\partial^2 c}{\partial x^2}\right)+e_m\left(\frac{\partial^2 c}{\partial x^2}\right) \qquad \text{2-13}$$

$e_t$ is typically approximately 6 orders of magnitude greater than $e_m$, therefore the last term in Eq. 2-10 may be dropped for all practical situations.

Turbulence can be treated similarly in all three directions such that the advection-diffusion equation, Eq. 2-3, becomes:

$$\frac{\partial \bar{c}}{\partial t}+\bar{u}\frac{\partial \bar{c}}{\partial x}+\bar{v}\frac{\partial \bar{c}}{\partial y}+\bar{w}\frac{\partial \bar{c}}{\partial z}=e_{t_x}\frac{\partial^2 \bar{c}}{\partial x^2}+e_{t_y}\frac{\partial^2 \bar{c}}{\partial y^2}+e_{t_z}\frac{\partial^2 \bar{c}}{\partial z^2} \qquad \text{2-14}$$

where $e_{t_x}$ , $e_{t_y}$ and $e_{t_z}$ are turbulent diffusion coefficients in $x$, $y$ and $z$-direction, respectively. Since turbulent diffusion is anisotropic it has different values in different directions. In contrast with the molecular diffusion coefficient, the turbulent diffusion coefficient is a property of the flow and varies with the velocity, turbulence and geometry of the flow. A few of the flow and turbulence properties which affect the turbulent diffusion and mixing, in general, are introduced here.

One of the turbulence characteristics is turbulence intensity. This is defined as the ratio of the root-mean-square of the velocity fluctuations over the mean velocity, Eq. 2-15:

$$I=\frac{u_{rms}}{\bar{u}}=\frac{\sqrt{\frac{1}{N}\sum_{i=1}^{i=N}u'^2}}{\bar{u}} \qquad \text{2-15}$$

where $I$ is the turbulence intensity. Another property of flow that affects the turbulent diffusion is shear or the spatial variation of velocity. Shear generates turbulence and the stronger the shear, the stronger the turbulence (Nepf, 2008). A parameter that is a measure of the strength of the shear (and is also proportional to many turbulent properties) is the shear velocity $u*$, defined as:

$$u*=\sqrt{\frac{\tau_0}{\rho}} \qquad \text{2-16}$$

where $\tau_0$ is the bed shear and $\rho$ is the fluid density. For uniform open channel flow, the bed shear is balanced by gravity, thus:

$$u^* = \sqrt{ghS} \tag{2-17}$$

where $S$ is the channel slope, $h$ is the depth of the flow and $g$ is acceleration due to gravity. The relationships between the above-mentioned parameters and different mixing coefficients are discussed in detail in the following sections.

### 2.3.2 Shear Dispersion

The main mixing processes i.e. advection, molecular and turbulent diffusion which have been introduced so far, are independent specific physical processes. While shear dispersion, as will be explained further, is not a physical property, but an approximation to account for the shear effect of differential advection and diffusion. As a result of the shear, different parts of a tracer cloud will advect at different speeds, i.e. differential advection. It will cause the tracer cloud to be stretched, or in other words, spread longitudinally more quickly than a cloud released into a uniform flow. Another effect of differential advection is the transverse concentration gradient, which in turn increases the transverse diffusion both molecular and turbulent, Figure 2-3, (Nepf, 2008).

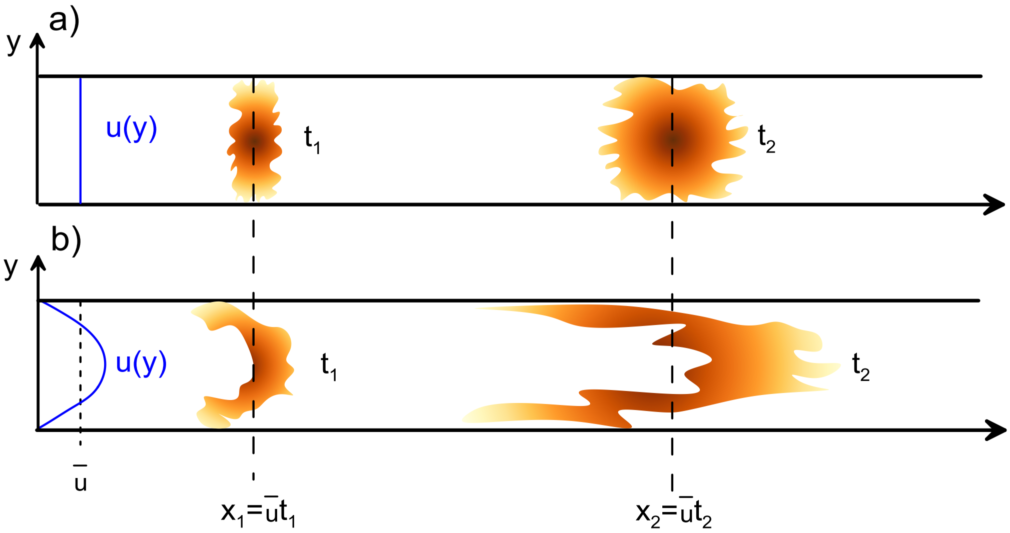

**Figure 2-3 Reproduced Figure 8-1 from Nepf (2008) effect of shear dispersion in a) a uniform velocity profile b) non-uniform velocity profile with the no-slip boundary condition**

Two boundary conditions are shown in Figure 2-3, the top channel shows the condition where the side walls allow slip, and thus the velocity is uniform across the channel, while the bottom channel has the no-slip boundary condition which results in a transverse velocity profile and velocity shear, $\frac{\partial u}{\partial y}$ . Although the mean longitudinal velocity is the same for both channels and the centre of mass for both clouds advects at $\bar{u}$ , velocity shear in the bottom channel stretches the tracer cloud and this cloud spreads longitudinally more rapidly than the cloud in the uniform channel (Nepf, 2008).

The transverse concentration gradient caused by differential advection increases the turbulent diffusion. Turbulent diffusion, in turn, acts to decrease the concentration gradient by increasing the transverse mixing. One way to measure all these processes is to measure them individually which is not always possible, as it requires precise velocity and turbulence measurements or modelling. The other option which is widely used in the field, laboratory and modelling, is depth and/or width averaging the effects of velocity distributions, and express them as a vertical, longitudinal or transverse dispersion coefficient. More detailed explanations on longitudinal and transverse dispersion are provided in the next sections. As all the models used in this thesis are two-dimensional planar models, the vertical mixing is not explained here, for the sake of brevity.

## 2.3.3 Transverse Dispersion

Natural watercourses usually have a large width to depth ratio; thus point sources of pollution become vertically well mixed within a distance equivalent to few water depths, a region termed near-field. Then over the mid-field region, the fully transverse mixing happens and finally, the longitudinal mixing is concerned with the development of a plume in the far-field. Hence it is normal to use a depth-averaged form of the advection-dispersion equation for evaluating the transverse mixing, Eq. 2-18

$$\frac{\partial c}{\partial t} + u\frac{\partial c}{\partial x} = D_y \frac{\partial^2 c}{\partial y^2} \qquad \text{2-18}$$

where $D_y$ is the transverse dispersion coefficient, representing the combined effects of molecular and turbulent diffusion and dispersion.

The transverse dispersion coefficient can be evaluated from Eq. 2-5 which was presented in §2.2.2, but by investigating the change in transverse variance with distance, i.e. Eq. 2-19

$$D_y = \frac{u_0}{2} \frac{d\sigma_y{}^2}{dx} \qquad 2\text{-}19$$

Eq. 2-19, has been used along with recorded temporally averaged transverse concentration profiles, i.e. concentration versus transverse distance profiles in order to estimate $D_y$. Numerous researchers have investigated transverse mixing under idealised laboratory conditions, i.e. straight, rectangular channels with uniform flow conditions. An example is a study done by Webel and Schatzmann (1984) who carried out 63 experiments in a 20.00 m long, 1.82 m wide rectangular flume set with 4 different bed slopes and 3 different effective roughness heights. A range of velocities from 0.056 m/s to 0.171 m/s resulting in *Re* number of 1900 to 13300 were tested.

Two nondimensionalized forms of $D_y$ were used as $D_y / u^*h$ and $D_y / ud$ and their behaviour over different $B/h$ ratios, $B$ is the width of the flume, was investigated. Using $h$ and $u^*$ for nondimensionalizing is very common as $h$ governs the upper length scale of turbulent eddies and $u^*$ is a measure of the flow resistance generating turbulence. $u^*$ was calculated from Eq. 2-17. The results ranged from 0.010 to 0.020 for $D_y / ud$ and from 0.130 to 0.180 for $D_y / u_* h$. Rutherford (1994) reports the results of several similar studies as Figure 2-4 and an overall range of 0.10 to 0.26 for $D_y / hu_*$ as well as a constant rough value of 0.13.

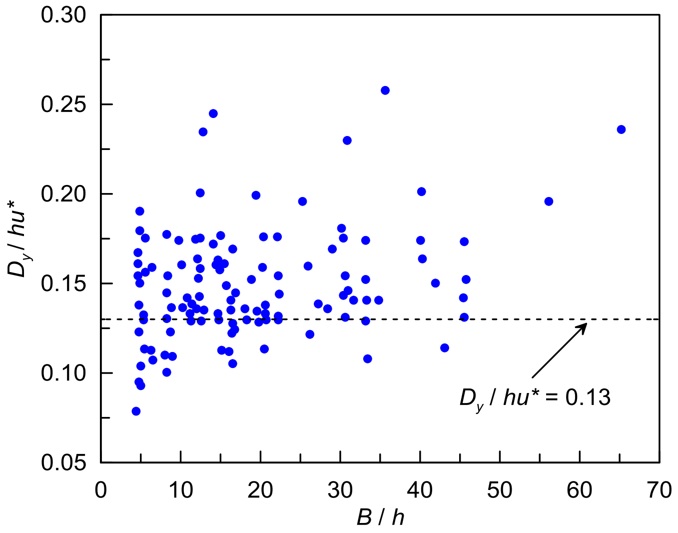

**Figure 2-4 Reproduced Figure 3.2 from Rutherford 1994, a summary of experimental measurements of the transverse diffusion coefficient in straight, rectangular laboratory channels.**

Several studies, e.g. Boxall and Guymer (2004) and Guymer and Dutton (2005) have investigated the effect of natural conditions such as bending on transverse mixing coefficient, but as this thesis is focused on straight rectangular channels, these studies are not reviewed here.

## 2.3.4 Longitudinal Dispersion

Figure 2-5 shows the cross-sectional averaged dye concentrations versus time measured at six sites downstream of an instantaneous dye injection to the Waikato River, New Zealand (Rutherford, 1994). It can be seen from Figure 2-5 that as the tracer is carried downstream the peak concentration decreases and the cloud has the tendency to disperse over the channel length. This process is termed longitudinal dispersion. One example of the applications of longitudinal dispersion is the environmental studies downstream of a polluting discharge, e.g. a factory, a road tanker accident or Combined Sewer Overflows (CSOs).

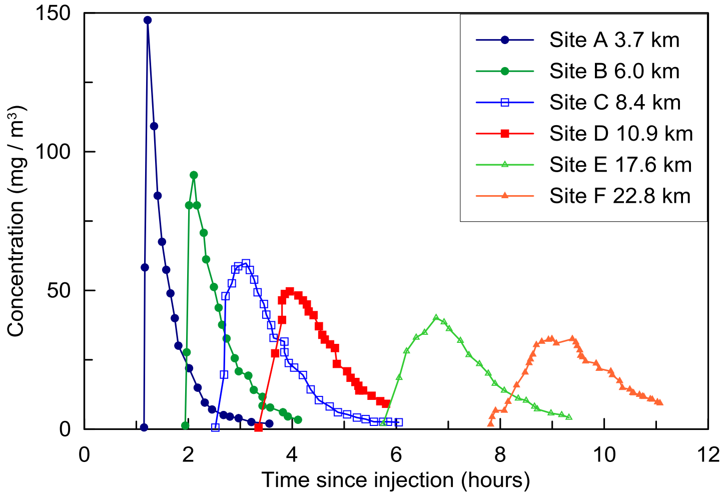

**Figure 2-5 Reproduced Figure 4.1 from Rutherford, 1994, Cross-sectional averaged dye concentrations measured at six sites on the Waikato River below an instantaneous transverse line source**

Studies on similar data sets to that presented in Figure 2-5 have shown that the tracer cloud at the beginning is very much affected by the velocity profile across the channel. Thus the region close to the source is termed the advective zone to emphasise the importance of advective processes over diffusion and dispersion processes. Within the advective zone, the longitudinal concentration profiles are negatively skewed i.e. the rising limb is shorter than the falling limb, as can be seen in Figure 2-5. The behaviour of variance and skewness of the longitudinal concentration profiles over different regions of the channel is shown in Figure 2-6.

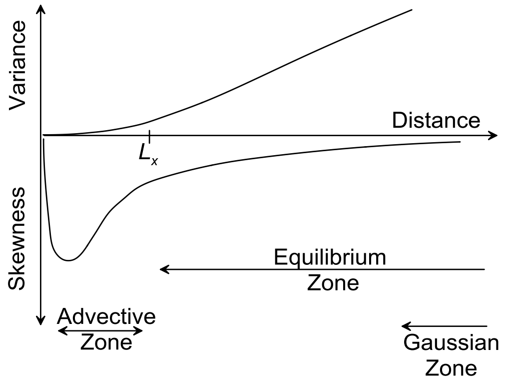

**Figure 2-6 Reproduced figure 4.4 from Rutherford, 1994, Fickian model predictions of how the variance and skewness of a concentration profile change with time**

$L_x$ in Figure 2-6 is the length of the advective zone and it is at this point where an equilibrium between transverse velocity shear, which promotes longitudinal dispersion and transverse diffusion which counteracts longitudinal dispersion, becomes established. “Beyond this point two things happen. Firstly, the longitudinal variance of the cross-sectional averaged tracer concentration increases linearly with time. Secondly, any skewness introduced by velocity shear in the advective zone or by the initial distribution of tracer begins to decay slowly and eventually the spatial tracer distribution becomes Gaussian. The zone in which the variance increases linearly is known as the equilibrium zone” (Rutherford, 1994). Shucksmith et al. (2007) studied the importance of advective zone in longitudinal mixing experiments and explained that the advective zone is equivalent to the distance for each particle to travel to experience the complete flow regime.

The advection-dispersion equation for the cross-sectional averaged concentration, within the equilibrium zone, is as Eq. 2-20

$$\frac{\partial c}{\partial t}+u\frac{\partial c}{\partial x}=D_x\frac{\partial^2 c}{\partial x^2} \qquad 2\text{-}20$$

where $D_x$ is the longitudinal dispersion coefficient. $D_x$ includes the effects of velocity shear and turbulent mixing, both transverse and vertical, thus its value depends on the hydraulic properties of the channel. If $u$ and $D_x$ are assumed to be constant then the general solution to Eq. 2-20, for an instantaneous injection is, Eq. 2-21,

$$c(x,t)=\frac{M}{A\sqrt{4\pi D_x t}}exp\left[-\frac{(x-ut)^2}{4D_x t}\right] \qquad 2\text{-}21$$

where $M$ is the mass of the injected tracer and $A$ is the cross-sectional area of the channel.

The majority of studies on longitudinal dispersion coefficient are on natural streams and data on laboratory flumes is less available. The range of values reported for $D_x$ is wider than that for $D_y$. Rutherford (1994) reports the range of 30 to 3000 for $D_x / hu^*$ previously measured for 56 different rivers around the world.

Elder (1959) is one of the most cited studies on $D_x$ in laboratory channels. He expanded the application of the analysis used by Taylor (1954) to the case of turbulent flow in a channel. He considered the von Karman logarithmic velocity profile with the von Karman constant equal to 0.4 and suggested the value of $5.93hu_*$ for the longitudinal dispersion coefficient, where $h$ is the channel depth.

## 2.4 Flow around Cylinders

The fundamental concepts of mixing in open channel flow was covered in previous sections. The focus of this thesis is on mixing within cylinder arrays. Cylinder arrays provide specific hydraulic conditions which introduce new mixing processes to what exist in open channel flows. Zdravkovich (1997) provides one of the most comprehensive collections of studies on flow around circular cylinders. It contains guidance through flow phenomena, experiments, applications, mathematical models and computer simulations, up to its date. This book has been the main source for the brief introduction on flow within cylinder arrays, presented here.

Five regions of disturbed flow have been defined for the flow past a circular cylinder, based on the variation in velocity, as shown in Figure 2-7.

(i) One narrow region of retarded flow
(ii) Two boundary layers attached to the surface of the cylinder
(iii) Two sidewise regions of displaced and accelerated flow
(iv) One wide downstream region of separated flow called the wake

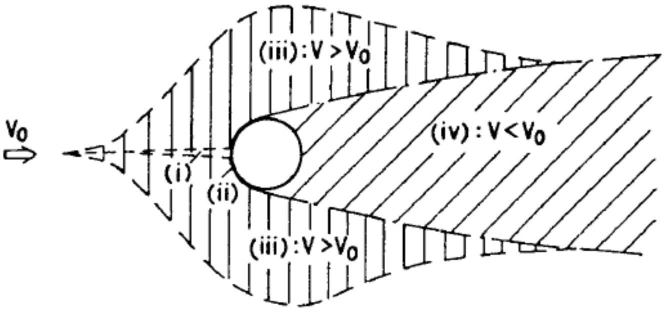

**Figure 2-7 Regions of disturbed flow around a circular cylinder, Zdravkovich (2003)**

A large number of studies have been focused on the wake region. The state of flow being laminar, transitional or turbulent affects the formation and decay of the flow structures in the wake. Reynolds dimensional analysis was first used by Rayleigh, (1896) who considered the external diameter of the cylinder as the characteristic length and used it in the field of acoustic studies. Henceforth this Reynolds number is referred to as $Re_d$, i.e. Reynolds number based on the diameter considered as the characteristics length. $Re_d$ has been singled out as the governing parameter for specifying different stages of flow around a nominally two-dimensional cylinder. Different stages of flow around a cylinder have been defined as below:

L1: creeping flow or non-separation regime; $0 < Re_d < 4$ to 5

L2: steady separation of the closed near-wake regime; 4 to $5 < Re_d < 30$ to 48

L3: periodic laminar regime; 30 to $48 < Re_d < 180$ to 200

Creeping flow is firmly attached to the surface of the cylinder all around the circumference and separation happens when a distinct, steady, symmetric and closed near-wake is formed. An example of creeping flow is provided in Figure 2-8 from Dyke (1982), a comprehensive collection of fluid motion pictures.

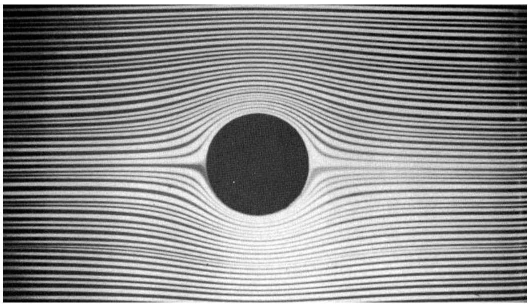

**Figure 2-8 Dyke (1982), Figure 1, Creeping flow around a circular cylinder**

Separation starts at $Re_d = 4$ to 5, and a distinct, steady, symmetric, and closed near-wake is formed, Figure 2-9. The stretched closed near-wake becomes unstable for $Re_d > 30\text{-}48$ and a sinusoidal oscillation of shear layers commences at the confluence point. The onset of oscillation is sensitive to disturbance and the transition $Re_d$ depends on particular experimental arrangements. The amplitude of the trail oscillation increases with rising $Re_d$ and for $Re_d > 45\text{-}65$ the shear layers roll up at crests and troughs and finally a staggered array of laminar eddies is formed, Figure 2-10, a, b, and c.

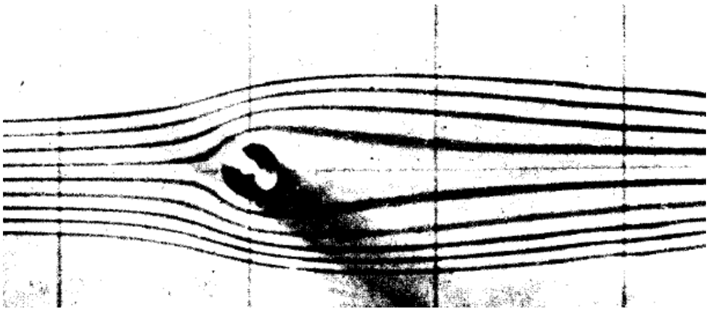

**Figure 2-9 Zdravkovich (2003) Figure 1.5, Steady closed near-wake $Re_d = 23$**

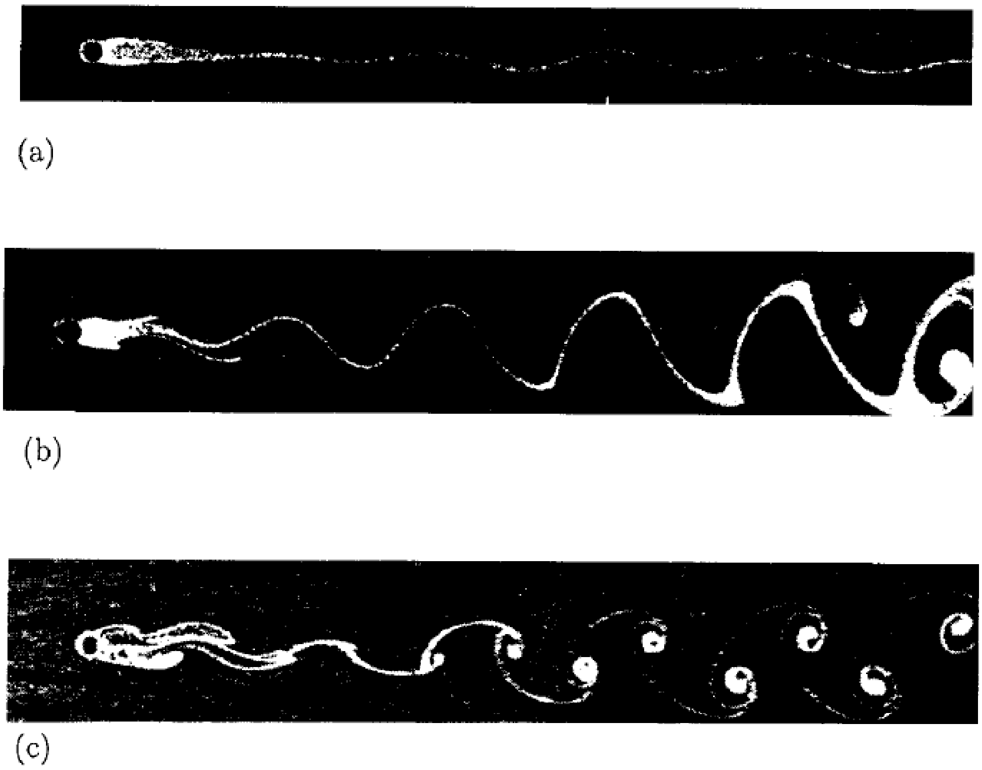

**Figure 2-10 Zdravkovich (2003), Figure 1.6. Periodic laminar wake: a) $Re_d$ = 54, b) $Re_d$ = 65, c) $Re_d$ = 102**

Teodor von Karman was one of the first to observe and discuss the formation of eddies behind a cylinder. Thus the repeating pattern of eddies is referred to as a 'Von Karman Street' in the literature.

After this stage, as $Re_d$ increases, the laminar periodic wake becomes unstable further downstream in the wake, Figure 2-11a. Transition spreads gradually upstream with increasing $Re_d$ until the eddy becomes turbulent during its formation, Figure 2-11b. This state can be divided into two regimes:

Tr1) Transition of laminar eddies in the wake from 180-200 < $Re_d$ < 220-250

Tr2) Transition of an irregular eddy during its formation, from 220-250 < $Re_d$ < 350-400

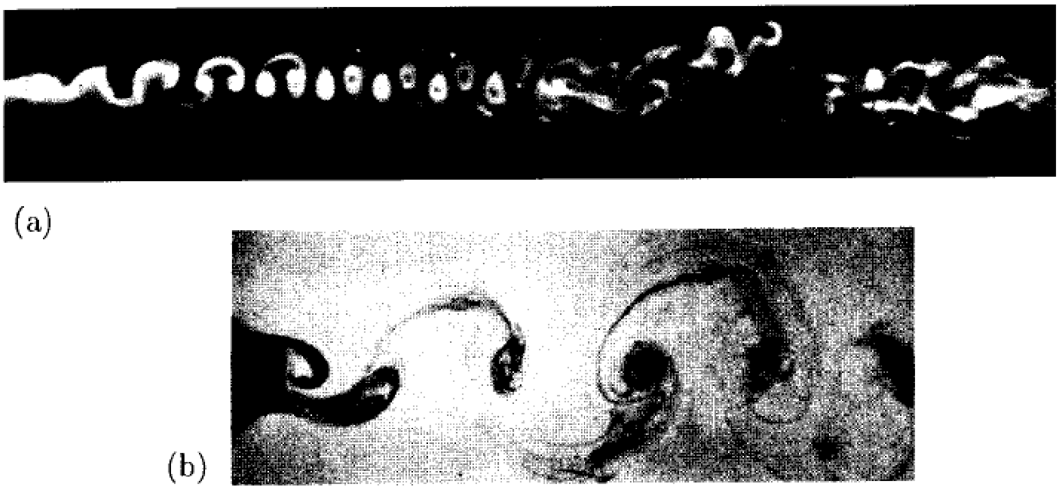

**Figure 2-11 Zdravkovich (2003) Figure 1.8 Transition in the wake a) $Re_d$ = 190, b) $Re_d$ = 340**

A similar categorisation has been used in other studies e.g. Nepf et al. (1997a), Nepf et al. (1997b), Nepf (1999) and Tanino and Nepf (2008b) where for $10 < Re_d < 100$ "a steady recirculation bubble containing a pair of counter-rotating vortices appears behind the cylinder and extends approximately one diameter downstream. In this regime, no turbulence is contributed to the downstream wake. At $Re_d = O(100)$, vortices begin to shed from the cylinder, creating turbulence in the wake" (Nepf et al. 1997b). The order of magnitude of the $Re_d$ values attributed to different stages of flow past a cylinder is very close for the two above mentioned categorizations. The only difference is in calling the vortex shedding as a laminar or turbulent regime, which does not make them totally different as both appreciate the effect of vortex shedding on the hydrodynamics of the flow and on mixing in turn. The models to be presented in this thesis cover only the range of $Re_d < 500$, thus the flow condition at higher $Re_d$ values is not discussed here.

These flow structures and patterns determine the magnitude, direction and time-variation of the fluid dynamic forces exerted on the cylinder. For example, the steady, laminar stages i.e. L1 and L2 exert a steady resistance or drag on the cylinder while the periodic laminar state, L3, generates a regular periodic force with components in different directions. In the same manner, one can say that the force generated at transitional states would have irregular and random oscillations. The fluid dynamics force, i.e. the drag force depends on the dynamic pressure, $\frac{\rho u^2}{2}$, $\rho$ being the density of water and the projected area of the cylinder facing the stream.

The drag force is usually reduced to a non-dimensional force coefficient, i.e. drag coefficient, Eq. 2-22

$$C_D = \frac{2F_{Drag}}{\rho u^2} \tag{2-22}$$

where $F_{Drag}$ is drag force. There are numerous studies on the drag force exerted on a single cylinder at different flow regimes but they are not mentioned here for the sake of brevity as the drag force and drag coefficient within the cylinder arrays are different from those of a single cylinder.

When two cylinders are placed close to each other the interference effects might cause considerable changes in flow patterns, the magnitude of forces, and eddy shedding. The interference effects strongly depend on the arrangement of the two cylinders and their orientation to the free stream. Different arrangements of cylinders include 1) The inline category which consists of square and rectangular arrays where the interstitial flow is mostly straight through the array, Figure 2-12a). 2) The staggered category which consists of a rotated square, Figure 2-12 b) normal triangle Figure 2-12 c), and parallel triangle array, Figure 2-12 d), where the interstitial flow is forced along wavy paths through the array. 3) The random distribution, Figure 2-12 e), where the interstitial flow is forced along random paths which can be a combination of the other two categories.

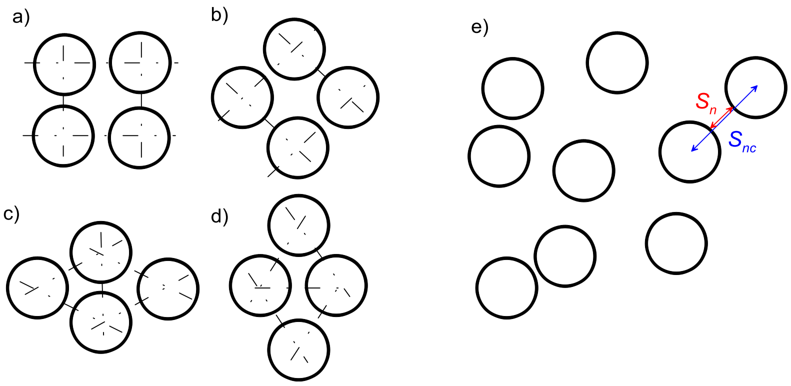

**Figure 2-12 Different cylinder array arrangements a) square, b) rotated square, c) normal triangle, d) parallel (rotated) triangle, e) random distribution**

There are numerous studies on the effect of the first two distributions on the hydrodynamics of the flow but as the arrangement used in this thesis is the random arrangement, they are not mentioned here.

Two basic metrics are used to describe the random arrays, the centre to centre distance between one cylinder and its nearest neighbour, $S_{nc}$, and the surface to surface distance between once cylinder and its nearest neighbour, $S_n$. The ensemble averages of these two metrics over the whole array are commonly used in the literature, i.e. $<S_{nc}>_A$ and $<S_n>_A$, where $< >_A$ denotes an average over many cylinders in the array (Tanino and Nepf, 2008).

Other metrics used in the literature to describe the random cylinder arrays include Solid Volume Fraction, mentioned in this thesis by the symbol ø. The solid volume fraction is defined as the area occupied by cylinders per unit horizontal area. Thus, in an array consisting of $n$ cylinders of diameter $d$, the solid volume fraction would be calculated as Eq. 2-23,

$$ø = n\pi d^2 \big/ 4 \qquad \text{2-23}$$

where ø is the solid volume fraction and $n$ is the number of cylinders per unit horizontal area.

Another metric is the frontal cylinder area per unit volume, $a$, calculated based on Eq. 2-24,

$$a = nd = \frac{dh}{<S_n>_A{}^2\, h} = \frac{d}{<S_n>_A{}^2} \qquad \text{2-24}$$

where $n$ is the number of cylinders per unit area, $S_n$ is the average spacing between cylinders, $h$ is the flow depth, and $d$ is the cylinder diameter. A dimensionless population density has been defined and used in the literature as $ad = \frac{d^2}{<S_n>_A{}^2}$.

$ad$ for a cylinder array represents the fractional volume of the flow domain occupied by cylinders and has been used in investigating the effect of density on drag.

## 2.5 Laboratory Studies on Flow and Turbulence within Cylinder Arrays

Due to its implication in engineering, flow around cylinders has been the subject of many studies. A comprehensive collection of studies conducted up to 1997 are provided in a Zdravkovich (1997) in two volumes covering the fundamentals and applications of flow around cylinders. A more recent collection can be found in

Bearman (2011), who provided a review of research on vortex-induced vibrations of single cylinders. Most of the more recent studies on flow around a single cylinder have investigated the effect of an additional element such as a plane wall, e.g. Price et al. (2002), or a splitter plate e.g. Akilli et al. (2005), Shukla and Henthom (2009) and Yayla and Teksin (2018) on vortex shedding. Flow around perforated or permeable cylinders has also been the subject of many recent studies e.g. Pinar et al. (2015) and Gao et al. (2017).

A comprehensive review of numerical and laboratory studies on flow around two cylinders is provided in Sumner (2010) who reviewed more than 70 studies conducted from 1934 to 2009. A considerable number of researchers have studied the flow around a group of four cylinders, e.g. Lam and Lo (1992), who conducted a visualization study of flow around four cylinders in different square configurations at $Re_d = 2100$. The same set of laboratory experiments was repeated by Wang et al. (2013) at $Re_d = 8000$ and also by a great number of other researchers during this time.

Among the recent laboratory studies on flow within staggered cylinder arrays, Liu et al. (2008) provided a detailed study of flow within a 3.0 m long and 3.0 m wide staggered array of 0.006 m diameter cylinders. This study provided comprehensive longitudinal and vertical velocity and turbulence measurements at $u$ = 0.1 to 0.3 m/s. Both submerged and emergent arrays were studied. Their measurements on the emergent cylinder arrays showed that “the turbulence intensity remains relatively constant through the entire flow depth at a given location.” Other similar studies include Paul et al. (2008), Ozturk et al. (2016), and da Silva et al. (2018).

An innovative study was conducted by Ricardo et al. (2014) who measured velocity and turbulence within randomly distributed cylinder arrays of constant diameter but non-uniform density through the array. The tests were performed in a 10.1 m long and 0.40 m wide flume. The array was formed of 0.011 m diameter cylinders forming a minimum and maximum density of $ø = 0.04$ and of $ø = 0.15$ equivalent to $n = 400$ stems/m$^2$ and $n = 1600$ stem/m$^2$, respectively, as shown in Figure 2-13. “The dashed rectangles show the regions where horizontal velocity maps (PIV) were acquired for each longitudinal position (P1-P8). The solid lines aligned with flow direction indicate the location of the vertical planes measured with PIV. The points along lines perpendicular to the flow direction represent the location of LDA measurements (P3-P8)" (Ricardo et al. 2014). The variation of $n$, the number of stems per area, along the flume is also shown in Figure 2-13.

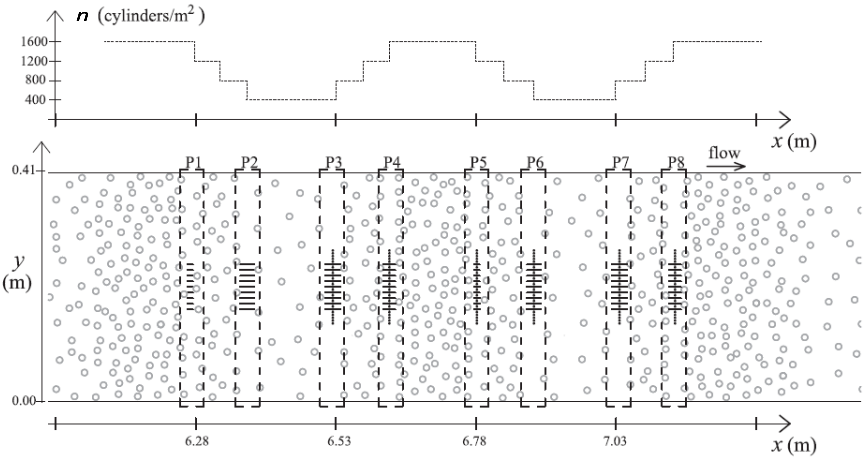

**Figure 2-13 Ricardo et al. (2014) figure 1, plan view of the cylinder array**

An example of measured longitudinal velocity contour maps is shown in Figure 2-14

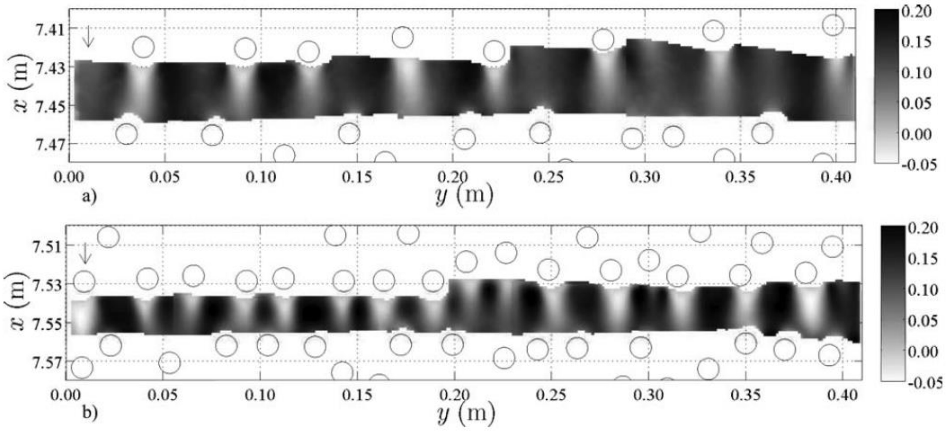

**Figure 2-14 Ricardo et al. (2014) figure 2, contour plots of longitudinal velocity, *u* (m/s) for measuring gaps a) P7 and b) P8. The arrow indicates the flow direction**

A similar study was conducted by Ricardo et al. (2016) in which the array used in Ricardo et al. (2014) was compared with a randomly distributed array of uniform density, $ø = 0.09$ and $n = 980$ stems/m$^2$. The vertical profiles were shown to comprise three layers. The layer close to the bottom, "where the flow is highly 3D due to interaction with the bed; a thin layer close to the free surface, which is affected by the oscillations of the free surface; and an intermediate layer, sufficiently away from the bed and from the free surface, where the flow is controlled by the vertical stems and the flow properties are approximately constant in the vertical direction" (Ricardo et al. 2016). Their measurements were focused on the last stem-dominated layer, where time-averaged vertical velocity is nearly zero. An example of the measured velocity profiles for longitudinal, *u*, transverse, *v*, and vertical, *w*, components is shown in Figure 2-15(a). The corresponding Reynolds stresses are shown in Figure 2-16. Case A in these figures refers to the non-uniform density array shown in Figure 2-13 and case B refers to the uniform density array.

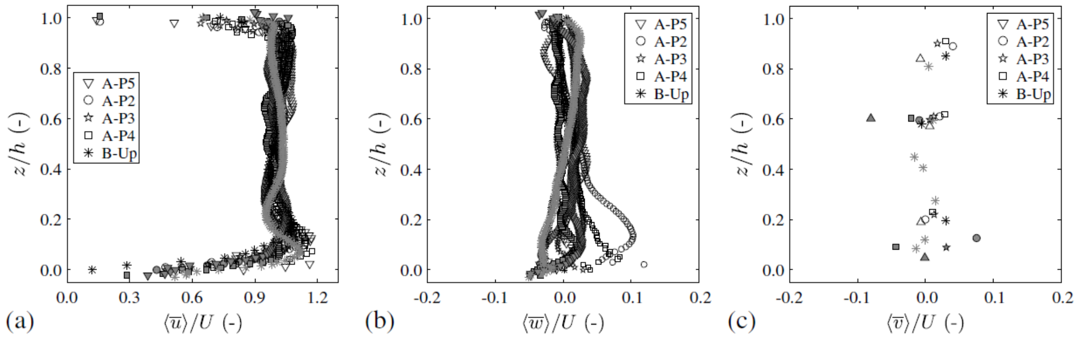

**Figure 2-15 Ricardo et al. (2016) figure 3, time and space-averaged velocity profiles normalized by *u*, a) longitudinal, b) vertical, c) lateral components**

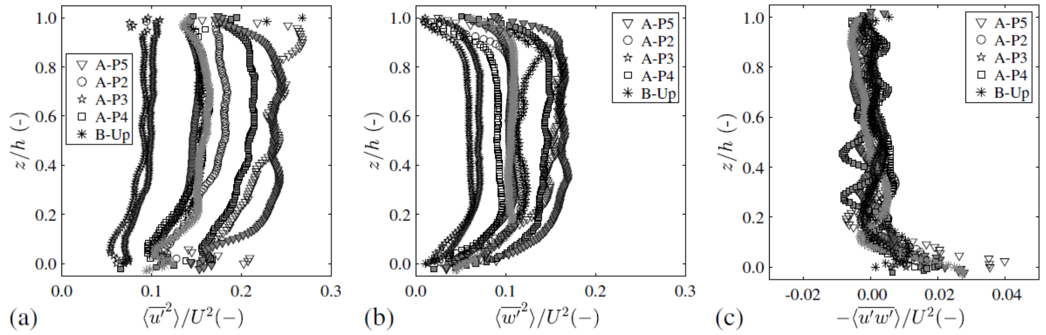

**Figure 2-16 Ricardo et al. (2016) figure 4, time and space-averaged Reynolds stress profiles normalized by *u*$^2$, a) longitudinal, b) vertical, c) lateral components**

The results of these two studies confirm the acceptability of modelling the random cylinder arrays as two-dimensional planar models, for $0.2 < z/h < 0.9$, Figure 2-15(a). They also provide a potentially valuable data set which can be used to validate the Computational Fluid Dynamics (CFD) models. These datasets, along with the results of studies on mixing within cylinder arrays, presented in the next section, will be compared with the results of the CFD models provided in this thesis in the following chapters.

## 2.6 Laboratory Studies on Mixing within Cylinder Arrays

The similarity between rigid cylinder arrays and “the stem regions of the marsh grass *Juncus roemerianus* (needle rush) and *Spartina alterniflora* (smooth cordgrass), which under normal tidal conditions exhibit only limited bending” (Nepf et al. 1997b) has been mentioned in the literature as a justification for studying flow and mixing within cylinder arrays. A new surge of studies on flow and mixing within cylinder arrays started around 1997, which include developing numerical models to describe mixing processes such as turbulent diffusion and dispersion as well as comprehensive laboratory experiments. As understanding the more recent studies such as Tanino and Nepf (2008) would be difficult without following the previous steps taken in developing this set of studies; a chronological review of these studies is provided in this section. It should be mentioned that the studies concerned with submerged cylinder arrays, flexible/real vegetation and also partially vegetated channels are not included here. Thus only the studies that are directly related to this thesis are reviewed in this section, i.e. those concerned with flow and mixing within emergent rigid cylinder arrays randomly distributed across the full channel width.

### 2.6.1 Transverse Mixing

Dividing the flow field into the wake and non-wake fields, Nepf et al. (1997b) suggested a modification to the random walk model previously suggested by Fischer et al. (1979) to describe the turbulent diffusion taking place within cylinder arrays. They suggested Eq. 2-25

$$D_y = \omega u d WF \tag{2-25}$$

where $\omega$ is a scale factor of $O$ (1), $d$ is the cylinder diameter and $WF$ is the area fraction occupied by wakes.

The value of $WF$ in an array is not equal to the summation of the wakes of all the cylinders, as by increasing the number of cylinders their wakes get overlapped by other cylinders. In other words, the product of ø and $M$, $M$ being the ratio of wake area to stem area for each cylinder, is more than $WF$. A nonlinear relation between ø and $WF$ was suggested by Nepf et al. (1997b) which is presented in Figure 2-17.

It was explained that for low ø values, *WF* increases linearly while as ø increases the relationship becomes more nonlinear. A linear function is included for reference.

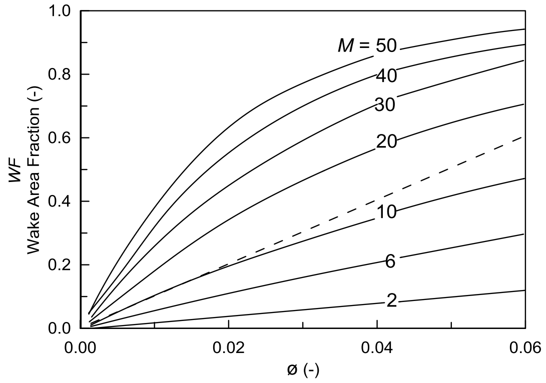

**Figure 2-17 Reproduced Figure 2 from Nepf et al. (1997b), wake area fraction versus ø**

Two sizes of cylinders $d = 0.006$ and 0.012 m were tested and five densities of $ø = 0.006$, 0.014, 0.017, 0.035, and 0.053 were considered. No explanation for the distribution of the cylinders was provided but it can be realized from a schematic figure provided in the paper that the cylinders were randomly distributed.

Longitudinal and vertical velocities were measured using two-dimensional Laser Doppler Velocimetry (LDV) and the concentration of the tracer injected as a continuous injection was measured using laser-induced fluorescence (LIF). A range of $66 < Re_d < 1800$ was tested, and by observing the streak patterns of dye the onset of vortex shedding was reported to be between $Re_d = 150$ and 200.

The transverse dispersion coefficients were estimated by fitting Gaussian profiles to the observed concentration profiles. The coefficients were nondimensionalized by open stream velocity, $u$, and cylinder diameter, $d$. A curve was fitted based on $M = 10$ as shown in Figure 2-18. The fitted value of $A$ was not reported. It is interesting to note that the value of $M = 40$ was previously suggested for a single cylinder, i.e. a $2d$ wide and $20d$ long wake, and for the tested arrays this value reduced 4 times. The fact that results of $Re_d < 200$ did not follow the fitted line, was justified by no vortex shedding at this stage.

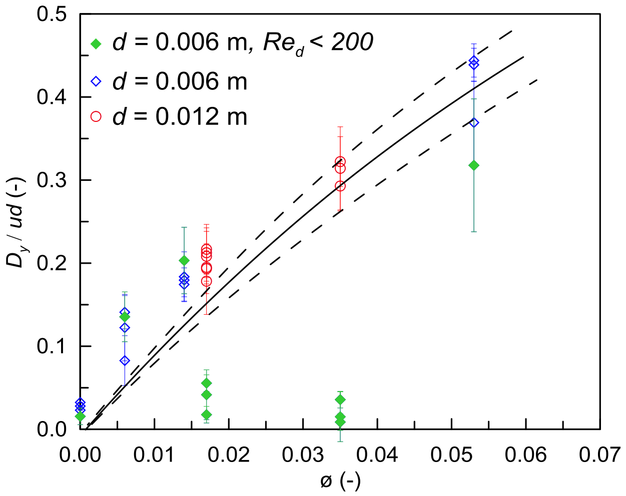

**Figure 2-18 Reproduced Figure 6 of Nepf et al. (1997b) based on the data provided in Table 1 of Nepf et al. (1997b)**

Figure 2-18 was produced based on the data provided in Table 1 of Nepf et al. (1997b) and shows discrepancies with the figure provided in the paper, i.e. figure 6 from Nepf et al. (1997b). No explanation on the difference between the data provided in the table and presented in the figure was provided in the paper.

A similar laboratory setup was used by Nepf (1999) who measured velocity and turbulence as well as drag force and transverse dispersion coefficient in random arrays made of 0.0064 m diameter wooden dowels. The density of the arrays was between $a = 1.2$ and 10.5 $\mathrm{m}^{-1}$ with $ad = 0.008$ to 0.07 which is equivalent to $n = 200$ to 2000 stems per $\mathrm{m}^2$ (refer to Eq. 2-24). A 3-D acoustic Doppler velocimeter (ADV) and a 2-D laser Doppler velocimeter (LDV) were used, positioned at the mid-length of the array to provide the velocity components, $u$, $v$, and $w$, i.e. longitudinal (streamwise), transverse and vertical velocities. Measurements were done at five transverse positions and the mean and turbulent velocity statistics were then averaged. The surface slope, $\Delta h$, was measured using a pair of resistance-type surface displacement gauges with 0.0002 m resolution.

The drag coefficient for the whole array was calculated based on Eq. 2-26,

$$(1-ad)C_B u^2 + \frac{1}{2}C_D ad\left(\frac{h}{d}\right)u^2 = gh\frac{\Delta h}{\Delta x} \qquad \text{2-26}$$

where the first term on the left is the drag exerted by channel bed, $C_B$ is the bed drag coefficient which was considered equal to 0.001 based on a previous study, and the second term on the left is the drag exerted by the cylinders. The resulting

$C_D$ values of this study are presented in Figure 2-19 against *ad* values. The measurements were also done for a staggered array as well as a field of real vegetation, but only the results of the random array are represented here Figure 2-19.

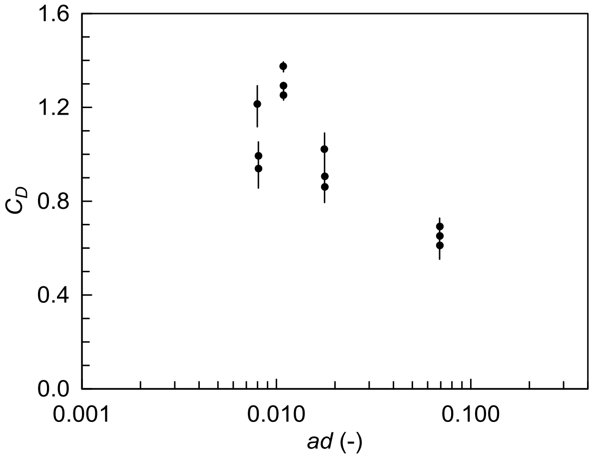

**Figure 2-19 Reproduced Figure 6 of Nepf (1999), drag coefficient against *ad*, only the results of random arrays are included**

It was suggested that there is a balance between the wake production energy, i.e. the work input at the wake area, and the viscous dissipation. The wake production energy was defined as the product of the drag force and the longitudinal velocity, Eq. 2-27,

$$p_w = \frac{1}{2} C_D a u^3 \qquad 2\text{-}27$$

where $p_w$ is the wake production energy. By assuming the stem diameter as the characteristic length scale, the dissipation rate was suggested to be scaled based on Eq. 2-28, as was suggested before by Tennekes and Lumley (1990).

$$\varepsilon \sim k^{3/2} d^{-1} \qquad 2\text{-}28$$

where $\varepsilon$ is the viscous dissipation rate and $k$ is the turbulent kinetic energy per unit mass. By equating Eq. 2-27 with Eq. 2-28 and introducing a scale coefficient, Eq. 2-29 was suggested for turbulence intensity,

$$\frac{\sqrt{k}}{u} = \alpha_1 \left( C_D a d \right)^{1/3} \qquad 2\text{-}29$$

where $\alpha_1$ is an $O\,(1)$ scale coefficient and $\frac{\sqrt{k}}{u}$ is the turbulence intensity. The observations of this study confirmed the above assumption. The values of turbulence intensity measured in this study are presented against $C_Dad$ in Figure 2-20 in logarithmic scale. $\alpha_1$ was suggested to be equal to 0.9 ± 0.1, Eq. 2-29 is shown as the solid line on Figure 2-20.

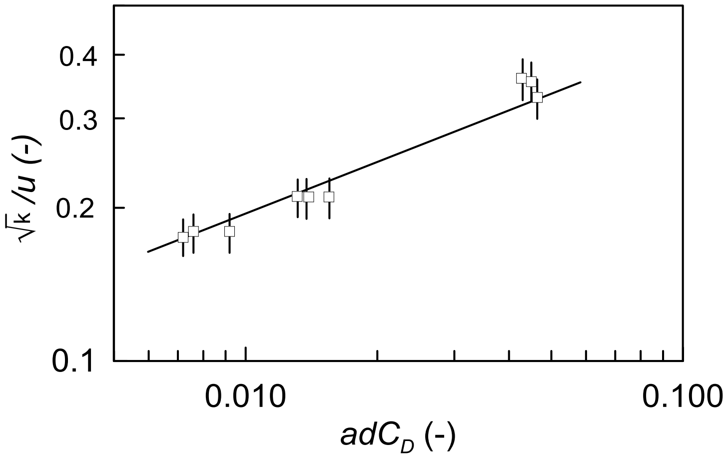

**Figure 2-20 Reproduced figure 9 from Nepf (1999), turbulence intensity for $Re_d$ = 400-900**

Again by assuming stem diameter as the characteristic length scale, and introducing another scale factor, the turbulent diffusion within arrays was suggested to be estimated based on Eq. 2-30,

$$e_t = \alpha_2 \sqrt{k} d \qquad \text{2-30}$$

where $\alpha_2$ is a scale factor and $e_t$ is the turbulent diffusion coefficient.

The concept of Mechanical dispersion (also referred to as mechanical diffusion in some studies) which was introduced for the first time by Koch and Brady (1989) for porous media, was reintroduced for cylinder arrays. It was explained that two different particles injected at the same location will experience different paths, and by going around different cylinders they will have different journey times, increasing the dispersion of the tracer, Figure 2-21.

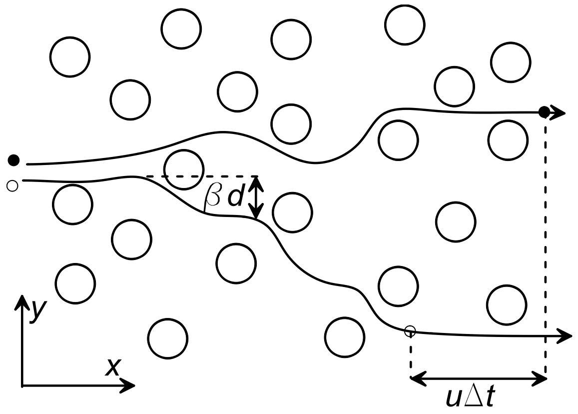

**Figure 2-21 Reproduced Figure 2 from Nepf (1999) Mechanical dispersion caused by physical obstruction of the flow by stems**

As shown in Figure 2-21, the two imaginary particles will have the distance of $\Delta x = u\Delta t$. At the same time, each particle has the probability of $a\Delta x$ to encounter a stem and change its path to the right or left along the *y*-axis. This transverse displacement is scaled by the stem diameter, i.e. $\beta d$ where $\beta$ is an *O* (1) scale factor. On average and after many steps the transverse position of an individual particle is given by a Gaussian probability distribution with the variance:

$$\sigma^2 = (a\Delta x)(\beta d)^2 \frac{t}{\Delta t} = \beta^2 (ad) udt \qquad \text{2-31}$$

where $\sigma^2$ is the variance of the transverse concentration profile.

Recalling Eq. 2-5 the mechanical dispersion coefficient can be defined as Eq. 2-33,

$$D_{mech} = \frac{\beta^2}{2} aud^2 \qquad \text{2-32}$$

where $D_{mech}$ is the mechanical dispersion coefficient. As turbulent diffusion and mechanical dispersion are independent processes, it was justified that their contribution to the transverse dispersion is additive and can be expressed as, Eq. 2-33,

$$\frac{D_y}{ud} = \alpha (C_D ad)^3 + \frac{\beta^2}{2} ad \qquad \text{2-33}$$

where the transverse dispersion coefficient is used in the non-dimensional form and $\alpha$ is the combination of $\alpha_1$ and $\alpha_2$.

The recorded transverse dispersion coefficients in this study are presented in Figure 2-22. The values of scaling factors $\alpha_1$, $\alpha_2$ and $\beta$ were suggested to be equal to 0.9, 0.9 and 1, respectively.

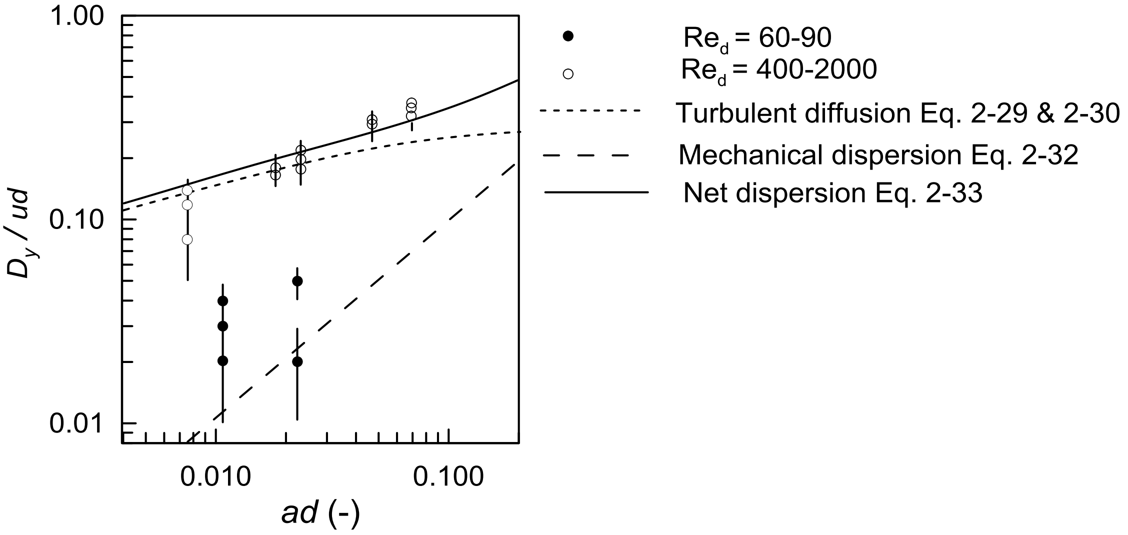

**Figure 2-22 Reproduced figure 10 from Nepf (1999) nondimensionalized transverse dispersion coefficient values, field data is excluded**

The fact that the laminar data, $Re_d$ = 60-90 generally fall above the mechanical dispersion line was attributed to the bed-generated turbulence. It was also mentioned that assuming $\beta = 2$ the mechanical dispersion line would fall directly through the middle of the laminar data (the filled circles), but it was not shown on the figure. The agreement between turbulent results (the white circles) confirmed the theoretical model.

Another laboratory study on transverse dispersion coefficient is the study done by Serra et al. (2004), who modelled a real wetland as a random cylinder array. The experiments were conducted in a 12 m long and 0.41 m wide channel, a scaled-down (20:1) model of the real wetland. The random cylinder array was made of 0.01 m diameter rigid plexiglass rods forming solid volume fractions of ø = 0.10, 0.20 and 0.35. The $Re_d$ was varied between 10 and 100 (the typical $Re_d$ of the real wetland = 16). The tracer, a fluorescein dye was continuously injection and an argon ion laser beam was used to record the concentration. The typical distances from the injection point to where the concentration was recorded was between 0.08 to 0.26 m, which can be regarded as a limitation.

The importance of the ratio of $d / <S_n>_A$ was introduced for the first time and two characteristic lengths, $d$ and $S_n$, were considered. Considering high values of solid volume fraction which means very small values of $<S_n>_A$, the stem diameter, $d$, was considered as the most appropriate value to scale the dispersion. Thus, following the same approach as Nepf (1999), Eq. 2-34 and Eq. 2-35 were considered as the basis for their theoretical model.

$$D_y = \beta C_D u \frac{d^2}{<S_n>_A} \qquad 2\text{-}34$$

or

$$\frac{D_y}{ud}\frac{<S_n>_A}{d} = \beta C_D \qquad 2\text{-}35$$

$G$ a geometric parameter taking into account the geometry of the array, was defined as the product of $n$ and $<S_n{}^2>_A$.

$$G = n < S_n >_A{}^2 \qquad 2\text{-}36$$

For each ø = 0.05, 0.10, 0.20 and 0.35, five different combinations of $S_n$ and $d$ were produced using a computer program, i.e. for each ø, five different arrays were designed based on different diameters and different distances between cylinders. The range of these values was not mentioned in the paper. Recalling $ø = n\pi d^2/4$, and combining it with Eq. 2-36, the values of ø for these 15 geometries were plotted against $(d / <S_n>_A)^2$ in Figure 2-23 to find the value of $G$, based on Eq. 2-37,

$$ø = G\pi/4(d/<S_n>_A)^2 \qquad 2\text{-}37$$

The slope of the solid line, i.e. $G\pi / 4$ in Figure 2-23 is approximately equal to 2.67 which means G ≈ 3.4. The horizontal error bars represent the standard deviation of different geometries, i.e. array instances.

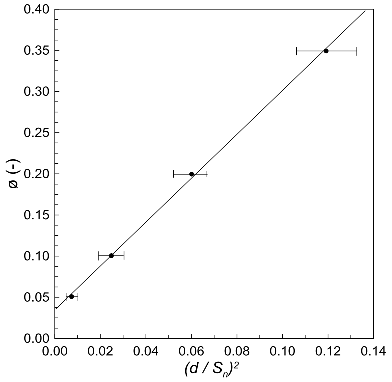

**Figure 2-23 Reproduced figure 1 form Serra et al. (2004) solid volume fraction against $(d / \langle S_n \rangle_A)^2$ *for imaginary arrays of ø* = 0.05, 0.10, 0.20 and 0.35**

It can be seen from Figure 2-23 that as ø increases the range of $d / \langle S_n \rangle_A$ values also increases. Nonetheless based on the results of these 15 cases this value of *G* was considered a general value and was used to nondimensionalize the previously published data.

The resulting transverse dispersion coefficients were plotted in the nondimensionalized form as presented in Eq. 2-35, against $Re_d$. Two flow depths of 0.034 m and 0.047 m were tested as it is included in Figure 2-24. The cylinders were emergent for both depth conditions. The previously published data from Nepf et al. (1997b) was also nondimensionalized assuming a constant value of $G$ = 3.4.

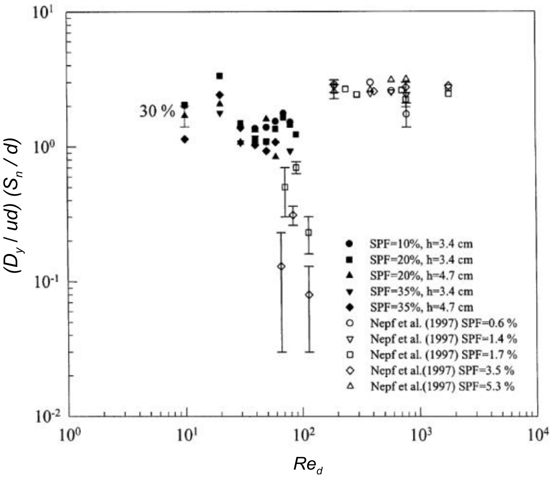

**Figure 2-24 Serra et al. (2004) figure 1, nondimensionalized transverse dispersion coefficients against $Re_d$ along with previously published data from Nepf et al. (1997)**

Based on Eq. 2-35 the "interesting trends" (which were not clearly explained in the paper) in Figure 2-24 was interpreted as the dependency of the $C_D$ on $Re_d$. It was concluded that $\beta C_D$ has the tendency to slightly decrease from 4 to 1 within the Re$_d$ range of 10 to 100. Most of the discussion provided was on the relation between $C_D$, $ø$ and $Re_d$ but the effect of these parameters on the dispersion coefficient was not discussed. The discrepancy between the previously published and new data was suggested to be due to the difference in the solid volume fractions of the two datasets. One can say that other reasons could include the difference between the materials that cylinders were made of i.e. wood and plexiglass and also assuming a constant value for $G$.

Arrays of $ø$ = 0.20 and 0.35 have been tested with two different depths and there is a noticeable difference between the results of each depth, but no explanation was provided on this matter. The fact that even after nondimensionalizing the $D_y$ values there is still a dependency on the depth of the flow, may suggest that the distance between the injection and recording has not been sufficient, i.e. the vertical mixing may not be completed yet.

The results were also compared with those from Nepf et al. (1997) and with the mechanical dispersion model suggested by Nepf (1999), as shown in Figure 2-25. The error bars show the variance of different experiments conducted at the same $ø$. The solid line is the best fit for both data series together, and follows a power law of the form $D_y / ud \sim (d^2 / \langle Sn \rangle_A{}^2)^p$, $p$ = 1.1, the value of $p$ for the relation suggested by Nepf (1999), i.e. Eq. 2-32, recalling Eq. 2-24, was equal to 1.0. It was concluded that further data are necessary to ascertain whether the Nepf (1999) model applies over a wide range of solid volume fractions.

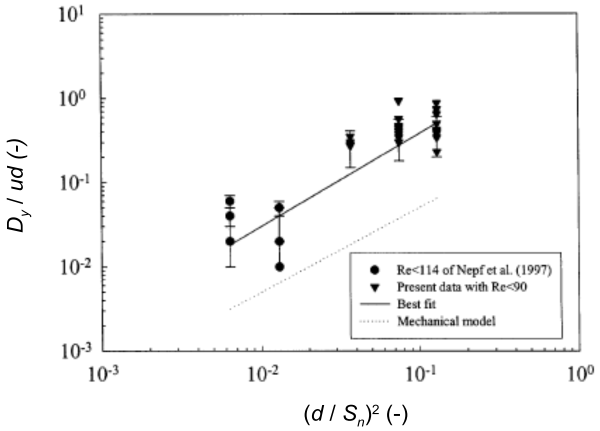

**Figure 2-25 Serra et al. (2004) Figure 6, nondimensionalized transverse dispersion coefficient against ($d$ / <$S_n$>$_A$)$^2$ along with the mechanical dispersion model**

Although a useful data set was collected by Serra et al. (2004), the discussion could be stronger by investigating the effect of ø on the dispersion coefficient for the whole range of tested $Re_d$. In order to do so, the data provided in Table 1 of Serra et al. (2004) is presented against solid volume fractions in Figure 2-26.

The difference between the results of different depths is again clear in this figure. It should be mentioned that the relationship between $D_y$ and depth is not consistent, i.e. not always the higher value corresponds to the higher depth or vice versa. Ignoring the effect of different depths, it can be seen from Figure 2-26 that $D_y$ increases with $Re_d$. It can also be seen that $D_y$ increases from ø = 0.10 to 0.20 and then decreases, for all $Re_d$ values except for $Re_d$ = 10. The difference between the results of different solid volume fractions increases with $Re_d$, which can be interpreted as some levels of turbulence introduced to the flow, although all the data are for $Re_d$ < 90 and is considered as laminar wake regime. The observed critical $Re_d$ for onset of vortex shedding was not mentioned in the paper to provide the chance of examining this possibility. More discussion on this dataset will be provided in Chapter 4, where it is compared with the results of this thesis.

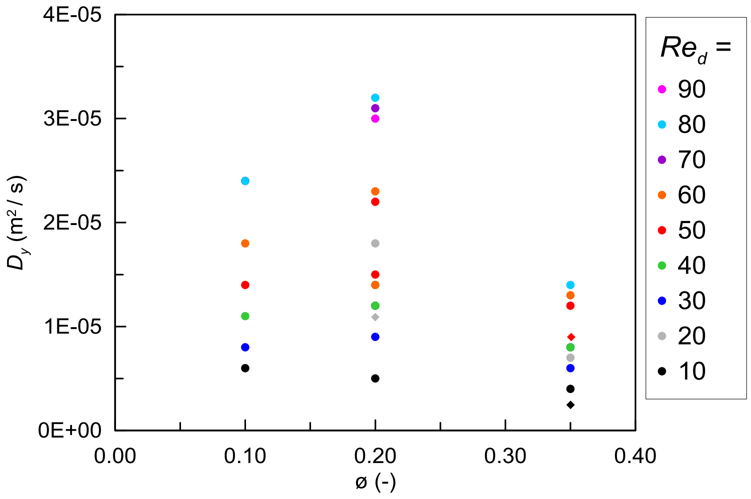

**Figure 2-26 Transverse dispersion coefficients from Serra et al. (2004) table 1, diamonds represent *h* = 0.047 m and circles represent *h* = 0.034, some data points are overlapped**

Tanino and Nepf (2008a) studied the drag coefficient within randomly distributed cylinder arrays with the similar laboratory condition to that of Nepf (1999). The solid volume fractions investigated were ø = 0.091, 0.150, 0.200, 0.270 and 0.350 and $Re_d$ was in the range of 25 to 685. The overall depth-averaged $C_D$ was estimated based on Eq. 2-38.

$$\frac{C_D^2}{2}nd = -(1-ø)g\frac{\Delta h}{\Delta x} \qquad 2\text{-}38$$

A relation based on what was previously suggested by Ergun (1952) for pressure drop in packed columns, was suggested for estimating $C_D$, Eq. 2-39,

$$C_D = 2(\frac{\theta_0}{Re_d} + \theta_1) \qquad 2\text{-}39$$

were $\theta_0$ is a function of ø and $\theta_1$ is a constant. The results of this study are shown in Figure 2-27. The dashed line indicates the drag coefficient for an isolated cylinder.

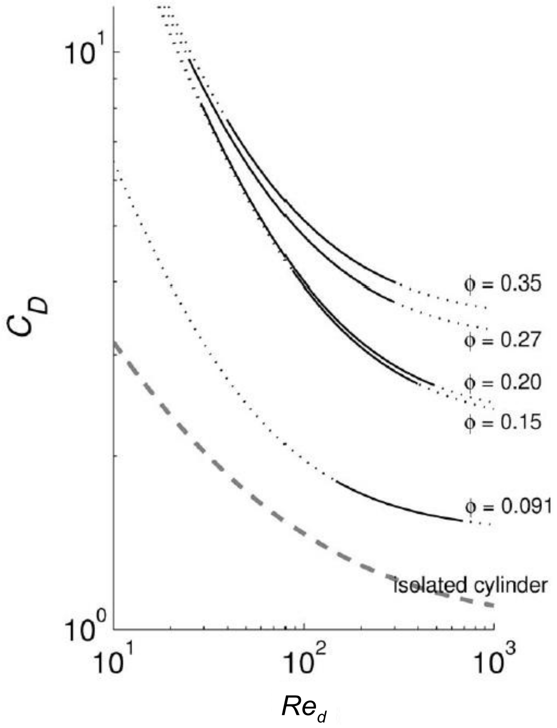

**Figure 2-27 Tanino and Nepf (2008a) figure 5, $C_D$ as a function of $Re_d$**

Based on the results presented in Figure 2-27, $\theta_1$ was suggested to be estimated based on Eq. 2-40,

$$\theta_1 = (0.46 \pm 0.11) + (3.8 \pm 0.5)ø \qquad 2\text{-}40$$

and $\theta_0$ to increase from 25±12 at ø = 0.091 to 84±14 at ø = 0.150, but to remain constant within uncertainty at 83.8 for ø = 0.150-0.350.

Sonnenwald et al. (2017) combined the results of Tanino and Nepf (2008a) and Tinoco and Cowen (2013) who also used the same equation to estimate $C_D$ and suggested Eq. 2-41 and Eq. 2-42 for $\theta_0$ and $\theta_1$.

$$\theta_0 = 7276.43d + 23.55 \tag{2-41}$$

$$\theta_1 = 32.70d + 3.01ø + 0.42 \tag{2-42}$$

Tanino and Nepf (2008b) investigated flow field and turbulence as well as transverse dispersion coefficient within random cylinder arrays. Flow and mixing measurements were done in separate channels as a result of practical issues. Flow measurements were done in a 0.670 m long and 0.203 m wide channel with random cylinder arrays of $d$ = 0.0064 m and ø = 0.010, 0.031, 0.060, 0.091, 0.150, 0.200 and 0.350. Solute transport measurements were done in a 0.284 m long and 0.400 m wide channel with random cylinder arrays of $d$ = 0.0064 m and ø = 0.010, 0.031, 0.060, 0.091, 0.150, 0.200, 0.027 and 0.350. Thus the distribution of the cylinders was different in each channel, i.e. arrays of the same ø had two different geometry instances in each channel. This shortcoming, as well as the relatively short length of the laboratory channels, has been overlooked in the literature citing this study.

The location of the cylinders was specified using the MATLAB random number generator. None of the exact distributions of the solid volume fractions is available in the literature. However, the fact that velocity measurements within a distribution of cylinders of a specific ø has been used and combined with mixing measurements within another distribution of cylinders but with the same ø, suggests the acceptability of comparing the results with any other distribution of cylinders which has the same ø but a different distribution of cylinders. This fact will be used in the validation process presented in the next chapter.

The range of flow conditions tested in this study was expressed using both $Re_d$ and $Re_S$ i.e. Reynolds number calculated based on $\langle S_n \rangle_A$ as the characteristic length. The range of $Re_d$ tested was from 67 to 480 and the range of $Re_s$ was from 53 to 660. All the $Re$ numbers were calculated from the velocity of the flow within the array which is calculated based on Eq. 2-43,

$$u_p = \frac{Q}{hw(1-\o)} \qquad 2\text{-}43$$

where *Q* is the flow discharge, *h* is the flow depth and *w* is the channel width.

An example of the velocity and turbulence intensity profiles, transverse and vertical, measured and reported by Tanino and Nepf (2008b) are presented in Figure 2-28 and Figure 2-29, respectively.

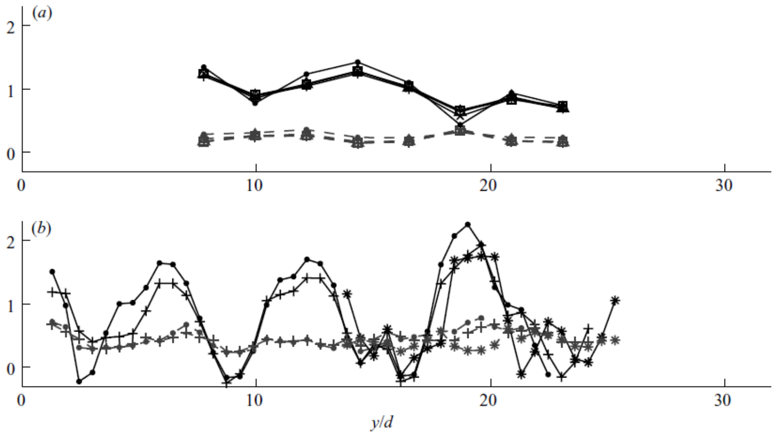

FIGURE 7. Lateral transects of $\overline{u}/U_p$ (solid line) and $\sqrt{k_t}/U_p$ (grey, dashed line) at (a) $\phi = 0.010$, $Re_s = 620$–690 (dot), 1600–1700 (×), 2400–2600 (△), 2700–2900 (square), and 3100–3300 (+) and at (b) $\phi = 0.15$, $Re_s = 130$–140 (dot), 400–430 (+), and 510–600 (∗). Flume sidewalls were at $y = 0$ and 32.0$d$.

**Figure 2-28 Tanino and Nepf (2008b) figure 7, transverse velocity and turbulence intensity profiles, the original caption of the figure is kept as it included the legend and reproducing the figure was not possible due to overlapping data points**

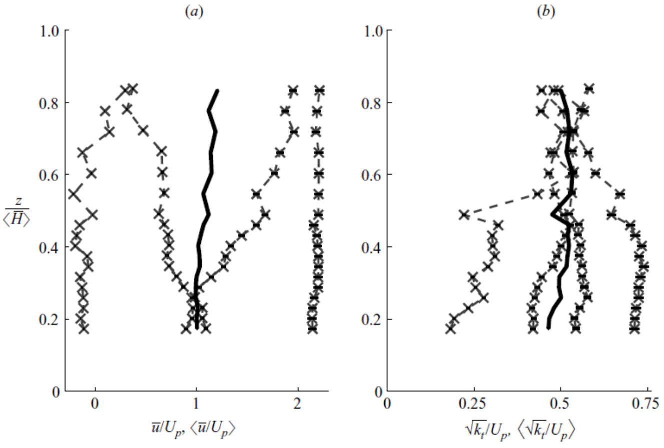

FIGURE 8. Vertical profiles of (a) $\overline{u}/U_p$ and (b) $\sqrt{k_t}/U_p$ at four positions, 1.0$d$ apart, along a lateral transect (×). The lateral average of the four profiles is presented as a thick solid line. Horizontal bars reflect the uncertainty in $U_p$. $\phi = 0.20$, $Re_s = 440$–490, $\langle H\rangle = 17.3$–17.4 cm.

**Figure 2-29 Tanino and Nepf (2008b) figure 8, vertical velocity and turbulence intensity profiles the original caption of the figure is kept as it included the legend and reproducing the figure was not possible due to overlapping data points**

It was mentioned that as the transverse velocity profiles remain of the same shape at different $Re_d$ one can say that "the spatial variability is largely dictated by the cylinder configuration" as shown in Figure 2-28 (Tanino, 2008). It was also mentioned that as a result of arrays being vertically uniform, the vertical velocity and turbulence intensity profiles are approximately uniform in depth. This latter fact suggests the possibility of comparing the results of this study and similar studies to two dimensional (planar) Computational Fluid Dynamics (CFD) models.

As was mentioned before, two characteristic lengths of *d* and $<S_n>_A$ were considered in the Tanino and Nepf (2008b) study. As a result of investigating turbulence features and the eddy sizes the minimum of these two metrics was concluded to be considered as the characteristic length, refer to Tanino (2008) figure 2-9. The values of turbulence intensity measured in their study plotted against $d/<S_n>_A$, shown in Figure 2-30 confirms their conclusion. The solid lines on this figure are Eq. 2-44 and Eq. 2-45 suggested by Tanino and Nepf (2008b), for $d/<S_n>_A < 0.56$ and $d/<S_n>_A > 0.56$, respectively.

$$\frac{\sqrt{k}}{u_p} = (1.07 \pm 0.09)\left[C_D \frac{\text{ø}}{(1-\text{ø})\pi / 2}\right]^{1/3} \tag{2-44}$$

$$\frac{\sqrt{k}}{u_p} = (0.88 \pm 0.02)\left[C_D \frac{<S_n>_A}{d} \frac{\text{ø}}{(1-\text{ø})\pi / 2}\right]^{1/3} \tag{2-45}$$

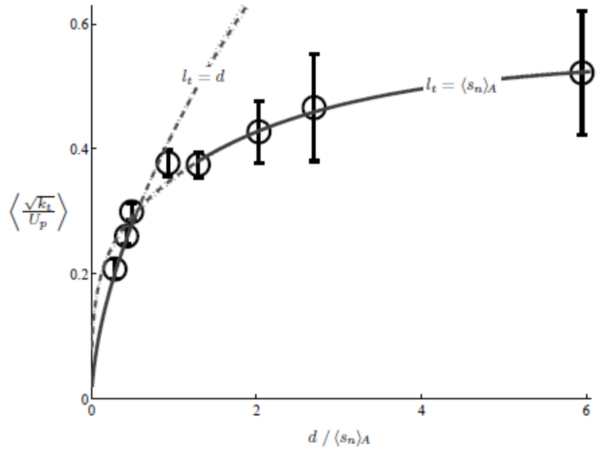

**Figure 2-30 Tanino and Nepf (2008b) figure 14, turbulence intensity versus *d* / $<S_n>_A$**

Building on previously proposed relations for estimating $D_y$, by Koch and Brady (1986) and Nepf (1999), a more comprehensive model was suggested by

Tanino and Nepf (2008b) for estimating transverse dispersion coefficient as Eq. 2-46,

$$\frac{D_y}{ud} = \gamma_1 \frac{4}{\pi}\frac{\sqrt{k_t}}{u}\left(\frac{<S_n>_A}{d}\right)^2 p_{S_{nc}>2d} + \gamma_2 \frac{\pi}{4096}\left(\frac{d}{<S_n>_A}\right)^3 \frac{1-\o}{\o^2} p_{S_{nc}<5d} \tag{2-46}$$

where the first term on the left describes turbulent diffusion and the second term describes mechanical dispersion, $\gamma_1$ and $\gamma_2$ are scaling constants and $p_{S_{nc}>2d}$ and $p_{S_{nc}<5d}$ are “the probability that a single cylinder in a random array will have a nearest neighbour farther than *2d* and within 5*d*, respectively” (Tanino and Nepf, 2008b). It was explained that the reason behind multiplying by these probabilities is that only those distances allowing eddies of sizes greater than 2*d* are considered to contribute in turbulent diffusion while those smaller than 5d contribute in tortuosity of flow or mechanical dispersion.

The results of their study along with the data point for ø = 0 from Nepf et al. (1997) are shown in Figure 2-31. The solid line is Eq. 2-46 with $\gamma_1$ and $\gamma_2$ equal to 4.0 and 0.34, respectively. The dashed-dotted line is the turbulent dispersion, i.e. the first term on the right in Eq. 2-46 and the dashed line is the mechanical dispersion, i.e. the second term Eq. 2-46.

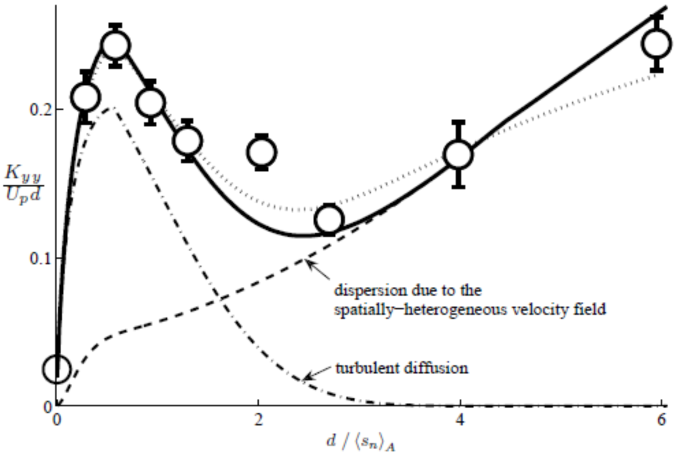

**Figure 2-31 Tanino and Nepf (2008b) figure 18, nondimensionalized transverse dispersion coefficients along with their suggested models**

The good agreement between the observed data points and the suggested model confirmed the background theory and the theoretical concepts. However, one should bear in mind that $\gamma_1$ and $\gamma_2$ are chosen based on the best fit to the data and are limited for this specific laboratory setup. Thus, a more comprehensive study may suggest adjustments to the equation. Also, this equation was only tested for arrays of one single cylinder diameter, so one way to generalize the equation is to investigate the transverse mixing within arrays of different cylinder diameters or arrays of a number of cylinder diameters with a different distribution of diameters.

In summary, as the understanding of transverse mixing within random cylinder arrays has evolved, two main processes have been considered in estimating the value of $D_y$: turbulent diffusion and mechanical dispersion and their contribution to the net transverse mixing have been the question of recent studies. This question has been answered by defining two length scales: i) long enough distances between cylinders needed for certain eddy sizes to shape and ii) small enough distances between cylinders to bend the streamlines and cause tortuosity.

### 2.6.2 Longitudinal Mixing

The literature on longitudinal mixing is not as comprehensive as that on transverse mixing, (Rutherford, 1994). Nepf et al. (1997a) investigated the longitudinal dispersion coefficient, $D_x$, within randomly distributed 0.0064 m diameter, cylinder arrays of ø = 0.010, 0.015, and 0.055. The laboratory setup used in their study was similar to that of Nepf et al. (1997b) and velocity and turbulence intensity were measured as vertical profiles. The theoretical model was based on Eq. 2-47, previously proposed by Fischer et al. (1979),

$$D_x = \frac{S_x}{D_z} \qquad \text{2-47}$$

where $D_z$ is the vertical turbulent diffusion and $S_x$ reflects the mean shear in the longitudinal velocity profile. The observed longitudinal dispersion coefficients are compared with the model-predicted values in Figure 2-32. The data points corresponding to ø = 0.000 are also included which are displaced from the y-axis for visual purposes.

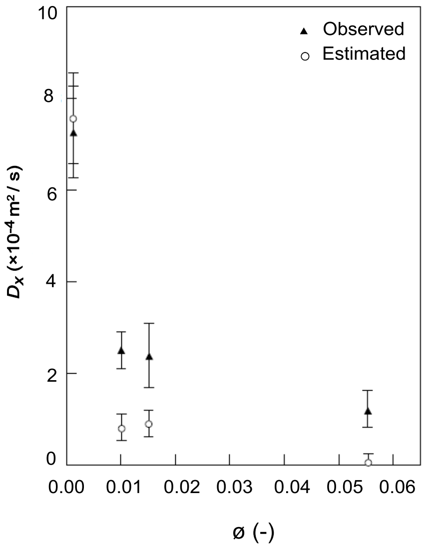

**Figure 2-32 Reproduced figure 7 from Nepf et al. (1997a), observed and estimated longitudinal dispersion coefficients**

The discrepancy between the observed and estimated data points was suggested to be due to mechanical dispersion and trapping in dead zones which were neglected in the theoretical model.

A similar laboratory setup including $d = 0.006$ m diameter randomly distributed cylinder arrays was used by White and Nepf (2003). The arrays had $ad$ or $(d / <S_n>_A)^2$ (recall Eq. 2-24) of 0.013, 0.025, and 0.082 equivalent to ø = 0.010, 0.020, and 0.065, respectively. $Re_d$ was ranging between 65 to 650. They considered two main regions within the cylinders and their effect on the longitudinal dispersion, the primary and the secondary wake, the green and blue regions in Figure 2-33, respectively.

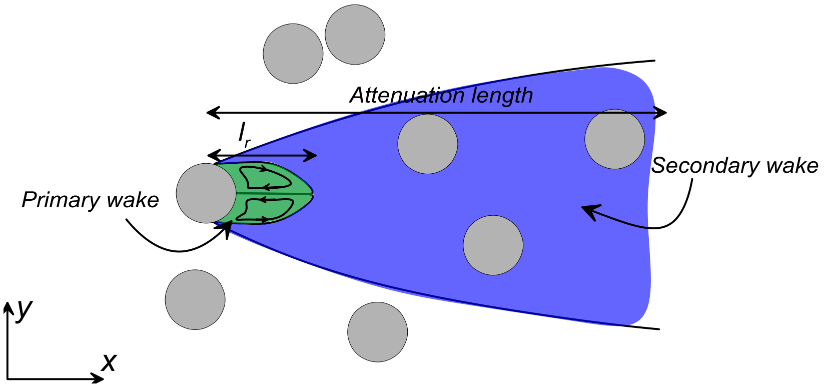

**Figure 2-33 Reproduced figure 1 from White and Nepf (2003) the primary wake, shown in green, and the secondary wake, shown in blue**

The primary wake is the unsteady recirculation zone close to each cylinder, where the time-averaged velocity field shows recirculation. The size of the primary wake region is of the order of cylinder diameter, referred to as recirculation length, $l_r$, the residence time of the particle getting trapped in this area was suggested to be inversely proportional to the frequency of the oscillation and to be estimated based on Eq. 2-48,

$$\tau_{pw} = \frac{\beta_{pw}}{f_s} \tag{2-48}$$

where $\tau_{pw}$ is the residence time of particle trapped in the primary wake, $\beta_{pw}$ is the constant of proportionality and is a function of $Re_d$ and $f_s$ is the frequency of oscillation estimated based on

$$f_s = Stu / d \tag{2-49}$$

where $St$ is the Strouhal number. The total fluid volume occupied by primary wakes, $\varepsilon_{pw}$, was suggested to be estimated based on Eq. 2-50,

$$\varepsilon_{pw} = \kappa_{pw} ad \tag{2-50}$$

where $\kappa_{pw}$ is a function of $Re_d$ and $ø$. So the dispersion coefficient corresponding to the primary wake $D_{xpw}$ was defined as Eq. 2-51,

$$D_{xpw} = \frac{\beta_{pw}\kappa_{pw}}{St} adud \tag{2-51}$$

The secondary wake is the velocity defect area which extends downstream beyond $l_r$ and decays over the attenuation length, suggested being scaled by $1 / C_D a$. After a comprehensive study on the random distribution of velocity and pressure within the secondary wake the contribution of secondary wake into the longitudinal dispersion coefficient, $D_{xsw}$, was suggested to be as Eq. 2-52,

$$D_{xsw} = \frac{\gamma_w}{8} \sqrt{C_D{}^3 Re_d \frac{Sc_t}{Sc_t + 1}} ud \tag{2-52}$$

where $\gamma_w$ is an incomplete gamma function and $Sc_t$ is the turbulent Schmidt number. It was mentioned that a good approximation for the effective Schmidt number at $Re_d$ of $O$ (100) is unity. Thus by assuming $Sc_t \approx 1$, as they did when they compared the model with laboratory observed results, the net longitudinal dispersion coefficient can be estimated based on Eq. 2-53.

$$\frac{D_x}{ud} = \frac{\beta_w k_w}{St} ad + \frac{\gamma_w}{8}\sqrt{\frac{C_D{}^3 Re_d}{2}} \qquad 2\text{-}53$$

The concentration profiles were recorded at a distance ranging from 0.5 m to 3.5 m from the injection point. The resulting nondimensionalized longitudinal dispersion coefficient values for each ad are shown in Figure 2-34.

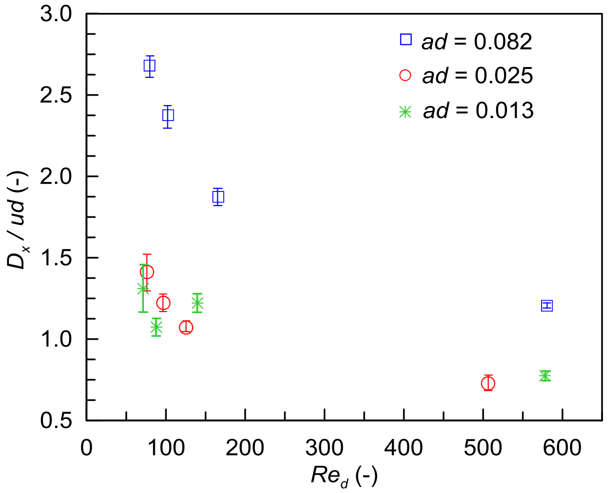

**Figure 2-34 Reproduced figure 8 from White and Nepf (2003) nondimensionalized longitudinal dispersion coefficients for the different *ad* and *Re*$_d$ scenarios**

Two main trends were explained in Figure 2-34, first for all *ad* values, $D_x / ud$ decreases with increase in $Re_d$, second for all $Re_d$, $D_x / ud$ increases sharply for the highest *ad*, i.e. *ad* = 0.082 while its values are comparable for the two low *ad*, i.e. *ad* = 0.013 and *ad* = 0.025. The dependence of $D_x / ud$ on $Re_d$ was explained to be consistent with the dependence of both primary and secondary wakes' size on $Re_d$ as the primary wake size and residence time, as well as the drag coefficient all decrease with increasing $Re_d$.

It was also explained that vortex trapping dispersion increases in proportion to *ad*, whereas secondary wake dispersion has a lower dependency on *ad*. Thus the fact that the values of $D_x / ud$ are close at *ad* = 0.013 and *ad* = 0.025 can suggest that secondary wake dispersion dominates at this range. While this domination is passed to the vortex trapping domination when *ad* increases to 0.082 and causes $D_x / ud$ to suddenly increase at this density.

A direct comparison between the proposed models and the observed dispersion values was not feasible as the values of $\beta_w$ and $k_w$ were not available for their data. These values were taken from a study by Duan and Wiggins (1997) and were interpolated for $Re_d$ = 100 and $Re_d$ = 190. The estimated results are compared with the observed ones in Figure 2-35. It should be mentioned that no parameter adjustment was done in depicting the lines presenting the theoretical values in Figure 2-35.

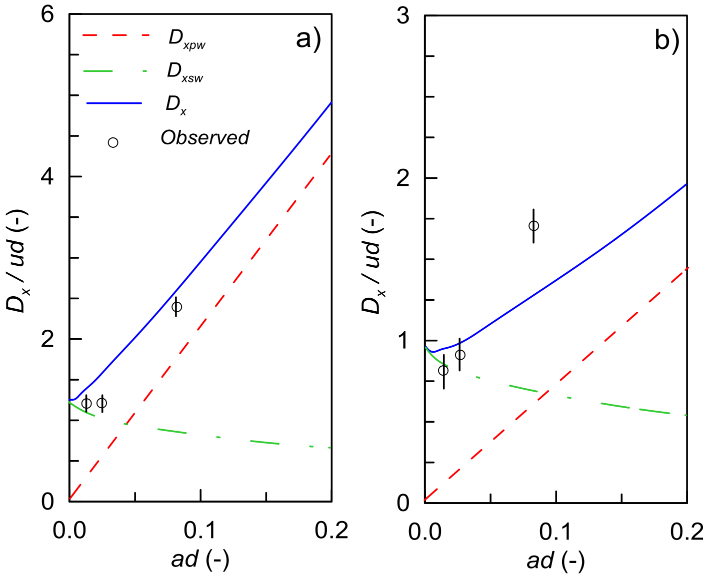

**Figure 2-35 Reproduced figure 11 from White and Nepf (2003), comparison of theory and experiment for a) $Re_d$ = 100 and b) $Re_d$ = 190**

The agreement between the model-prediction and the observed values was described as satisfactory and it was explained that the dependence on *ad* has been captured by the model. However it was appreciated that for high *ad* values at $Re_d$ = 190, the model underestimated the laboratory results, and this was attributed to the fact that this $Re_d$ is close the turbulent transition.

Although the research by White and Nepf (2003) benefited from a very strong theoretical investigation of the processes contributing in longitudinal dispersion, their model includes parameters that need sophisticated measurements e.g. residence time of the particles within the primary wake. Moreover, only three values of *ad* were tested in their laboratory study, which is due to difficult practical conditions in conducting these type of experiments in the laboratory.

In all of the above-mentioned laboratory experiments transverse and longitudinal dispersion coefficients were measured separately i.e. in none of them both coefficients were measured for the same array. Measuring both coefficients at the same time and on the same channel can have the advantage of investigating their effect on each other, or comparing the effects of different conditions on them. in a recent study by Sonnenwald et al. (2017) both longitudinal and transverse dispersion coefficients in the same channel were measured simultaneously for the first time. However this study was on regularly distributed cylinder arrays, so their results are not discussed here.

## 2.7 Flow Equations and Turbulence Models

All the models used and presented in this thesis are based on two-dimensional open channel flow. Thus, an introduction of two dimensional Navier-Stokes Equations and the discretization method used for solving them in this thesis is provided in this section. The two-dimensional Navier-Stokes Equations include the continuity and momentum equations. The two-dimensional continuity equation for a steady incompressible flow is as Eq. 2-54,

$$\frac{\partial u}{\partial x}+\frac{\partial v}{\partial y}=0 \tag{2-54}$$

where $x$ and $y$ are the longitudinal (stream-wise) and transverse coordinates, respectively and $u$ and $v$ are the longitudinal and transverse velocity, respectively.

The longitudinal and transverse momentum equations are shown as Eq. 2-55 and Eq. 2-56, respectively,

$$\frac{\partial \rho uu}{\partial x}+\frac{\partial \rho uv}{\partial y}=-\frac{\partial p}{\partial x}+\frac{\partial}{\partial x}\left(\mu\frac{\partial u}{\partial x}\right)+\frac{\partial}{\partial y}\left(\mu\frac{\partial u}{\partial y}\right)+\frac{\partial}{\partial x}\left(\mu\frac{\partial u}{\partial x}\right)+\frac{\partial}{\partial y}\left(\mu\frac{\partial v}{\partial x}\right)+F_x \tag{2-55}$$

$$\frac{\partial \rho uv}{\partial x}+\frac{\partial \rho vv}{\partial y}=-\frac{\partial p}{\partial y}+\frac{\partial}{\partial x}\left(\mu\frac{\partial v}{\partial x}\right)+\frac{\partial}{\partial y}\left(\mu\frac{\partial v}{\partial y}\right)+\frac{\partial}{\partial x}\left(\mu\frac{\partial u}{\partial y}\right)+\frac{\partial}{\partial y}\left(\mu\frac{\partial v}{\partial y}\right)+F_y \tag{2-56}$$

where $\rho$ is the density, $p$ is the pressure, $\mu$ is the dynamic viscosity and $F_x$ and $F_y$ are the external forces exerted on the flow in the longitudinal and transverse directions respectively. Recalling the Reynolds decomposition, Eq. 2-6 to Eq. 2-8, each velocity term comprises the mean and turbulence components. When the

Reynolds decomposition are replaced in the momentum equation, it will contain $u'u'$, $u'v'$ and $v'v'$ terms, i.e. Reynolds stress terms, which are extremely difficult to calculate if not impossible and need to be modelled through an assumption approach. Versteeg and Malalasekera (2007) explain: “These equations cannot be solved directly in the foreseeable future. Engineers are content to focus their attention on certain mean quantities. However, in performing the time-averaging operation on the momentum equations, we throw away all details concerning the state of the flow contained in the instantaneous fluctuations. As a result, we obtain six (or three in the two-dimensional case) additional unknowns, the Reynolds stresses, in the time-averaged momentum equations.”

To estimate the values of Reynolds stresses and close the equation system, a turbulence model, or more specifically a turbulence closure which adds the required additional equations, is needed. Boussinesq introduced the concept of eddy viscosity, which is an analogy between the viscous stresses in laminar flow and the turbulent stresses in turbulent flow. It assumes that the turbulent stresses are proportional to the mean velocity gradients. Eq. 2-57

$$-\overline{u_i'u_j'} = \nu_t\left(\frac{\partial u_i}{\partial x_j}+\frac{\partial u_j}{\partial x_i}\right)-\frac{2}{3}k\delta_{ij} \qquad \text{2-57}$$

“where $\nu_t$ is the turbulent or eddy viscosity, *k* is the turbulent kinetic energy, and $\delta_{ij}$ is Kronecker delta and is equal to one for *i=j* and zero for *i≠j*. $\nu_t$, in contrast to the molecular viscosity, is not a fluid property but deepens strongly on the state of turbulence, $\nu_t$ may vary significantly from one point in the flow to another and also from flow to flow” (Rodi, 1993). A widely used group of the classical turbulence models also known as Reynolds Averaged Navier-Stokes (RANS) models, e.g. *k*-ε and *k*-ω, are built based on this assumption. For example, in the *k*-ε model, the turbulent viscosity is calculated based on turbulent kinetic energy, *k* and the rate of dissipation of turbulent kinetic energy per unit mass, ε, shown in Eq. 2-58,

$$\nu_t = C_\mu \frac{k^2}{\varepsilon} \qquad \text{2-58}$$

where $C_\mu$ is a constant equal to 0.09. In this model two transport equations are solved for *k* and ε, shown in Eq. 2-59 and Eq. 2-60, respectively.

$$\frac{\partial(k)}{\partial t}+\frac{\partial(ku_i)}{\partial x_i}=\frac{\partial}{\partial x_j}\left[\left(\nu+\frac{\nu_t}{\sigma_k}\right)\frac{\partial k}{\partial x_j}\right]+\frac{G_k}{\rho}-\varepsilon \quad \text{2-59}$$

$$\frac{\partial(\varepsilon)}{\partial t}+\frac{\partial(\varepsilon u_i)}{\partial x_i}=\frac{\partial}{\partial x_j}\left[\left(\nu+\frac{\nu_t}{\sigma_\varepsilon}\right)\frac{\partial \varepsilon}{\partial x_j}\right]+C_{1\varepsilon}G_k\frac{\varepsilon}{\rho k}-C_{2\varepsilon}\frac{\varepsilon^2}{k} \quad \text{2-60}$$

where $\sigma_k$ , $\sigma_\varepsilon$ , $C_{1\varepsilon}$ and $C_{2\varepsilon}$ are constants equal to 1.00, 1.30, 1.44, and 1.92, respectively, recommended by Launder and Spalding (1974). $G_k$ is the rate of generation of turbulence kinetic energy due to mean velocity gradients, calculated based on Eq. 2-61.

$$G_k=\rho\nu_t\left(\frac{\partial u_i}{\partial x_j}+\frac{\partial u_j}{\partial x_i}\right)\frac{\partial u_j}{\partial x_i} \quad \text{2-61}$$

The RANS models, and specifically the *k*-*ε* model, have achieved notable success in calculating a wide range of flows, particularly in confined flows. These models have been used frequently in modelling environmental flows, such as pollutant dispersion in the atmosphere and in lakes. However, they are reported not to perform well in a variety of flows such as far wakes, mixing layers, curved boundary layers and swirling flows and specifically in modelling flows with strong streamline curvature. Among the reasons mentioned in the literature is the assumption of isotropic Reynolds stress. This limitation is removed in a more complex turbulence closure model, the Reynolds Stress Model (RSM), also called the second-order or second-moment closure model. In RSM models, the turbulent viscosity approach is avoided and additional transport equations for the Reynolds stresses, as well as an equation for the dissipation rate, are solved. RSM is recommended when the flow to be modelled has curved streamlines, such as flow within cylinder arrays. The description of RSM in the ANSYS FLUENT manual, ANSYS, Inc., 2012, reads as follows:

“Since the RSM accounts for the effects of streamline curvature, swirl, rotation, and rapid changes in strain rate in a more rigorous manner than one-equation and two-equation models, it has greater potential to give accurate predictions for complex flows. The RSM might not always yield results that are clearly superior to the simpler models in all classes of flows to warrant the additional computational expense. However, use of the RSM is a must when the flow features of interest are the result of anisotropy in the Reynolds stresses. Among the examples is cyclone flows, highly swirling flows in combustors, rotating flow passages, and the stress-induced secondary flows in ducts.” The equation for the transport of Reynolds stresses solved in RSM is as Eq. 2-62.

$$
\begin{aligned}
&\frac{\partial\left(\rho\overline{u_i'u_j'}\right)}{\partial t}+\frac{\partial\left(\rho u_k\overline{u_i'u_j'}\right)}{\partial x_k}= \\
&-\frac{\partial}{\partial x_k}\left[\rho u_k'\overline{u_i'u_j'}+\overline{p\left(\delta_{kj}u_i'+\delta_{ik}u_j'\right)}\right]+\rho\frac{\partial}{\partial x_k}\left[\nu\frac{\partial}{\partial x_k}\left(\overline{u_i'u_j'}\right)\right] \qquad \text{2-62} \\
&-\left(\rho\overline{u_i'u_k'}\frac{\partial u_j}{\partial x_k}+\overline{u_j'u_k'}\frac{\partial u_i}{\partial x_k}\right)+\overline{p\left(\frac{\partial u_i'}{\partial x_j}+\frac{\partial u_j'}{\partial x_i}\right)}-2\rho\nu\left(\frac{\partial u_i'}{\partial x_k}\frac{\partial u_j'}{\partial x_k}\right)
\end{aligned}
$$

Considering the characteristics and the advantages of RSM models, it seems to be an ideal option for modelling flow within cylinder arrays. The capability of RSM in modelling flow past cylinders has been tested and confirmed by several authors, e.g. Palkin et al. (2015), Jakirlić et al. (2016) and Maduta et al. (2017). A number of these studies are reviewed in detail in the following section.

Among the more advanced turbulence models, Large Eddy Simulation (LES) models have been frequently used to model flow within cylinders. LES models are based on the self-similarity theory of Kolmogorov. It states that the small eddies are universal while the larger eddies depend on the geometry, i.e. if large eddies are solved explicitly then the small eddies can be implicitly solved using a subgrid-scale model also known as SGS model. Thus the governing equations of LES are obtained by filtering the Navier-Stokes equations using different types of filtering operators. A similar process to Reynolds decomposition in RANS models applies to the Navier-Stokes equations and splits any field into filtered and sub-filtered portions. The filtered equations are solved in LES and the sub-filter portion is calculated using a filter kernel. Although LES is less computationally expensive than Direct Numerical Simulation (DNS), the required computational resources are still too large for most practical applications. More explanation about LES can be found in Sagaut (2006). A number of CFD studies similar to this thesis are reviewed in the following section.

## 2.8 CFD Studies on Flow and Mixing within Cylinder Arrays

Considering the numerous engineering applications of cylinder-shaped bodies, there are a great number of numerical studies on flow past cylinders, among them are: heat exchangers design studies e.g. Paul et al. (2008) and Parrondo et al. (2018); offshore structures and ocean engineering e.g. Kamath et al. (2015); and scour management e.g. Solaimani et al. (2017). There are a considerable number of studies focused on modelling flow and mixing in porous media. Porous media in these studies have been modelled in some cases as a very high-density cylinder array. As the densities considered in these studies are much higher than the densities considered in this thesis, they are not discussed here. However, a few studies which have investigated a similar scenario to the one considered in this thesis are reviewed briefly along with the studies directly investigating flow and mixing within cylinder arrays as rigid artificial vegetation.

There are a considerable number of LES studies modelling flow within cylinder arrays as rigid artificial vegetation. Etminan et al. (2017) modelled the flow within a small number of emergent cylinders as a 3D model in Open-FOAM using LES and investigated the drag force. Six solid volume fractions of $ø$ = 0.016, 0.04, 0.08, 0.12, 0.20 and 0.25 were built using two cylinders for the lowest $ø$ and four cylinders for the rest. Four $Re_d$ = 200, 500, 1000 and 1340 were tested, the velocity results of $Re_d$ = 1340 are shown in Figure 2-36. They had to repeat the computational domain of four cylinders for presentation purposes to be able to show a relatively short array, Figure 2-36. This shows that this type of CFD model, i.e. 3D LES are extremely computationally expensive and impractical for modelling a relatively long array of cylinders such as those modelled in this thesis, i.e. approximately $300d$ long arrays.

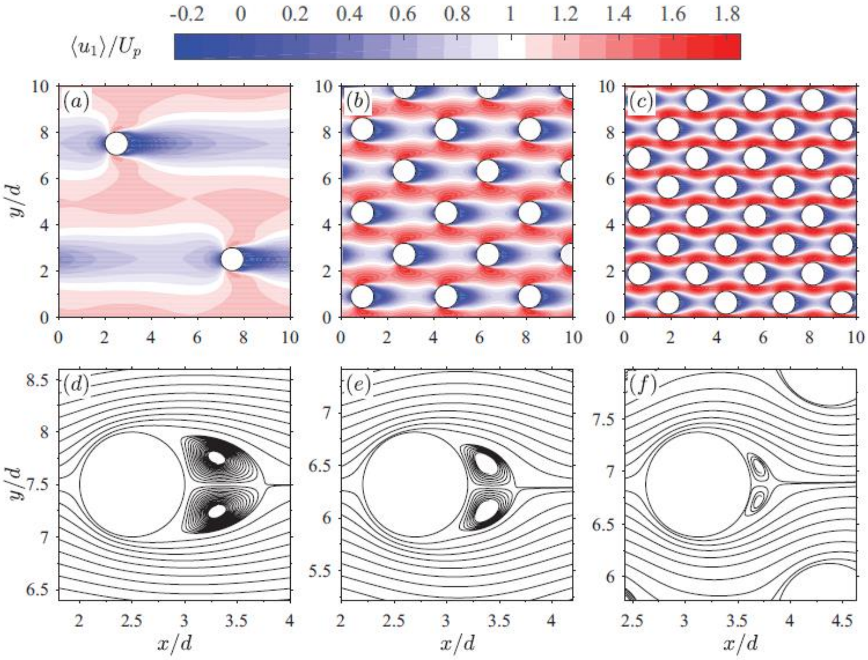

**Figure 2-36 Etminan et al. (2017) figure 4, contours of the dimensionless temporally and vertically averaged streamwise velocity $u/u_p$ (upper row) and streamlines (lower row) at three densities, (a,d) ø = 0.016, (b,e) ø = 0.12, (c,f) ø = 0.25, $Re_d$ = 1340, contours in figures 4b and c are presented by repeating the computational domain (of four cylinders) to keep the dimensions of each of the three figures in the upper row consistent.**

Etminan et al. (2017) also modelled flow within a group of randomly distributed cylinders in a 9*d* wide and 18*d* long channel. The velocity contours of this array are shown in Figure 2-37, the wake areas can be seen in blue colour. They mentioned that the velocity and turbulence intensity were both almost constant in the vertical direction. This statement, which is consistent with previous laboratory observations (e.g. Tanino (2008) and Ricardo et al. (2014)), confirms the acceptability of 2D planar models for modelling flow within cylinder arrays. The velocity contours reported by Etminan et al. (2017) also have the potential of being compared with the dataset produced in this thesis.

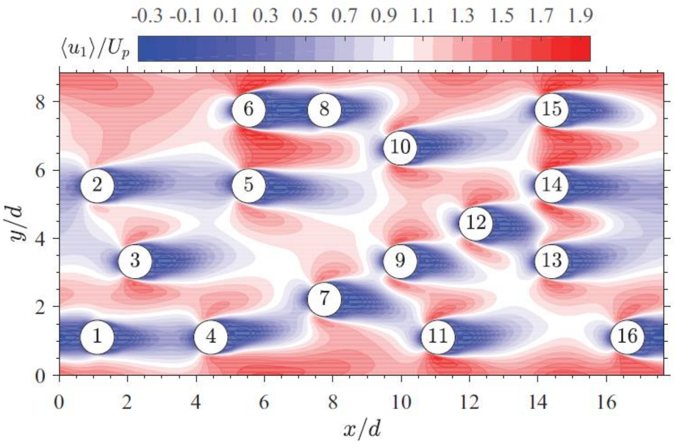

**Figure 2-37 Etminan et al. (2017) figure 11, contours of dimensionless temporally and vertically averaged streamwise velocity $u/u_p$ for the randomly distributed cylinder array, ø = 0.08, $Re_d$ = 500**

Stoesser et al. (2010), modelled the laboratory study of Liu et al. (2008) (previously mentioned in §2.5) using LES modelling. The geometry dimensions used in this study were similar to those of Etminan et al. (2017). Three densities (ø = 0.016, 0.063 and 0.251) were tested in combination with two $Re_d$ (500 and 1340). The drag coefficient was investigated in this study and compared with the results of Tanino and Nepf (2008a), Figure 2-38. These results will be compared with the results of the current study.

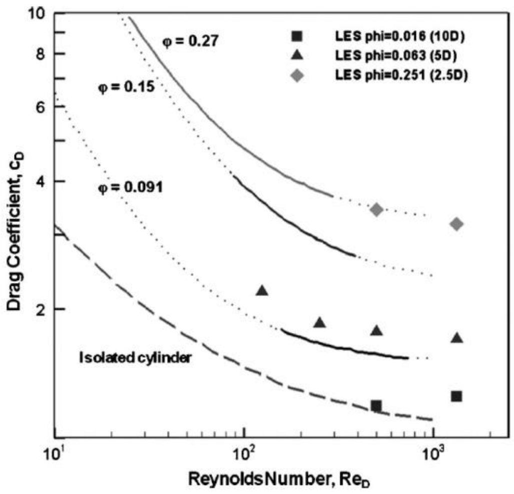

**Figure 2-38 Stoesser et al. (2010) figure 14, drag coefficient as a function of Reynolds number for various vegetation densities (lines represent experimental data from Tanino and Nepf 2008)**

Two studies which have used ANSYS FLUENT for modelling cases similar to the one investigated in this thesis are Elghanduri (2015) and Li et al. (2016). The dispersion of tracer within and over a porous zone was modelled by Elghanduri (2015) as a 2D vertical plane model in ANSYS FLUENT 12. The porous media was modelled as two different cylinder arrays of $d = 0.010$ and 0.0115 m, forming porosities of 0.8126 and 0.440, respectively. The $k$-$\varepsilon$ turbulence model was used to model the flow and the Discrete Phase Model (DPM) was used to model the tracer dispersion. An example of the tracer concentration contours reported in this study is shown in Figure 2-39.

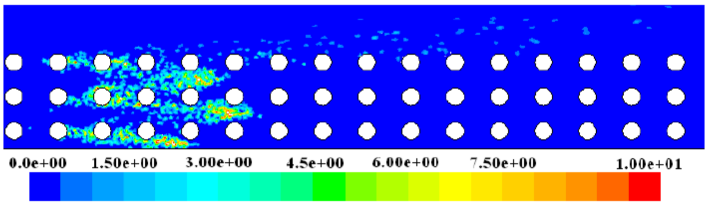

**Figure 2-39 Elghanduri (2015) figure 4, contours of concentration**

Li et al. (2016) also modelled a very narrow passage of cylinders, a section of a pin fin, employing 6 different turbulence models (including RSM) provided in ANSYS FLUENT 6. The advantages of RSM models were not highlighted in their work as the small size of their case study allowed them to use LES models, as well. However, it was appreciated that RSM models account for the anisotropy characteristics of the flow. Their results showed good comparability with the laboratory measurements of Ostanek (2012), and Ostanek and Thole (2012), Figure 2-40, which provides confidence in lower-order RANS models e.g. $k$-$\varepsilon$.

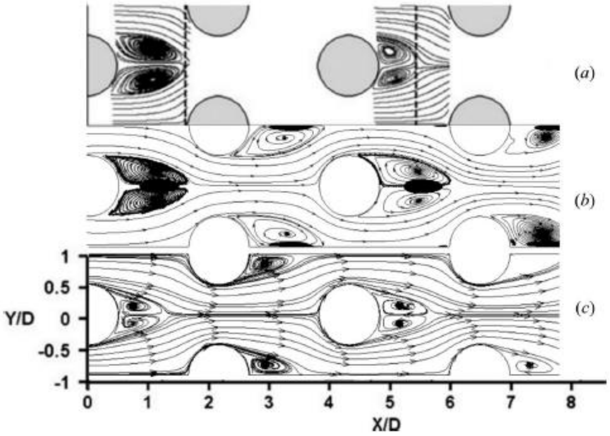

**Figure 2-40 Li et al. (2016) figure 4, time-averaged streamlines for the channel centre plane, (a) Experimental measurements from Ostanek and Thole (2012), (b) $k$-ω model results, (c) $k$-$\varepsilon$ results**

There are also a great number of CFD studies employing 3D LES to model flow past one or a couple of cylinders e.g. Kitagawa and Ohta (2008), Afgan et al. (2011) and Rodriguez et al. (2015), as well as a group of four cylinders, e.g. Lam and Zou (2009). Flow and turbulence structures within a patch of cylinders were modelled by Chang and Constantinescu (2015), also as a 3D LES model. The densities of ø = 0.023, 0.05, 0.1 and 0.2 and $Re_d$ = 10000 were tested. An example of the results of their study is shown in Figure 2-41. Due to the very high $Re_d$ these results may not be comparable with the results of this thesis.

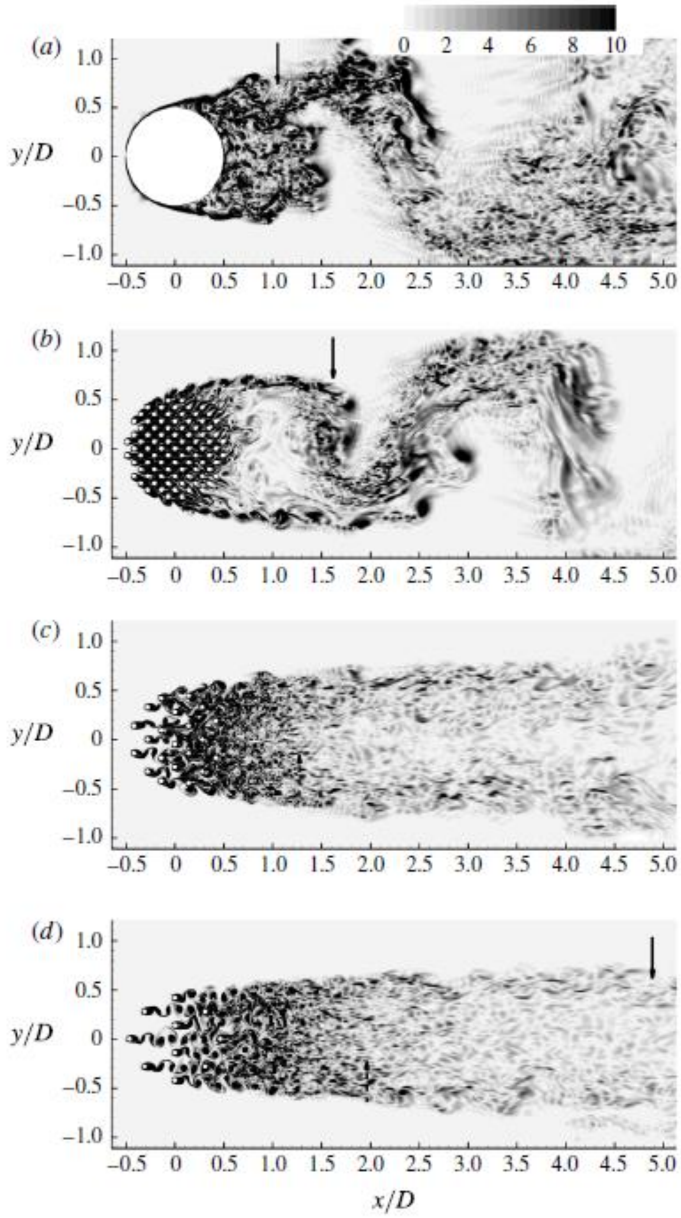

**Figure 2-41 Chang and Constantinescu (2015) figure 7, instantaneous vertical vorticity magnitude, (a) single cylinder, (b) ø = 0.2, (c) ø = 0.05, (d) ø = 0.023**

The 3D LES models provide very high-resolution flow and turbulence data, but they are computationally very expensive. Modelling a real-scale channel filled with cylinder arrays is not practical using this approach. Also, it is worth mentioning that only a few studies have considered CFD modelling of solute transport within cylinder arrays and this therefore needs further study.

Representing vegetation in CFD models as a porous zone has been considered recently by a number of researchers, e.g. Saggiori (2010), Tsavdaris et al. (2013), and Sonnenwald et al. (2016). The vegetation in this approach is defined as a momentum sink which depends on the bulk drag coefficient, $C_D$, frontal facing area, $a$, and solid volume fraction, $\o$. The porous media approach allows real-scale water bodies to be modelled. For instance, approximately 40 m long ponds were modelled in ANSYS FLUENT, by Sonnenwald et al. (2017). The parameters used in the porous media approach depend on the vegetation characteristics such as density and diameter and need to have good estimates for an accurate representation of specific vegetation. Thus, a data set on flow and mixing within vegetation of different densities and diameters, such as the one to be provided in this thesis, will effectively serve the porous media approach. This, in turn, will serve practical environmental engineering applications.

## 2.9 Discussion and Conclusion

In this chapter, the basic mixing concepts and also the characteristics of the flow past cylinders have been explained by reviewing both classic textbooks and papers. Laboratory studies with the potential of being used as validation data were reviewed followed by a review of CFD studies with a similar approach to the methodology of this thesis. Thus a collection of up-to-date knowledge on flow and mixing within random cylinder arrays has been provided, along with the suggested relationships to predict the hydrodynamics and mixing characteristics of them which will be tested in the following chapters.

The detailed review of the laboratory studies that are going to be reproduced in this thesis provided the basic introduction to the methodology as will be explained in the next chapter. The review also clarified the shortcomings of a number of studies e.g. the short length of the tested arrays or measuring velocity and mixing in two different channels in Tanino and Nepf (2008b). From reviewing the laboratory studies, it can be stated that there are practical challenges and expensive equipment is required, such as ADV and LIF.

The review on CFD studies showed that most of the studies have modelled a small number of cylinders due to the practical limitations of the employed models. No study has aimed to model a full-scale channel with a large number of cylinders comparable with the laboratory setups. Also, no study has reproduced the laboratory scalar transport experiments within cylinder arrays. To establish a CFD setup with the capacity of providing similar datasets to the laboratory ones, these two items should be tested and validated employing an industrially acceptable turbulence model and computational resources.

The conclusions from the literature review can be listed as below:

- The mixing characteristics of flows can be quantified and represented as transverse and longitudinal dispersion coefficients, $D_x$ and $D_y$, respectively;
- There is a collection of laboratory studies on randomly distributed cylinder arrays each investigating either of $D_x$ or $D_y$, separately, with a greater number of studies focussing on $D_y$, which provide a collection of data sets to be considered as a source of validation data;
- A set of relationships is suggested in the literature to predict $D_x$ or $D_y$ based on the characteristics of the flow and the array, i.e. $Re_d$, $d$, $a$ and ø; and
- The previous CFD studies on flow around cylinders have modelled a single, a couple or a small patch of cylinders mostly using computationally expensive models such as 3D LES.

The areas that have not been studied or need more investigation can be listed as follows:

- Measuring the length of the advective zone over a randomly distributed cylinder array
- Measuring both $D_x$ and $D_y$ simultaneously over the same array;
- Investigating the effect of array length on $D_x$ and $D_y$;
- Investigating the effect of different diameters on $D_x$ and $D_y$;

- Employing a CFD modelling method with industrially acceptable computational resources to model flow and mixing within randomly distributed cylinder arrays;
- CFD modelling of a full-scale channel with a large number of cylinders which allows testing the effect of different array lengths on the derived dispersion coefficients; and
- Testing previously suggested relations for predicting $D_x$ and $D_y$ for different diameters and densities.

# 3 PRELIMINARY STUDIES

## 3.1 Introduction

This chapter contains the preliminary studies done to define the methodology used in the rest of the thesis. The first study presented in §3.2 is a validation of the general methodology using a previously published experimental data set. The second study, §3.3, is the sensitivity analysis on the injection point location followed by a comparison study on two different meshing methods, §3.4. Estimations of advective zone length and the minimum required reach length are presented in §3.5 which lead to a decision on dimensions and geometries used for the main models presented in the next chapter.

## 3.2 Validation of the General Methodology

The aim of this section is to validate the general 2D CFD modelling methodology proposed to be used in the thesis. After a brief introduction to the laboratory data used for validation, the methodology is explained in detail, the CFD results are compared with the laboratory data and the method is assessed and validated. It should be borne in mind that the 2D model is only valid for $0.2 < z/h < 0.9$, refer to the vertical velocity profiles presented in § 2.5.

### 3.2.1 Laboratory Data Used for Validation

A laboratory investigation of transverse dispersion coefficient, $D_y$, within randomly distributed emergent cylinders with a diameter of $d = 0.0064$ m, was undertaken by Tanino (2008). The arrays were built based on solid volume fractions of $ø = 0.010\text{-}0.350$. A range of mean pore velocities, $u_p$, were tested and the transverse dispersion coefficient was measured for each case, over variable longitudinal distances from the injection point, $x$. It was suggested and experimentally shown, that the net transverse dispersion can be expressed as the linear superposition of turbulent diffusion and mechanical dispersion, caused by the heterogeneous velocity field within the array. A more detailed explanation can be found in Tanino and Nepf (2008b) and Tanino (2008). The reported results and characteristics of the laboratory setup are presented in Table 3-1, in which $<S_n>_A$ is the average surface-to-surface distance between a cylinder in the array and its nearest neighbour and $Re_d$ and $Re_{<Sn>_A}$ are the stem diameter and pore Reynolds numbers, respectively. For all the cases $d$ is 0.0064 m.

**Table 3-1 Experimental conditions of laboratory data used for validation (Table 3.3 from Tanino, 2008, all values are presented here with the original precision)**

| $ø$ | $d/<S_n>_A$ | $D_y/(u_p d)$ | $u_p$ [m/s] | $Re_d$ | $Re_{<Sn>A}$ | $x/d$ |
|---|---|---|---|---|---|---|
| 0.010 | 0.28 | 0.21±0.02 | 0.014-0.031 | 83-190 | 290-660 | 55-168 |
| 0.031 | 0.58 | 0.24±0.01 | 0.010-0.027 | 67-180 | 120-310 | 7-174 |
| 0.060 | 0.93 | 0.20±0.01 | 0.015-0.026 | 97-170 | 100-180 | 23-124 |
| 0.091 | 1.3 | 0.18±0.01 | 0.032-0.066 | 230-480 | 180-370 | 22-134 |
| 0.15 | 2.0 | 0.17±0.01 | 0.031-0.058 | 190-370 | 94-180 | 43-223 |
| 0.20 | 2.7 | 0.13±0.01 | 0.038-0.065 | 210-340 | 78-130 | 80-225 |
| 0.27 | 4.0 | 0.17±0.02 | 0.045-0.070 | 300-480 | 74-120 | 27-152 |
| 0.35 | 5.9 | 0.24±0.02 | 0.046-0.056 | 320-390 | 53-66 | 36-145 |

To validate the CFD modelling results, for each value of ø, the minimum, the maximum, and the midpoint of the $Re_d$ ranges presented in Table 3-1 were modelled and compared with the laboratory data.

### 3.2.2 Flow setup

The experiments were modelled using ANSYS Fluent 16.1 (ANSYS® Academic Research, Release 16.1). Limitations of the mesh building tool in ANSYS 16.1 mean that the maximum $ø$ that may be represented decreases as the physical size of the channel model increases. It was, therefore, necessary to decide on the minimum channel length and width that would be representative of the mixing characteristics of the array. The process of finding the minimum representative channel length and width is explained in this section. The rest of the models were built based on the same method but with a different geometry, i.e. with the minimum representative channel length and width but differing solid volume fractions.

### Geometry

The initial set-up was based on the scenario with ø = 0.010, i.e. the first row in Table 3-1. A two dimensional 0.40 m wide, 1.40 m long channel, with 175 cylinders of *d* = 0.0064 m, was set as the geometry. This geometry formed the solid volume fraction of ø = 0.010 which can be seen in Figure 3-1. The cylinders were randomly distributed along the channel using the `rand` function in MATLAB. The code can be found in Appendix 1. The original code for producing the geometry files, was written by Dr Fred Sonnenwald, a Research Associate in the Department of Civil and Structural Engineering, the University of Sheffield. The laboratory cylinder array was built using a similar approach (Tanino 2008). This arrangement of cylinders resulted in an average edge to edge spacing of $<S_n>_A$ = 0.021 m.

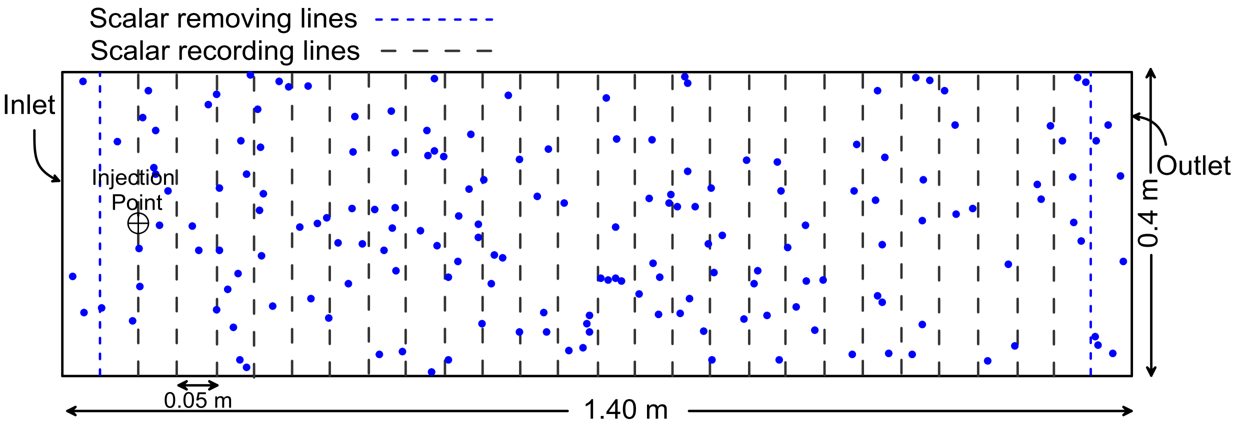

**Figure 3-1 Geometry used to find the minimum representative channel length, ø = 0.010, *d* = 0.0064 m**

The channel was modelled in 2D. The array used in the laboratory study was vertically uniform and the vertical profiles of longitudinal velocity (Figure 3-7 in Tanino, 2008) showed that the vertical variations in velocity were negligible compared with transverse ones. Therefore one can justify that a two-dimensional model can be representative of the laboratory channel and the CFD results will be comparable to the laboratory ones.

### Mesh

The channel was meshed with global 0.001 m mesh cells. The model was proved to be mesh-independent at this cell size. Then the region surrounding each of the cylinders was meshed with a 3 level finer mesh, in a way that each edge was meshed with 80 cells of 0.00025 m, which in total summed up to 689,778 nodes and 1,362,316 elements for the whole channel. All the mesh cells were triangular, built based on the proximity and curvature Advanced Size Function. This function is designed by ANSYS to automatically refine the mesh based on local proximity and local curvature of the geometry (ANSYS® Academic Research, Release 16.1). Both the inlet and the outlet of the channel were match controlled making it possible to set a periodic boundary condition, as will be explained in the next section. A sample of meshing around the cylinders is shown in Figure 3-2.

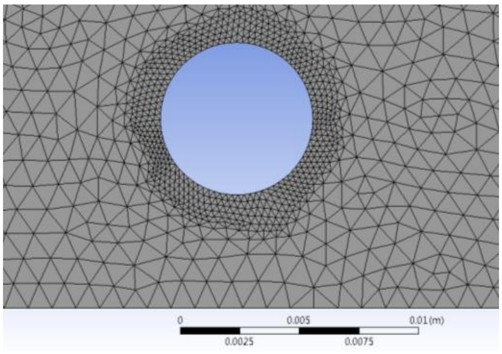

**Figure 3-2 A sample of meshing around the cylinders, *d* = 0.0064 m**

### Flow and turbulence setup

The inlet and outlet boundaries were set as periodic boundaries which was chosen to provide a developed flow field independent of the length of the channel. The inlet mass flow was set equal to 8.983 kg/s which is equivalent to an inlet velocity of 0.023 m/s. This inlet velocity is the midpoint value of the reported $u_p$ range used in the laboratory for this solid volume fraction, $ø$ = 0.010, i.e. $u_p$ = 0.014-0.031 m/s in Table 3-1. This solid volume fraction is the minimum of the experimentally tested range and was chosen to find the minimum representative channel length because as the solid volume fraction increases the minimum representative channel length decreases, i.e. with higher $ø$ values a shorter length of the channel would be sufficient for the tracer to fully experience the channel geometry.

The Reynolds Stress Model (RSM) turbulence closure model was set along with the enhanced wall treatment as the near-wall treatment method. RSM is the most complete 2D turbulence model available in ANSYS Fluent as it allows for anisotropic Reynolds stresses development. The RSM model constants were left at default values (ANSYS® Academic Research, Release 16.1). All the cylinder edges and the left and the right sides of the channel were set as wall boundaries with no-slip condition. The method for spatial discretization of all the variables was set to second order upwind using the coupled scheme solver.

### 3.2.3 Scalar Transport Setup

After solving the flow and turbulence equations in steady state, the model was switched to transient and set for scalar transport modelling. A user-defined scalar was defined with the same density and molecular diffusivity as water and the Schmidt number of 1.0. See Appendix 1 for the code. The original code for producing the geometry files was written by Dr Fred Sonnenwald, a Research Associate in the Department of Civil and Structural Engineering, the University of Sheffield.

The spatial discretization of the scalar and the transient formulation were set to second order upwind and second-order implicit, respectively. The flow and turbulence equations were deactivated and the scalar was released at the injection point, shown in Figure 3-1, for 100 time steps of $\Delta t = 0.01$ s, i.e. a 1.00 s pulse injection.

Once the pulse injection was stopped, the simulation was continued at $\Delta t = 0.01$ s, allowing the scalar to be advected and dispersed along the channel. Two lines were defined at $x = 0.05$ m and at $x = 1.35$ m to remove the scalar from the channel, (Figure 3-1), in order to stop the plume recirculating through the periodic boundary. The scalar concentration was recorded at each time step at every 0.05 m over 25 cross-sectional recording lines, Figure 3-1. This concentration data was then used to calculate the longitudinal and transverse dispersion coefficients.

Considering the available two dimensional mixing data for this model, both two and one dimensional optimizations were possible to estimate the dispersion coefficients. A comparison between two and one dimensional optimizations on the advection-dispersion coefficient was performed by Sonnenwald et al. (2017) for a similar problem and it was shown that the difference for ideal data is negligible. So in this study one dimensional optimizations were done separately, to estimate the longitudinal and transverse mixing coefficients.

For the longitudinal dispersion, concentration values were transversely averaged and depicted over time, resulting in concentration versus time profiles for each cross section. These profiles were then used as pairs in order to estimate the longitudinal dispersion coefficient corresponding to the reach between them. The optimization process is based on the longitudinal advection dispersion equation, Eq. 3-1,

$$\frac{\partial C}{\partial t} + u\frac{\partial C}{\partial x} = D_x \frac{\partial^2 C}{\partial x^2} \qquad 3\text{-}1$$

where $C$ is the tracer concentration; $t$ is time; $u$ is the longitudinal velocity and $D_x$ is the longitudinal dispersion coefficient, and based on its Taylor solution, Eq. 3-2,

$$C(x_2,t) = \int_{\tau=-\infty}^{\infty} \frac{C(x_1,t)u}{\sqrt{4\pi D_x \left(\Delta x/u\right)}} exp\left[-\frac{u^2\left(\left(\Delta x/u\right)+\tau-t\right)^2}{4D_x\left(\Delta x/u\right)}\right] \mathrm{d}\tau \qquad 3\text{-}2$$

where $C(x_1,t)$ is the upstream observed concentration versus time profile, $C(x_2,t)$ is the predicted downstream concentration versus time profile, $\bar{t}_1$ and $\bar{t}_2$ are the centroids of the upstream and the downstream profiles, $\bar{t}_2$ being calculated based on Eq. 3-3,

$$\bar{t}_2 = \bar{t}_1 + \frac{x_2 - x_1}{u} \qquad 3\text{-}3$$

and $\tau$ is the dummy time variable for integration (Rutherford, 1994).

The steps for estimating the dispersion coefficient used in this thesis can be summarised as follows:

1- The centroid of upstream and downstream profiles are found (in seconds) and used along with the distance between the two transverse lines to provide an initial guess for the longitudinal velocity, $u$.

2- An initial guess for the $D_x$ value is estimated using the method of moments.

3- The initial guess values of $u$ and $D_x$ along with $C(x_1,t)$ , $\bar{t}_1$ and $\bar{t}_1$ are used as inputs for Eq. 3-2, to provide an initial guess for $C(x_2,t)$ i.e. estimated downstream concentration versus time profile.

4- The difference between the estimated downstream profile and the observed downstream profile is minimized by optimizing the values of $u$ and $D_x$ using the `fmincon` function in MATLAB. See Appendix 1 for the code. The original code for producing the geometry files was written by Dr Fred Sonnenwald, a

Research Associate in the Department of Civil and Structural Engineering, the University of Sheffield.

The resulting optimized longitudinal velocity was then used for estimating travel time in the optimization of $D_y$ and also for nondimensionalizing $D_y$.

For the transverse dispersion, concentration values were temporally averaged over each recording line, resulting in concentration versus transverse distance profiles for each cross section. Between each pair of cross sections, the downstream concentration was predicted and the transverse dispersion coefficient was estimated based on a similar set of steps to those listed for estimating $D_x$, but based on the transverse version of the routing solution of the advection dispersion equation, i.e. Eq. 3-4,

$$C(x_2,y)=\int_0^y \frac{C(x_1,y)\Delta x}{\sqrt{4\pi D_y\left(\Delta x/u\right)}}\, exp\left[\frac{-\left(\lambda-y-v\left(\Delta x/u\right)\right)^2}{4D_y\left(\Delta x/u\right)}\right] d\lambda \qquad 3\text{-}4$$

where $C(x_1,y)$ is the upstream observed concentration versus transverse distance profile, $C(x_2,y)$ is the predicted downstream concentration versus transverse distance profile, and $\lambda$ is the dummy width variable for integration.

### 3.2.4 Flow Field Results

The resulting longitudinal velocity field after solving the flow and turbulence equations, is shown in Figure 3-3.

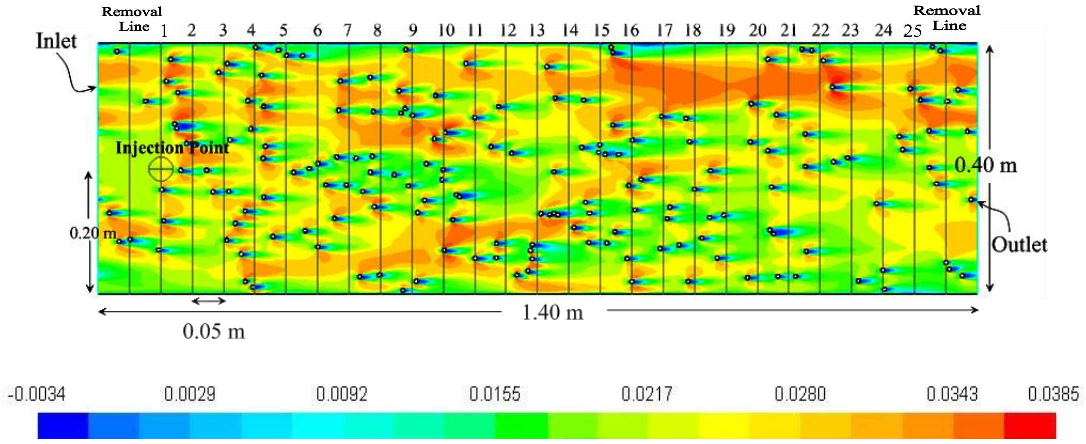

**Figure 3-3 Longitudinal velocity contours, ø = 0.010, inlet velocity = 0.023 m/s**

### 3.2.5 Scalar Transport Results

The recorded concentration values at line number 5 and line number 25 on Figure 3-3 are presented against time and transverse distance as contour plots in Figure 3-4. The transversely averaged concentration profiles and the temporally averaged concentration profiles are also provided in Figure 3-4.

The dashed lines on the concentration profiles show the predicted profiles based on the optimized values of $D_x$ and $D_y$. A strong agreement between the recorded downstream profiles and the predicted ones can be seen in Figure 3-4.

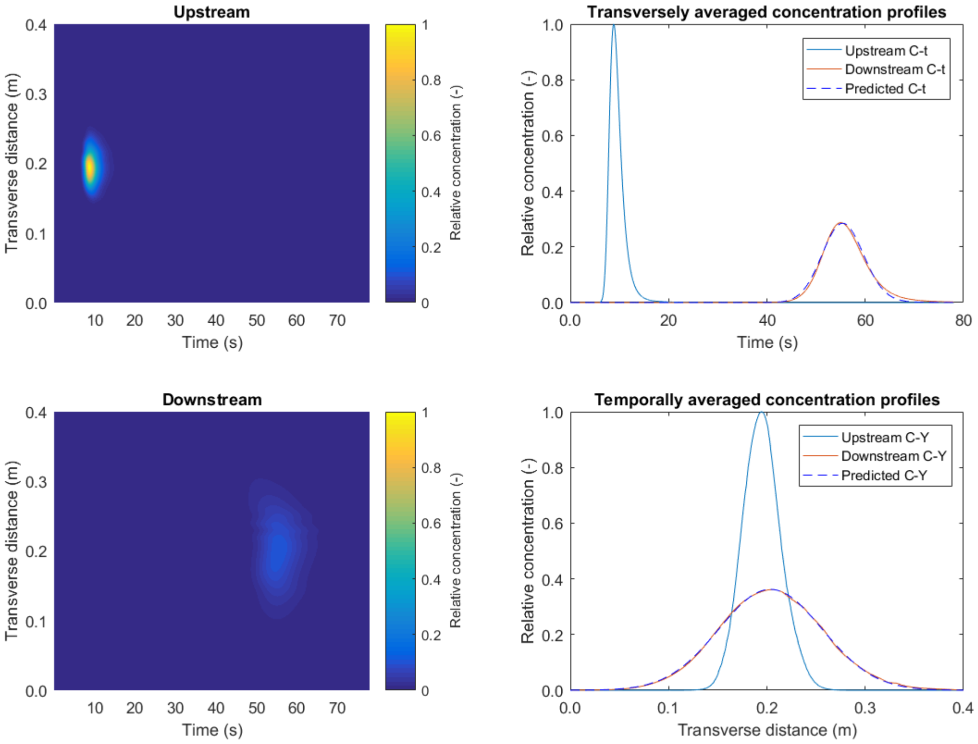

**Figure 3-4 concentration contour plots and profiles for $d$ = 0.0064 m, ø = 0.010, $Re_d$ = 147.2, $D_x$ = 8.05e-5 $m^2/s$, $D_y$ = 2.59e-5 $m^2/s$ (Upstream: line No. 5 and downstream: line No. 25 on Figure 3-3)**

### 3.2.6 Finding the Minimum Representative Channel Size

The transverse dispersion coefficients were estimated between all the cross-section pairs on Figure 3-3, the values were then grouped based on the distance between the upstream and downstream cross-sections. The injection point cross section was not considered to avoid possible numerical dispersion. From cross-section number 2 to cross-section number 25 there are 276 different possible scenarios grouped in 24 groups of channel units with the length varying from 0.05 m to 1.15 m, at 0.05 m intervals. The mean and standard deviation of transverse dispersion coefficients for each group were calculated and are shown in Figure 3-5. Figure 3-5a shows the mean and standard deviation values compared with the general mean of all the values, while Figure 3-5b shows the standard deviation values nondimensionalized using the mean value of each group.

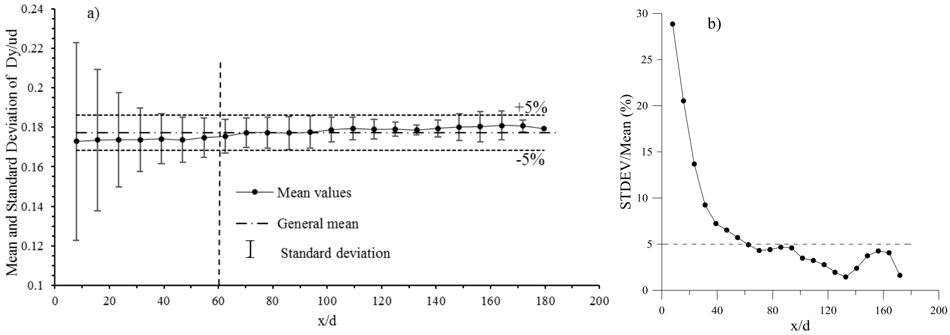

**Figure 3-5 a) Mean and standard deviation and b) Non-dimensional standard deviation of non-dimensional transverse dispersion coefficient for $\o = 0.010$, $d = 0.0064$ m, $Re_d = 147.2$,**

Taking a standard deviation of less than 5% of the mean value as a criterion for an acceptable value, then one can say that, for $\o = 0.010$, the minimum length required to fulfil this criterion is 0.384 m, ($x/d = 60$ and $d = 0.0064$).

If the above conclusion is generalized, and also assuming that with increasing the solid volume fraction the required representative array length decreases, then the minimum required length would be 0.38 m or less. This length would be equivalent to the distance between line No. 2 and line No. 9 on Figure 3-3. The spread of the plume over the width of the channel over this longitudinal distance, i.e. from line No. 2 to line No. 9 on Figure 3-3, is less than 0.20 m as shown in Figure 3-6.

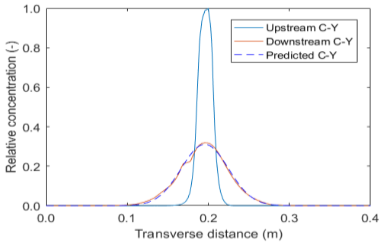

**Figure 3-6 Spread of tracer plume over the channel width (upstream: line No. 2 and downstream: line No. 9 on Figure 3-3)**

Thus, the rest of the cases were built as 0.20 m wide and 0.60 m long channels. Considering the upstream and downstream tracer removal lines at $x$ = 0.05 m and at $x$ = 0.55 m respectively, and the injection point at $x$ = 0.10 m, this leaves 0.35 m for the tracer to be advected and dispersed over the channel length and width. The remaining cases with different solid volume fractions presented in Table 3-1 were modelled using this geometry and based on the same method as explained above. The resulting transverse dispersion coefficients are compared with the laboratory data in §3.2.7.

### 3.2.7 Validation

Eight geometries, representing the different values of solid volume fractions presented in Table 3-1, were modelled following all the procedures explained in previous sections. Three different inlet velocities, i.e. the minimum, midpoint and maximum of the reported range of velocities in Table 3-1, were set as input velocity for each geometry. An example channel geometry with longitudinal velocity contours for $ø$ = 0.091 and inlet velocity of 0.049 m/s is shown in Figure 3-7. The scalar was injected at $x$ = 0.10 m from the inlet and its concentration was recorded every 0.05 m. The transverse dispersion coefficient was then estimated based on the concentration on line number 2 (at $x$ = 0.15 m) and on line number 9 (at $x$ = 0.50 m).

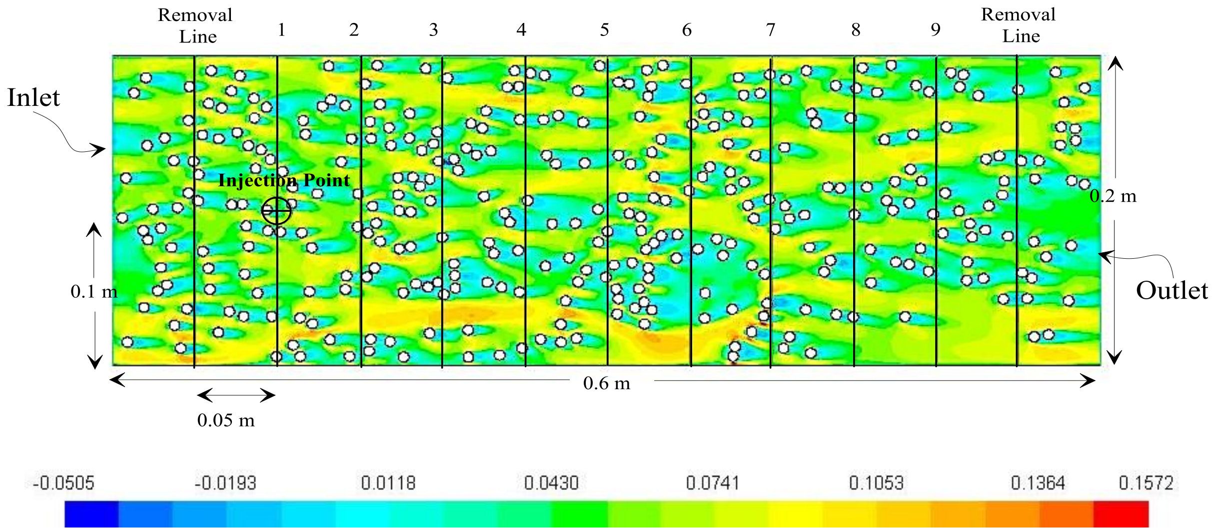

**Figure 3-7 Longitudinal velocity contours, $\phi$ = 0.091, inlet velocity = 0.049 m/s**

A sample of upstream and downstream concentration contour plots and profiles along with the predicted downstream concentration profiles for $\phi$ = 0.091 is shown in Figure 3-8.

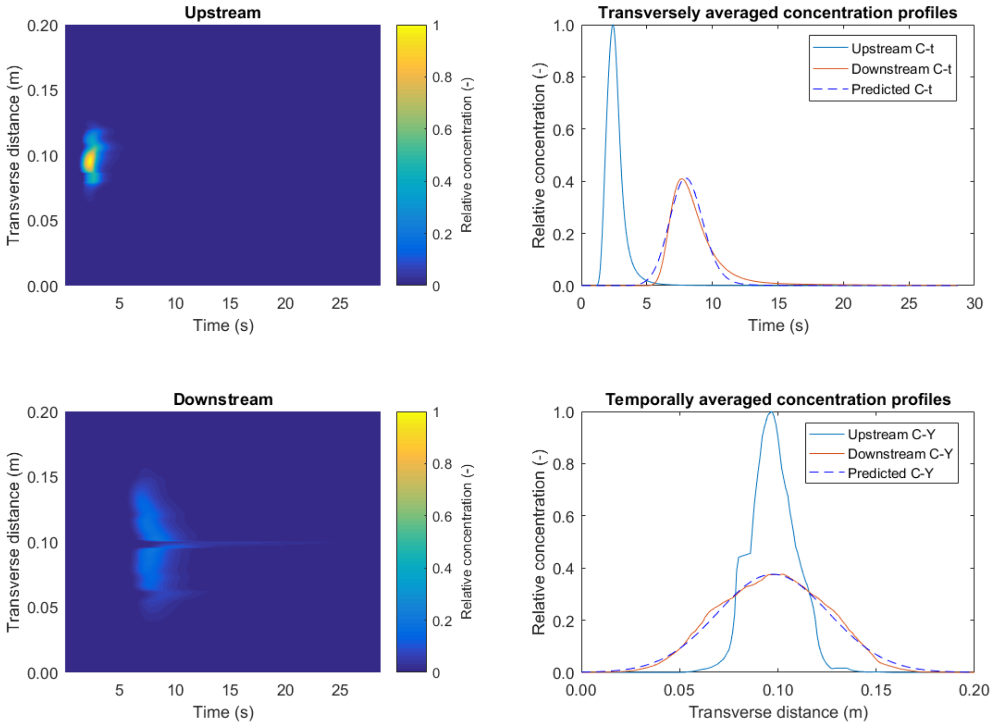

**Figure 3-8 Upstream and downstream concentration along with the predicted downstream concentration for $ø = 0.091$, $D_x = 3.43e\text{-}4$, $D_y = 6.13e\text{-}5$ (upstream: line No. 2, downstream: line No. 9 in Figure 3-7.)**

The resulting transverse dispersion coefficients were nondimensionalized by the cylinder diameter i.e. 0.0064 m and the optimized longitudinal velocity for each case. The normalized transverse dispersion coefficients resulting from CFD models are compared with laboratory data from Tanino and Nepf 2008, in Figure 3-9.

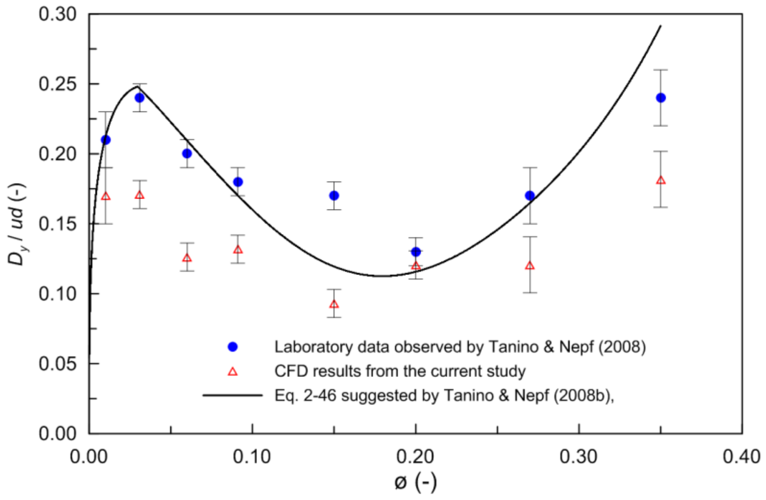

**Figure 3-9 Comparison between CFD results and previously published laboratory data**

It can be observed from Figure 3-9, that the trend of laboratory data is regenerated by the CFD results. This led to the validation of the CFD method used in this study and also supports the theoretical relations suggested by Tanino and Nepf (2008b), i.e. that the net transverse dispersion can be expressed as the linear superposition of turbulent diffusion and mechanical dispersion.

### 3.2.8 Discussion and Conclusion

The difference between CFD results and laboratory data can be investigated from different aspects. The CFD models used in this study were 2D models which means neglecting the effect of bed in the mixing processes. Not all of the laboratory condition can be modelled and regenerated in CFD models, e.g. the wooden dowels used in the laboratory have a certain wall friction which was not modelled in CFD, and the same is true for the channel boundaries. On the other hand, the laboratory errors and uncertainties also should be considered as a source of difference between CFD and laboratory data.

Another important difference between the CFD model and the laboratory setup is the exact position and arrangements of the cylinders. The solid volume fractions used for the CFD study were the same as those reported for the laboratory data with a random distribution. However, since the exact location of each cylinder for the laboratory data was not available, it was not possible to make the geometries exactly similar to those used for the laboratory study.

In general, it can be concluded that the described CFD modelling tool and procedure provides an acceptable way of representing and quantifying mixing within cylinder arrays. The use of this tool can be justified to investigate other conditions such as different solid volume fractions and different cylinder diameters, which are presented in the next chapter. It should be mentioned that the preliminary validation presented in this chapter was only based on transverse dispersion coefficients, a general and comprehensive validation for both transverse and longitudinal dispersion coefficients will be presented in the next chapter.

## 3.3 Sensitivity to the Injection Point Location

As a pulse injection was used in all the modelling it was important to analyse the effect of the injection point location on the resulting dispersion values. In this section, the effect of injection point location within two different arrays is investigated. The results presented in this section also provide a comparison between a regular and a random array.

## 3.3.1 Geometry and Modelling Setup

Two 1.5 m long, 0.5 wide channels consisting of regular and random distributions of 0.004 m diameter cylinders were used as geometry, both with the same solid volume fraction of $ø = 0.005$ and frontal facing area of $a = 0.016$ cm$^{-1}$. This density was initially chosen to reproduce laboratory results of Sonnenwald et al. (2017). The geometries of the regular and random arrays, along with the channel dimensions, are shown in Figure 3-10 a) and Figure 3-10 b), respectively.

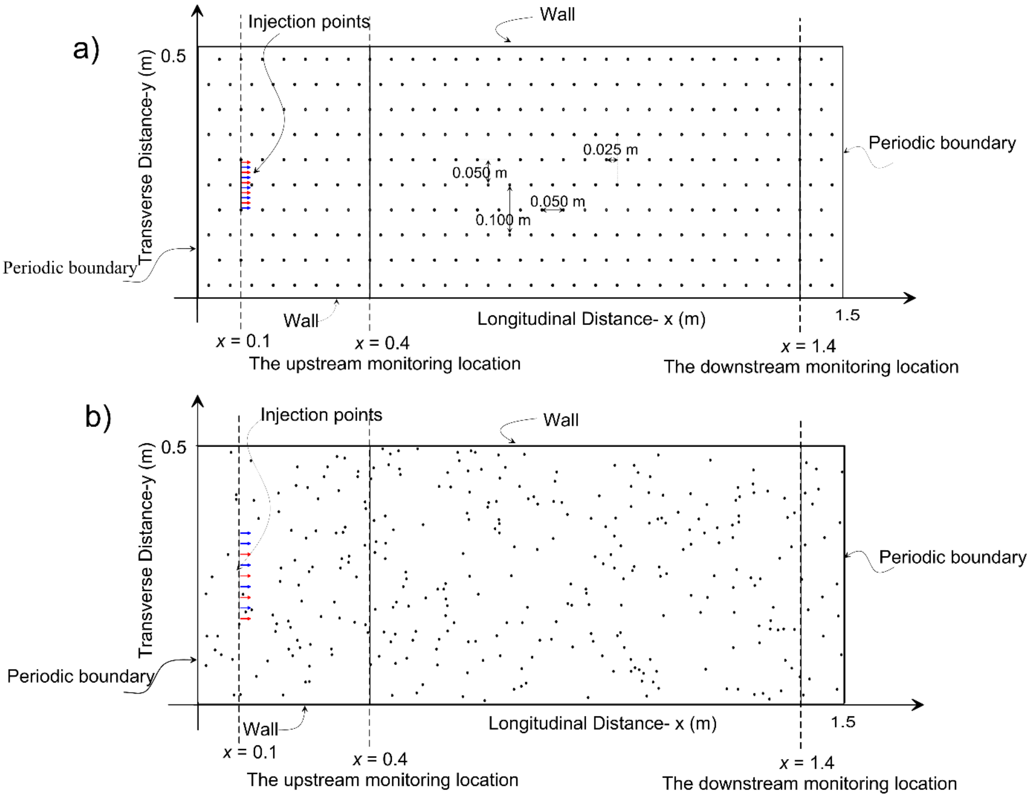

**Figure 3-10 Channel dimensions, boundary conditions and injection points: a) The regular array, b) The random array**

Both models were meshed using a uniform 0.001 m triangular mesh with approximately $1.6\times10^6$ cells for each array. The conditions and settings used for solving the flow and turbulence equations and also for running the scalar transport was similar to what was explained in §3.2 and are not repeated here for the sake of brevity.

### 3.3.2 Velocity Field Results

The inlet mass flow for both models was set based on a mean velocity of 0.017 m/s, which corresponds to a Reynolds number of $Re_d = 67.2$, based on the cylinder diameters. The longitudinal velocity contours are shown in Figure 3-11a and Figure 3-11b for the regular and random array, respectively.

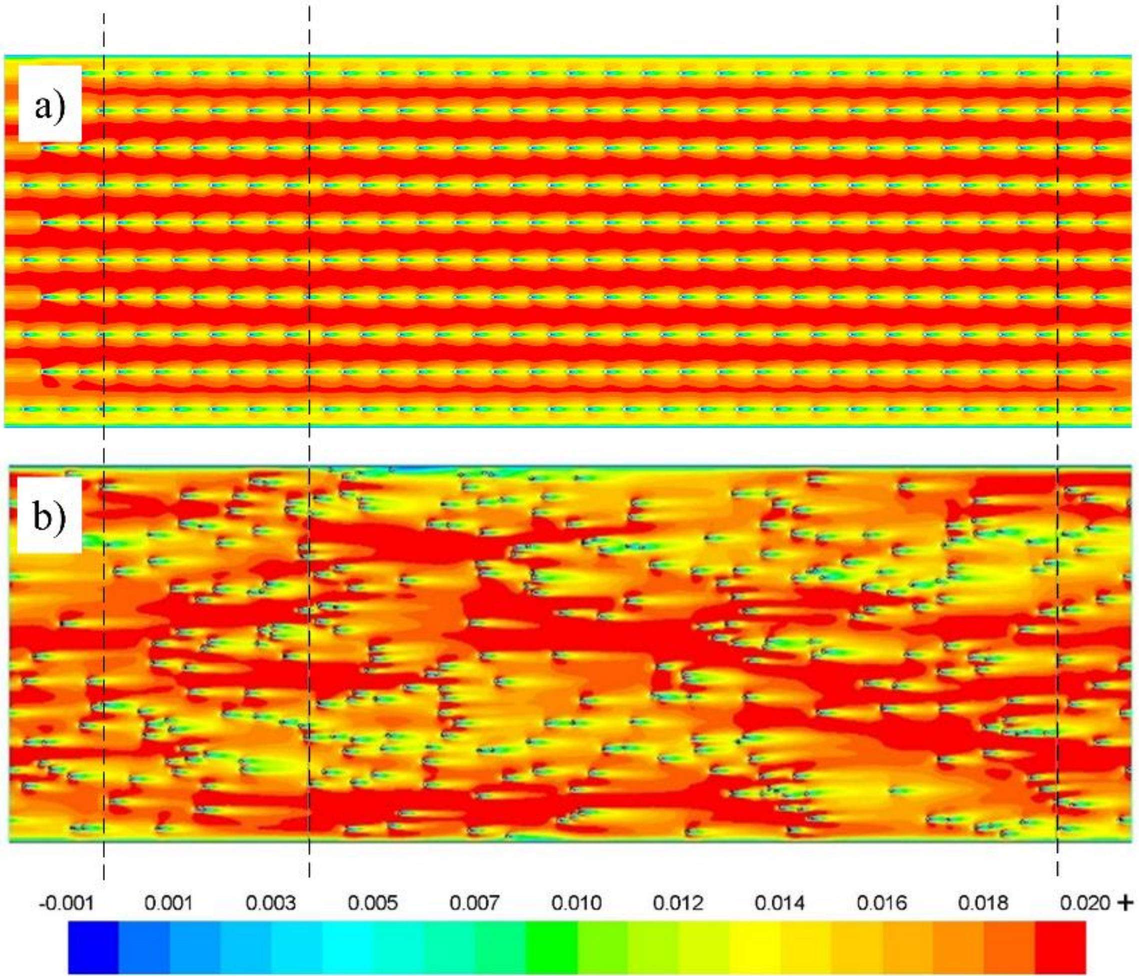

**Figure 3-11 Longitudinal velocity contours: a) Regular array, b) Random array; the maximum value is 0.027 m/s**

The resulting shear can have a determining effect on the mixing coefficients. In order to compare the shear in each flow field, transverse profiles of longitudinal velocity, $u$ and transverse velocity, $v$, recorded at $x = 0.4$ m for both regular and random fields are shown in Figure 3-12a and Figure 3-12b, respectively.

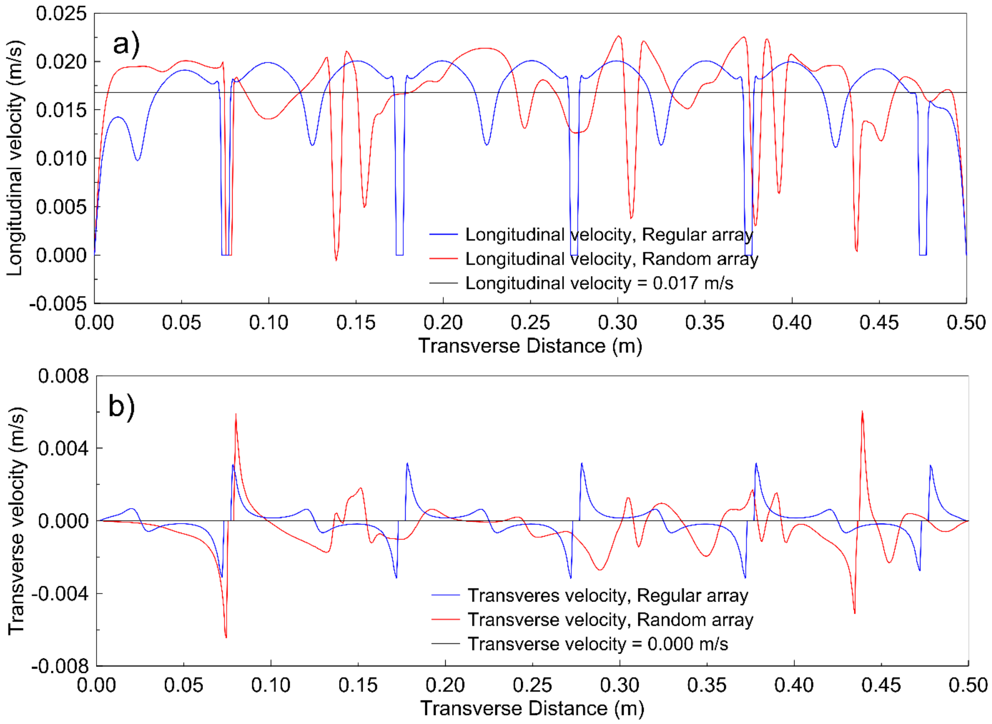

**Figure 3-12 Velocity profiles recorded at *x* = 0.4 m: a) Longitudinal velocity, b) Transverse velocity**

The regular array results in a regular flow field with fast flow between the cylinders and dead zones behind the cylinders; whereas the random array results in a random distribution of peak velocity values. In order to quantify the corresponding velocity shear in each flow field, the rates of changes in longitudinal velocity values over the channel width, i.e. |*du*/*dy*|, were calculated between adjacent cells on 21 cross sections (0.4 m ≤ *x* ≤ 0.6 m) in each flow field. The mean and standard deviation of velocity shear, |*du*/*dy*| for each cross section are shown in Figure 3-13.

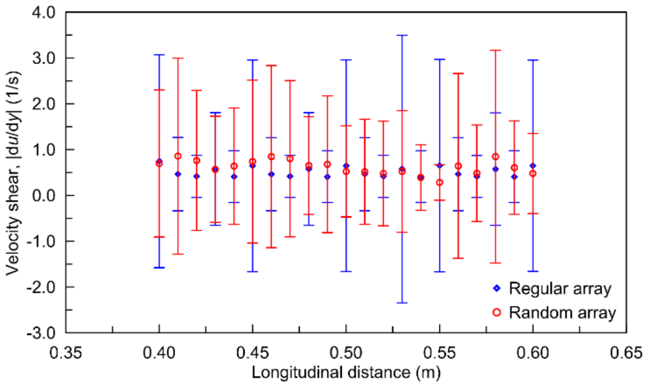

**Figure 3-13 Mean and standard deviation of velocity shear, |d*u*/d*y*|**

Although the mean values of the velocity shear in both arrays are very close to each other, the randomly distributed array has a higher standard deviation of velocity shear, |d$u$/d$y$| over more than half of the cross-sections. Higher dispersion coefficients are therefore expected for the random array.

It was expected that the transverse position of the tracer injection would influence the tracer's path and in turn affect its transverse and longitudinal distribution. These effects are dependent on whether the injection point falls immediately behind a stem or within the fast flow. Therefore, the injection point location was varied systematically within the mid-section of each channel, as was shown in Figure 3-10. These effects can be investigated by comparing the resulting mixing coefficients.

### 3.3.3 Scalar Transport Results

The scalar was injected at each of the injection points during a separate scalar transport modelling and was recorded on the recording lines shown in Figure 3-10 for each geometry. The resulting longitudinal and transverse dispersion coefficients are presented and compared in this section.

### 3.3.4 The sensitivity of Longitudinal Dispersion Coefficient, $D_x$ to injection point location

The transversely averaged temporal concentration profiles are presented in Figure 3-14a) and Figure 3-14b), for the regular and random arrays, respectively. The predicted downstream concentration distributions for the tracer released at $y$ = 0.22 m for the regular array and at $y$ = 0.25 m for the random array are included to illustrate the typically good fit between observed profiles and those predicted from the fitted value of $D_x$. It should be noted that the profiles for the tracers released in the regular array between $y$ = 0.24 m and $y$ = 0.28 m are not presented considering the symmetric nature of the velocity field. And also some of the concentration distributions of the random array are not included for sake of readability.

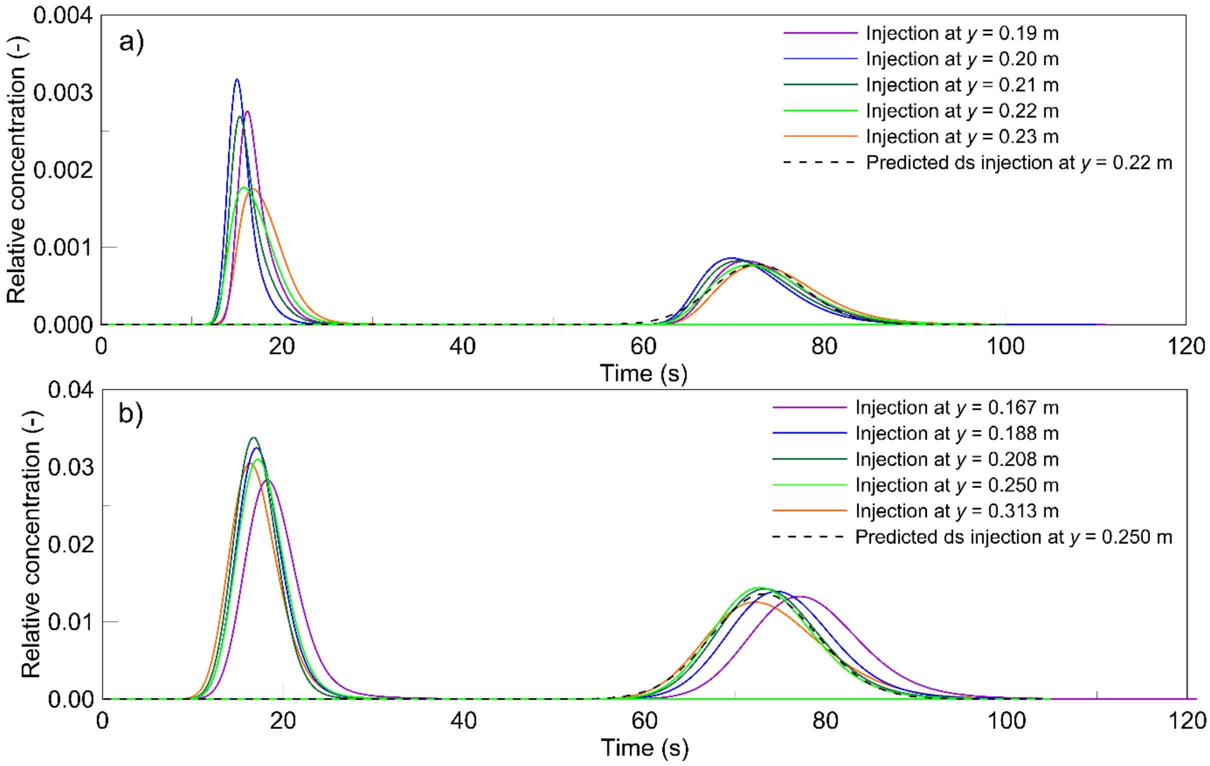

**Figure 3-14 Width-averaged concentration versus time for a) the regular array, b) the random array**

The longitudinal distributions of tracer released at different lateral injection points in the regular array are quite similar, except for those released at $y = 0.20$ m, which corresponds to the maximum longitudinal velocity value. Moving with the maximum longitudinal velocity, the tracer particles released at $y = 0.20$ m pass the monitoring positions before those released from other injection points. The same effect can be seen in the random array for tracer released at $y = 0.208$ m, which also corresponds to a high longitudinal velocity. To provide a more detailed comparison between different scenarios, the longitudinal dispersion values calculated for the regular and random arrays along with the mean value for each group are presented in Figure 3-15. The lines corresponding to ±10% of the mean values are also shown in the figure in order to facilitate the comparison. The exact location of the injection points for each array is also shown on the velocity field contours.

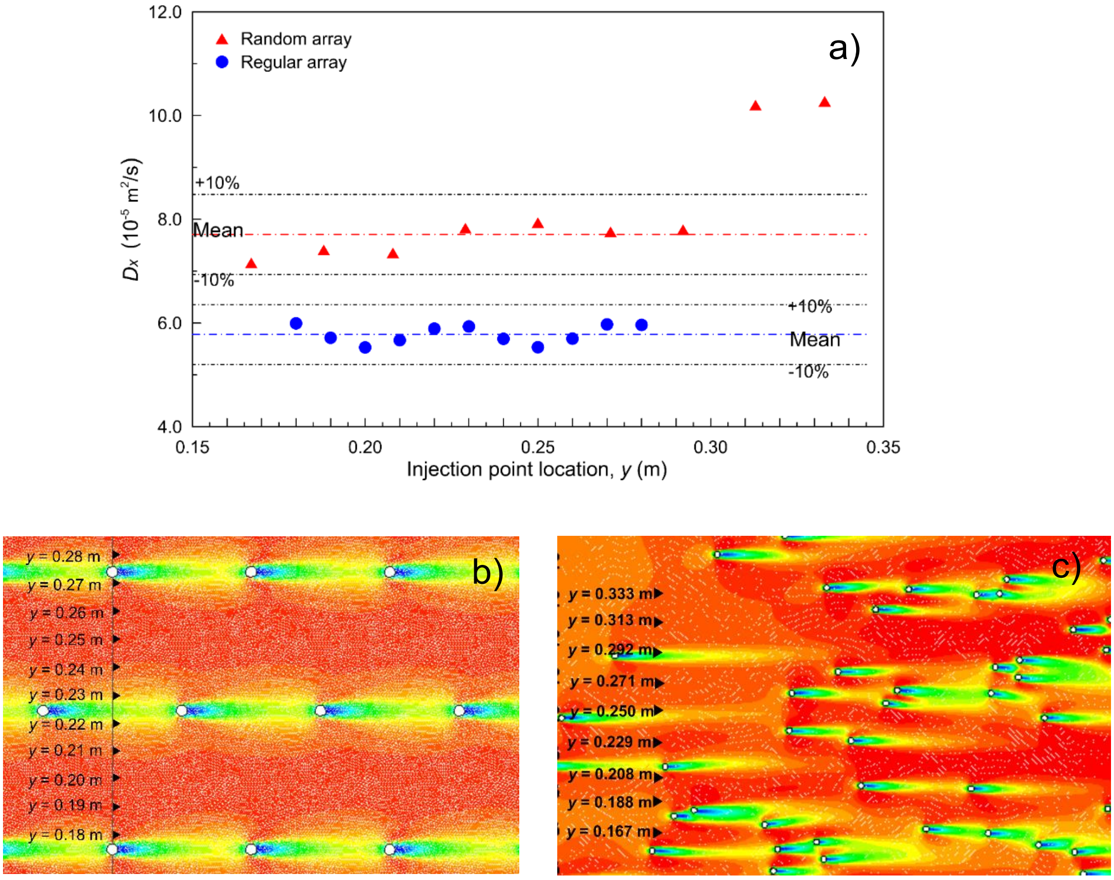

**Figure 3-15 a) Longitudinal dispersion coefficients resulting from different injection point locations for b) regular and c) random arrays along with the injection point location within the longitudinal velocity field of each array**

Comparing Figure 3-15 a), with Figure 3-15 b) and c) shows the relation between the injection point location and the value of $D_x$ in each array. The periodic pattern of the longitudinal dispersion values resulting from the regular array shows that the conditions and the velocity at the injection point location have a direct effect on the degree of mixing tracer experiences along the channel. Considering this effect, the random pattern of the longitudinal dispersion values from the random array seems reasonable and also reliable. Considering the location of injection points regarding the velocity field in the regular array, it can be said that the injection point located at higher velocity values, i.e. in the space between the stem rows, have resulted in relatively lower $D_x$ values. The reason for this can be the relatively uniform velocity field shaped in between the stem rows resulting in less turbulence and less mixing and lower $D_x$ values, in turn. While the scalar released from the injection points closer to the stems experiences more shear which results in higher $D_x$ values.

The range of variation of the resulting $D_x$ values, for both arrays, is less than ±10% for all of the injection points except for $y = 0.313$ m and for $y = 0.333$ m in the random array. The value of $D_x$ for these two injection points is approximately 30% higher than the mean $D_x$ value. One justification for this fact can be the remote location of these two points from the cylinders. All the other injection points in the random array happen to be relatively close to the cylinders and are affected by their wake effects, while these two points happen to be in a relatively uniform velocity field and this may result in a different mixing condition for the scalar injected from them comparing to other injection points.

The values of $D_x$ corresponding to the four middle injection points located at $y = 0.229$ m to $y = 0.292$ m are very close, which regarding their relative location to the stems can be interpreted as a low sensitivity of $D_x$ value to the injection point location in random arrays. In other words, as long as the injection point location happens to be relatively close to the stems and surrounded by them, the resulting $D_x$ value has a low sensitivity to injection location. One can also say that by increasing the solid volume fraction, the injection point location is more likely to happen in the proximity of the cylinders, which decreases the sensitivity of the results to its location. It should be mentioned that the solid volume fractions modelled in this thesis are all higher than the solid volume fraction of the two arrays presented in this section.

Comparing $D_x$ values resulting from regular and random arrays reveals that the sensitivity of results on the injection point location is lower in random arrays. This also leaves more freedom in choosing the injection point location for the rest of the models in the thesis as they are all random arrays. The same investigating on the sensitivity of $D_y$ values on the injection point location is presented in the next section.

### 3.3.5 The Sensitivity of Transverse Dispersion Coefficient, $D_y$, to injection point location

Figure 3-16 shows the transverse distributions of time-averaged tracer over the width of the channel at both the downstream and the upstream monitoring locations for the regular and random arrays respectively. Some of the concentration distributions are not included for the sake of readability.

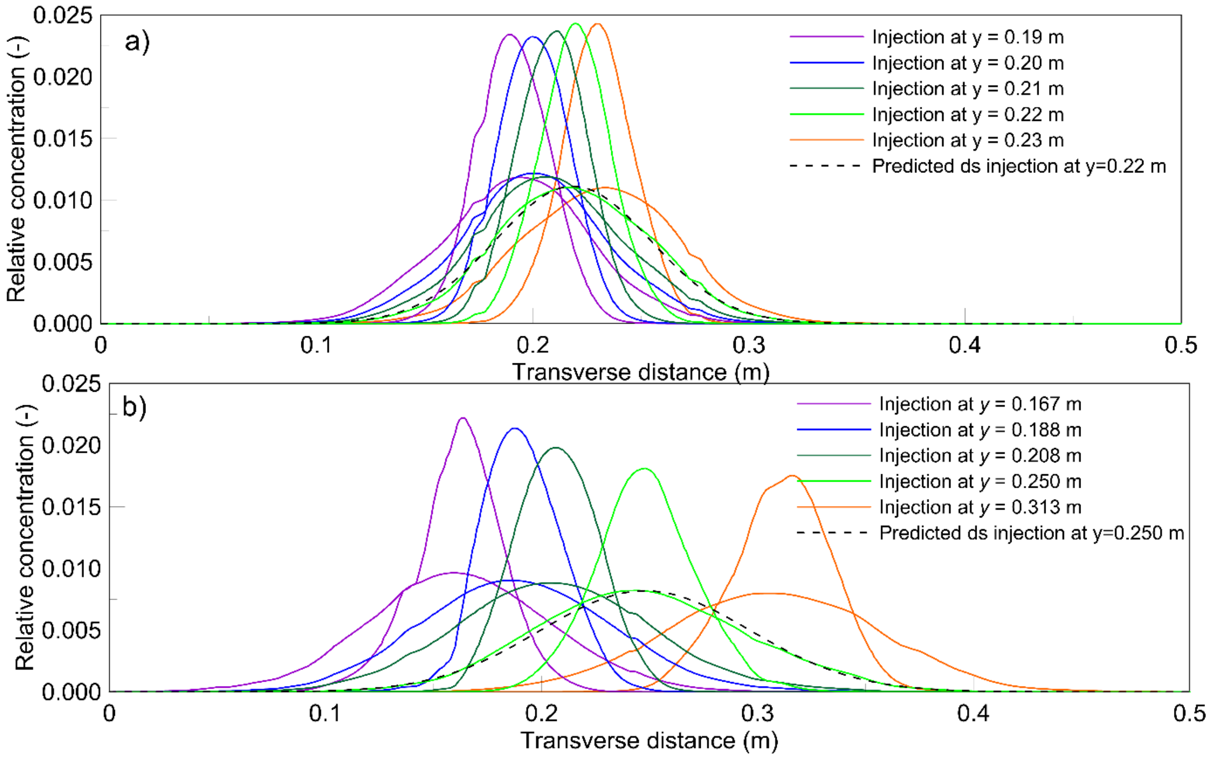

**Figure 3-16 Time-averaged concentration versus transverse distance a) for the regular array, b) for the random array**

Comparing the transverse concentration profiles resulting from different injection points, in Figure 3-16 shows a very similar behaviour for all of the profiles, which suggest a low sensitivity of the dispersion coefficients on the location of the injection point. In other words, regardless of the transverse location of the injection point, the scalar injected from different injection points will experience similar mixing conditions, even though it might have started its journey with a different longitudinal velocity depending on its injection point location. The transverse dispersion values calculated for the regular and random arrays along with their mean values are presented in Figure 3-17. The lines corresponding to ±10% of the mean values are also shown in the figure in order to facilitate the comparison. The exact location of the injection points for each array is also shown on the velocity field contours.

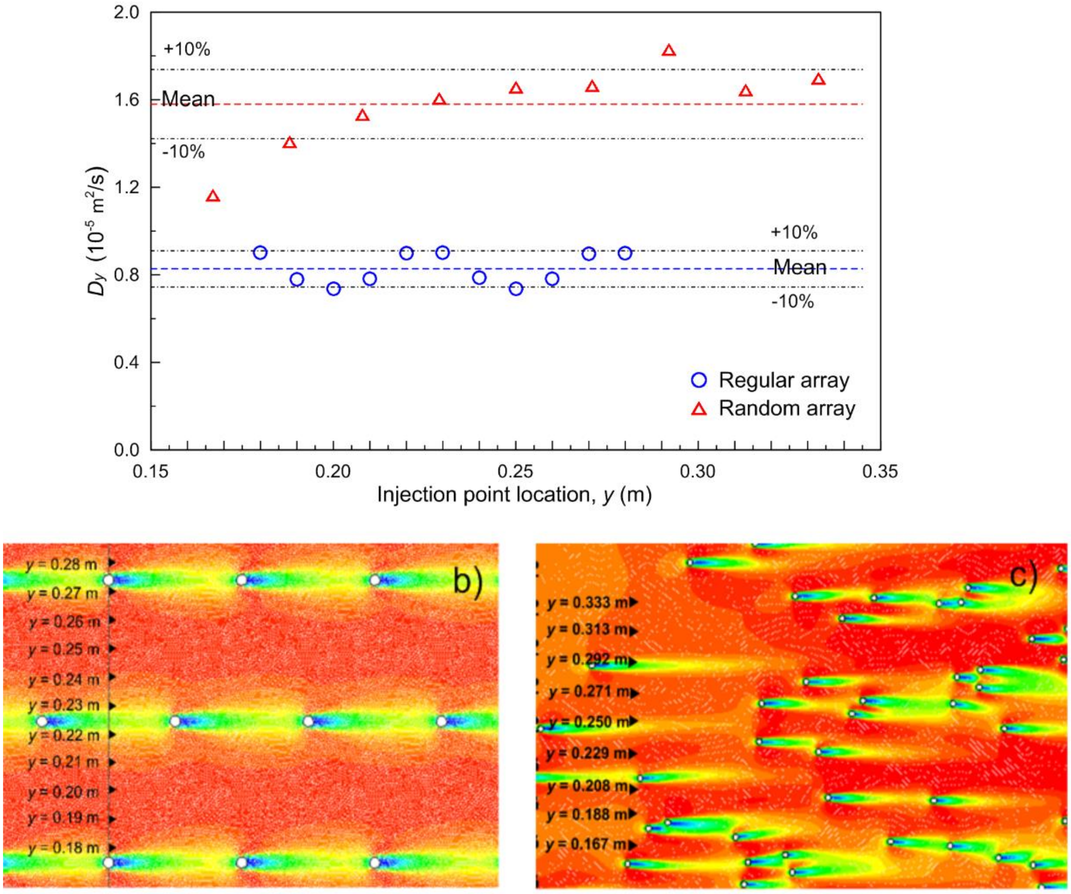

**Figure 3-17 a) Transverse dispersion coefficients resulting from different injection point locations for b) regular and c) random arrays along with the injection point location within the longitudinal velocity field of each array**

$D_y$ values corresponding to the regular array show a similar pattern to $D_x$ values but it can be said that the sensitivity of $D_y$ is higher than $D_x$ as the range of the variations in $D_y$ is higher than that in $D_x$ presented in Figure 3-15. The same justification on the relation between the location of the injection point and the mixing experienced by the scalar released from them that was mentioned for $D_y$ values stands true for $D_x$ as well.

$D_y$ values corresponding to the random array show a different pattern from that shown by $D_x$ values of the same array in Figure 3-15, which can be interpreted as the different nature of longitudinal and transverse dispersion coefficients. As was observed for $D_x$ values, the range of variation in $D_y$ is higher for the random array, i.e. the results of the regular array are within ±10% of their mean value while the results of the random array occasionally fall in approximately ±30% of their mean value.

The injection point located at y = 0.167 m in random array has resulted in the minimum value of $D_y$ which can be justified regarding its location relative to the stems. It can be seen on the random velocity field in Figure 3-17 that this point happens to be in a similar location to those in the regular array located in the fast velocity region formed between the cylinder rows, e.g. at y = 0.20 m in the regular array. So the resulting low value of $D_y$ can be justified in a similar way as it was for the random array although in the random array the scalar won't experience a straight uniform path as it does in the regular array. So one can say there are other factors in the path experienced by the scalar such as tortuosity (Figure 2-21), in the random array that caused a low value of $D_y$ resulting from this injection point.

The injection point located at y = 0.292 m in the random array happens to be in the wake zone of a cylinder and has resulted in a relatively high $D_y$ value. This can be as a result of high degree of velocity shear experienced by the scalar injected at this point which results in higher mixing and higher dispersion value in turn. The other injection points on the random array have resulted in relatively similar values of $D_y$ which can be justified in a similar way as it was done for $D_x$ values.

In general, one can conclude a low sensitivity of both $D_x$ and $D_y$ values on the location of the injection point as long as the location point happens to be in proximity of cylinders, which will be satisfied by solid volume fractions modelled in this thesis and presented in the next chapter.

### 3.3.6 General Comparison between All the Dispersion Values

Figure 3-18 provides a general comparison between all the different dispersion values calculated in this section. The laboratory collected values of dispersion coefficients for a regular array (Sonnenwald et al., 2017), the same array as the regular array used in this section, are also included.

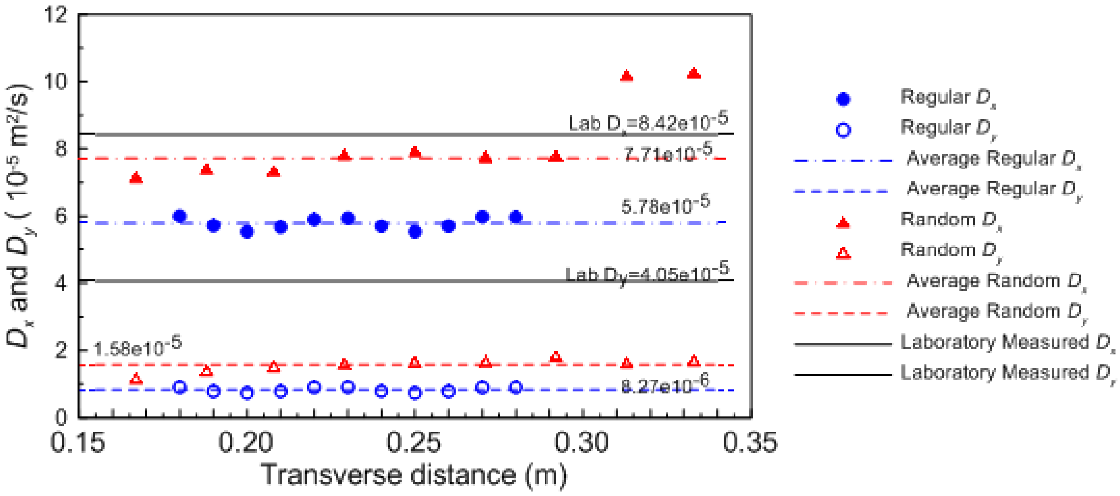

**Figure 3-18 Longitudinal and transverse dispersion coefficients for the random and regular arrays**

The mean longitudinal dispersion coefficient is approximately 1.2 times greater in the random array compared with the regular array. The $D_y$ values are approximately one-fifth of the $D_x$ values, but again the random array exhibits greater transverse dispersion when compared with the regular array.

Comparing the laboratory measured values for the dispersion coefficients, which were measured in a regular array similar to the regular array in this study by Sonnenwald et al. (2017), with those estimated in this study shows that both the longitudinal and the transverse dispersion coefficients are underestimated in this study. This could be a limitation of the two-dimensional CFD modelling and not considering the effect of vertical velocity distribution over the channel depth. Other sources of error could be the turbulence model’s approximations and ignoring the roughness of cylinders and channel walls. Also, it should be considered that in the model used in this study the tracer had only 0.3 m to be dispersed before the upstream monitoring location, whereas in the laboratory the tracer was injected 1 m before the upstream monitoring location.

### 3.3.7 Discussion and Conclusion

The comparison between the regular and random arrays’ flow fields showed the effect of randomness on velocity distribution. The random flow field had higher local maximum longitudinal velocity values, and higher standard deviations of velocity shear, |d*u*/d*y*|, which is consistent with the higher dispersion coefficients.

Both the longitudinal and transverse dispersion coefficients were underestimated in this study, but the estimation for the longitudinal coefficient was closer to the laboratory measured value compared with the transverse one.

Nepf et al. (1997) reported values of transverse dispersion measured within random cylinder arrays, for a solid volume fraction of 0.006 – which is very close to the one used in the current study – but with higher $Re_d$ numbers i.e. 192, 390, 588 and 786 and cylinder diameter of d = 0.006 m. Considering a linear relation between the normalized dispersion coefficient and $Re_d$, these values can be used to estimate a $D_y$ value for the current study. The linear extrapolation results in a normalized transverse dispersion coefficient of $D_y/ud = 0.16$ which in turn results in $D_y = 8.9\times10^{-6}$ m$^2$/s, which is approximately 0.6 of the estimated value of $D_y$ in the current study.

The relation between transverse eddy viscosity, transverse turbulent length scale, and the rate of longitudinal velocity change over the width of the channel can be described by Prandtl's mixing length hypothesis, Eq. 3 (Rutherford, 1994):

$$D_y = L_t^2 \left| \frac{du}{dy} \right| \qquad 3\text{-}5$$

where $L_t$ is the transverse turbulent length scale.

Using the mean values of velocity shear, |du/dy| over all the cross sections for the regular and the random arrays, i.e. 0.513 s$^{-1}$ and 0.619 s$^{-1}$ respectively, and the mean value of transverse dispersion coefficients, i.e. $D_y$(regular) = $8.27\times10^{-6}$ m$^2$/s and $D_y$(random) = $1.58\times10^{-5}$ m$^2$/s, results in estimated $L_t$ of 0.004 m and 0.005 m for the regular and the random array respectively. The estimated value for the regular array is almost exactly equal to the cylinder diameter i.e. $d = 0.004$ m, which helps to confirm the numerical accuracy of the RSM turbulence model. The slightly higher estimated mixing length scale for the random array is likely to be due to the combined effects of turbulent diffusion with transverse mechanical dispersion, as suggested by Tanino and Nepf (2008). The regular array would not be expected to exhibit significant mechanical dispersion due to its regular geometry.

In conclusion regarding the injection point location, no specific location relative to the cylinders is suggested for future modelling, as a low sensitivity on the injection point location was shown for both $D_x$ and $D_y$ values.

## 3.4 Comparing two different meshing methods

The flow field and mixing results of two different meshing methods were compared to decide on the appropriate meshing method to be used for the future modelling. The first meshing method, named here as "the refined mesh", is based on a uniform 0.001 m triangular mesh in the space between the cylinders and a 3 level finer mesh around the cylinders. The Curvature Normal Angle in the refined mesh model was kept at its default value i.e. 18˚. "Curvature Normal Angle is the maximum allowable angle that one element edge is allowed to span. You can specify a value from 0 to 180 degrees or accept the default." (ANSYS® Academic Research, Release 16.1). This meshing method is the same as the one used for the validation of the general methodology in §3.2. A sample of a refined mesh can be seen in Figure 3-20.

The second method, named here as "the graded mesh" is based on a gradually changing non-uniform mesh with a minimum size of 0.0001 m, maximum face size of 0.001 m and a Curvature Normal Angle of 4˚ in order to allow more cells to be built around each cylinder. A sample of the graded mesh can be seen in Figure 3-21.

### 3.4.1 Geometries

A 1.0 m long,0.4 m wide *2D* channel with randomly distributed 0.008 m diameter cylinders resulting in $ø$ = 0.100 was used as the geometry and meshed with both methods. The channel geometry along with the injection point, the scalar recording lines and the velocity recording line, are shown in Figure 3-19

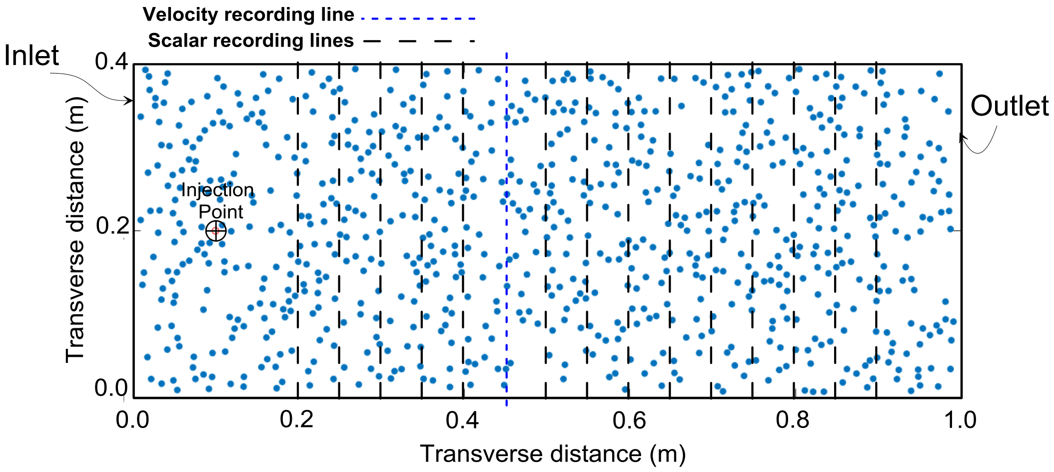

**Figure 3-19 The geometry used for both refined and graded meshing methods, *d* = 0.008 m, ø = 0.100**

### 3.4.2 Meshing Methods

The characteristics of the refined and the graded mesh are shown in Figure 3-20 and, Figure 3-21, respectively.

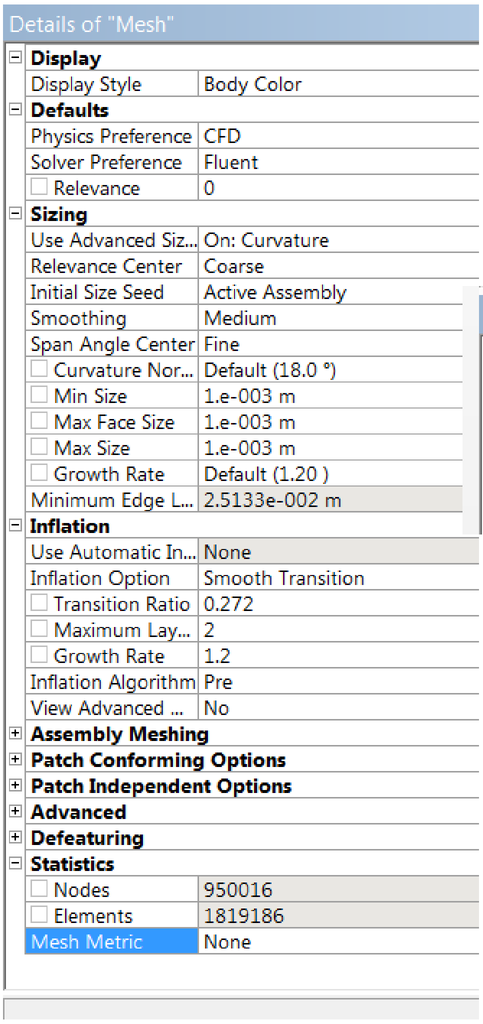

Details of "Mesh"

| | |
|---|---|
| ⊟ **Display** | |
| Display Style | Body Color |
| ⊟ **Defaults** | |
| Physics Preference | CFD |
| Solver Preference | Fluent |
| ☐ Relevance | 0 |
| ⊟ **Sizing** | |
| Use Advanced Siz... | On: Curvature |
| Relevance Center | Coarse |
| Initial Size Seed | Active Assembly |
| Smoothing | Medium |
| Span Angle Center | Fine |
| ☐ Curvature Nor... | Default (18.0 °) |
| ☐ Min Size | 1.e-003 m |
| ☐ Max Face Size | 1.e-003 m |
| ☐ Max Size | 1.e-003 m |
| ☐ Growth Rate | Default (1.20 ) |
| Minimum Edge L... | 2.5133e-002 m |
| ⊟ **Inflation** | |
| Use Automatic In... | None |
| Inflation Option | Smooth Transition |
| ☐ Transition Ratio | 0.272 |
| ☐ Maximum Lay... | 2 |
| ☐ Growth Rate | 1.2 |
| Inflation Algorithm | Pre |
| View Advanced ... | No |
| ⊞ **Assembly Meshing** | |
| ⊞ **Patch Conforming Options** | |
| ⊞ **Patch Independent Options** | |
| ⊞ **Advanced** | |
| ⊞ **Defeaturing** | |
| ⊟ **Statistics** | |
| ☐ Nodes | 950016 |
| ☐ Elements | 1819186 |
| Mesh Metric | None |

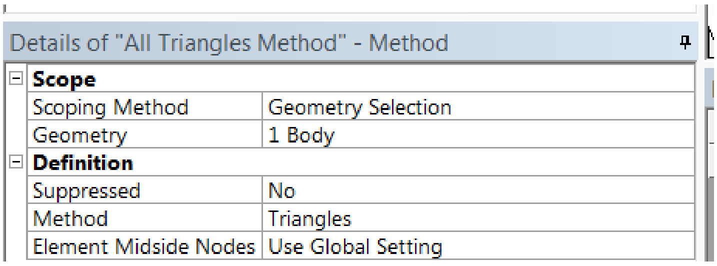

Details of "All Triangles Method" - Method

| | |
|---|---|
| ⊟ **Scope** | |
| Scoping Method | Geometry Selection |
| Geometry | 1 Body |
| ⊟ **Definition** | |
| Suppressed | No |
| Method | Triangles |
| Element Midside Nodes | Use Global Setting |

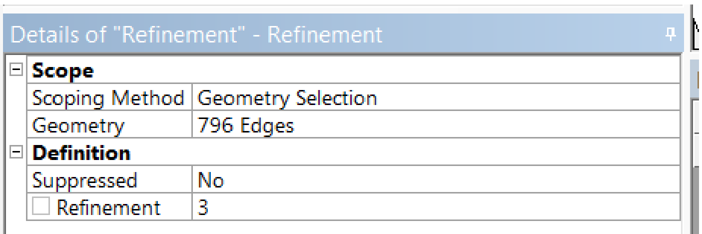

Details of "Refinement" - Refinement

| | |
|---|---|
| ⊟ **Scope** | |
| Scoping Method | Geometry Selection |
| Geometry | 796 Edges |
| ⊟ **Definition** | |
| Suppressed | No |
| ☐ Refinement | 3 |

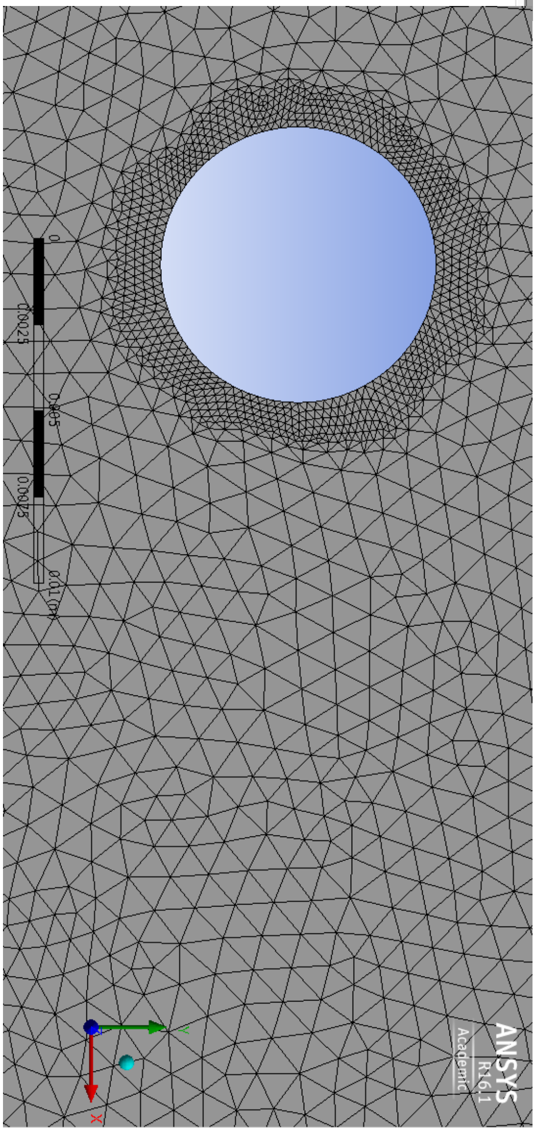

**Figure 3-20 Characteristics of the refined mesh**

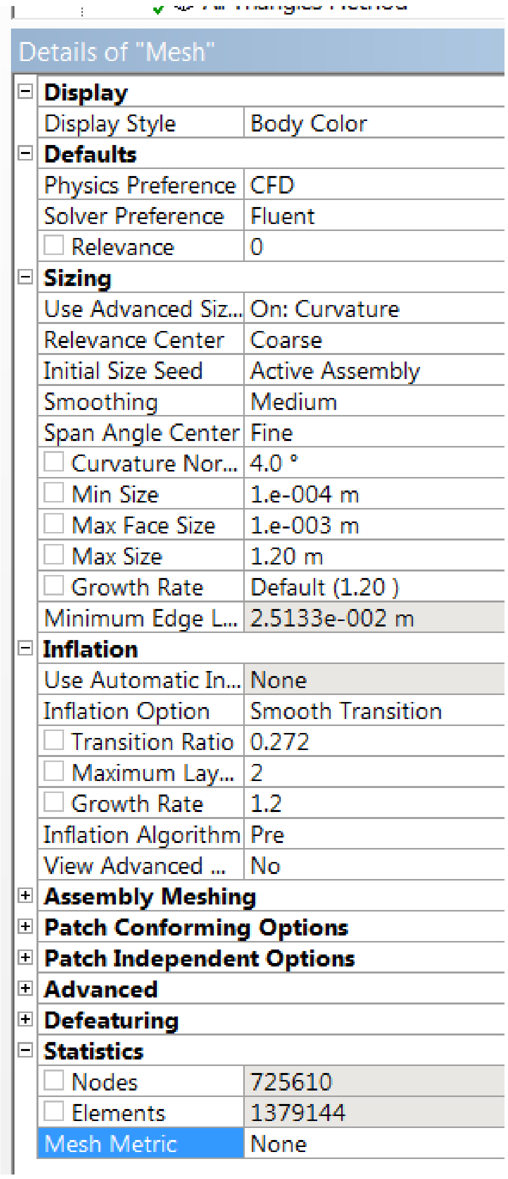

Details of "Mesh"

| | |
|---|---|
| **Display** | |
| Display Style | Body Color |
| **Defaults** | |
| Physics Preference | CFD |
| Solver Preference | Fluent |
| ☐ Relevance | 0 |
| **Sizing** | |
| Use Advanced Siz... | On: Curvature |
| Relevance Center | Coarse |
| Initial Size Seed | Active Assembly |
| Smoothing | Medium |
| Span Angle Center | Fine |
| ☐ Curvature Nor... | 4.0 ° |
| ☐ Min Size | 1.e-004 m |
| ☐ Max Face Size | 1.e-003 m |
| ☐ Max Size | 1.20 m |
| ☐ Growth Rate | Default (1.20 ) |
| Minimum Edge L... | 2.5133e-002 m |
| **Inflation** | |
| Use Automatic In... | None |
| Inflation Option | Smooth Transition |
| ☐ Transition Ratio | 0.272 |
| ☐ Maximum Lay... | 2 |
| ☐ Growth Rate | 1.2 |
| Inflation Algorithm | Pre |
| View Advanced ... | No |
| **Assembly Meshing** | |
| **Patch Conforming Options** | |
| **Patch Independent Options** | |
| **Advanced** | |
| **Defeaturing** | |
| **Statistics** | |
| ☐ Nodes | 725610 |
| ☐ Elements | 1379144 |
| Mesh Metric | None |

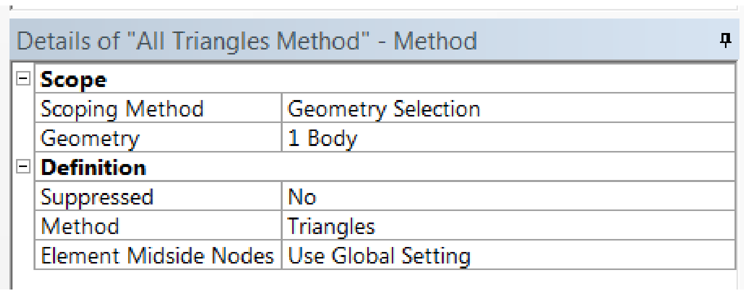

Details of "All Triangles Method" - Method

| | |
|---|---|
| **Scope** | |
| Scoping Method | Geometry Selection |
| Geometry | 1 Body |
| **Definition** | |
| Suppressed | No |
| Method | Triangles |
| Element Midside Nodes | Use Global Setting |

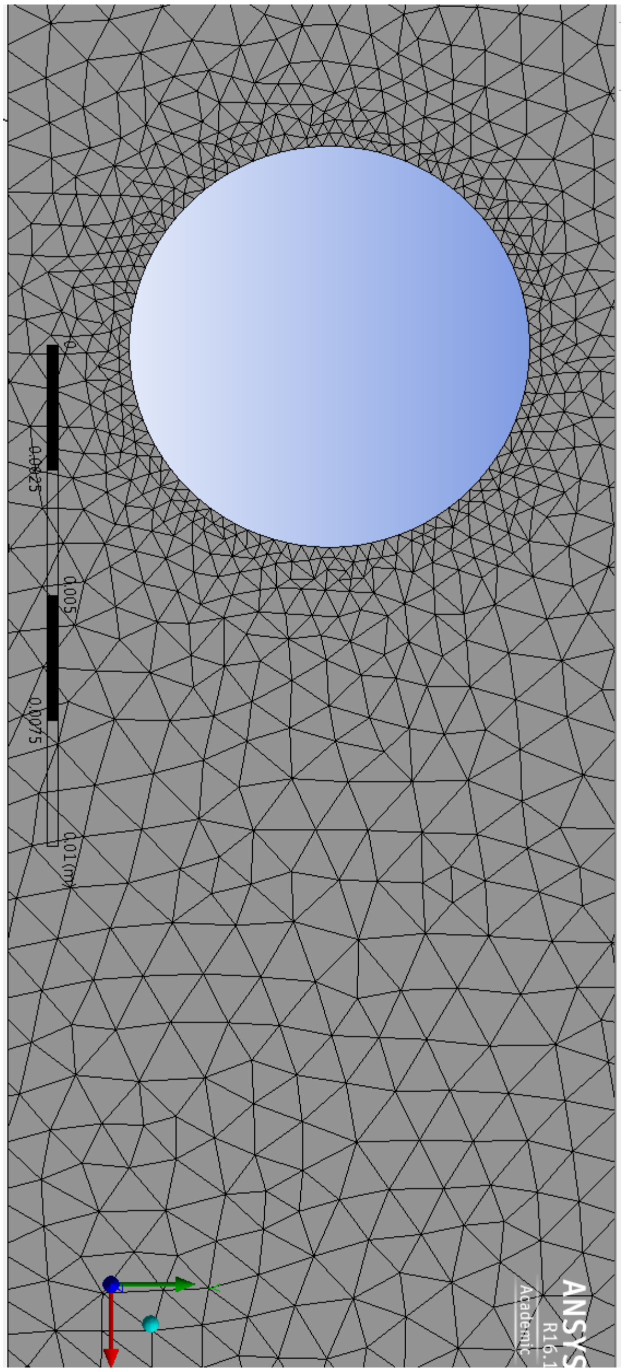

Figure 3-21 Characteristics of the graded mesh

### 3.4.3 Model settings, residuals and convergence

Both models were set as steady RSM models with periodic boundaries as inlet and outlet and inlet mass flow of 9.982 kg/s, equivalent to an inlet velocity of 0.025 m/s. The residual condition can be seen in Figure 3-22 and Figure 3-23 for the refined and the graded meshing methods respectively. The iterations have been continued until it was justified that each model was converged and that continuing the iteration would not improve the solution.

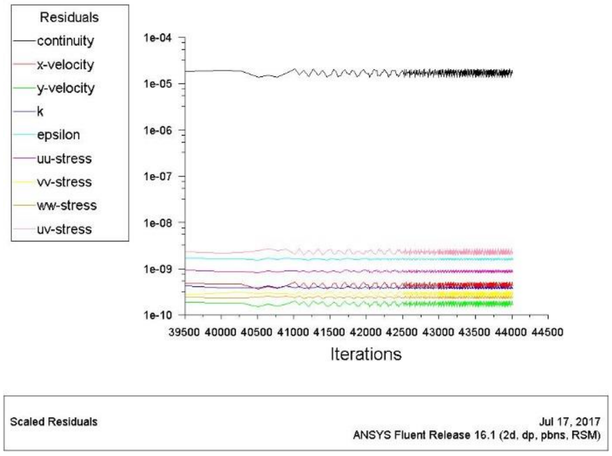

**Figure 3-22 Scaled residuals for the refined mesh**

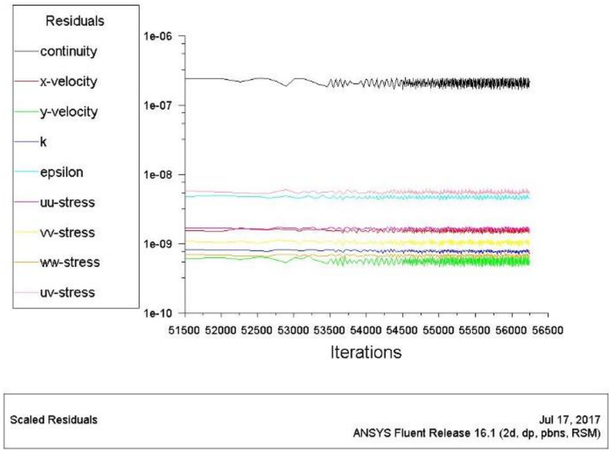

**Figure 3-23 Scaled residuals for the graded mesh**

As it can be seen in Figure 3-22 and Figure 3-23, the iterations were left to continue until the residuals reach to a constant value where no longer will improve by continuing the iterations, i.e. reach the fully converged state. This convergence criteria has been considered for all the models presented in this thesis.

### 3.4.4 Comparing the Flow Field Results

The longitudinal velocity contours for the refined and the graded mesh models are shown in Figure 3-24.

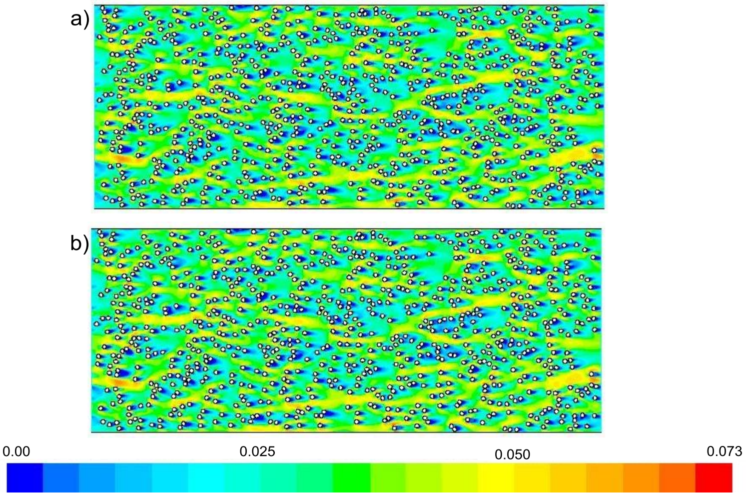

**Figure 3-24 Longitudinal velocity contours resulting from models with a) the refined meshing method b) the graded meshing method, values are in (m/s)**

The velocity contours seem to be completely similar. To have a more precise comparison, the longitudinal velocity profiles recorded at the inlet and at $x = 0.45$ m for both models are shown in Figure 3-25. As the velocity profiles completely overlap, it can be said that the models are identical in terms of velocity distribution.

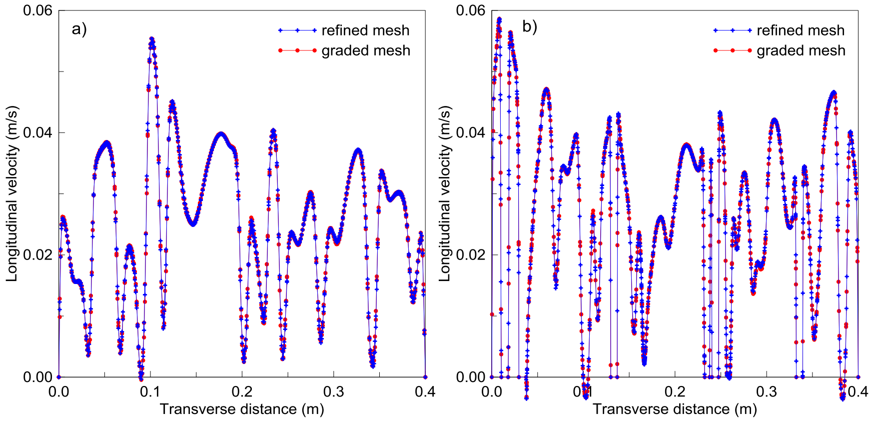

**Figure 3-25 Longitudinal velocity profiles a) at the inlet b) at $x$ = 0.45 m**

### 3.4.5 Comparing the Scalar Transport Results

The scalar was injected at $x = 0.10$ m, $y = 0.2$ m in both models and was recorded at different transverse recording lines with 0.05 m intervals i.e. lines located at $x = 0.20$ m to $x = 0.90$ m on Figure 3-19. Upstream and downstream observed concentration contour plots and profiles along with the downstream predicted profiles, for both models for the reach between the lines located at *x* = 0.20 m and at *x* = 0.90 m are presented in Figure 3-26.

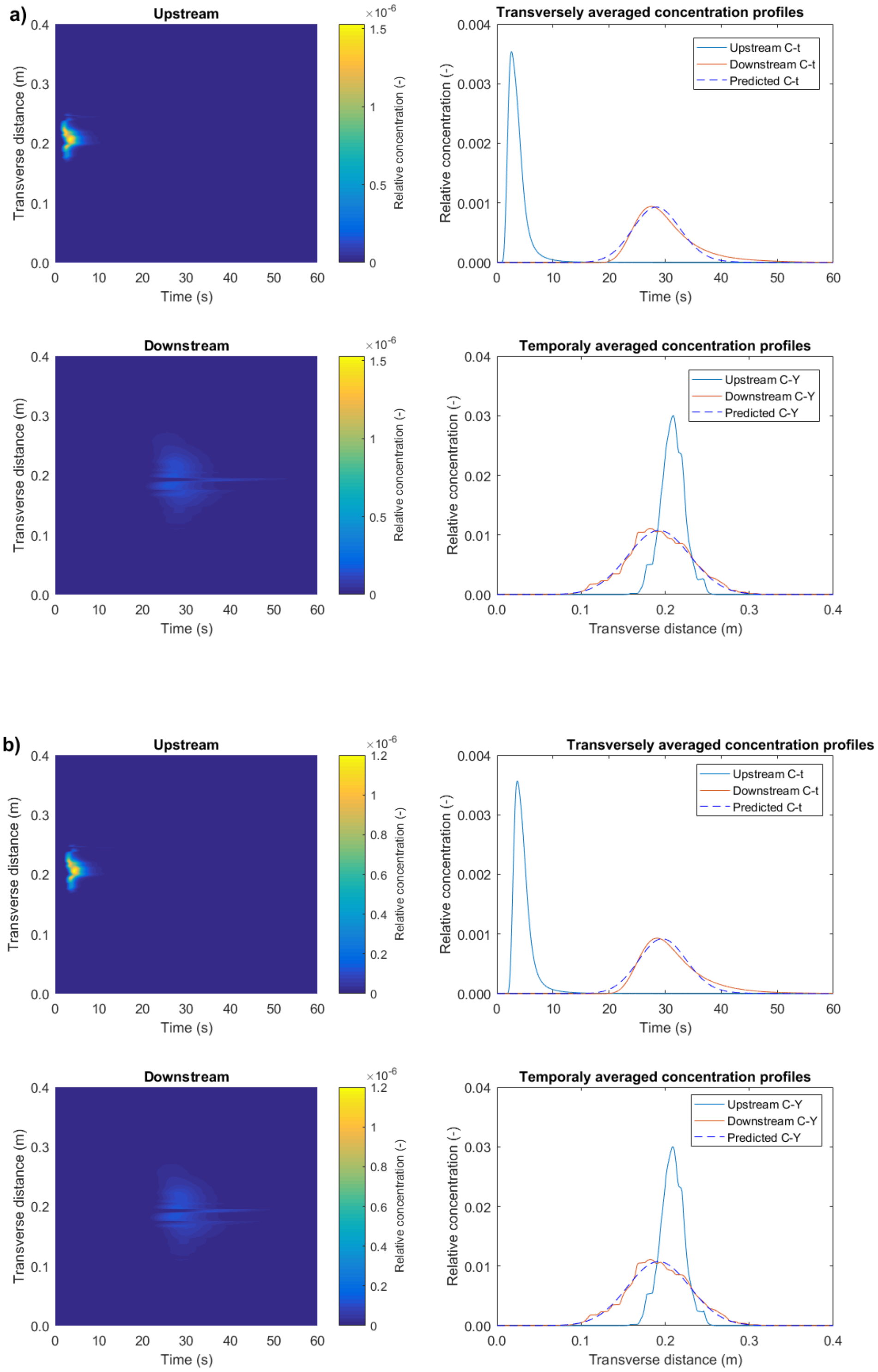

**Figure 3-26 Scalar transport results from a) the refined mesh model b) the graded mesh model, upstream: line at *x* = 0.20 m, downstream: line at *x* = 0.90 m**

To compare the scalar transport results of the two meshing methods, the optimized values of longitudinal and transverse dispersion coefficients and velocities along with the $Rt^2$ values as a measure of goodness of fit, are presented in Table 3-2. The differences between the parameters of the two models, are presented as percentages of the refined mesh results, in Table 3-2 and can be considered negligible for all the parameters.

**Table 3-2 Scalar transport results of the refined and the graded meshing methods**

| **Parameter**<br>**Method** | $D_x$ (m$^2$/s) | $D_y$ (m$^2$/s) | $u$ (m/s) | $v$ (m/s) | $Rt^2$ for $D_x$ (-) | $Rt^2$ for $D_y$ (-) |
|---|---|---|---|---|---|---|
| Refined Mesh | 2.50100e-4 | 2.33630e-5 | 0.0280 | 0.0006 | 0.9784 | 0.9924 |
| Graded Mesh | 2.54400e-4 | 2.33440e-5 | 0.0279 | 0.0006 | 0.9787 | 0.9923 |
| Difference (%) | 1.72% | -0.08% | -0.36% | 0.00% | | |

Since the concentration profiles of two models and also all the values reported in Table 3-2 are very similar, it can be said that the models are identical in terms of mixing characteristics.

To provide a more detailed comparison between the two models, the longitudinal and transverse dispersion coefficients resulting from all of the reaches in both models are presented in Figure 3-27. The reach lengths in each model ranged from 0.05 m to 0.70 m depending on considering different recording lines in Figure 3-19 as the upstream and downstream recording lines.

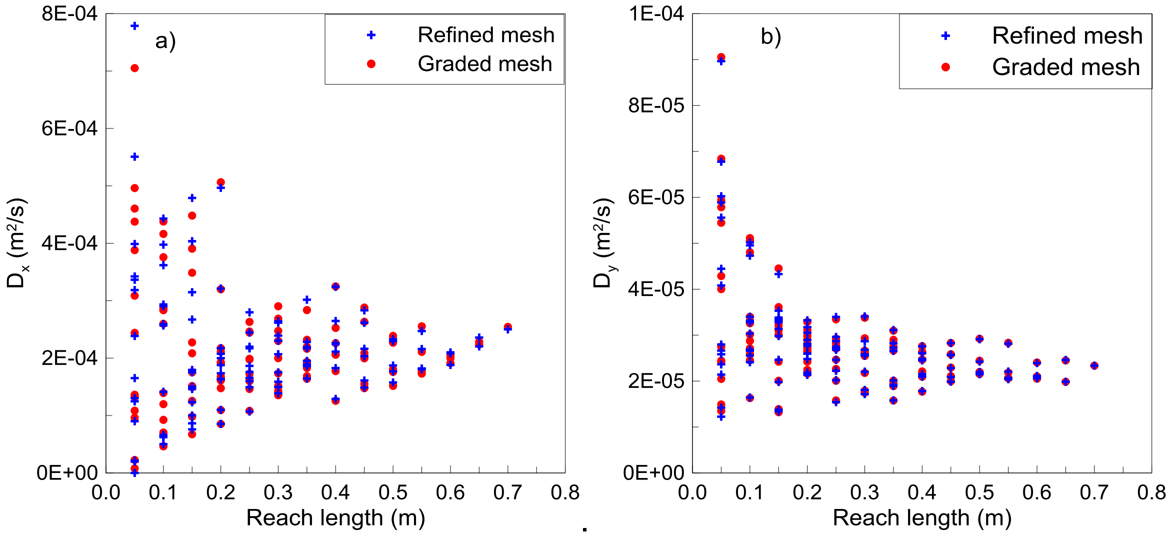

**Figure 3-27 a) $D_x$ and b) $D_y$ calculated for the refined and the graded mesh models**

The difference between mixing coefficients resulting from the refined and the graded mesh models are negligible in reaches longer than 0.20 m, which confirms that the models are identical in terms of mixing properties. The small differences in shorter reaches can be explained by the insufficient length of these reaches to allow the tracer to fully experience the array.

### 3.4.6 Grid Convergence Index

The grid convergence index was calculated for the graded meshing method suggested and used by (Roache 1998). Three mesh sizes were considered: 0.0001 m, 0.0002 m and 0.0004 m and the resulting area averaged longitudinal velocity values were used to calculate the convergence index. Figure 3-28 shows the trend of the results as well as the predicted value by performing Richardson extrapolation.

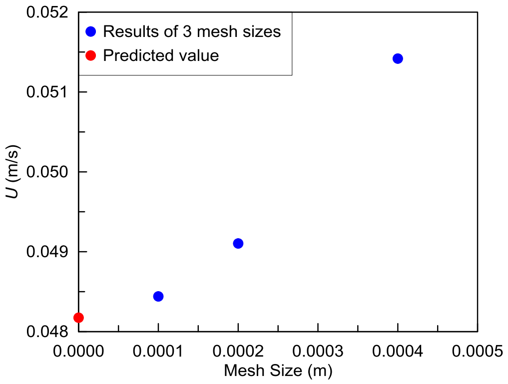

**Figure 3-28**

Considering a safety factor of 1.25, convergence index values of 2.37 % and 0.69 % were calculated for (0.0001 m, 0.0002 m) and for (0.0002 m, 0.0004 m), respectively. The ratio between the two convergence indices divided by the refinement ratio (2.0) to the power of the order of convergence (1.8), is equal to 0.99 which is very close to 1.00 and confirms that we are in the asymptotic range of convergence, and 0.0001 m is an acceptable mesh size to be considered for future models.

### 3.4.7 Conclusion

As the graded meshing method is more efficient in terms of computational power and time and was proved to produce the same results as the refined method, this method, i.e. the graded meshing method was chosen to be used as the main meshing method for models reported in the next chapter.

## 3.5 Estimation of advective zone length and the minimum required reach length for the scalar transport

### 3.5.1 Introduction

The advective zone length and also the minimum required reach length for scalar transport for 0.008 m diameter cylinder arrays are estimated in this section.

### 3.5.2 Geometry and Modelling Setup

A two dimensional 2.00 m long 0.70 m wide channel planted with 0.008 m diameter cylinder random array with a solid volume fraction of ø = 0.025 was built as the geometry. The scalar was injected at *x* = 0.10 m and y = 0.35 m and was recorded along the channel on the recording lines starting at *x* = 0.15 m and continuing to *x* = 1.90 m with the spacing of 0.05 m. The channel geometry, along with the injection point and the recording lines, is shown in Figure 3-29.

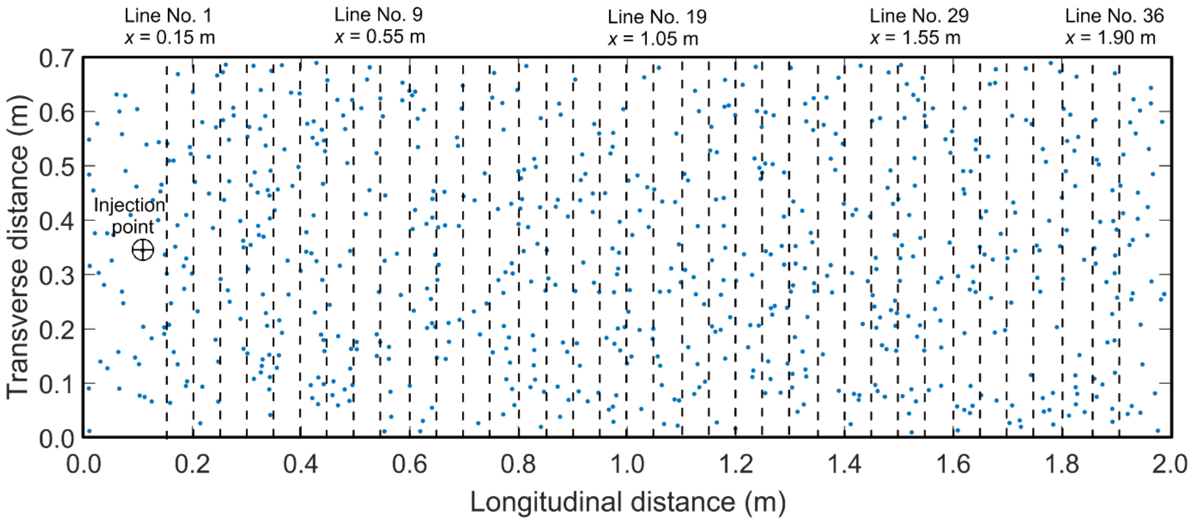

**Figure 3-29 Channel Geometry used to estimate the advective zone**

The conditions and settings used for solving the flow and turbulence equations and also for running the scalar transport was similar to what was explained in §3.2 and are not repeated here for the sake of brevity.

### 3.5.3 Velocity field results

The flow field was modelled using an inlet velocity equal to 0.025 m/s which is equivalent to $Re_d = 200$. The resulting longitudinal velocity contour plot is shown in Figure 3-30.

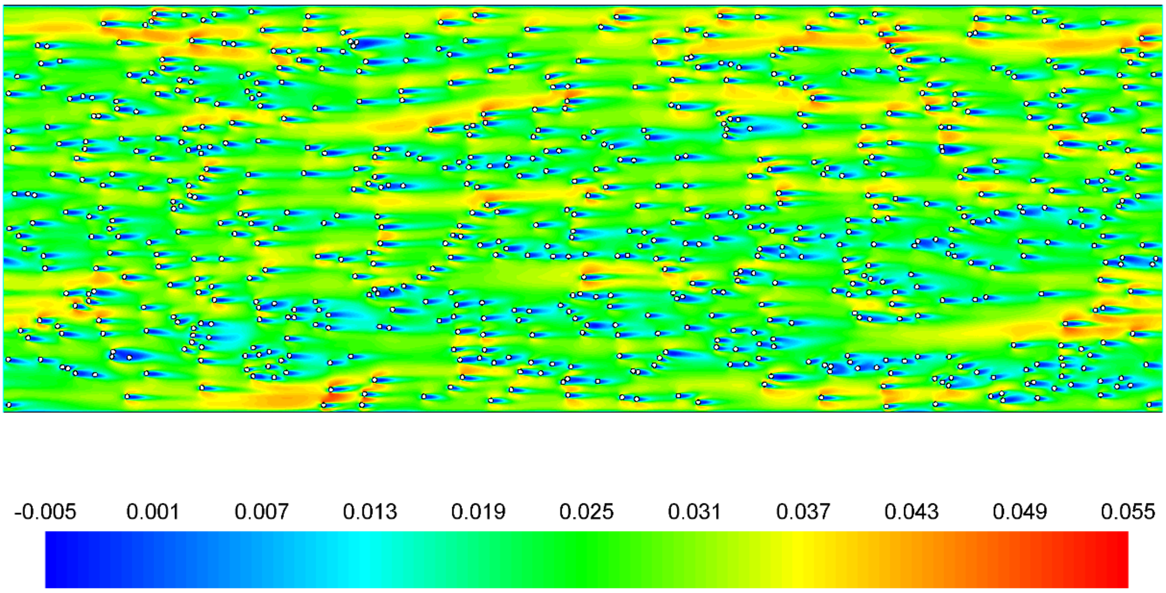

**Figure 3-30 Contours of longitudinal velocity (m/s),$u_{inlet}$ = 0.025 m/s, ø = 0.025, $Re_d$ = 200**

### 3.5.4 Scalar transport results

The tracer was injected at the injection point, at $x = 0.1$ and $y = 0.35$ and its concentration was recorded over all the 36 recording lines shown in Figure 3-29. For sake of clarity, only the longitudinal profiles recorded at lines No. 1, 9, 19, 29 and 36 are presented in Figure 3-31. The concentration values are normalized by dividing to the maximum concentration of the profile recorded at line No. 1 at $x$ = 0.15 m.

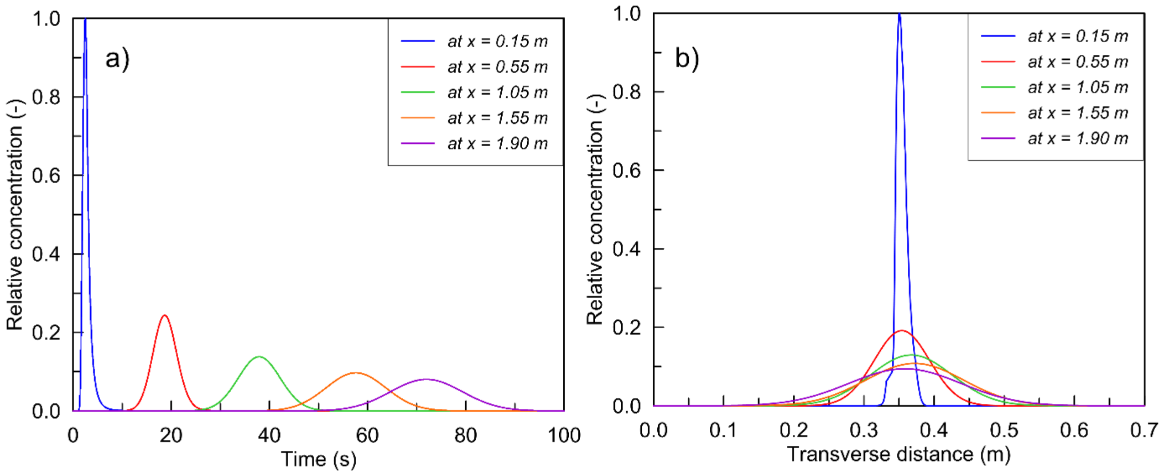

**Figure 3-31 a) longitudinal b) transverse concentration profiles at lines No. 1, 9, 19, 29 and 36 on Figure 3-29**

The longitudinal and transverse concentration profiles are shaped based on and contain the mixing characteristics of the cylinder array, these characteristics can be revealed by established analysing methods such as the method of moments. The length of the advective zone, one of the mixing characteristics of a channel, along with other mixing characteristics of the array presented in Figure 3-29 are calculated in the next section using the method of moments.

## 3.5.5 Advective Zone Length

The characteristics of the longitudinal concentration profiles recorded at line No.1 to line No. 36 Figure 3-29 were calculated based on Eq. 3-6 to Eq. 3-12,

$$M_0 = \int c dt \qquad 3\text{-}6$$

$$M_1 = \int c t dt \qquad 3\text{-}7$$

$$\bar{t} = \frac{M_1}{M_0} \qquad 3\text{-}8$$

$$M_2 = \int c \left(t - \bar{t}\right)^2 dt \qquad 3\text{-}9$$

$$M_3 = \int c \left(t - \bar{t}\right)^3 dt \qquad 3\text{-}10$$

$$Variance = \frac{M_2}{M_0} \qquad 3\text{-}11$$

$$Skewness = \frac{\frac{M_3}{M_0}}{\left(\frac{M_2}{M_0}\right)^{1.5}} \qquad 3\text{-}12$$

where $M_n$ is the nth moment of the concentration profile and $\bar{t}$ is the centroid of the longitudinal concentration profile. These values are shown in Figure 3-32a to Figure 3-32h. It was assumed that the channel was at least two times longer than the length of the advective zone. Thus, the variance values corresponding to the second half of the channel were used to find a linear fit. This line and its equation are plotted in Figure 3-32f.

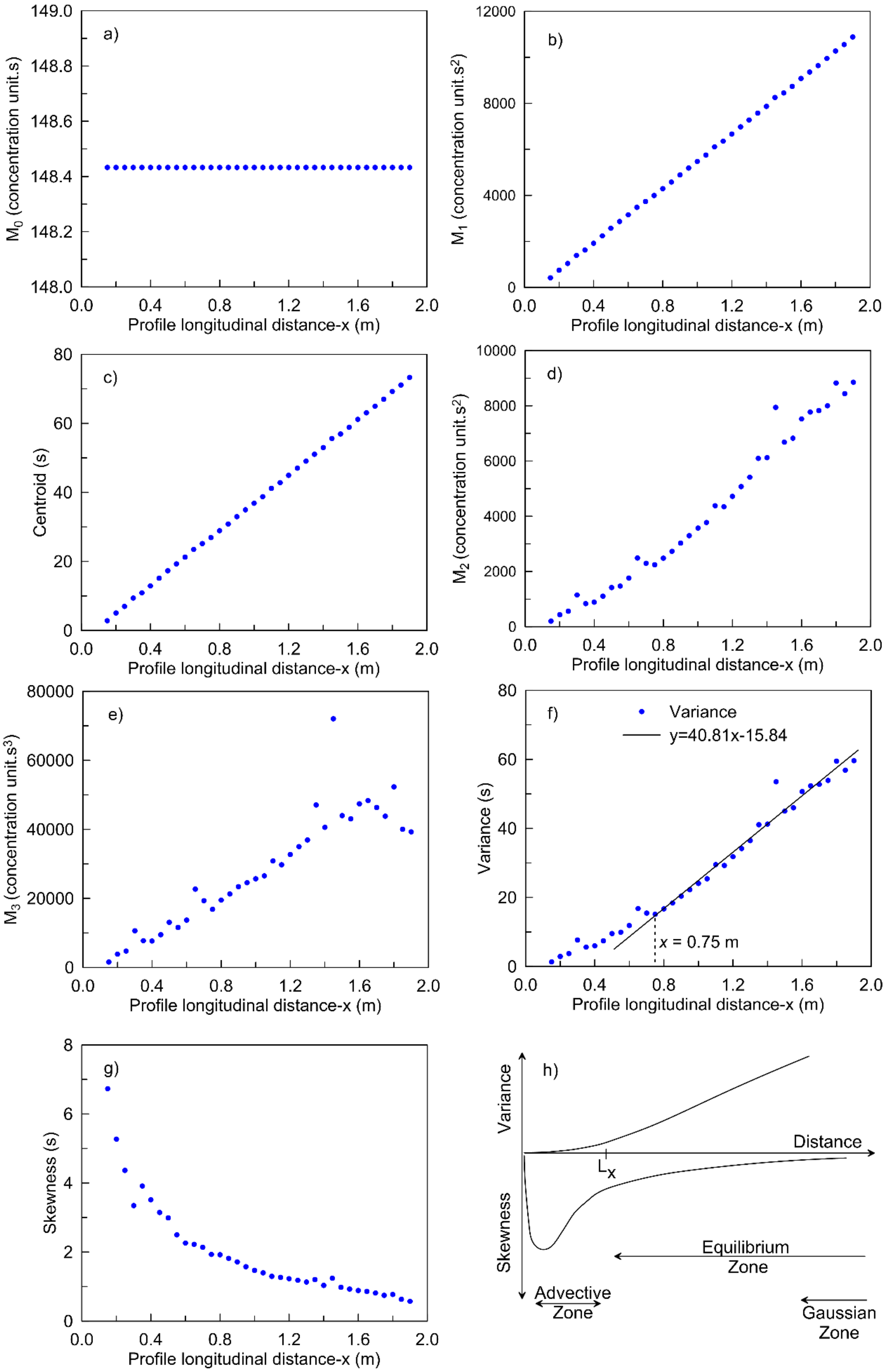

**Figure 3-32 Characteristics of longitudinal profiles, a) $M_0$ b) $M_1$ c) $\bar{t}$ d) $M_2$ e) $M_3$ f) Variance g) Skewness h) Rutherford (1994) Figure 4.4. Fickian model prediction of variance and skewness**

Figure 3-32a shows a constant value of $M_0$ which confirms the conservation of mass as $M_0$ is the integration of the concentration profile, Eq. 3-6. The linear growth shown in Figure 3-32b and Figure 3-32c are also reasonable as they both show the change in the location of the centroid of the longitudinal profiles and their slope is equal to the reverse of the mean longitudinal velocity i.e. 0.025 m/s. $M_2$ and $M_3$ show the growth in the spread of the longitudinal concentration profiles and they confirm the skewness of the profiles.

As explained in § 2.3.4 and shown in Figure 3-32h, the variance of the longitudinal concentration profiles shows a linear growth after the advective zone. Thus the start of this linear growth is the length of the advective zone. The trend of the variance values deviates from the linear fit at $x = 0.75$ m so one can say that the advective zone of this channel is 0.75 m long. The skewness values shown in Figure 3-32g, are in agreement with the Fickian model shown in Figure 3-32h as they converge to zero. After determining the length of the advective zone, the minimum required reach length is determined in the next section.

### 3.5.6 The minimum required reach length

The longitudinal and transverse dispersion coefficients for all the possible reaches between all of the 36 recording lines shown in Figure 3-29, were estimated based as was explained in §3.2.3, and are shown in Figure 3-33a and Figure 3-33b respectively.

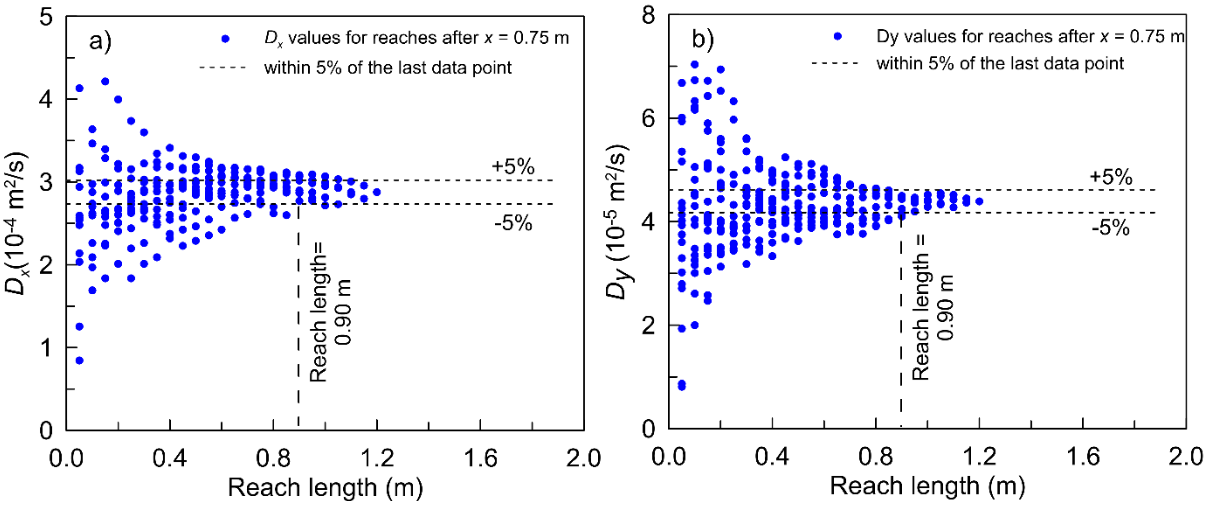

**Figure 3-33 a) longitudinal and b) transverse dispersion coefficients for reaches starting after *x* = 0.75 m**

As shown in Figure 3-33 the dispersion coefficients corresponding to the longest reach, i.e. the last data point, was considered the most accurate value. The data points within ±5% correspond to the reaches longer than 0.90 m for both $D_x$ and $D_y$.

### 3.5.7 Discussion and Conclusion

The characteristics calculated based on the method of moments confirmed the Fickian predictions described in Rutherford (1994). The trend of variance becomes linear after a certain distance from the injection point and $x$ = 0.75 m is suggested as the point where the increase in variance becomes linear and thus indicates the end of the advective zone, based on a linear fit on the second half of the data. To conclude the advective zone length for arrays of 0.008 m diameter cylinders, with solid volume fraction of $ø$ = 0.025 and inlet velocity of 0.025 m/s is suggested to be equal to 0.75 m.

To decide on the minimum required reach length for the scalar transport, both longitudinal and transverse optimized dispersion coefficients resulting from all the reaches were presented and compared and it was observed that the dispersion coefficient values resulting from the short reaches are more spread which shows the need for a minimum required length for tracer to experience the array, or in other words for the dispersion coefficient value to be representative of the whole array.

The dispersion values resulting from the longest reach i.e. the reach between line No. 1 to line No. 36 was assumed to be the representative absolute dispersion coefficient but as it includes the advective zone, the coefficients resulting from the reach between line No. 13 and line No. 36 are suggested to be the most representative values. Thus the coefficients resulting from the reaches starting after $x$ = 0.75 (line No. 13) were presented and compared in Figure 3-33. Accepting a 5% error from the most representative value, a minimum reach length of 0.90 m is suggested, which was confirmed with both longitudinal and transverse dispersion values.

To conclude for the future models of the arrays of 0.008 m diameter, it is proposed to record the concentration after $x$ = 0.75 m and on reaches with a minimum length of 0.90 m.

It should be mentioned that the strategy used in this section was to choose a low value of solid volume fraction as it was considered to be the worst case, i.e. needing the longest length for the tracer to fully experience the array. Also, a low-velocity value was chosen as it was assumed that increasing the velocity would increase the dispersion coefficients, i.e. the lower the velocity the longer the advective zone and the minimum reach length. So one can assume that the suggestions given for recording the data in future models, will provide representative results.

## 3.6 Discussion and Conclusion

A series of preliminary studies were undertaken in this chapter to define the methodology that will be used throughout this thesis. A preliminary validation of a general set of model settings and configurations was presented. This validation was based on the comparison between previously published laboratory data and the results of the CFD models in that section, i.e. §3.2. The channel sizes tested in this section were relatively small, i.e. 0.2 m wide and 0.6 m long. Thus, to ensure the robustness of the analysis longer channels were tested in the remaining sections.

The sensitivity of the resulting transverse and longitudinal dispersion coefficients on the relative location of the injection was analysed in §3.3. Two arrays were tested, a random and a regular array. The injection point was moved across each array and the corresponding scalar transport results were compared. A low sensitivity of both $D_x$ and $D_y$ values to the location of the injection point was observed and thus no specific limitation for the relative location of the injection point was suggested.

Two different meshing methods were compared in §3.4. The first method included very fine mesh (cell sizes of $10^{-6}$ m) around each cylinder to ensure accurate modelling of the flow around each cylinder, and coarser mesh (cell sizes of $10^{-3}$ m) covering the open area between the cylinders. This meshing method was less efficient in terms of the required time to be built, requiring around 24 hours. The second method, however, was much more efficient, requiring only around 2 hours. This mesh included minimum cell sizes of $10^{-4}$ m around the cylinders and maximum cell sizes of $10^{-3}$ m covering the open area between the cylinders. Detailed velocity profiles and scalar transport results comparison between these two meshing methods, showed no significant difference. Thus the more efficient meshing method was selected to be used for future models.

A unique investigation on the behaviour of longitudinal and transverse dispersion coefficients is presented in §3.5. Concentration profiles were recorded over transverse recording lines at the interval of 0.05 m. Concentration profiles were then analysed based on the Method of Moments (MoM). The characteristics of each longitudinal concentration profile, including centroid, the first and the second moments, variance and skewness were calculated. The advective zone was then estimated based on the Fickian model description. To the author's knowledge, this is the first time such a study is presented for cylinder arrays. The length of the advective zone i.e. the reach over which advection dominates dispersion, was estimated to be 0.75 m. This means the Fickian model of dispersion is valid downstream of this point and using the concentration profiles upstream of this point to estimate dispersion coefficients will affect the accuracy of the estimations. Thus, it was concluded that the channels to be modelled in the next chapter must be long enough to allow recording concentration profiles after the advective zone.

After excluding all the concentration profiles upstream of the advective zone, the remaining concentration profiles were used to estimate longitudinal and transverse dispersion coefficients over every 0.05 m reach of the remaining length of the channel, i.e. from $x$ = 0.75 m to $x$ = 2.00 m. The resulting longitudinal and transverse dispersion coefficients were then grouped based on the length of their corresponding reach. The dispersion values were then depicted against their corresponding reach length. This is the very first time that longitudinal and transverse dispersion coefficients are compared in this way at high resolution. As the length of the corresponding reaches increases, the values of dispersion coefficient converge to a single value which corresponds to the longest reach, here the reach between $x$ = 0.75 m and $x$ = 2.00 m. This value was considered as the value with the highest level of accuracy and by considering a range of ±5% difference, the minimum required reach length was suggested to be 0.90 m.

Thus, the future models which will be presented in Chapter 4, the concentration will be recorded after $x$ = 0.75 m from the injection point and on reaches with a minimum length of 0.90 m, and the geometries will be meshed using the more efficient meshing method.

# 4 RESULTS

## 4.1 Introduction

In this chapter, the effects of stem density and Reynolds number on transverse and longitudinal dispersion in randomly distributed cylinder arrays are investigated. Two diameters of $d$ = 0.0064 m and $d$ = 0.0080 m are considered. The settings applied for the modelling were chosen based on the results of the preliminary studies presented in the previous chapter. The specific geometry and features used in this chapter are explained in detail in §4.2, the rest of the settings are the same as those explained in Chapter 3. The flow field results, along with the turbulence features are presented in §4.3 and are followed by the solute transport results in §4.4. Effects of density and $Re_d$ on transverse and longitudinal dispersion coefficients are investigated in §4.5 and §4.6. Drag coefficient, turbulent kinetic energy and dispersion coefficients are compared with previously published laboratory data in §4.7, followed by discussion and conclusion in §4.9.

## 4.2 Model setup

The general model settings are presented in Table 4.1.

**Table 4-1 General model settings**

| Modelling feature | Setting | Modelling feature | Setting |
|---|---|---|---|
| Fluent version | 17.1 & 18.2 | Turbulence model | RSM (Reynolds Stress Model) |
| Dimension | 2D | Near-wall treatment | Enhanced wall function |
| Precision | Double precision | Fluid density | 998.2 (kg/m$^3$) |
| Solver type | Pressure-based | Fluid viscosity | 0.001003 (kg/m-s) |
| Velocity formulation | Absolute | Inlet-outlet boundary condition | Periodic |
| Flow solver | Steady | Pressure-velocity coupling scheme | Coupled |
| Scalar solver | Transient | Spatial discretization | Second order & second order upwind |
| Solver 2D space | Planar | Initialization | Standard from inlet |

The following sections outline the specific model features used for the models presented in this chapter.

### 4.2.1 Geometry and Mesh

The geometries comprised two-dimensional, 2.20 m long 0.70 m wide channels filled with 0.0064 m or 0.0080 m diameter randomly distributed cylinder arrays to form solid volume fractions of ø = 0.025, 0.050, 0.075, 0.100, 0.200 and 0.350. The arrays were built using the `rand` function in MATLAB.

Based on the discussion presented in §3.5.7, a minimum length of 0.75 m should be allowed between the injection point and the upstream monitoring line for the advective zone, and the reach length over which the dispersion coefficient is measured should be at least 0.90 m. Thus the tracer injected at $x = 0.10$ m was recorded at $x = 0.90$ m, $x = 1.00$ m and $x = 1.10$ m (upstream recording lines), and at $x = 1.90$ m, $x = 2.00$ m and $x = 2.10$ m (downstream recording lines). To prevent the tracer from re-entering the channel as a result of periodic flow boundaries the tracer was removed at $x = 0.05$ m and $x = 2.15$ m, employing a user-defined function. An example of the channel geometry is shown in Figure 4-1.

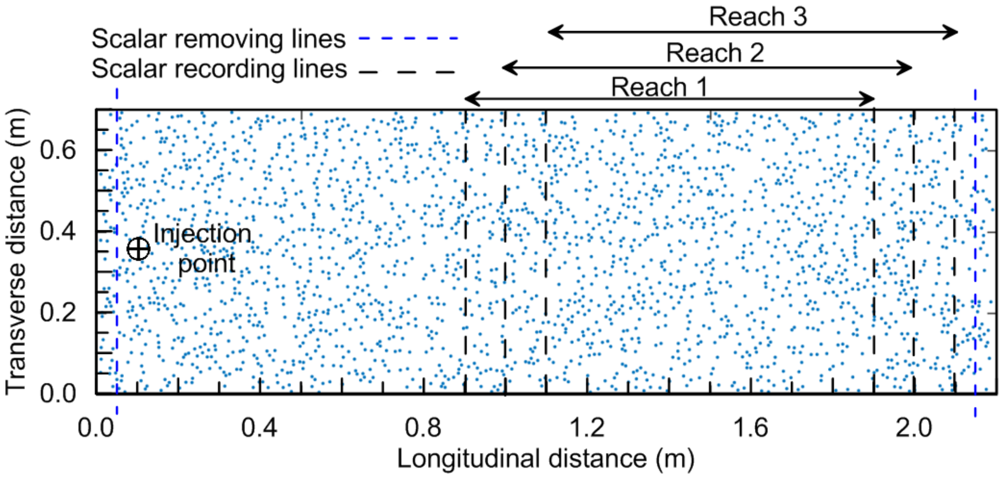

**Figure 4-1 Example channel geometry, *d* = 0.0080 m, ø = 0.075**

The three reaches shown in Figure 4-1 have an overlapping length of 0.8 m, i.e. the majority of their geometry, but comparing their results should provide some evidence of the degree of sensitivity of dispersion processes to cylinder distributions. It was also considered efficient to use all possible available results from each geometry.

Based on the sensitivity analysis presented in §3.4, the more efficient meshing method presented in that section was used for all the channel geometries. A complete explanation can be found in §3.4. An expanded view of the mesh built for the example geometry shown in Figure 4-1 is shown in Figure 4-2, the mesh for the entire channel included 4,770,206 elements for this case.

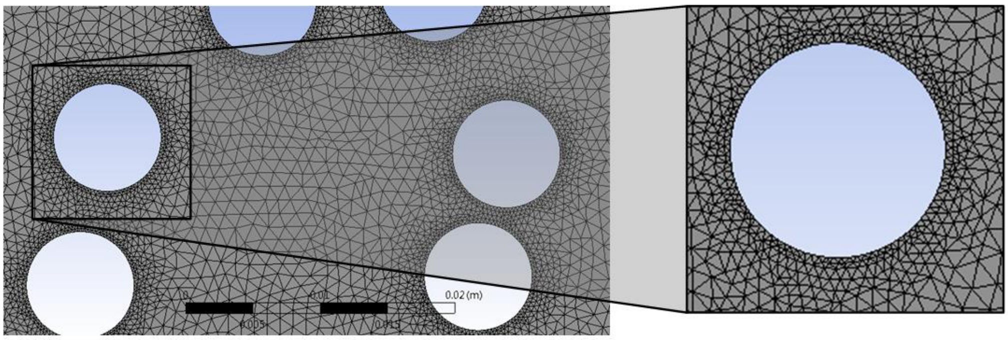

**Figure 4-2 Zoomed-in views of a sample area of the mesh built for the example channel geometry shown in Figure 4-1**

## 4.2.2 Flow settings

All the geometries were modelled as 2D planar models in ANSYS FLUENT. The inlet and outlet boundaries were set as periodic boundaries, providing a fully developed flow field independent of the length of the channel. The Reynolds Stress Model (RSM) was selected as the turbulence closure model, along with the enhanced wall treatment as the near-wall treatment method. The RSM model constants were left at default values (ANSYS, Inc., 2015). All the cylinder edges and the left and right sides of the channel were set as wall boundaries with the no-slip condition. The method for spatial discretization of all the variables was set to second order upwind using the coupled solver scheme. After considering a target $Re_d$ equal to 100, 300 and 500, the target $u_p$ was calculated for each case. Then the inlet velocity was estimated by multiplying $u_p$ by (1-$ø$), based on the continuity principle. The inlet mass flow was then calculated based on the inlet velocity, water density and the width of the channel and was used as input for the periodic boundary condition.

A list of all the modelled cases is provided in Table 4-2. For each solid volume fraction and velocity a single geometry has been used.

**Table 4-2 Modelled Cases**

| **Diameters, *d* (m)** | **0.0064 & 0.0080** | | | | | |
|---|---|---|---|---|---|---|
| Solid Volume Fractions, ø | 0.025* | 0.050* | 0.075 | 0.100 | 0.200 | 0.350 |
| $<S_n>_A$ (m) for $d$ = 0.0064 (m) | 0.0124* | 0.0076* | 0.0056 | 0.0044 | 0.0023 | 0.0012 |
| $<S_n>_A$ (m) for $d$ = 0.0080 (m) | 0.0155* | 0.0096* | 0.0069 | 0.0055 | 0.0029 | 0.0014 |
| $Re_d$ (-) | 100, 300, 500 | | | | | |
| $u_p$ (m/s) for $d$ = 0.0064 (m) | 0.0156, 0.0469, 0.0781 | | | | | |
| $u_p$ (m/s) for $d$ = 0.0080 (m) | 0.0125, 0.0375, 0.0625 | | | | | |
| Number of estimated coefficients, $D_x$ & $D_y$ | 108 & 108 (2 diameters, 6 ø, 3 reaches, 3 $Re_d$ ) | | | | | |

* for these cases *d* is smaller than $<S_n>_A$

## 4.2.3 Scalar Transport Settings

After solving the flow and turbulence equations in steady state, and achieving a fully converged condition, the model was switched to transient and set for scalar transport modelling. A user-defined scalar, with the same density and molecular diffusivity as water, was used. The spatial discretization of the scalar and the transient formulation were set to second order upwind and second-order implicit, respectively. The flow and turbulence equations were deactivated and the scalar was released at the injection point shown in Figure 4-1, for 100 time-steps of $\Delta t = 0.01$ s i.e. a 1.00 s pulse injection. Thus the flow field was kept as the converged solution and did not change during the scalar transport modelling.

Once the pulse injection was stopped, the simulation was continued at $\Delta t = 0.01$ s, allowing the scalar to be advected and dispersed along the channel. The scalar concentration was recorded at each time step at all the 6 cross-sectional recording lines shown in Figure 4-1. This concentration data was then used to calculate the transverse and longitudinal dispersion coefficients for each reach.

## 4.2.4 Post-processing

To estimate the longitudinal dispersion coefficient, the recorded concentration values were averaged over the channel width, resulting in width averaged concentration versus time profiles. For each pair of temporal concentration profiles, i.e. for each reach, the downstream concentration was predicted and the longitudinal dispersion coefficient was estimated based on the routing solution to the longitudinal advection-dispersion equation, Eq. 3-2. The resulting optimized longitudinal velocity was then used for estimating travel time for the transverse optimization.

For transverse dispersion, the recorded concentration values were temporally averaged over each recording line, resulting in temporally averaged concentration versus transverse distance profiles for each cross section. For each pair of cross sections, i.e. for each reach, the downstream concentration was predicted and the transverse dispersion coefficient was estimated based on the transverse advection-dispersion equation, Eq. 3-4.

## 4.3 Flow Field Results

To provide examples of the flow fields, the results of the highest and lowest solid volume fractions of $d = 0.008$ m, i.e. $ø = 0.025$ and $ø = 0.350$ are presented in Figure 4-3 to Figure 4-6 along with their geometries. The dashed line shows the location of the recorded velocity and turbulence feature profiles shown in the following sections.

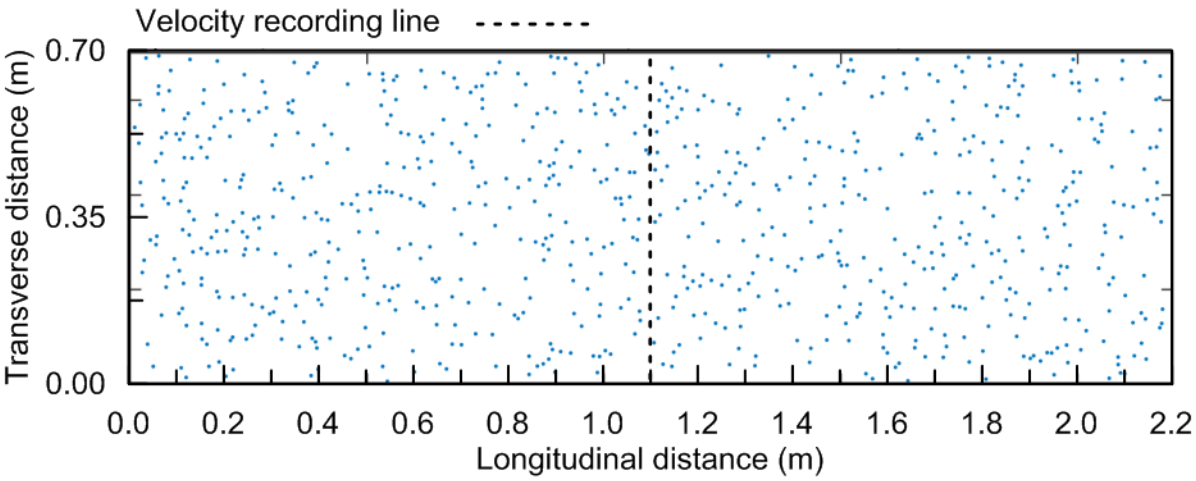

**Figure 4-3 Geometry of *d* = 0.008 m, *ø* = 0.025**

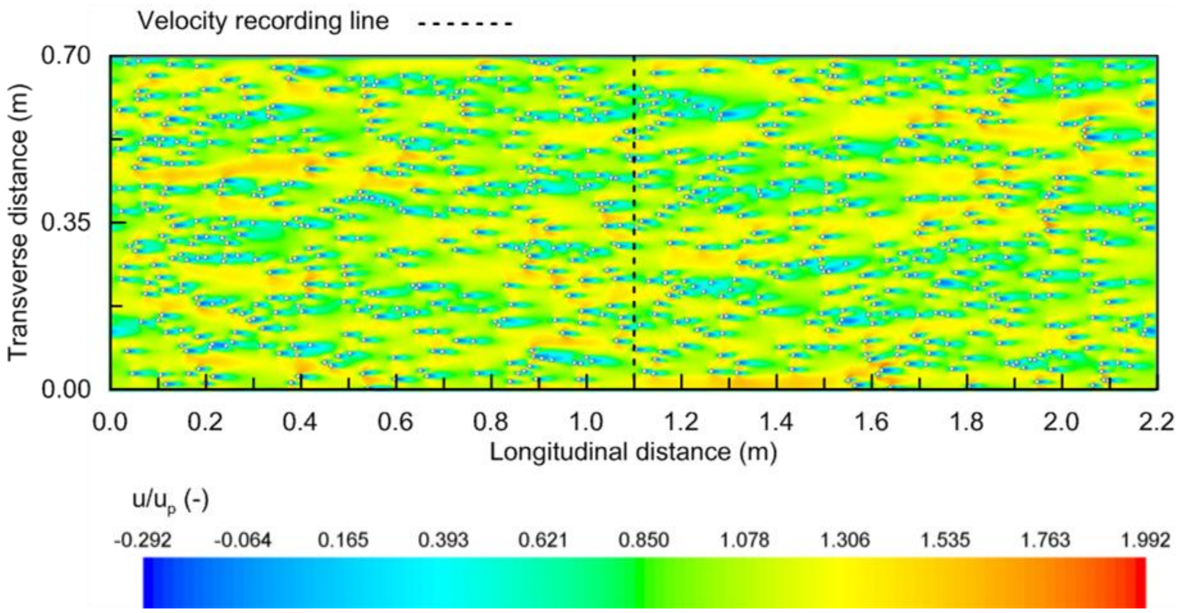

**Figure 4-4 Nondimensionalized longitudinal velocity contour plot $u/u_p$, *d* = 0.008 m, *ø* = 0.025, $Re_d$ = 300, $u_p$ = 0.0375 m/s**

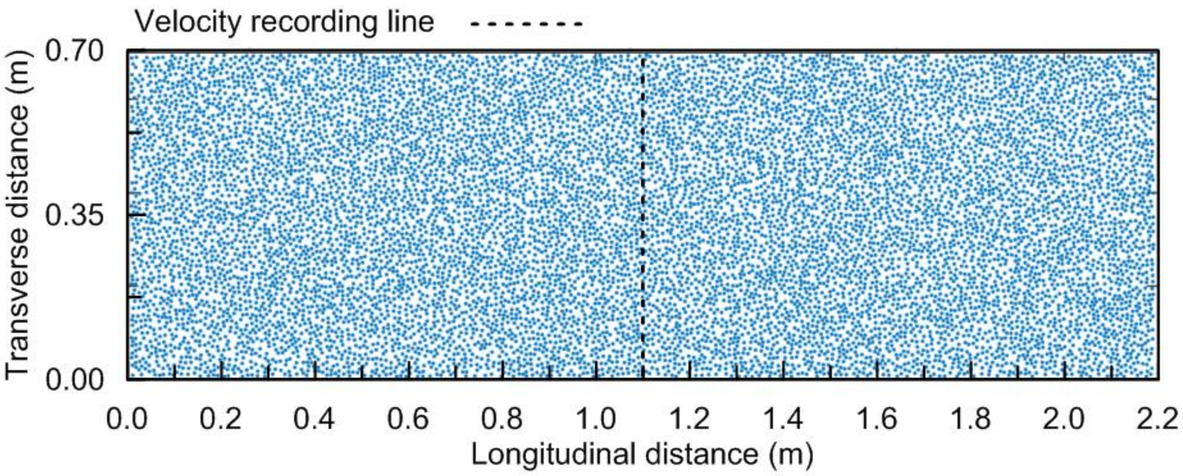

**Figure 4-5 Geometry of *d* = 0.008 m *ø* = 0.350**

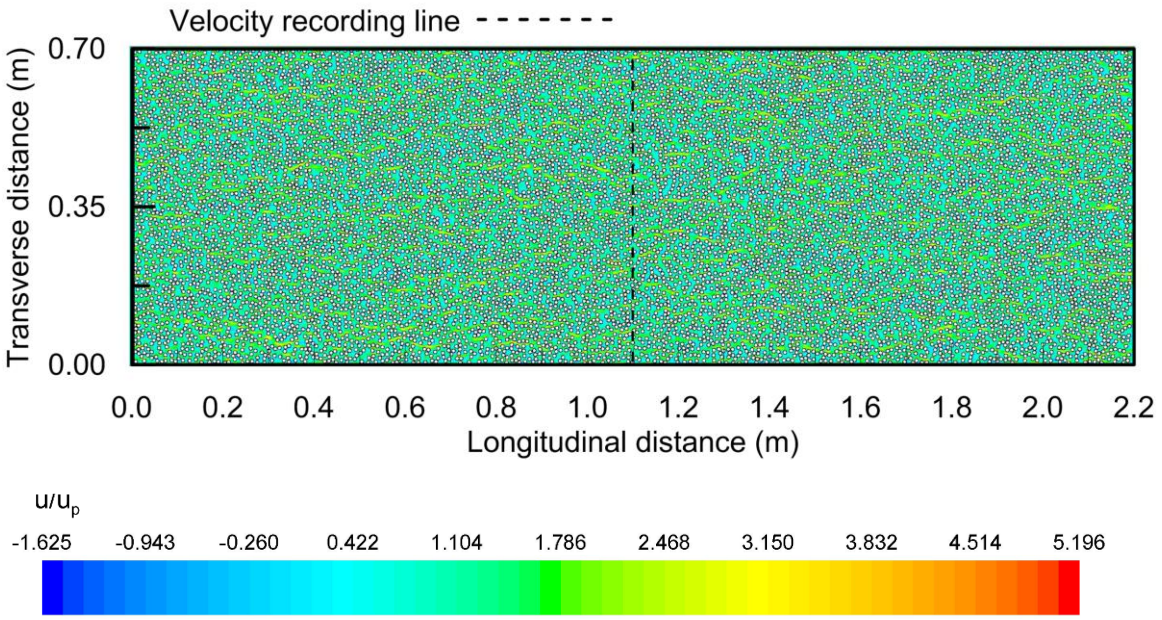

**Figure 4-6 Example of longitudinal nondimensionalized velocity contour plot $u/u_p$, *d* = 0.008 m, *ø* = 0.350, $Re_d$ = 300, $u_p$ = 0.0375 m/s**

In Figure 4-4 the randomness of the velocity field, the wake effect and low and negative velocities generated downstream of each stem, are clear. These changes are not visible in Figure 4-6. However, comparing the values of $u/u_p$ presented in Figure 4-4 with Figure 4-6 shows that at *ø* = 0.350, as a result of less free space between the stems, the nondimensionalized velocity range is 3 times larger than that of *ø* = 0.025.

To provide a more detailed comparison between the velocity fields, the longitudinal velocity profiles recorded at *x* = 1.1 m, nondimensionalized using the target $u_p$ of each channel, are shown in Figure 4-7. The transverse recording line, i.e. $x = 1.1$ m, is shown on each channel. For the sake of clarity, the profiles are depicted by solid lines as the data is available for each 0.0001 m of channel width and using symbols would make the profiles difficult to read. To provide an easier comparison, the middle section of the channel width i.e. the section between $y = 0.3$ m and y = 0.4 m in Figure 4-7 a) and b) is expanded and shown in Figure 4-7 c) and d), respectively.

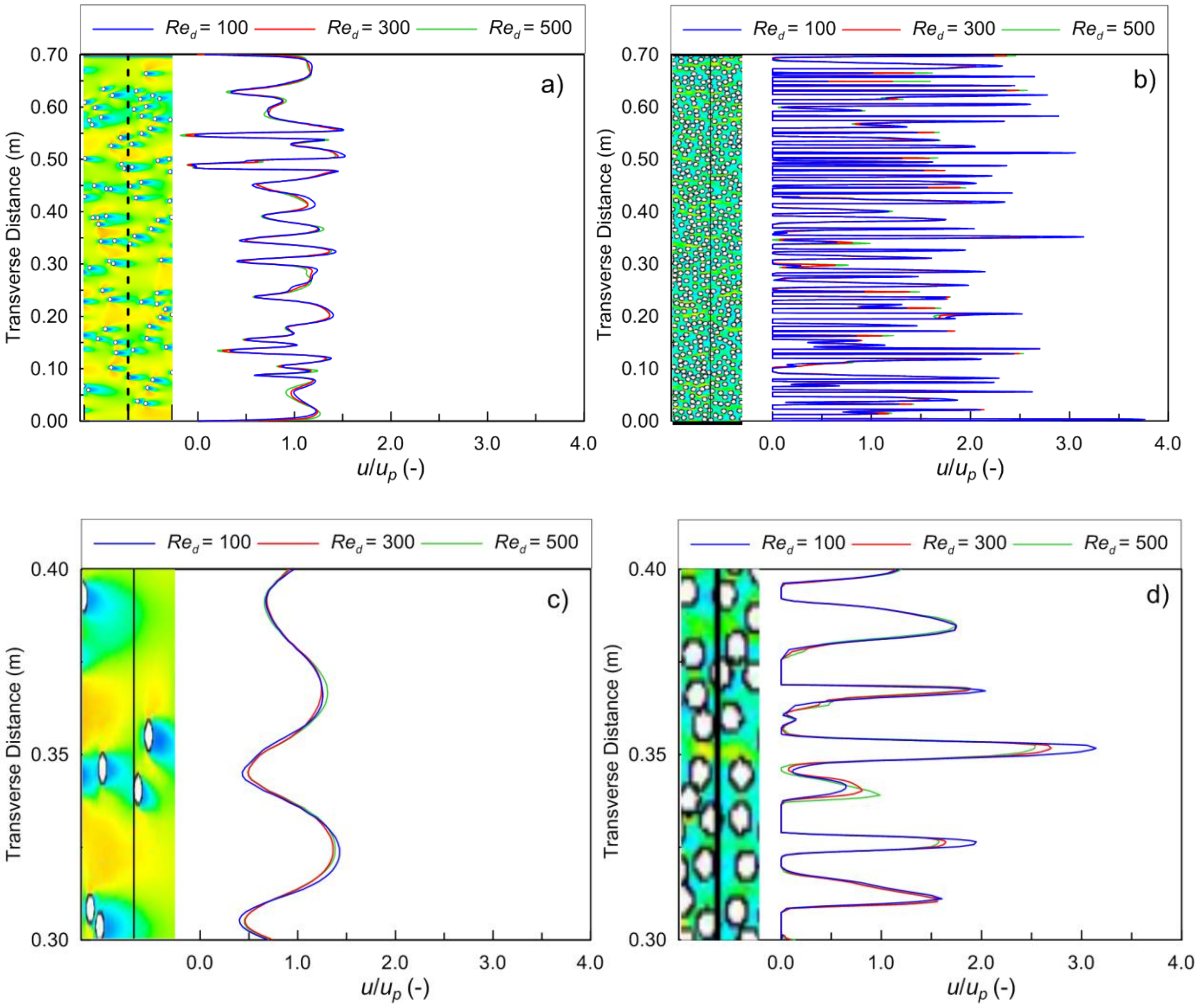

**Figure 4-7 Nondimensionalized longitudinal velocity profiles recorded at *x* = 1.1 m, *d* = 0.0080 m a) ø =0.025 b) ø = 0.350, c) and d) are the zoomed-in of a) and b) for y = 0.3 to 0.4 m**

The velocity profiles presented in Figure 4-7 reveal the diverse flow conditions generated within arrays of different solid volume fractions. They also display the wake effect and high-velocity regions generated between the cylinders. The average value of $u/u_p$ at ø = 0.025 and ø = 0.350 for all the three $Re_d$ is 0.95 and 0.89, respectively and the average deviation from mean velocity, calculated as the average of the difference between the value at each point and the average of the cross-section, at $\varnothing = 0.025$ and $\varnothing = 0.350$ is 0.25 and 0.66, respectively. This suggests that a higher amount of differential advection is expected at $\varnothing = 0.350$, and high solid volume fractions in general.

The levels of turbulence intensity, Eq. 2-15, recorded on the same line for both solid volume fractions for the three $Re_d$ are shown in Figure 4-8. The $u/u_p$ contour plots are also included to show the relative location of the recording line to the stems.

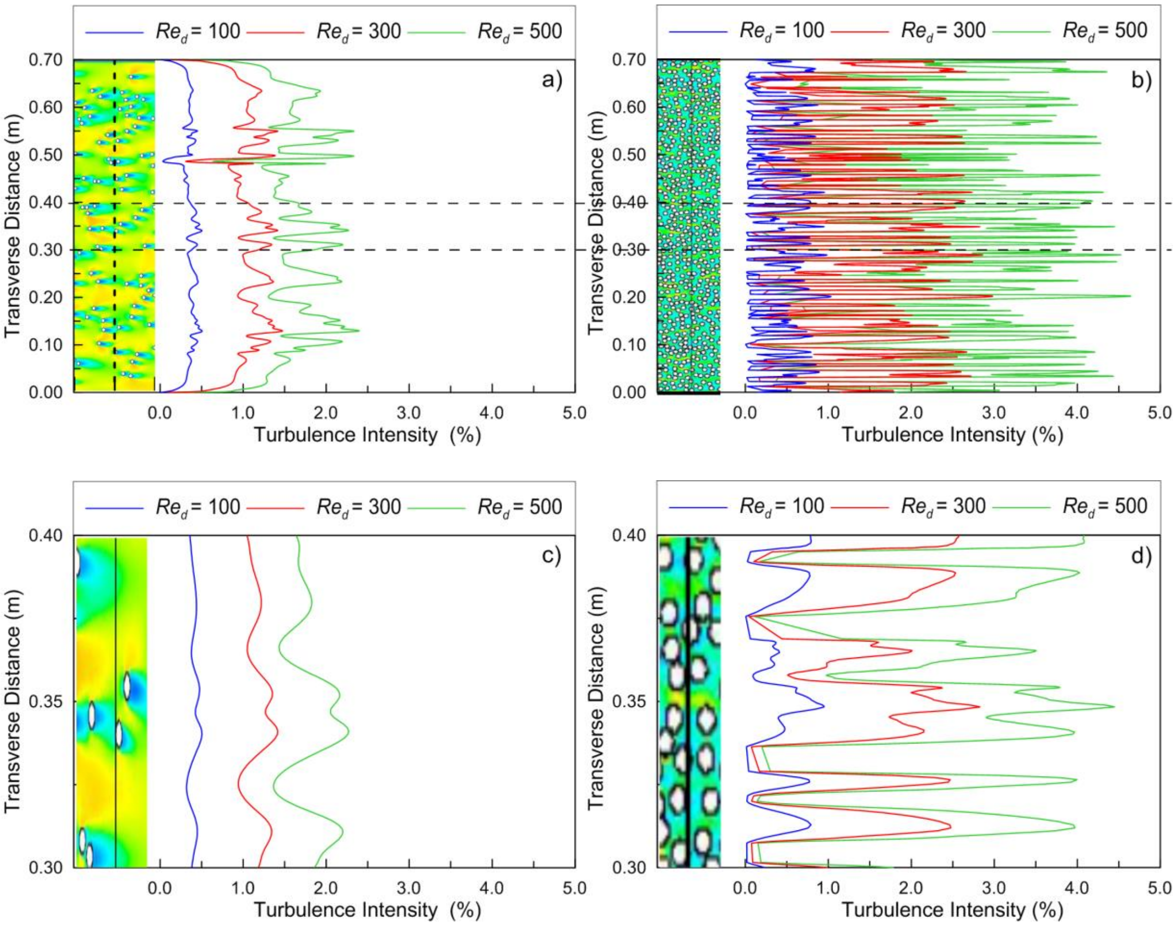

**Figure 4-8 Turbulence Intensity divided by $u_p$ recorded at $x$ = 1.1 m, $d$ = 0.0080 m a) $\varnothing$ =0.025, b) $\varnothing$ =0.350, c) and d) are the zoomed-in of a) and b) for y = 0.3 to 0.4 m, the contour plots are $u/u_p$**

Figure 4-8 shows that higher levels of turbulence intensity are produced at $\varnothing = 0.350$, which is consistent with the definition of turbulence intensity. At higher $\varnothing$ values as a result of a higher number of stems, a higher number of wake areas are shaped which can result in a higher level of turbulence intensity. Gambi et al. (1990), Nepf (1997b), and Tanino and Nepf (2008a) have also reported enhanced turbulence intensity with an increase in the solid volume fraction. The profiles in

Figure 4-8 for each ø are also consistent with the fact that that turbulence intensity increases with velocity.

To provide a comparison between all the cases, the area-weighted average turbulence intensity values recorded for the whole channel length versus solid volume fraction and $Re_d$, are presented in Figure 4-9 a) and b), respectively.

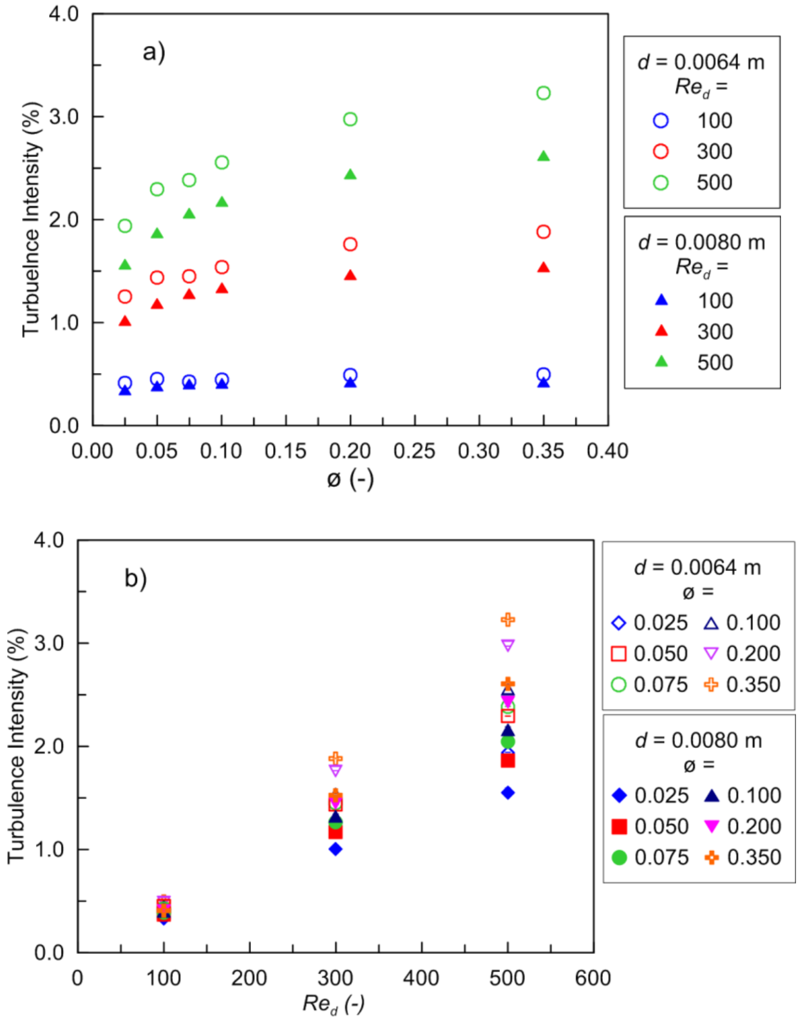

**Figure 4-9 Area-weighted average turbulence intensity versus a) ø, b) *Re<sub>d</sub>***

Figure 4-9 a) shows that for all the cases, a higher level of turbulence intensity is produced at *d* = 0.0064 m than at d = 0.0080 m. It is also interesting to note that the difference between the level of turbulence intensity for the two diameters increases with velocity, i.e. the difference between circle and triangle symbols at $Re_d$ = 500 is greater than that at $Re_d$ = 300 and 100. In general, one can say that turbulence intensity increases with increase in ø, with a higher slope for 0.025 < ø < 0.200 and a milder slope between ø = 0.200 and 0.350. This can be justified by recalling that, at lower densities, by increasing the number of stems, more wake areas and more turbulence are produced. However, at the same time, as density increases, more wakes are overlapped by other stems, which results in a milder growth of turbulence production and turbulence intensity.

Figure 4-9 b) confirms the linear growth of turbulence intensity with velocity, with $R^2$ values of 0.997 to 0.999. It also shows that cases with higher ø have a higher rate of increase in turbulence intensity, i.e. higher slope for higher ø. It can also be seen that the difference between the level of turbulence intensity for different solid volume fractions increases with $Re_d$, i.e. data points cover a wider range at $Re_d = 500$ than at $Re_d = 100$ and 300. Comparing the patterns observed in Figure 4-9 with the patterns in dispersion coefficients, which will be presented in future sections, will shed light on identifying different processes contributing to the dispersion.

The values of turbulent viscosity recorded on the line $x = 1.1$ m are shown in Figure 4-10 for both ø = 0.025 and ø = 0.350 and $Re_d$ = 100, 300 and 500.

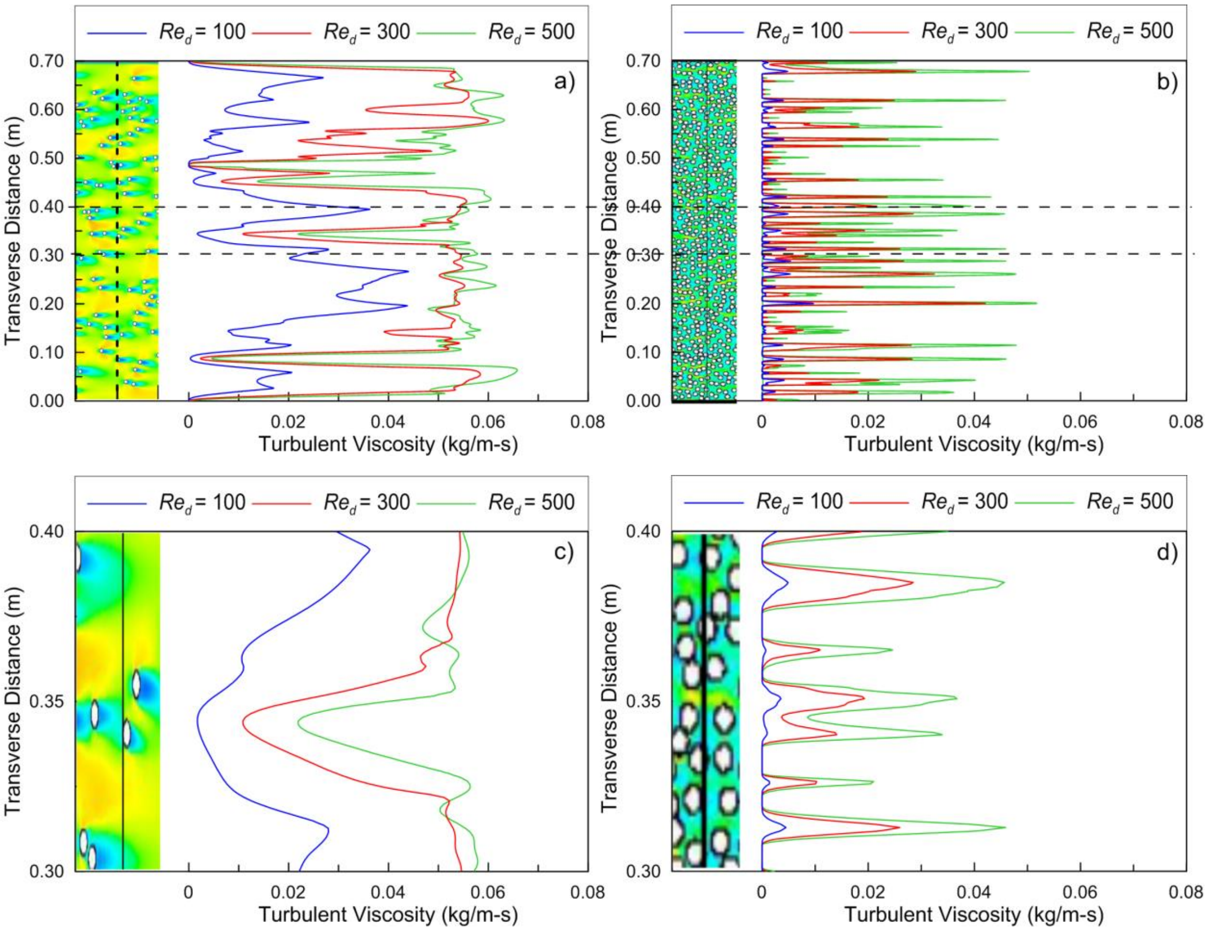

**Figure 4-10 Turbulence viscosity recorded at *x* = 1.1 m, *d* = 0.0080 m a) ø =0.025 b) ø =0.350, c) and d) are the zoomed-in of a) and b) for y = 0.3 to 0.4 m, the contour plots are $u/u_p$**

Figure 4-10 shows that the levels of turbulent viscosity for both solid volume fractions at $Re_d = 300$ and $Re_d = 500$ are close to each other and are relatively higher than that at $Re_d = 100$. Comparing the trend of the profiles with the relative location of the recording line to the stems shows that the value of turbulent viscosity increases in open areas between the stems, which is consistent with the definition of eddy viscosity. Turbulent viscosity, (also known as eddy viscosity), is a measure of momentum transfer by turbulent eddies, and as open areas allow larger eddies to form, greater values of turbulent viscosity are expected to be in the open spaces between the stems. It can be seen that, as a result of more stems in cross section at $ø = 0.350$, turbulent viscosity shows more variation and in general has a lower value which is consistent with smaller spaces between stems and smaller eddies at this ø.

To provide a comparison between all the cases, the area-weighted average turbulence intensity values recorded for the whole channel length versus solid volume fraction and $Re_d$, are presented in Figure 4-11 a) and b), respectively.

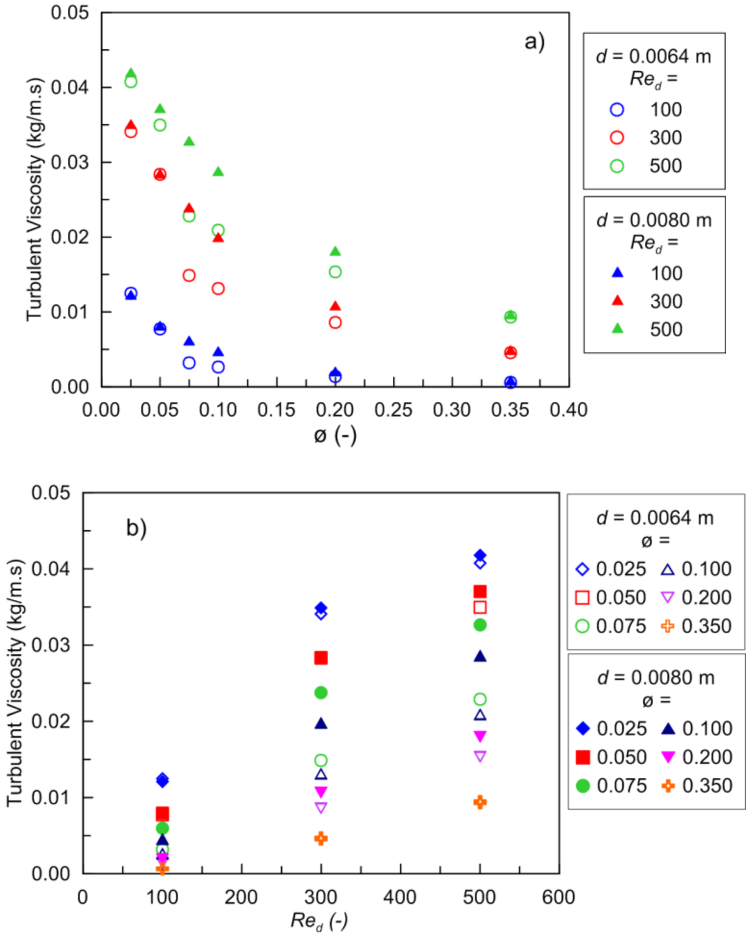

**Figure 4-11 Area-weighted average turbulent viscosity versus a) ø, b) $Re_d$**

Figure 4-11 a) shows that turbulent viscosity decreases as cylinder density increases, with a higher rate of change at lower densities. Comparison between the two diameters shows that both diameters have almost the same value of turbulent viscosity at ø = 0.025 and 0.050. Then values deviate at ø = 0.075, 100 and 200 and then again at ø = 0.350 data points are overlapped for each $Re_d$. As turbulent viscosity is an indicator of eddy size, this pattern in turbulent viscosity can suggest a change in characteristic turbulent length scale. Two turbulent length scales have been suggested and discussed for random cylinder arrays: diameter, *d*, and average stem spacing, $<S_n>_A$. Tanino and Nepf (2008b) suggested that at low densities, turbulent eddies are *O* (*d*) while for cases with stems spacing smaller than *d*, eddies are constrained by local cylinder separation, or $<S_n>_A$. As indicated in Table 4-2, among the cases modelled in the current study, only for cases at ø = 0.025 and 0.050, *d* is smaller than $<S_n>_A$. This confirms the pattern observed in Figure 4-11 a) and also confirms the suggestion made by Tanino and Nepf (2008b). However, the fact that at all $Re_d$, both diameters have the same value of turbulent viscosity still needs justification. Figure 4-11 b) shows that turbulent viscosity linearly increases with $Re_d$ with a rate that depends on both *d* and ø.

As the RSM turbulence closure model was employed and it solves the transport equations for the Reynolds stresses, it is worth investigating the profiles of the Reynolds stresses as well. Reynolds stress profiles were nondimensionalized by dividing by $u_p^2$ and are presented in Figure 4-12. The average value of each Reynolds stress over the whole channel width is shown on each profile. Only the zoomed-in profiles are shown here, for the sake of brevity.

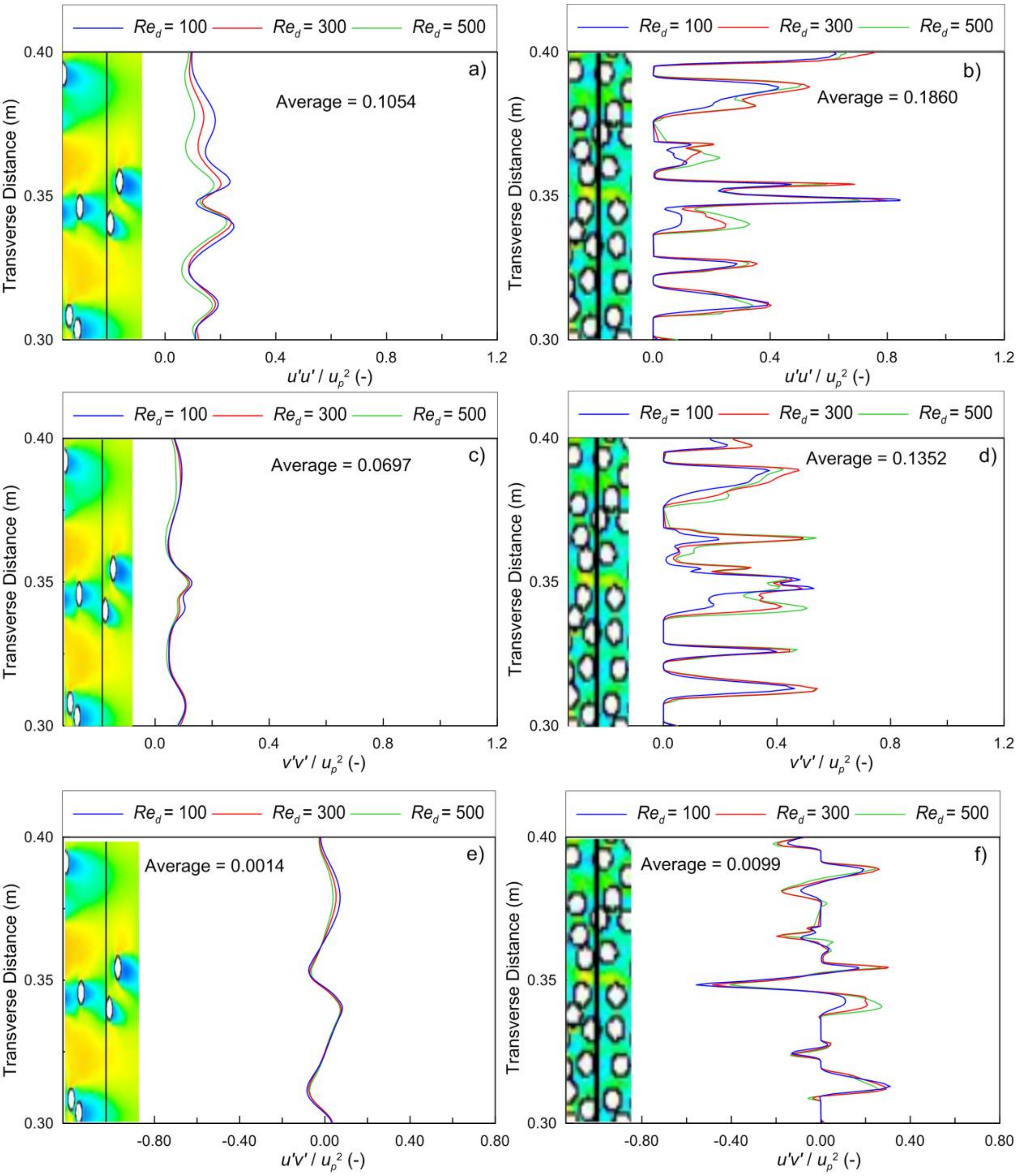

**Figure 4-12 Reynolds Stresses recorded at $x$ = 1.1 m for $y$ = 0.3 to 0.4 m, $d$ = 0.0080 m a) $u'u'$ at ø = 0.025, b) $u'u'$ at ø = 0.350, c) $v'v'$ at ø = 0.025, d) $v'v'$ at ø = 0.350, e) $u'v'$ at ø = 0.025 and f) $u'v'$ at ø =0.350, the contour plots are $u/u_p$**

It can be seen that for all the cases Reynolds stress has a higher value at ø = 0.350. $u'u'$ and $v'v'$ are almost 2 times higher at ø = 0.350 than at ø = 0.025 and $u'v'$ is approximately 7 times higher at ø = 0.350 than at ø = 0.025. These profiles can be compared to the profiles reported by Ricardo et al. (2016), shown in Figure, (previously presented in Figure 2-16). Although the laboratory measured values are recorded and presented as vertical profiles, their values are of similar direction and a similar order of magnitude to those in Figure 4-12. This confirms the validity of the models used in this thesis.

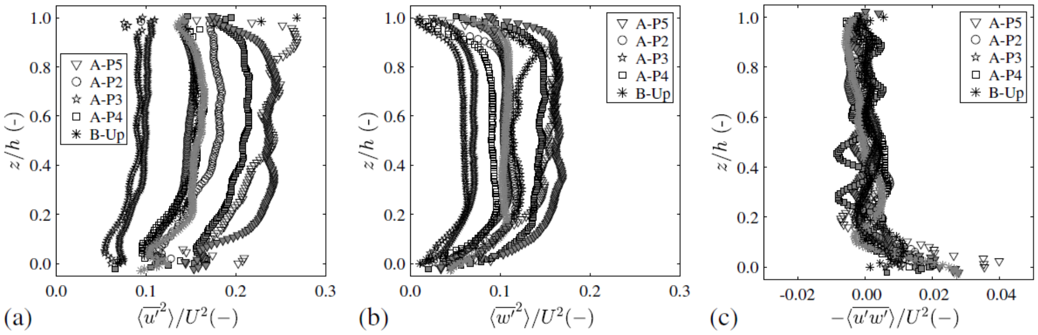

**Figure 4-13 Ricardo et al. (2016) figure 4, time and space-averaged Reynolds stress profiles normalized by $u^2$, a) longitudinal, b) vertical, c) lateral components**

Among the studies of flow within cylinder arrays, Stoesser et al. (2010), Ricardo et al. (2014) and Ricardo et al. (2016) have presented and discussed Reynolds stresses. The “state of the art” as Ricardo et al. (2016) explains, shows that the largest magnitudes of Reynolds stresses are found in the wake region and “in case of closely placed stems there is a strong interaction of the vortex streets of neighbouring stems being difficult to distinguish the turbulence generated by a given stem from the high background turbulence level”. It can be seen from Figure 4-12 that this statement holds true for ø = 0.350, where the maximum values correspond to the free spaces between the stems. However, comparing the profiles at ø = 0.025 with this statement shows that *u’u’* has maximas at *y* = 0.34 and *y* = 0.36 in Figure 4-12 a) with a local minimum at *y* = 0.35. This pattern matches with the presence of two stems downstream of the recording line, i.e. there is only one stem upstream of the recording line in Figure 4-12 a) while there are two stems in the downstream. This pattern is repeated for *v’v’* in Figure 4-12 c) where the two peaks are slightly lower than those for *u’u’*. This may suggest a relationship between the Reynolds stress values and the low-velocity (laminar boundary layer) region formed upstream of each stem. Examining this suggestion is possible by more investigation in the available data from this thesis, as the values of Reynolds stresses are available for the full channel for all the modelled cases. However, as the focus of this research is on the mixing characteristics and quantifying the dispersion coefficients, more investigation on Reynolds stresses is left for future studies.

## 4.4 Scalar Transport Results

The concentration of the tracer released at $x = 0.10$ m and $y = 0.35$ m was recorded over time for the six transverse recording lines shown in Figure 4-1. The recorded data was then used to estimate the transverse and longitudinal dispersion coefficients. To provide examples of the recorded data and the goodness of fit between the predicted and recorded concentration profiles, a set of concentration contour plots, along with longitudinal and transverse concentration profiles at $ø = 0.025$ and $ø = 0.350$ at $Re_d = 300$ for both $d = 0.0080$ m and $d = 0.0064$ m is presented in Figure 4-14 to Figure 4-17. For the sake of brevity, only the recorded concentration over Reach 1 for each channel is presented here. In these figures, $R_t^2$ is the goodness of fit between the downstream and predicted profiles, described by Young et al. (1980).

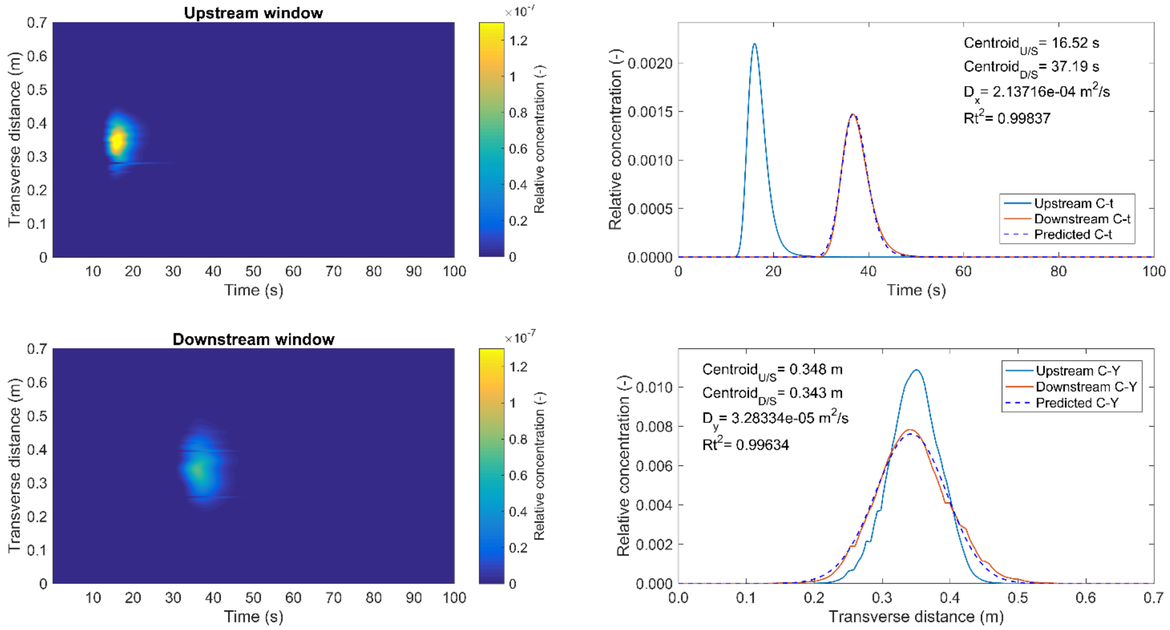

Figure 4-14 Concentration contours and profiles for *d* = 0.0064 m, ø = 0.025, *Re$_d$* = 300

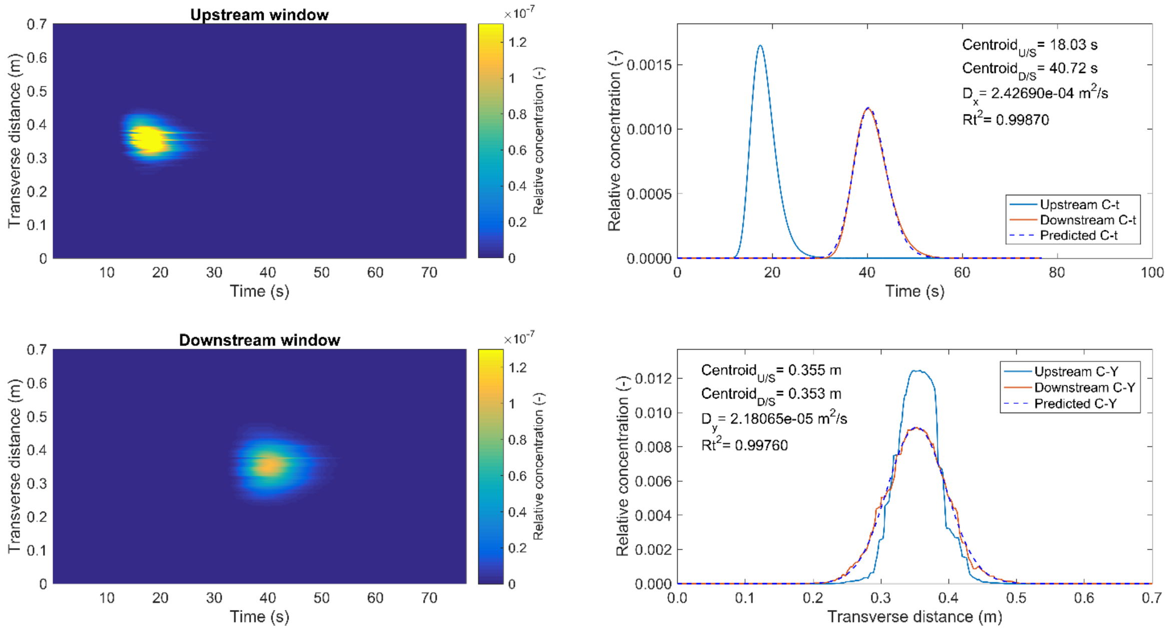

Figure 4-15 Concentration contours and profiles for *d* = 0.0064 m, ø = 0.350, *Re$_d$* = 300

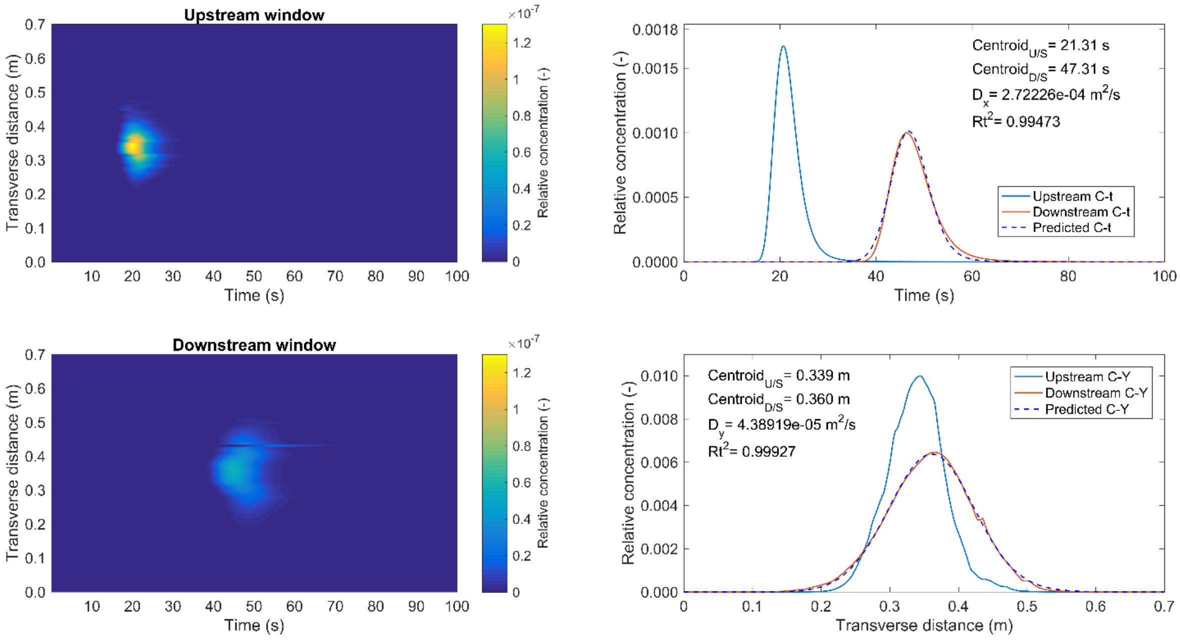

**Figure 4-16 Concentration contours and profiles for *d* = 0.0080 m, *ø* = 0.025, *Re_d* = 300**

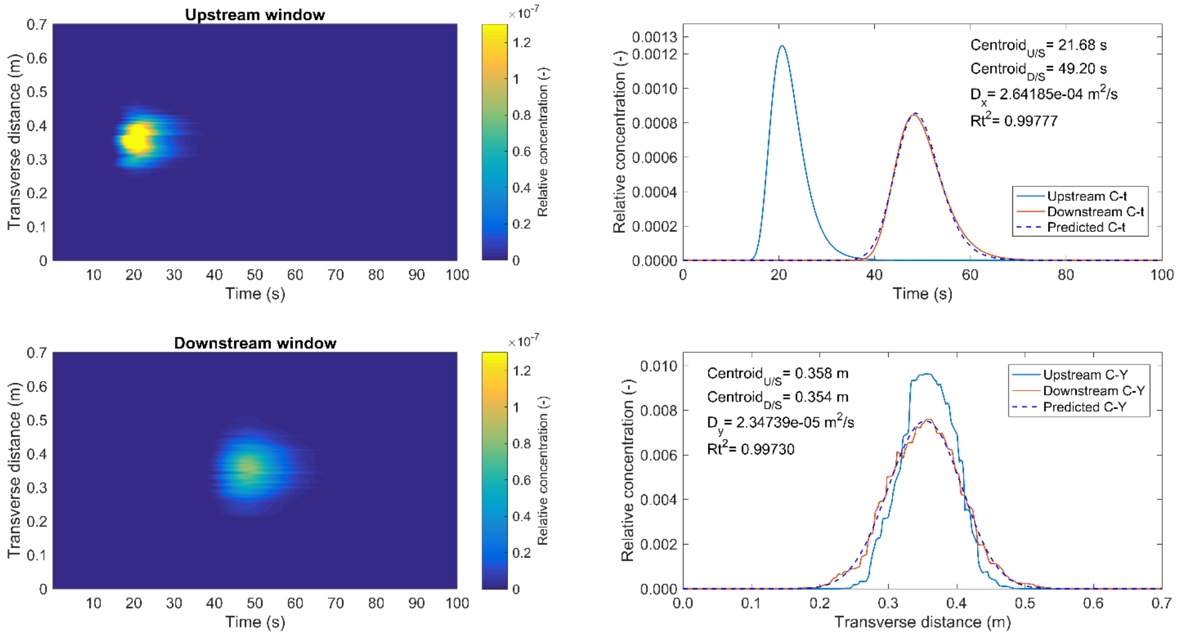

**Figure 4-17 Concentration contours and profiles for *d* = 0.0080 m, *ø* = 0.350, *Re_d* = 300**

A good agreement can be seen between the recorded and predicted longitudinal and transverse concentration profiles which leads to high values of $R_t^2$. The longitudinal and transverse dispersion coefficients for all of the cases are presented and discussed in the future sections.

## 4.5 Transverse dispersion coefficient

Transverse dispersion coefficients for all the cases are presented in this section. The effect of solid volume fraction and $Re_d$ on transverse dispersion coefficient are presented in §4.5.1 and §4.5.2, respectively.

### 4.5.1 Effect of density on $D_y$

Transverse dispersion coefficients for all the cases are depicted in Figure 4-18 a) versus solid volume fraction, ø. Each symbol represents the average of the three reaches of each case shown in Figure 4-1 and the vertical bars represent the standard deviation.

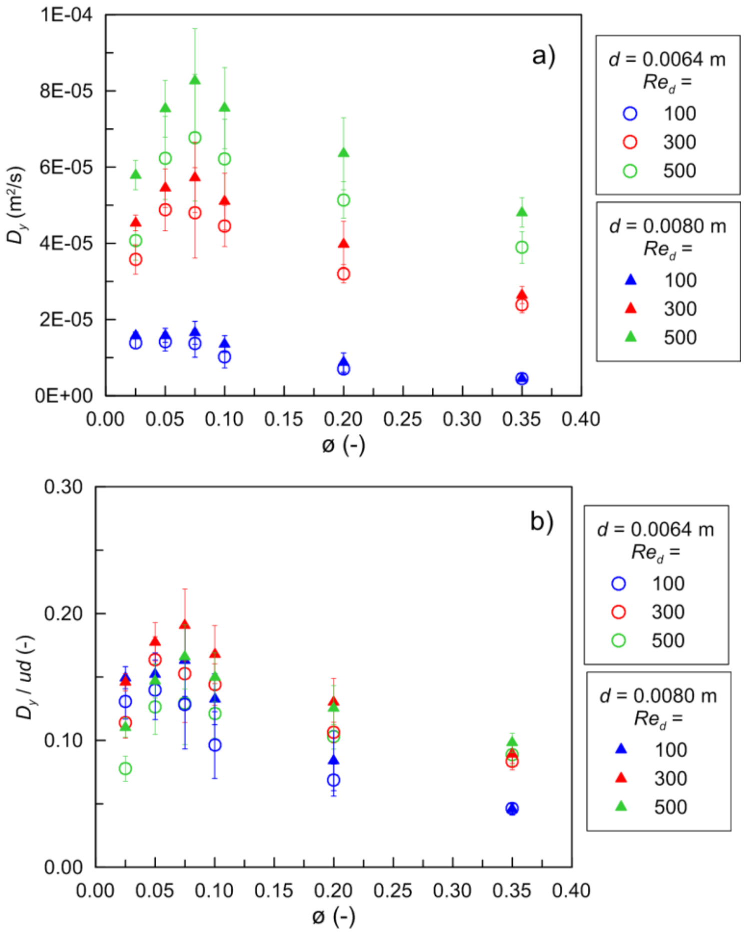

**Figure 4-18 a) Transverse dispersion coefficients and b) nondimensionalized transverse dispersion coefficients versus ø for *d* = 0.0064 m and *d* = 0.0080 m at $Re_d$ = 100, 300, and 500**

Transverse dispersion coefficients, nondimensionalized by the target velocity, $u_p$, and diameter, *d*, are shown in Figure 4-18 b). This method of nondimensionalizing has been employed in classic textbooks and recent studies, e.g. Rutherford (1994) who used the form of $D_y$ / $hu^*$ for rivers and Tanino and Nepf (2008b) who used the form of $D_y/ud$ for cylinder arrays.

Figure 4-18 a) shows that the transverse dispersion coefficients at $d = 0.0080$ m (triangles) are higher than those at $d = 0.0064$ m (circles) for all the cases. The value of $D_y$ increases with ø from ø = 0.025 to ø = 0.075 and then decreases until ø = 0.350 for all the three $Re_d$ values. The same trend exists for the size of the error bars i.e. the difference between the three reaches in each channel also has a maximum value at ø = 0.075. It is worth mentioning that $D_y$ scales with $Re_d$ and cases with $Re_d = 100$ have the lowest value of $D_y$. The effect of velocity and diameter has been removed in Figure 4-18 b) as a result of nondimensionalizing. Figure 4-18b) confirms that the results at $Re_d = 100$ follow the same trend as those at $Re_d = 300$ and $Re_d = 500$, which was not obvious in Figure 4-18 a). However, the effect of $Re_d$ on the results still exists and the data at $Re_d = 100$ deviates from those at $Re_d = 300$ and 500.

## 4.5.2 Effect of $Re_d$ on $D_y$

Values of transverse dispersion coefficient, $D_y$, are depicted against $Re_d$ in Figure 4-19. The results at different solid volume fractions and at different diameters are shown using different symbols as specified in the legends.

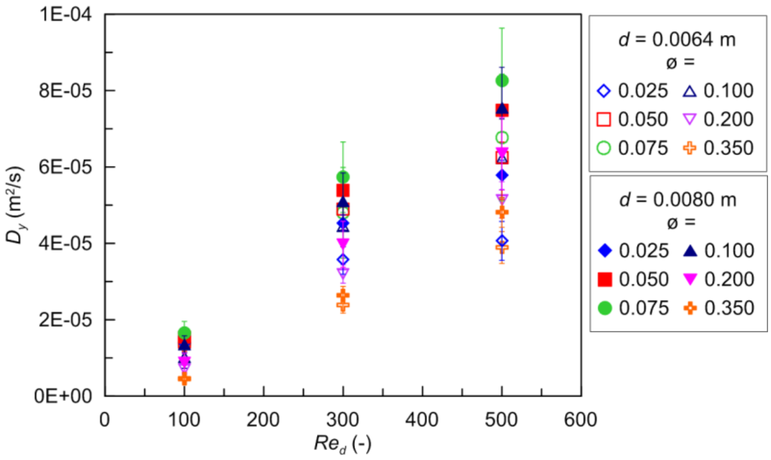

**Figure 4-19 Transverse dispersion coefficients versus $Re_d$ for $d$ = 0.0064 m and $d$ = 0.0080 m**

Figure 4-19 shows a linear increase of $D_y$ with $Re_d$, with $R^2$ values between 0.821 and 1.00, which is consistent with the expected behaviour of $D_y$. Rutherford (1994) reported linear growth of transverse dispersion coefficient with discharge in natural rivers. However, to the author's knowledge, dispersion coefficient has not been related to $Re_d$ in previous studies on cylinder arrays. It can also be seen from Figure 4-19 that the variation due to solid volume fraction increases with $Re_d$, i.e. values of $D_y$ at $Re_d = 100$ are very close together while those at $Re_d = 300$ and $Re_d = 500$ cover a wider range, almost an order of magnitude.

## 4.6 Longitudinal dispersion coefficient

Longitudinal dispersion coefficients for all the cases are presented in this section. The effect of solid volume fraction and $Re_d$ on longitudinal dispersion coefficient are presented in §4.6.1 and §4.6.2, respectively.

### 4.6.1 Effect of density on $D_x$

Values of $D_x$ for all the cases are depicted versus density in Figure 4-20 a), along with the values of $D_x/ud$ in Figure 4-20 b).

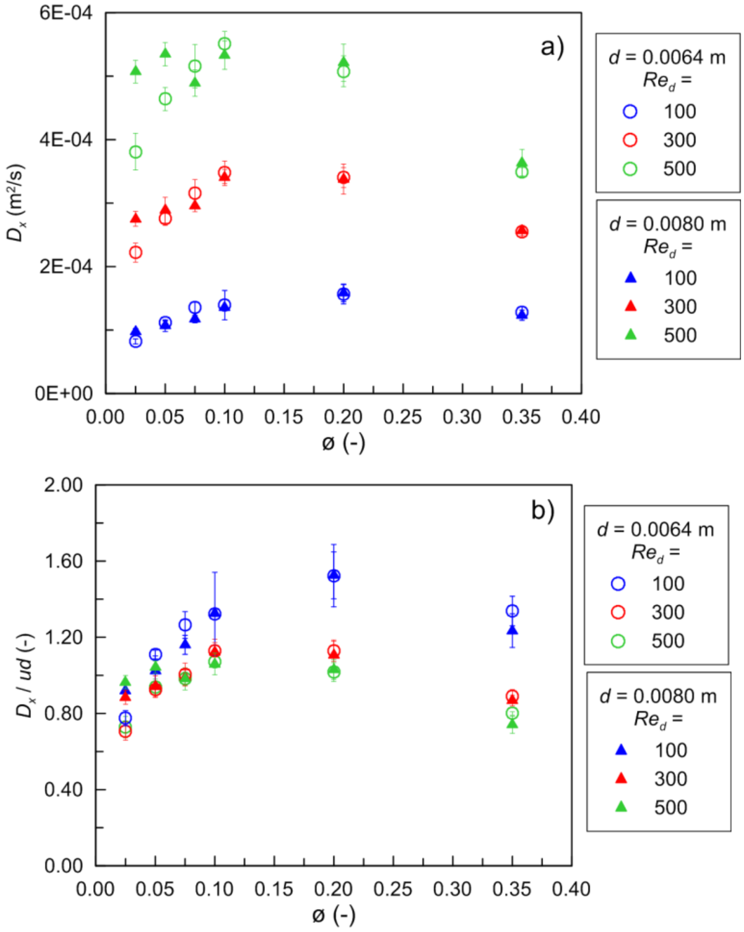

**Figure 4-20 a) Longitudinal dispersion coefficients and b) nondimensionalized longitudinal dispersion coefficients versus ø for $d = 0.0064$ m and $d = 0.0080$ m at $Re_d = 100$, 300, and 500**

Figure 4-20 a) shows that longitudinal dispersion coefficients at the two diameters are very close except for a few cases at low densities. It also shows the scaling effect of velocity which is largely removed in Figure 4-20 b). The values of both $D_x$ and $D_x/ud$ increase up to ø = 0.100 and then decrease. The maximum value of $D_x$ seems to fall between ø = 0.100 and 0.200, but as no case was modelled with a solid volume fraction in this range, the exact ø at which the maximum happens cannot be specified. A similar trend can be seen in Figure 4-20 b), although the values of $D_x/ud$ at $Re_d$ = 100 falls higher than those at other $Re_d$. It can also be seen that the difference between reaches (the standard deviation shown by error bars) has the highest value at $Re_d$= 100 at all the solid volume fractions.

Comparing Figure 4-18 a) and Figure 4-20 a) shows that the scaling effect of velocity on $D_x$ is different to that on $D_y$. It also shows that the values of $D_x$ are one order of magnitude higher than $D_y$ which is consistent with previously published data, e.g. Sonnenwald et al. (2017).

### 4.6.2 Effect of $Re_d$ on $D_x$

Figure 4-21 is presented in this section to investigate the effect of $Re_d$ on longitudinal dispersion coefficient.

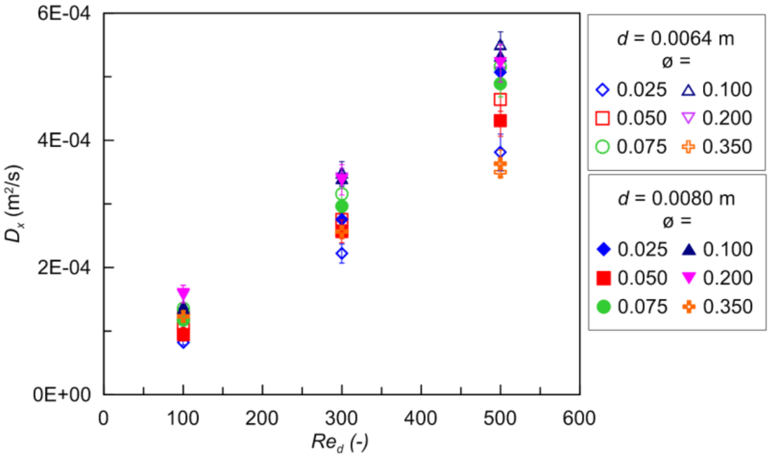

**Figure 4-21 Longitudinal dispersion coefficients against $Re_d$ for $d$ = 0.0064 m and $d$ = 0.0080 m**

Values of $D_x$ in Figure 4-21 show a generally linear increase with $Re_d$, which is consistent with the expected behaviour of $D_x$. Rutherford (1994) reported a linear growth of longitudinal dispersion coefficient with discharges in natural rivers. However, to the author’s knowledge, dispersion coefficient has not been related to

$Re_d$ in previous studies on random cylinder arrays. It can also be seen from Figure 4-21 that by increasing $Re_d$ the variation due to solid volume fraction increases, i.e. values of $D_x$ at $Re_d = 100$ are very close together while those at $Re_d = 300$ and $Re_d = 500$ cover a wider range of values.

## 4.7 Comparison with Previously Published Studies

The results of the current study are compared with previously published data-sets and suggested relationships. An effort has been made to compare the results with as many of the data-sets reviewed in Chapter 2 as possible, provided that the reported graphs were readable enough or the data-set was provided in a table with all the required characteristics i.e. *d*, *ø* and $Re_d$. As a number of suggested relationships require drag coefficient and turbulent kinetic energy, before comparing dispersion coefficients, the estimated drag coefficients and turbulent kinetic energy values from the current study are presented and compared with previously published data-sets and relationships in §4.7.1 and §4.7.2, respectively. Transverse and longitudinal dispersion coefficients are presented in §4.7.3 and §4.7.4, respectively.

### 4.7.1 Drag Coefficient

Drag force exerted on the cylinder array was estimated based on the pressure gradient provided in ANSYS FLUENT and multiplying it with the length of the channel. Drag coefficient was then calculated using Eq. 2-22 presented in §2.4. Drag coefficients for all cases are depicted in Figure 4-22 a) & b) versus solid volume fraction and $Re_d$, respectively. As drag force values were calculated for the whole channel, error bars representing the difference between reaches are not presented in this figure.

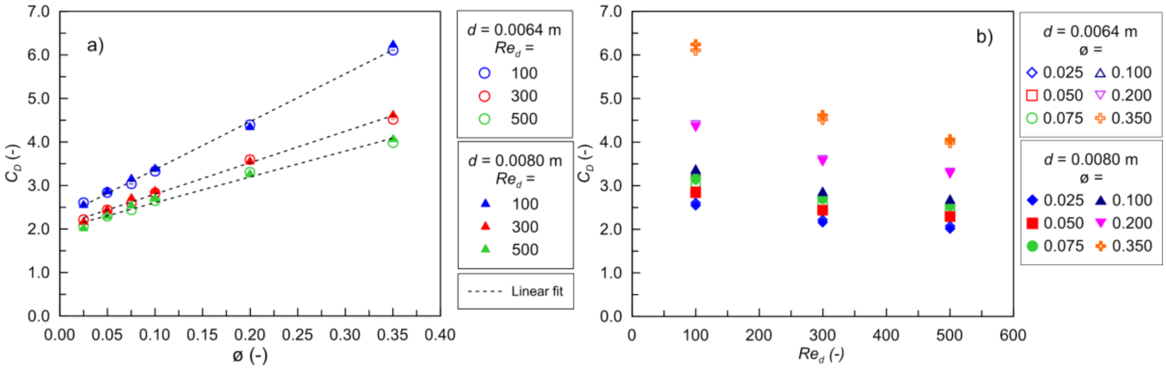

**Figure 4-22 Drag coefficient a) versus solid volume fraction b) versus $Re_d$**

Figure 4-22 a) shows a linear increase in $C_D$ with ø for each $Re_d$. It also shows that the results for both stem diameters fall on the same line. It is worth noting that $C_D$ values corresponding to $Re_d = 300$ and $Re_d = 500$ are close to each other, while those corresponding to $Re_d = 100$ deviate from them. This can also be attributed to a different flow regime and wake structure at $Re_d = 100$, as mentioned before.

The dashed lines on Figure 4-22 show the linear fits for each $Re_d$ as a function of ø. A linear fit between the slopes of these three lines and $Re_d$ was considered, to provide a relationship describing $C_D$ as a function of ø and $Re_d$, as Eq. 4-1.

$$C_D=(-0.013Re_d+11.8)\o+2.3 \tag{4-1}$$

Nepf (1999) reported a set of $C_D$ values, for $d = 0.0069$ m and $ad = 0.01$ to 0.1, previously reported in Figure 2-19. $C_D$ values resulting from the current study are compared with those reported by Nepf (1999) in Figure 4-23. The values for $Re_d$ or velocity were not reported by Nepf (1999).

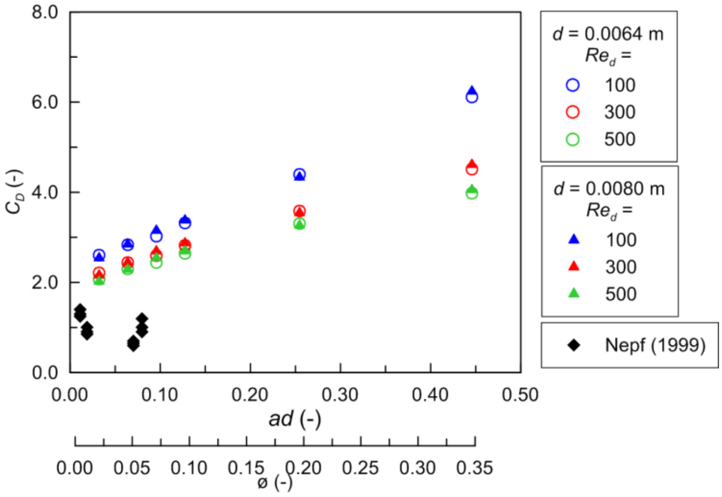

**Figure 4-23 Drag coefficients from the current study compared with reported value by Nepf (1999), figure 6**

Since velocity or $Re_d$ values for reported values of $C_D$ by Nepf (1999) are not known a direct comparison is not possible. It can only be said that the results of the current study cover a higher range of densities and the values of $C_D$ for the common range are of the same order of magnitude, but consistently higher.

Relationships to predict $C_D$ for different solid volume fractions and $Re_d$ was reported in Tanino and Nepf (2008a), figure 5 which was later compared by

Stoesser et al. (2010) to the $C_D$ values resulting from 3D LES models of Stoesser et al. (2010). $C_D$ values from the current study are compared with the results of these two studies in Figure 4-24.

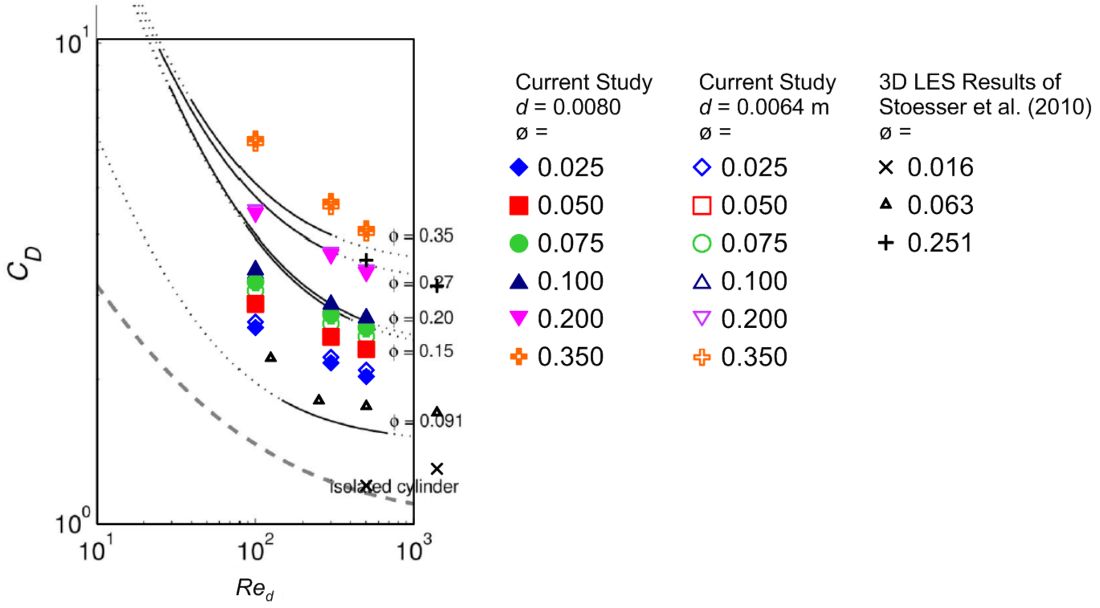

**Figure 4-24 Drag coefficient results of current study versus $Re_d$, depicted on Tanino and Nepf (2008a) figure 5, along with the results of Stoesser et al. (2010)**

It is evident from Figure 4-24 that the results of the current study follow the same trend as the trend suggested by Tanino and Nepf (2008a). However, the results of the current study deviate from lines corresponding to specific solid volume fractions. $C_D$ values at ø = 0.350 are the closest to the suggested line by Tanino and Nepf (2008a) but as ø decreases the difference between the two data-sets increases. The results of Stoesser et al. (2010) also have the same condition, i.e. it follows the general pattern but there is a deviation from suggested lines for specific solid volume fractions. It is worth mentioning that the results of the current study consistently fall higher than the suggested line by Tanino and Nepf (2008a). However, the results from Stoesser et al. (2010) does not show a consistent position relative to Tanino and Nepf (2008a).

Sonnenwald et al. (2017) combined experimental data reported by Tanino and Nepf (2008a) and Tinoco and Cowen (2013) and suggested an empirical best fit for the drag coefficient based on the stem diameter and solid volume fraction, previously presented as Eq.2-41 and Eq. 2-42 in § 2.6.1. $C_D$ values calculated based on this relationship are compared with the drag coefficients estimated in this study in Figure 4-25.

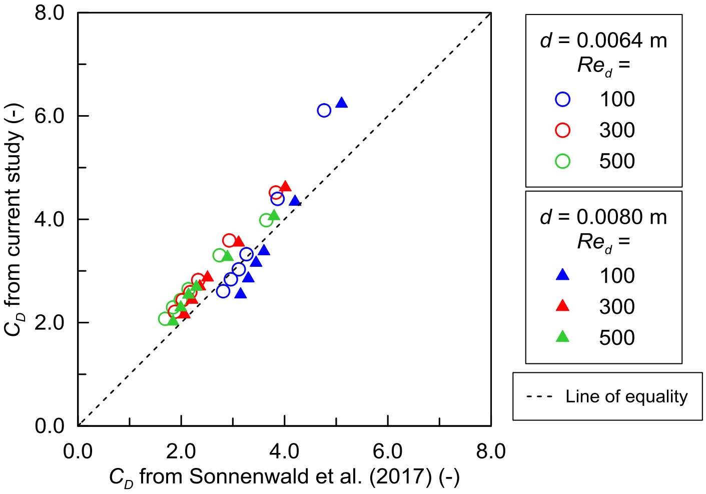

**Figure 4-25 Drag coefficients calculated in this study versus the expression suggested by Sonnenwald et al. (2017)**

Figure 4-25, shows a good agreement between the relationships suggested by Sonnenwald et al. (2017) and $C_D$ values estimated in this study. $C_D$ values corresponding to $Re_d = 100$ at $ø = 0.350$ i.e. two blue symbols at $C_D \approx 6$ deviate from the line of equality, which can be attributed to the different flow regime at this $Re_d$. More data at low $Re_d$ ($Re_d < 100$) are required to investigate this matter further.

## 4.7.2 Turbulent Kinetic Energy

Area-weighted means of turbulent kinetic energy for each channel over the whole length of the channel are presented in Figure 4-26.

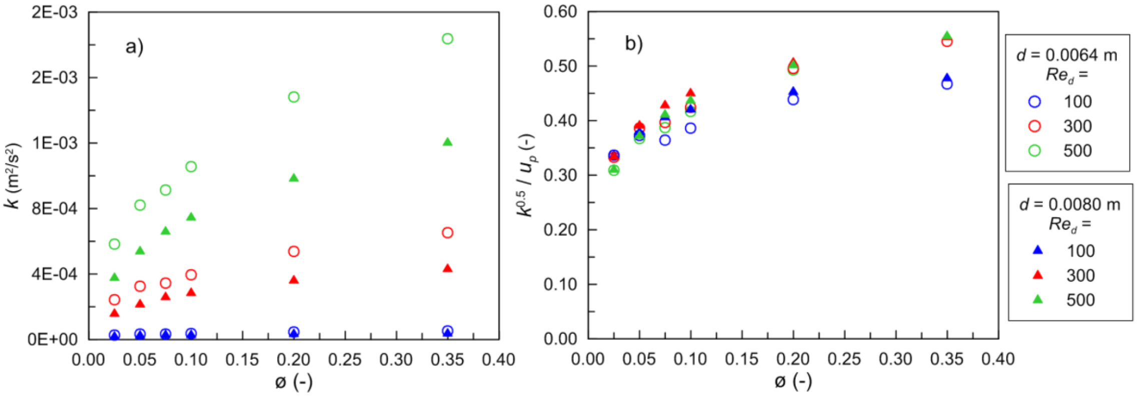

**Figure 4-26 a) Turbulent kinetic energy and b) nondimensionalized turbulent kinetic energy versus solid volume fraction**

Figure 4-26 a) shows that turbulent kinetic energy scales with velocity. It also shows that at all points $d = 0.0080$ has a higher turbulent kinetic energy, except for $Re_d = 100$ where the difference between the results of two diameters is not obvious due to the low values of $k_t$ at this $Re_d$. It is interesting to note that the effect of diameter on turbulent kinetic energy increases as $Re_d$ increases, i.e. the difference between two symbols is greater at $Re_d = 500$ than that at $Re_d = 100$.

The values of turbulent kinetic energy nondimensionalized by $u_p$ referred to also as the mean turbulence intensity in the literature, are presented in Figure 4-26 b). Removing the scaling effect of $Re_d$ (velocity), in Figure 4-26 b) confirms the difference in flow structure at $Re_d$, yet again, as data corresponding to $Re_d = 300$ and 500 overlap and deviate from $Re_d = 100$. It is also worth mentioning that at all the $Re_d$ values, the results of the two diameters are very close at low densities and from $ø = 0.075$ onwards deviate, which may suggest a transition at this solid volume fraction.

The square root of turbulent kinetic energy is plotted versus $u_p$ in Figure 4-27. It can be seen that both diameters of each solid volume fraction follow the same linear pattern. For each solid volume fraction, a linear equation was fitted, these fits are shown as dashed lines in Figure 4-27.

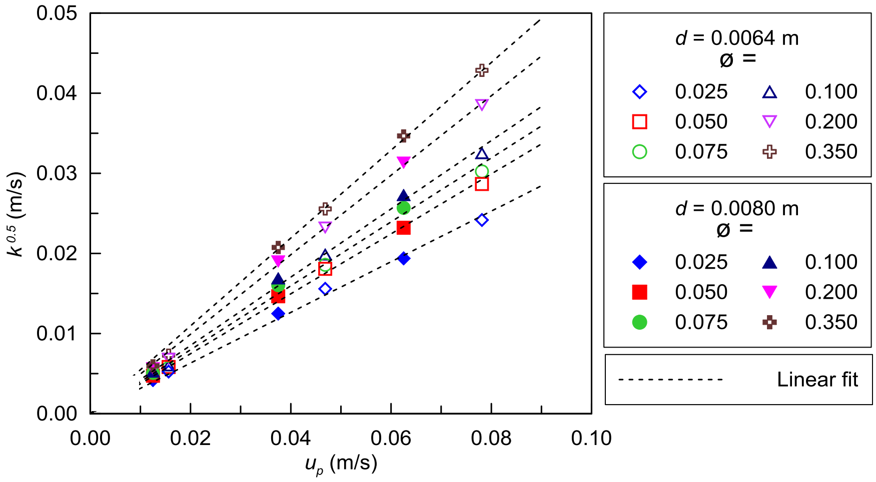

**Figure 4-27 Square root of turbulent kinetic energy versus $u_p$**

The slopes of the fitted lines in Figure 4-27 are plotted versus density in Figure 4-28.

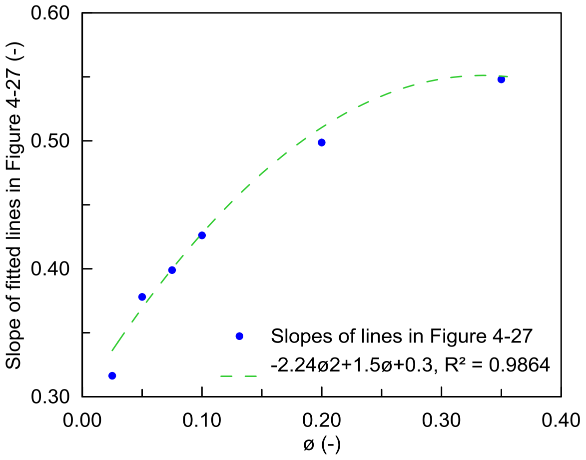

**Figure 4-28 Slopes of the fitted lines in Figure 4-27 along with the fitted polynomial**

A polynomial fit between the slopes of these lines and ø was considered as shown in Figure 4-28, to provide a single relationship describing $k_t^{0.5}$ as a function of ø and $u_p$ as Eq. 4-2. This equation will be useful in examining previously suggested models for predicting dispersion coefficients, as will be explained in coming sections.

$$\frac{k_t^{0.5}}{u_p} = \left(-2.24ø^2 + 1.5ø + 0.3\right) \qquad 4\text{-}2$$

Nepf (1999) suggested Eq. 2-29 with $\alpha_1$ equal to 0.9±1 as the relationship between turbulent kinetic energy and dimensionless parameter $adC_D$. To examine the validity of this relationship, the results of the current study are plotted along with figure 9 from Nepf (1999), on the same extended scale. The linear fit suggested by Nepf (1999) is extended and shown with a dashed line.

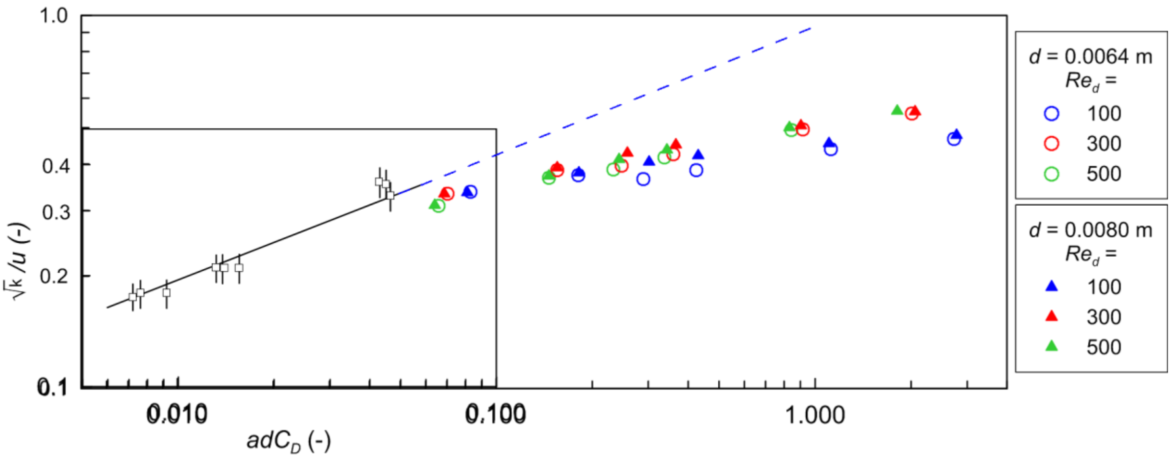

**Figure 4-29 Nondimensionalized turbulent kinetic energy versus $adC_D$ compared with figure 9 from Nepf (1999)**

Figure 4-29 shows that the results of the current study at the lowest value of $adC_D$ i.e at ø = 0.025 are close to the relationship suggested by Nepf (1999), but that as density increases, they deviate from the suggested line. It also shows that the densities investigated by Nepf (1999) only cover the lower range of densities.

Tanino and Nepf (2008b) suggested Eq. 2-44 and Eq. 2-45 as relationships between normalized turbulent kinetic energy (or turbulence intensity) and $d/\langle S_n \rangle_A$, ø and $C_D$. The results of the current study are plotted on figure 14 from Tanino and Nepf (2008b), in Figure 4-30 to compare them with the results of that study and also to examine the validity of the relationship suggested by them.

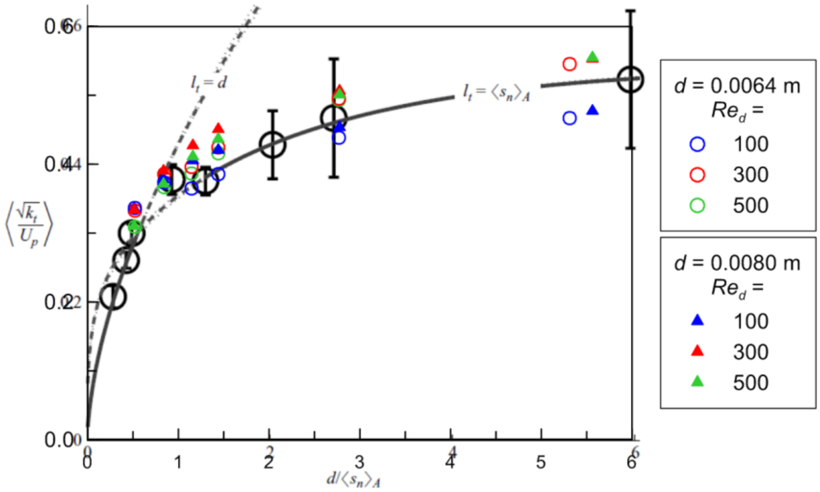

**Figure 4-30 Nondimensionalized turbulent kinetic energy versus $adC_D$ depicted in figure 14 from Tanino and Nepf (2008b), Eq. 2-44 and Eq. 2-45**

A strong agreement between the results of the current study and those of Tanino and Nepf (2008b) can be observed in Figure 4-30. Thus, one can conclude that the relationships suggested by them for estimating normalized turbulent kinetic energy (or turbulence intensity) i.e. Eq. 2-44 and Eq. 2-45 are confirmed by the results of the current study.

The flow field results of the current study were shown to be in agreement with those reported by Tanino and Nepf (2008b) and Ricardo et al. (2016) in Chapter 3. The agreement between drag coefficients estimated in the current study with the relationships suggested by Sonnenwald et al. (2017) was shown in § 4.7.1. These were further supported by the agreement between the estimated/modelled values of turbulent kinetic energy (or turbulence intensity) in the current study with those measured in the laboratory using Laser Doppler Velocimetry (LDV) and reported by Tanino (2008) and Tanino and Nepf (2008b) in this section.

### 4.7.3 Transverse Dispersion, $D_y$

Nepf (1997b) reported transverse dispersion coefficients measured over randomly distributed cylinder arrays of $d = 0.006$ and $0.012$ m forming five densities of $ø = 0.006$, 0.014, 0.017, 0.035, and 0.053. The results of the current study are compared with those reported by Nepf (1997b) in Figure 4-31. Since the results of Nepf (1997b) cover only a small section of the density range tested in the current study only those results of the current study with densities of up to $ø = 0.100$ are shown. The data points corresponding to $ø = 0.200$ and 0.350 both follow the pattern shown in the figure and fall lower than those corresponding to $ø = 0.100$ (previously shown in Figure 4-18 a)). This allows the suggested lines by Nepf (1997b) to be retained on the figure, as their equation is not given and producing them for other scales will not be as accurate.

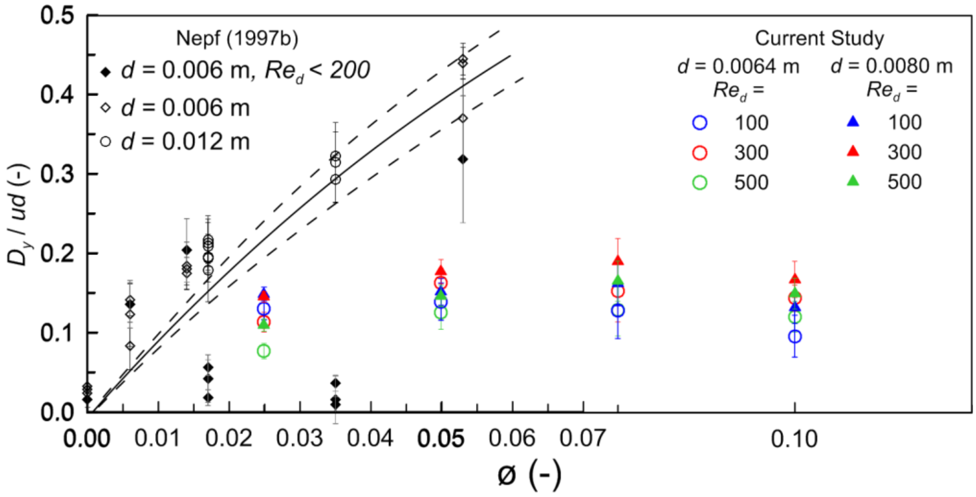

**Figure 4-31 Transverse dispersion coefficients depicted in figure 6, of Nepf (1997b), produced using data provided in table 1 of Nepf (1997b)**

As was explained in Chapter 1, Nepf (1997b) claimed that all the data points corresponding to $Re_d < 200$ fall below the solid line in Figure 4-31 (figure 6 of the original) which correspond to the line of $M = 10$ on **Error! Reference source not found.** b) (figure 2 of the original). The reason for this was the onset of vortex shedding which was reported to happen between $Re_d = 150$ and 200 based on the dye streak observation. However, reproducing Figure 4-31 from data provided in Table 1 of Nepf (1997b) shows that some of the data points corresponding to $Re_d <$

200, the black diamonds, fall higher than the solid line. Nevertheless, all the results of the current study regardless of $Re_d$ fall under the solid line, which can be interpreted as no vortex shedding at all $Re_d$ values.

Two points should be borne in mind, first is that the flow fields modelled in the current study were modelled and tested under both steady and transient conditions. Under none of these conditions was evidence of vortex shedding observed in terms of obvious changes in the velocity field. The second point is evidence regarding a different flow condition at $Re_d = 100$ from that at $Re_d = 300$ and 500 as noted while investigating the effect of density and $Re_d$ on transverse and longitudinal dispersion coefficients in previous sections. Considering these two points together one may conclude that although the effect of vortex shedding could not be observed in terms of changes in the velocity field and the flow fields were solved as a steady models, different behaviour of data points corresponding to $Re_d = 100$ (discussed in previous sections) confirms modelling a certain level of effects caused by onset of vortex shedding in flows of $Re_d$ higher than 150-200. Thus, the author suggests that the disagreement between the results of the current study with those reported by Nepf (1997b) in Figure 4-31 could be due to laboratory measurements errors and different optimization and routing methods used in two studies. Comparing the results of the current study with other studies will shed light on this matter.

Tanino (2008) and Tanino and Nepf (2008b) refer to Eq. 4-3 as one of the findings of Nepf (1999) for estimating transverse dispersion coefficient based on turbulence intensity, *k*.

$$\frac{D_y}{u_p d} = 0.9\left(\frac{\sqrt{k}}{u_p}\right) \qquad 4\text{-}3$$

The estimated values based on this equation are compared with the results of the current study in Figure 4-32.

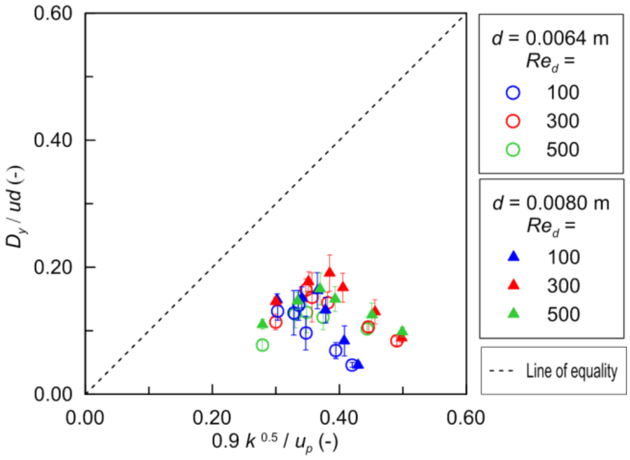

**Figure 4-32 Nondimensionalized transverse dispersion coefficients compared with the relationship suggested by Nepf (1999)**

It can be seen from Figure 4-32 that Eq. 4-3which only considers turbulence intensity as a contributing process to dispersion, underestimates the transverse dispersion coefficients. This shortcoming has been improved in later studies by Tanino (2008) and Tanino and Nepf (2008b) as will be discussed in coming sections. To find the proper constant coefficients (to replace 0.9) fitting the results of the current study, values of $D_y/ud$ are plotted against $k^{0.5}/u_p$ in Figure 4-33. It can be seen that data points corresponding to each solid volume fraction, for both $d$ = 0.0064 m and $d$ = 0.0080 m follow a specific linear trend. The linear fits for each solid volume fraction are shown as dashed lines in Figure 4-33.

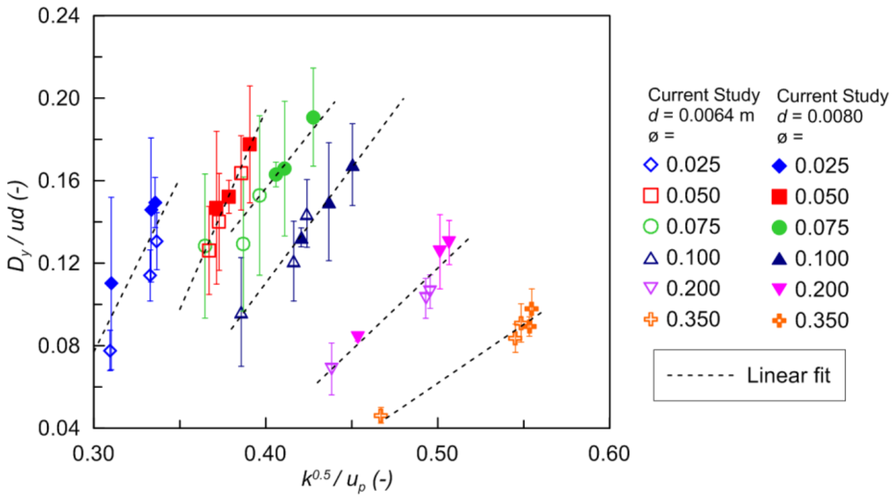

**Figure 4-33 Nondimensionalized transverse dispersion coefficient versus turbulence intensity for current study along with the linear fits for each solid volume fraction**

Considering the trends observed in Figure 4-33, Eq. 4-4, is suggested for estimating $D_y/ud$ based on turbulence intensity.

$$\frac{D_y}{ud} = \left(16.8\varnothing^2 - 9.9\varnothing + 2\right)\left(\frac{\sqrt{k}}{u_p}\right) - 2.4\varnothing^2 + 1.5\varnothing - 0.5 \qquad 4\text{-}4$$

Recalling Eq. 4-2, which suggested a polynomial relationship between the square root and velocity, Eq. 4-4 can be re-written as Eq. 4-5.

$$\frac{D_y}{ud} = \left(16.8\varnothing^2 - 9.9\varnothing + 2\right)\left(-2.2\varnothing^2 + 1.5\varnothing + 0.3\right) - 2.4\varnothing^2 + 1.5\varnothing - 0.5 \qquad 4\text{-}5$$

This equation will be compared with a similar equation suggested by Tanino and Nepf (2008b) (Eq. 2-46 in Chapter 2) in the following sections.

Nepf (1999) reported a set of laboratory data for randomly distributed cylinder arrays of *d* = 0.0064 and 60 < $Re_d$ < 2000. She also suggested considering two processes of turbulent diffusion and mechanical dispersion as contributing processes in net transverse dispersion, calculated based on Eq. 2-30 and Eq. 2-32, respectively. The results of the current study is depicted in figure 10 of Nepf (1999) (Figure 4-34 of this thesis) to be compared with the equations and data points reported by Nepf (1999). It should be mentioned that Nepf (1999) also reported a set of field data which are also shown in the figure. An additional axis is included to indicate the solid volume fraction values, as the original figure was based on ad, the results of current study corresponding to *ø* = 0.200 and *ø* = 0.350 are not included.

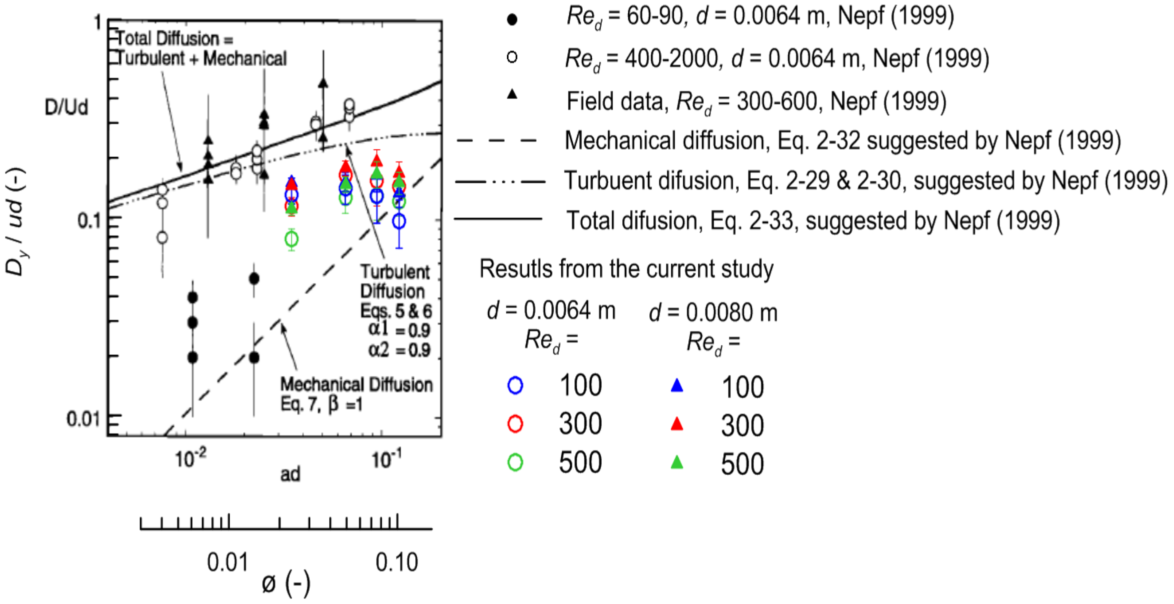

**Figure 4-34 Nondimensionalized transverse dispersion coefficient values, along with figure 10 from Nepf (1999), *d* = 0.0064 m**

It can be seen from Figure 4-34 that the results from the current study are close to and of the same order of magnitude as the laboratory data collected at $Re_d$ = 400-2000 by Nepf (1999) and the line corresponding to turbulent diffusion. Based on Nepf (1999) suggestion, it was expected that the results of the current study at $Re_d$ = 100 would fall on the dashed line corresponding to the mechanical dispersion in Figure 4-34. This expectation is fulfilled only for data corresponding to $d$ = 0.0064 m, at ø = 0.075 and ø = 0.100. However, it should be borne in mind that the data collected for $Re_d$ = 60-90 are of $O$ (0.01) and are almost insignificant, noting the logarithmic scale, and the mechanical diffusion is a small component comparing to turbulent diffusion.

Chronologically the next study on transverse dispersion coefficient within randomly distributed cylinder arrays is Serra et al. (2004), who used a specific normalization method for presenting their data, this method is not used in any other study. The results of the current study are compared with those of Serra et al. (2004) and Nepf et al. (1997) in Figure 4-35.

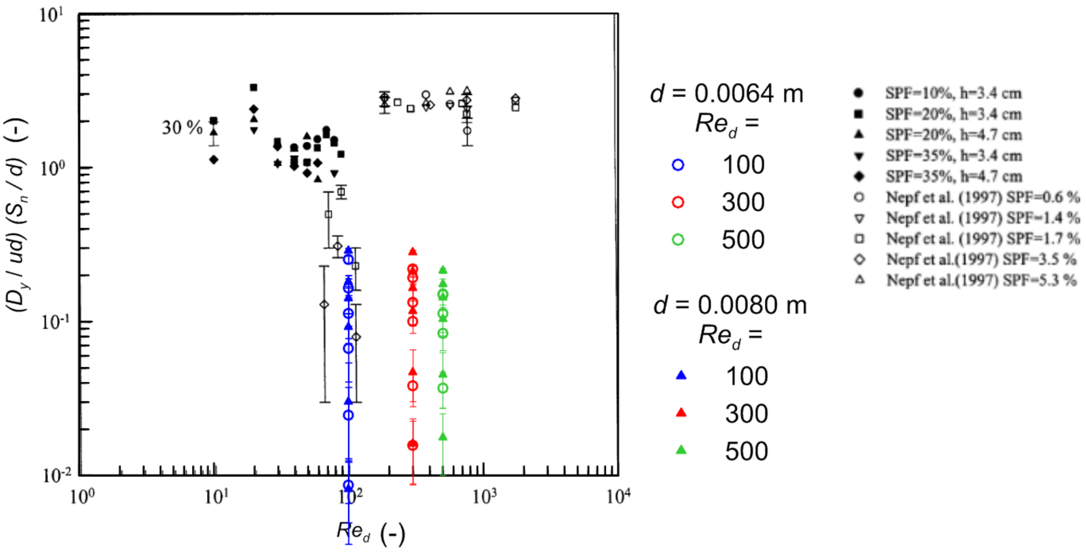

**Figure 4-35 $(D_y/ud)(<S_n>_A/d)$ versus $Re_d$ depicted on figure 1 of Serra et al. (2004), including previously published data from Nepf et al. (1997b), SPF is equivalent to ø**

Figure 4-35 shows that the nondimensionalizing method used by Serra et al. (2004) does not provide an appropriate scaling as no common pattern can be found between different data-sets using this scaling method.

As Serra et al. (2004) investigated cases with low $Re_d$ i.e. < 100, and based on Nepf (1999) mechanical dispersion is the main process contributing to the net dispersion, they compared their results with the suggested equation for estimating mechanical dispersion by Nepf (1999), i.e. Eq. 2-32, in Figure 4-35. The results of the current study at all $Re_d$ values are depicted in Figure 4-35 for sake of comparison between the range and behaviour of the two data sets. Based on Figure 4-36, the results of the current study don’t follow either Eq. 2-32 or the linear fit on the results of Serra et al. (2004).

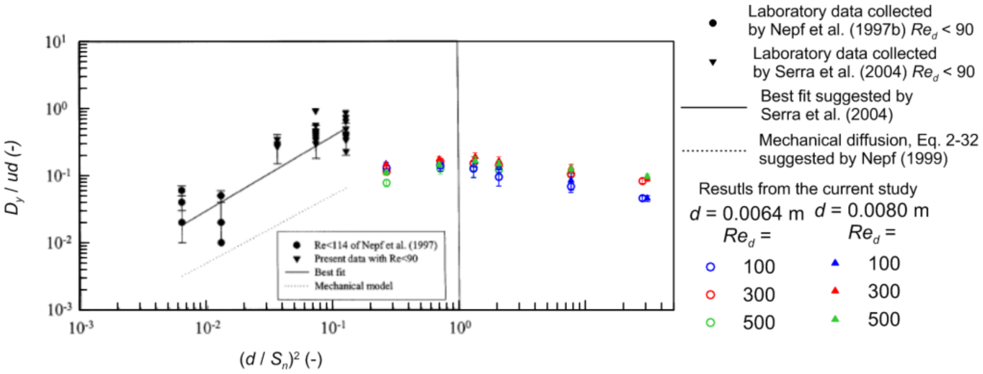

**Figure 4-36 Result of the current study depicted on Figure 6 of Serra et al. (2004), nondimensionalized transverse dispersion coefficient against ($d$ / $S_n$)$^2$ along with the mechanical dispersion model of Nepf et al. (1997b)**

Data points reported in Table 1, Serra et al. (2004) were re-presented in Figure 2-25 in Chapter 2, which is shown here in Figure 4-37 along with the results of the current study. This presentation shows that the results of Serra et al. (2004) fall very close to those of current study corresponding to $Re_d$ = 100, which is consistent with the fact that their data was collected for $Re_d$ < 100. This can be considered as a confirmation of the scalar transport results from the CFD model used in the current study. It is noticeable that although $Re_d$ is lower for all their data points, some of their results show higher $D_y$ values than those recorded in this study for $Re_d$ = 100. This can be interpreted as CFD possibly tending to underestimate dispersion coefficients.

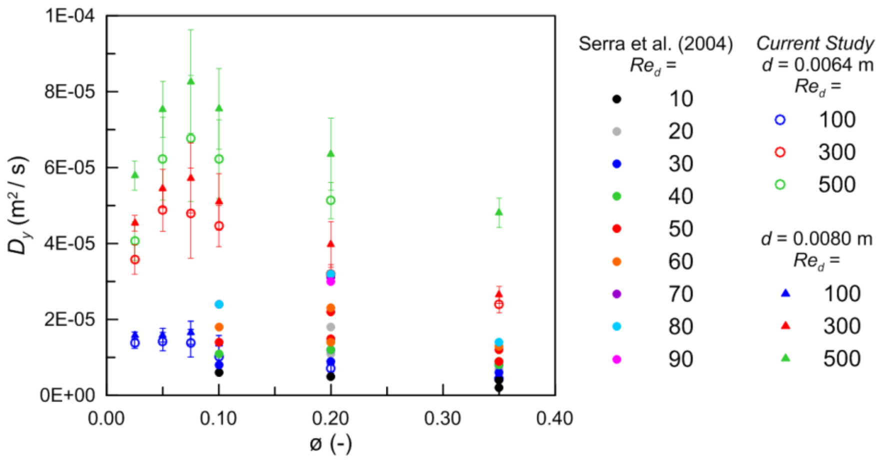

**Figure 4-37 Transverse dispersion coefficients from Serra et al. (2004) along with the results of the current study**

Finally the results of the most recent laboratory study investigating transverse dispersion confident, i.e. Tanino and Nepf (2008b) (and Tanino 2008) and their suggested fit (Eq. 2-46) are compared with the results of this thesis in Figure 4-38. The relationship suggested in this thesis (Eq. 4-5) which was derived based on the linear increase of $k^{0.5}$ with $u_p$ (Figure 4-27) along with the linear increase of $D_y/ud$ with $k^{0.5}$ (Figure 4-33) is also shown in Figure 4-38.

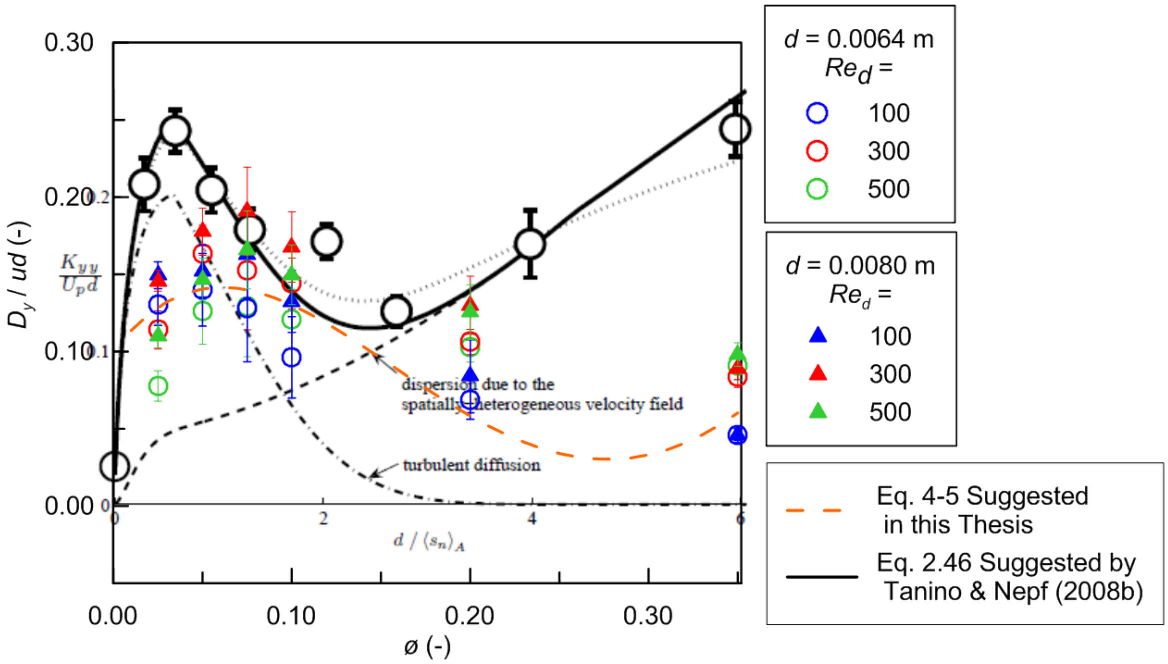

**Figure 4-38 Nondimensionalized transverse dispersion coefficients depicted in figure 18 of Tanino and Nepf (2008b), along with their suggested models and Eq. 4-5**

Figure 4-38 shows an overall agreement between the trend and the order of magnitude of the results from the current study and those of the laboratory data observed by Tanino and Nepf (2008b), which yet again confirms the suitability of the CFD tool used in this thesis to be used for future studies. It is worth recalling that Tanino and Nepf (2008b) derived equations to describe mechanical dispersion and turbulent diffusion based on *d*, ø, $<S_n>_A$ and $C_D$ and then defined the net dispersion as the summation of this two considering two fitting constants. Tanino and Nepf (2008b) also suggest relationships to describe all the terms used in their model based on ø and *d*. Thus, one can say that the relationship derived based on the results of the current study i.e. Eq. 4-5 is similar to the model suggested by Tanino and Nepf (2008b). However, it should be mentioned that their model was based on an analysis of the turbulent kinetic energy and the mean kinetic energy budgets, considering the work done by drag force and wake production, and thus included some assumptions as well as fitting constants, but at the same time had the advantage of basic theory analysis. The relationship derived in this thesis, on the other hand, is empirical and includes no assumption. Since no dependency on the diameter was observed through derivation of this relationships, the final equation is only a function of ø, however, testing it for other diameters is necessary and can improve it.

### 4.7.4 Longitudinal Dispersion, $D_x$

Fewer studies have investigated longitudinal dispersion compared to transverse dispersion. Nepf et al. (1997a) measured the longitudinal dispersion coefficient, $D_x$, within randomly distributed 0.0064 m diameter, cylinder arrays of ø = 0.010, 0.015, and 0.055. Three velocities were considered in their study, $u_p$ = 0.029, 0.055, and 0.074 m/s, which are equivalent to $Re_d$ = 185.6, 352.0, and 473.6, respectively. The results of the current study are depicted in figure 7 from Nepf et al. (1997a) in Figure 4-39. It should be mentioned that the results of the current study at ø = 0.200, 0.350 are not shown in this figure.

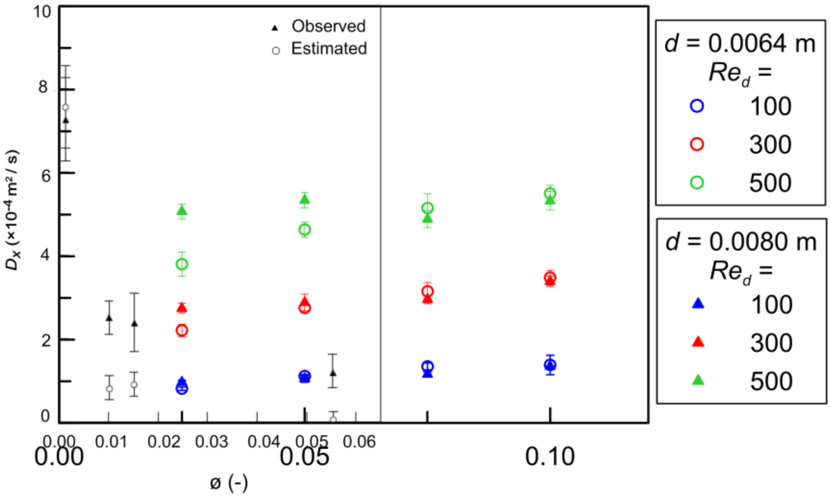

**Figure 4-39 longitudinal dispersion coefficients versus solid volume fraction along with figure 7 from Nepf et al. (1997a), observed and estimated longitudinal dispersion coefficients**

Figure 4-39 shows the results of the current study at $Re_d$ = 100 and $Re_d$ = 300 fall within the range of the values observed by Nepf et al. (1997a). This, considering the range of $Re_d$ tested by Nepf et al. (1997a) confirms the validity of the CFD models used in this thesis for estimating longitudinal dispersion coefficients. The suggested theoretical model by Nepf et al. (1997a) describes the longitudinal dispersion coefficient as a function of vertical dispersion. Since all the CFD models built in this thesis are 2D planar models, their theoretical model cannot be compared with the results of this study.

White and Nepf (2003) measured $D_x$ within randomly distributed cylinder arrays of $d$ = 0.0064 m forming $ø$ = 0.010, 0.020, and 0.065. Conditions of $65 < Re_d < 650$ were tested in their experiments. The results of the current study are depicted in figure 8 from White and Nepf (2003) in Figure 4-40.

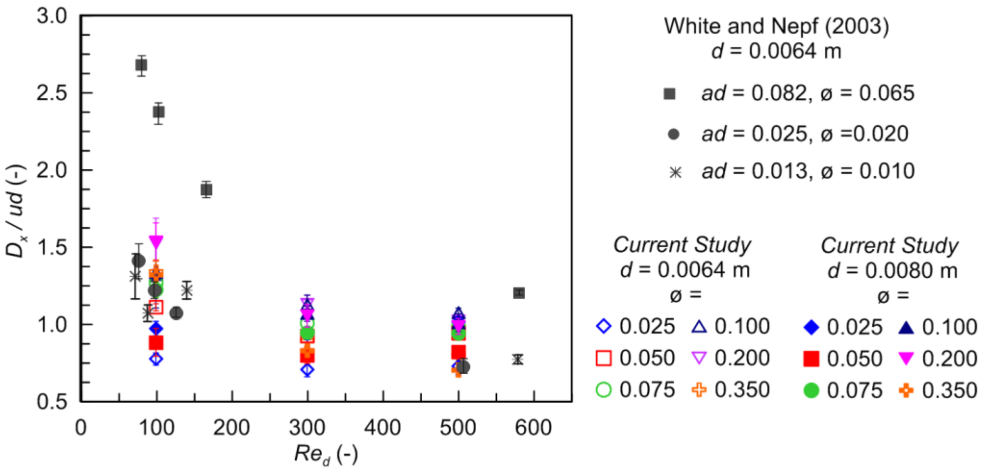

**Figure 4-40 Nondimensionalized longitudinal dispersion coefficients depicted in figure 8 from White and Nepf (2003)**

It can be seen from Figure 4-40 that the results from the current study show a considerable level of agreement with the values measured in the laboratory by White and Nepf (2003), at ø = 0.010 and 0.020. The fact that the laboratory results reported by White and Nepf (2003) at ø = 0.065 are considerably higher than those at ø = 0.010 and 0.020, may suggest errors caused by specific laboratory conditions. It was observed from Figure 4-39 that the value reported by Nepf et al. (1997a) for $D_x/ud$ at ø = 0.055, and $Re_d$ = 185.6, 352.0, and 473.6, is around 1.0 (shown by black triangle and error bar at ø = 0.055). This, along with the general trend of $D_x/ud$ versus ø, suggest that the expected value for $D_x/ud$ at ø = 0.065 should also be around 1.0 while the results reported by White and Nepf (2003) are considerably higher except at $Re_d$ = 560.

White and Nepf (2003) suggested a theoretical model which parametrized the longitudinal dispersion coefficient based on the contributions from primary and secondary wake areas. They compared the theoretical model with their laboratory measurements at $Re_d$ = 100 and $Re_d$ = 190. The results of the current study are compared with the laboratory measurements and the theoretical model suggested by White and Nepf (2003) in Figure 4-41 at $Re_d$ = 100. The dashed line and the dotted line on this figure represent the contribution from primary and secondary wakes, respectively.

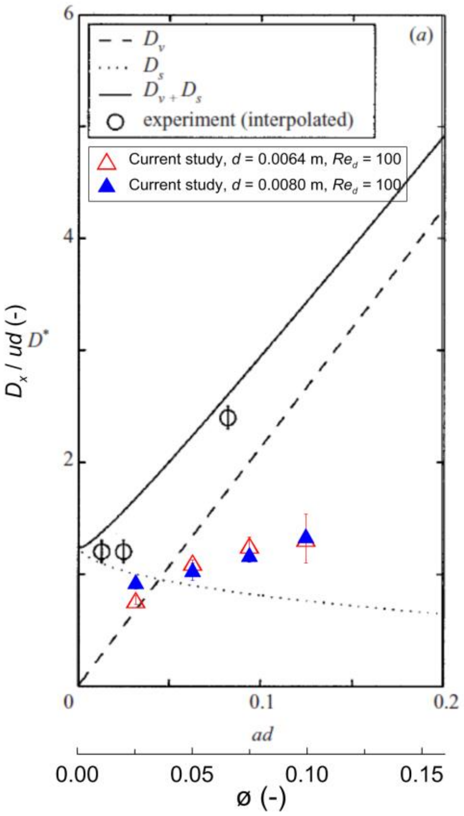

**Figure 4-41 Nondimensionalized longitudinal dispersion coefficients depicted in figure 11 from White and Nepf (2003), comparison of theory and experiment for *Re$_d$* = 100**

Figure 4-41 shows that CFD and experimental result are very close at small densities. However, for higher densities comparison is not possible due to insufficient available laboratory data.

Comparing the longitudinal dispersion coefficients estimated in this thesis with the two main studies on longitudinal mixing within random cylinder arrays, showed the validation of the CFD tool used in this thesis for modelling and measuring longitudinal mixing. This, along with the similar validations for transverse mixing presented earlier in this chapter, confirm the suitability of the tool introduced and tested in this thesis for modelling and estimating mixing within cylinder arrays. It also implies the validation of the flow and truculence results of the cases modelled in this thesis, which can be used in future studies focused on turbulence characteristics of random cylinder arrays.

## 4.8 The relationship between $D_x$ and $D_y$

To the author's knowledge, none of the previous studies on mixing within random cylinder arrays have measured both longitudinal and transverse dispersion coefficients simultaneously within the same array. Thus, there is almost no study on investigating the relationship between these two. Longitudinal dispersion coefficients resulting from the current study are depicted against transverse dispersion coefficients in Figure 4-42.

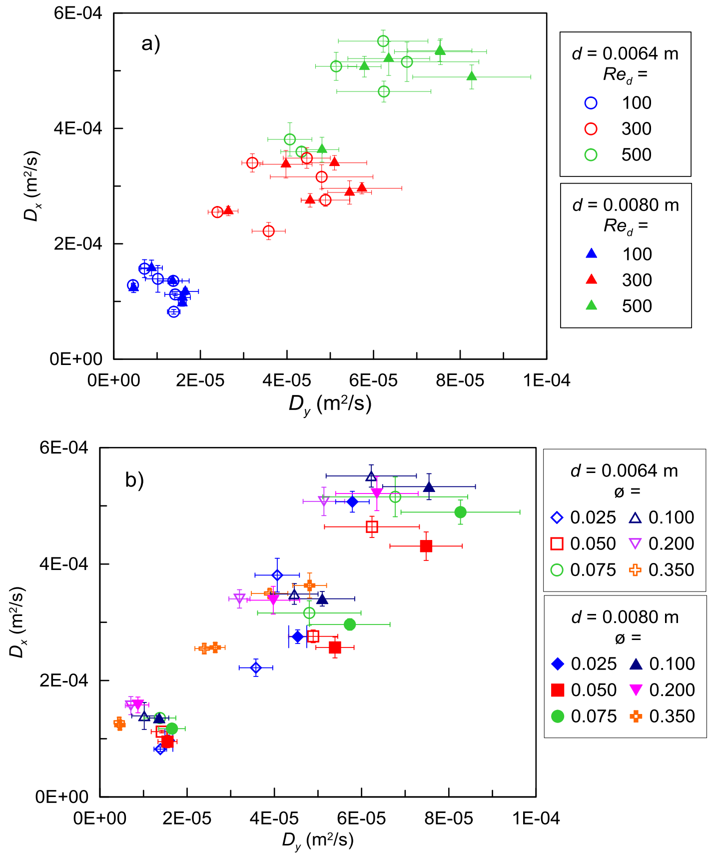

**Figure 4-42 Longitudinal versus transverse dispersion coefficients a) and b) represent the same figure, the difference is in the symbols used for representing data making it easy to distinguish the effects of $Re_d$ and ø**

Figure 4-42 is presented in two formats to clarify the effects of $Re_d$ and ø. A linear relationship between longitudinal and transverse dispersion coefficients can be observed in Figure 4-42, with $R^2$ equal to 0.850. Based on a linear fit in Figure 4-42, Eq. 4-6 can be suggested as the relationship between $D_x$ and $D_y$.

$$D_x = 6.14D_y + 0.00006 \tag{4-6}$$

By combining Eq. 4-5 with Eq. 4-6, Eq. 4-7 can be suggested to predict $D_x$ as a function ø,

$$\frac{D_x}{ud} = 6.14\left[\left(16.8ø^2 - 9.9ø + 2\right)\left(-2.2ø^2 + 1.5ø + 0.3\right) - 2.4ø^2 + 1.5ø - 0.5\right] + 0.00006 \tag{4-7}$$

Sonnenwald et al. (2017) reported laboratory simultaneously-measured longitudinal and transverse dispersion coefficients for regularly distributed cylinder arrays as well as real vegetation, *Carex* and *Typha*. However, the relationship between $D_x$ and $D_y$ was not investigated. The results from the current study along with Eq. 4-5 and Eq. 4-7 are depicted in figure 6 from Sonnenwald et al. (2017) in Figure 4-43. Low-density and High-density data in Figure 4-43 are measured within regularly distributed cylinder arrays of 0.004 m diameter with ø = 0.005 and ø = 0.02, respectively. Wadzuk and Burke (2006), Shucksmith et al. (2010) and Huang et al. (2008) are studies on real vegetation and more explanation on them can be found in Sonnenwald et al. (2017). The rest of the datasets are mentioned earlier in this thesis.

Figure 4-43 provides an overall comparison between the results from the current study and the previously published data on regularly and randomly distributed cylinder arrays and real vegetation. It can be seen that the suggested relationships in this thesis i.e. Eq. 4-5 and Eq. 4-7, provide an acceptable prediction of $D_y$ and $D_x$, especially for cylinder arrays. However, it should be borne in mind that these relationships are preliminary suggestions and need to be tested and improved for a wider range of conditions and cylinder diameters.

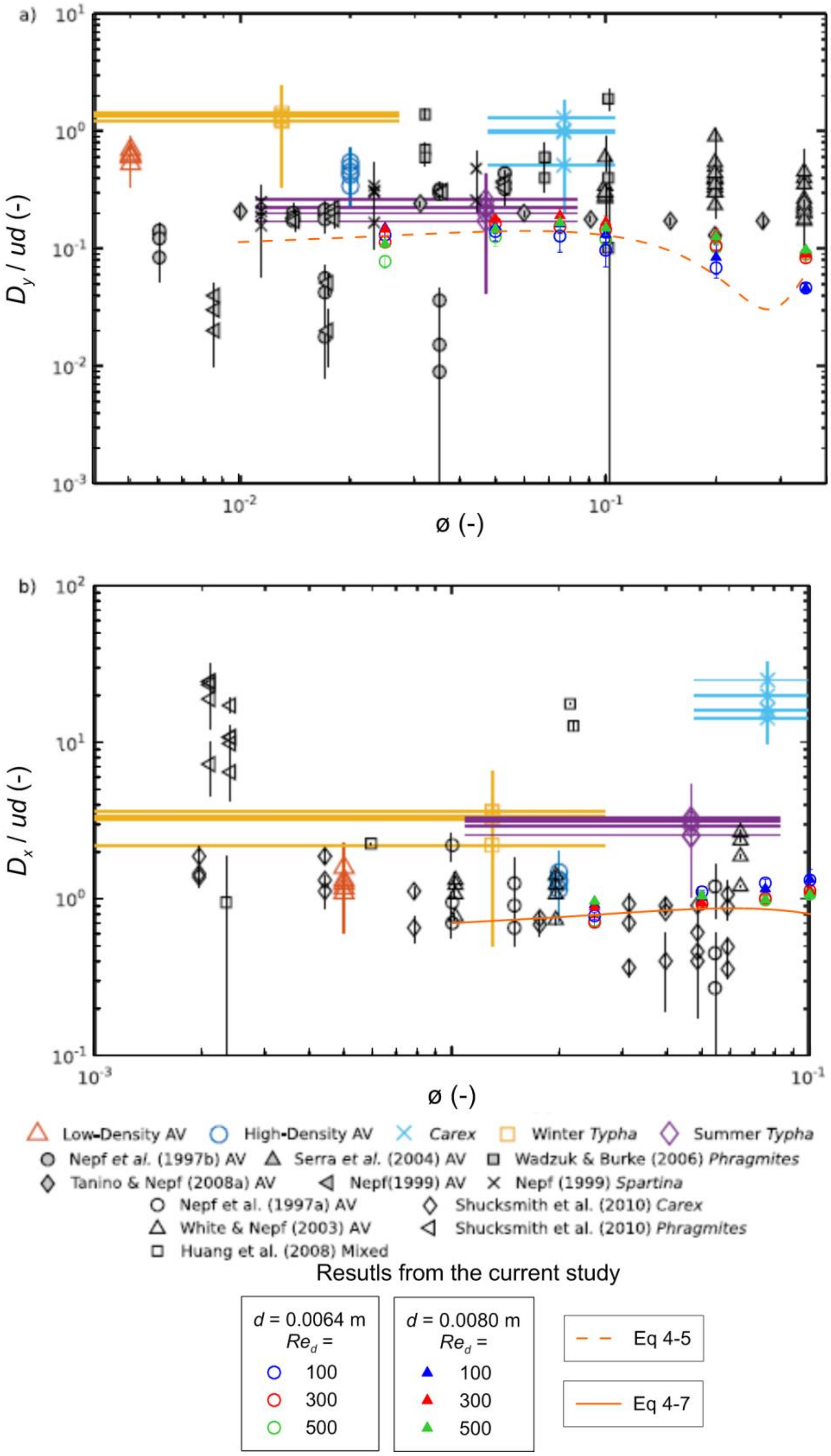

**Figure 4-43 Nondimensionalized longitudinal and transverse dispersion coefficients along with Eq. 4-5 and Eq. 4-7 depicted on figure 6 of Sonnenwald et al. (2017)**

## 4.9 Discussion and Conclusion

A new dataset of flow and dispersion coefficients for random cylinder arrays of $d$ = 0.0064 m and $d$ = 0.0080 m forming densities of ø = 0.025, 0.050, 0.075, 0.100, 0.200 and 0.350 at $Re_d$ = 100, 200 and 300 was produced and the data is presented in this chapter, using the methodology developed in Chapter 3. The tested geometries are advantageous over previously tested geometries both in laboratory and CFD studies, as they cover a wider and longer array, selected to provide the desired accuracy, based on the preliminary studies presented in Chapter 3.

A very high-resolution (with a maximum cell size of 0.001 m) flow and turbulence data set was presented. This dataset provides a better understanding of the flow and turbulence condition within random cylinder arrays. Comparing velocity contours and turbulence features with previously published laboratory measurements confirmed the accuracy of the dataset and validity and suitability of the methodology to be used for future studies. Investigating some of the turbulence features provided evidence for previously suggested theories such as the transition in turbulence characteristic length.

The drag coefficient for each case was estimated based on the pressure gradient provided in the software. Comparison between the drag coefficients estimated in this thesis with those previously published showed an acceptable level of agreement, however, a consistent overestimation was observed. This issue may be attributed to the pressure gradient used for estimating the coefficients since this gradient includes the effect of side-wall friction on the flow as well as the drag force exerted by the cylinder array on the flow.

The high-quality and high-resolution scalar concentration data were used to estimate both longitudinal and transverse dispersion coefficients, simultaneously measured over the same array for the first time. The estimated transverse and longitudinal dispersion coefficients were compared in detail with previously published data and relationships. The comparisons confirmed the validity and suitability of the scalar transport tool used in this thesis to be used for future studies as an alternative to traditional lab-based work. It also revealed the lack of a generic theoretical model.

By investigating the relationship between turbulent kinetic energy and longitudinal velocity, it was shown that for the two tested diameters, turbulent kinetic energy is independent of diameter and can be described as a linear function of solid volume fraction. A set of relationships was also derived that describes nondimensionalized transverse dispersion coefficients as a function of turbulent kinetic energy. By combining these two sets of relationships a single equation was suggested to predict nondimensionalized transverse dispersion coefficient based on the density of the randomly distributed cylinder arrays.

A relationship between longitudinal and transverse dispersion coefficients within randomly distributed cylinder arrays was derived by investigating their behaviour versus each other. This relationship was combined with the one suggested estimating the transverse dispersion coefficient as a function of ø to provide a single equation which describes $D_x$ as a function of ø.

Since a limited range of conditions were tested to derive the predictive equations, and more specifically since only two cylinder diameters were investigated, it is suggested that these equations be tested and improved for a wider range of conditions. However, it should be mentioned that all of the previously published studies and suggested theoretical models, were based on a single cylinder diameter.

# 5 CONCLUSIONS

## 5.1 Introduction

This chapter provides a summary of the work carried out within this thesis, followed by a list of main conclusions and key outcomes. Afterwards, a number of suggestions for possible further work are outlined.

## 5.2 Summary

An introduction to the background and importance of the subject of this thesis was provided in Chapter 1. Previous approaches to investigating the vegetation-flow interactions were briefly reviewed and their main challenges and practical issues were listed. This revealed the need for a robust, efficient and accurate alternative approach and the main aims and objectives of the thesis, i.e. developing and validating a commercial, computationally low cost, CFD methodology to provide datasets of high quality and accuracy.

A detailed literature review was provided in Chapter 2, which introduced the main concepts and processes involved in mixing. It covered advection, diffusion and dispersion in laminar and turbulent flows followed by reviewing classic textbooks and papers on flow past cylinders. Laboratory studies on flow and mixing within cylinder arrays were reviewed and their practical issues and shortcomings were revealed. A brief introduction on flow equations and turbulence models was provided in the next section which was followed by a review of CFD studies on flow and mixing within cylinder arrays. Shortcomings of the previous approaches such as being computationally expensive and not being suitable to be used as an alternative for laboratory setups were discussed, which led to the need for a new CFD methodology. The Reynolds Stress Model (RSM) available in ANSYS FLUENT was suggested to be used as the main tool, based on its advantages over other turbulence models.

A set of preliminary studies was presented in Chapter 3, which resulted in defining the methodology used to produce the result of this thesis. The main preliminary studies included validation of the general methodology, sensitivity analysis on the injection point location, a comparison of two meshing methods, estimation of advective length, and the minimum required mixing length to provide the desired accuracy. This was based on a unique investigation on the behaviour of longitudinal and transverse dispersion coefficients, undertaken for the first time, and included estimation of both transverse and longitudinal dispersion coefficients for all the possible reaches with a minimum length of 0.05 m along a 2.0 m long channel.

The methodology developed in Chapter 3 was employed in Chapter 4 to build a new data set, which contributed to a better understanding of flow and mixing conditions within randomly distributed cylinder arrays. A rich and high-resolution flow and turbulence dataset was produced that was confirmed to be accurate by comparing it with previously published laboratory data. This dataset has the potential to be used for more investigation on turbulence features of flow within cylinder arrays in future studies.

The scalar transport data was used to estimate longitudinal and transverse dispersion coefficients simultaneously over the same cylinder array for the first time. The effect of density, diameter and Reynolds number was investigated on each set of coefficients. Drag coefficients estimated in this thesis were compared with previously published values, and a general agreement was observed. A relationship was suggested for estimating drag coefficient based on density and Reynolds number. The behaviour of turbulent kinetic energy for different array densities was investigated and a set of linear equations was suggested to predict turbulent kinetic energy based on the mean longitudinal velocity within the arrays.

A detailed comparison between transverse and longitudinal dispersion coefficients estimated in this thesis and all the previously published laboratory studies was presented. This provided a convincing set of evidence that justifies the used of the CFD model and developed methodology as an alternative to traditional lab-based studies. Investigating the behaviour of transverse dispersion coefficient against turbulent kinetic energy in combination with the set of linear equations suggested for describing turbulent kinetic energy based on array density, led to a suggestion for predicating nondimensionalized transverse dispersion coefficient as a function of array density. This model was shown to provide similar results to those from the most comprehensive available model in the literature.

The relationship between longitudinal and transverse dispersion coefficients was investigated for the first time. A linear relationship between $D_x$ and $D_y$ was observed and an equation predicating $D_x$ as a function of $D_y$ was suggested, which was combined with the equation suggested for predicting $D_y$ based on array density and a similar equation was suggested for predicting $D_x$ as a function of array density.

In brief, a CFD methodology was developed that was employed to provide a new set of data with the advantage of covering a high range of densities, three Reynolds numbers and two diameters. The results were compared with previously published laboratory data and showed a very convincing set of evidence that confirmed the validity and suitability of the CFD methodology. This methodology, therefore, is suggested to be used in future studies and to provide datasets of a similar level of accuracy as those observed in laboratory studies.

## 5.3 Main Conclusions and key outcomes

For the sake of brevity, the main conclusions and key outcomes of this thesis are presented as a list here, detailed explanation of each can be found in the discussion and conclusion section of each chapter.

**Chapter 2**

- The available literature on mixing within randomly distributed cylinder arrays is mostly limited to a single diameter and a limited range of array densities and Reynolds numbers. Therefore, new datasets are needed to expand the available dataset for a wider ranges of densities, flow conditions and cylinder diameters.
- Due to practical issues, some of the key leading laboratory studies are based on data collected from very short channels which are not checked to provide the required advective zone length and minimum mixing length.
- A comprehensive comparison between the available data and suggested predictive models is needed to lead to developing a generic predictive model describing mixing coefficients based on the array characteristics.
- There are numerous CFD studies that have used 3D LES to model flow past one single or a few cylinders, but this approach is extremely computationally expensive and cannot be used as an alternative to laboratory setups.

- No study has aimed to model a full-scale channel with a large number of cylinders comparable with the laboratory setups. Also, no study has reproduced the laboratory scalar transport experiments. To establish a CFD setup with the capacity of providing similar datasets to the laboratory ones, these two items should be tested and validated employing an industrially acceptable turbulence model and computational resources.

**Chapter 3**

- A combination of the RSM model available in ANSYS FLUENT and scalar transport modelling was employed to model flow and mixing within randomly distributed cylinder arrays as 2D geometries and was generally validated through comparison with a previously published laboratory dataset.
- A low sensitivity of both $D_x$ and $D_y$ to the location of the injection point was observed and thus, no specific limitation for the relative location of the injection point was suggested.
- Two different meshing methods were compared, one requiring around 24 hours and the other around only 2 hours to be built. Detailed velocity profiles and scalar transport results comparison between these two meshing methods showed no significant difference. Thus, the more efficient meshing method was selected to be used for future models.
- The length of the advective zone, i.e. the reach over which advection dominates dispersion, was estimated to be 0.75 m. This means the Fickian model of dispersion is valid downstream of this point and using the concentration profiles upstream of this point to estimate dispersion coefficients will affect the accuracy of the estimations. Thus, it was concluded that the channels to be modelled in the subsequent chapter must be long enough to allow the recording of concentration profiles after the advective zone.
- The minimum required reach length, i.e. the minimum distance required between the upstream and downstream concentration profiles, was suggested to be 0.90 m. This was based on accepting ±5% deviation from the value estimated for the longest reach, i.e. between $x = 0.75$ m and $x = 2.00$ m

- The concentration was suggested to be recorded after $x = 0.75$ m and over reaches with a minimum length of 0.90 m in future models.

**Chapter 4**

- A new dataset of flow and dispersion coefficients for random cylinder arrays of $d = 0.0064$ m and $d = 0.0080$m forming densities of $ø = 0.025$, 0.050, 0.075, 0.100, 0.200 and 0.350 at $Re_d = 100$, 200 and 300 was produced and presented in this chapter, using the methodology developed in Chapter 3.
- The tested geometries are advantageous over previously tested geometries both in laboratory and CFD studies, as they cover a wider and longer array that was selected to provide the desired accuracy, based on the preliminary studies presented in Chapter 3.
- A very high-resolution (with a maximum cell size of 0.001 m) flow and turbulence data set was presented. This dataset provides a better understanding of the flow and turbulence condition within random cylinder arrays.
- A detailed comparison between velocities, turbulence features, and mixing coefficients, resulting from this thesis and previously published laboratory measurements confirmed the accuracy of the dataset and justified the use of the CFD tool for future studies as an alternative to traditional lab-based work.
- Investigating turbulence features provided evidence for previously suggested theories such as the transition in turbulence characteristic length.
- The explanatory power the predictor power of our data might be even more than what was presented in this chapter and future investigation on turbulence features within randomly distributed cylinder arrays is suggested using the rich, high-resolution, high-accuracy velocity and turbulence dataset, produced in this thesis.
- A new relationship was suggested to predict the drag coefficient as a function of cylinder diameter and array density.
- A new relationship was suggested to predict turbulence intensity as a function of array density, Eq. 4-2. This relationship was independent of the diameter for the two tested dimeters, previously no evidence has been given that it is independent of the diameter.

- A new relationship was suggested to predict nondimensionalized transverse dispersion coefficient as a function of turbulence intensity, Eq. 4-4, this relationship was also independent of the diameter for the two tested diameters, and previously no evidence has been given that it is independent of the diameter.
- Combining these two relationships, i.e. Eq. 4-2, and Eq. 4-4, a single relationship was suggested to predict nondimensionalized transverse dispersion coefficient as a function of array density, Eq. 4-5.
- The relationship between longitudinal and transverse dispersion coefficients in cylinder arrays was investigated for the first time.
- A new relationship was suggested to predict longitudinal dispersion coefficient as a linear function of the transverse dispersion coefficient, Eq. 4-6.
- Combining Eq. 4-5 and Eq. 4-6, a new relationship was suggested to predict longitudinal dispersion coefficient as a function of array density.
- The suggested equations in this chapter are based on a limited range of conditions and should to be tested and improved for a wider range of conditions, specifically for other cylinder diameters. However all previously published theoretical models have been based on only one single cylinder diameter, and in most of the cases a limited range of Reynolds number and array density.
- This chapter provided a comprehensive set of comparisons between all the available data on dispersion coefficients within randomly distributed cylinder arrays.

# 6 REFERENCES

Afgan, I., Kahil, Y., Benhamadouche, S. and Sagaut, P., 2011. Large eddy simulation of the flow around single and two side-by-side cylinders at subcritical Reynolds numbers. *Physics of Fluids*, *23*(7), p.075101.

Akilli, H., Sahin, B. and Tumen, N.F., 2005. Suppression of vortex shedding of circular cylinder in shallow water by a splitter plate. Flow Measurement and Instrumentation, 16(4), pp.211-219.

ANSYS, Inc. 2016, ANSYS Fluent® Academic Research, Release 16.1

ANSYS, Inc. 2017, ANSYS Fluent® Academic Research, Release 17.1

ANSYS, Inc. 2018, ANSYS Fluent® Academic Research, Release 18.2

Arnold, U.; Hottges, J.; Rouv, G. 1989.Turbulence and mixing mechanisms in compound open channel flow/Arnold, Uwe; Höttges, Jörg; Rouvé, Gerhard.

Bearman, P.W., 2011. Circular cylinder wakes and vortex-induced vibrations. Journal of Fluids and Structures, 27(5-6), pp.648-658.

Boxall, J. B. and Guymer, I. ‘Longitudinal Dispersion in an Extreme Meander Channel with Changes in Shape’, River Flow 2004, vol. 2, Editors Greco, Carravetta & Della Morte. Naples, Italy, June 23-25, 2004.

Britannica, R.E., Encyclopaedia Britannica.

Chang, K. and Constantinescu, G., 2015. Numerical investigation of flow and turbulence structure through and around a circular array of rigid cylinders. Journal of Fluid Mechanics, 776, pp.161-199.

da Silva, B.L., Luciano, R.D., Utzig, J. and Meier, H.F., 2018. Flow patterns and turbulence effects in large cylinder arrays. International Journal of Heat and Fluid Flow, 69, pp.136-149.

Duan, J. & Wiggins, S. 1997 Lagrangian transport and chaos in the near wake of the flow around an obstacle: a numerical implementation of lobe dynamics. Nonlinear Processes Geophy. 4,125–136.

Elder, J.W., 1959. The dispersion of marked fluid in turbulent shear flow. Journal of Fluid Mechanics, 5(4), pp.544-560.

Elghanduri, N.E., 2015. CFD Tracer Tracking within and over a Permeable Bed I: Detail Analysis. American Journal of Environmental Engineering, 5(3), pp.58-71.

Etminan, V., Lowe, R.J. and Ghisalberti, M., 2017. A new model for predicting the drag exerted by vegetation canopies. Water Resources Research, 53(4), pp.3179-3196.

Fischer, H. B., J. E. List, C. R. Koh, J. Imberger, and N. H. Brooks (1979), Mixing in Inland and Coastal Waters, Elsevier., San Diego, Calif

GAMBI, M., A. NOWELL, AND I. JUMARS. 1990. Flume observations on flow dynamics in Zostera marina (eelgrass) beds. Mar. Ecol. Prog. Ser. 61: 159-I 69. GERRARD, G. H. 1978. The

Gao, D.L., Chen, W.L., Li, H. and Hu, H., 2017. Flow around a circular cylinder with slit. Experimental Thermal and Fluid Science, 82, pp.287-301.

Golzar, M., Sonnenwald, F., Guymer, I. and Stovin, V , 2017, Transverse Mixing Coefficient in Random Cylinder Arrays –A CFD Validation Study” the 37th IAHR World Congress, 13-18 August 2017, Kuala Lumpur, Malaysia

Golzar, M., Sonnenwald, F., Guymer, I. and Stovin, V., 2018. A CFD based comparison of mixing due to regular and random cylinder arrays. In Free Surface Flows and Transport Processes (pp. 195-205). Springer, Cham.

Gualtieri, C., Angeloudis, A., Bombardelli, F., Jha, S. and Stoesser, T., 2017. On the values for the turbulent Schmidt number in environmental flows. Fluids, 2(2), p.17.

Huai, W.X., Wu, Z.L., Qian, Z.D. and Geng, C., 2011. Large eddy simulation of open channel flows with non-submerged vegetation. Journal of Hydrodynamics, 23(2), pp.258-264

Huang, Y. H., J. E. Saiers, J. W. Harvey, G. B. Noe, and S. Mylon (2008), Advection, dispersion, and filtration of fine particles within emergent vegetation of the Florida everglades, Water Resour.

J. K. Ostanek, Flowfield Interactions in Low Aspect Ratio Pin-Fin Arrays, Ph.D. thesis, Penn State University,2012.

Jakirlić, S. and Maduta, R., 2016. Sensitized-RANS Modelling of Turbulence: Resolving Turbulence Unsteadiness by a (Near-Wall) Reynolds Stress Model. In Progress in Wall Turbulence 2 (pp. 17-35). Springer, Cham.

Kamath, A., Chella, M.A., Bihs, H. and Arntsen, Ø.A., 2015. CFD investigations of wave interaction with a pair of large tandem cylinders. Ocean Engineering, 108, pp.738-748.

Kitagawa, T. and Ohta, H., 2008. Numerical investigation on flow around circular cylinders in tandem arrangement at a subcritical Reynolds number. Journal of Fluids and Structures, 24(5), pp.680-699.

Lam, K. and Lo, S.C., 1992. A visualization study of cross-flow around four cylinders in a square configuration. Journal of fluids and structures, 6(1), pp.109-131.

Launder, B.E. & Spalding, D.B. (1974). “The numerical computation of turbulent flows”, Computer methods in applied mechanics and engineering, 3(2), 269-289.

Levenspiel, O., 1958. Longitudinal mixing of fluids flowing in circular pipes. Industrial & Engineering Chemistry, 50(3), pp.343-346.

Li, W., Ren, J., Hongde, J., Luan, Y. and Ligrani, P., 2016. Assessment of six turbulence models for modeling and predicting narrow passage flows, part 2: Pin fin arrays. Numerical Heat Transfer, Part A: Applications, 69(5), pp.445-463.

Liu, D., Diplas, P., Fairbanks, J.D. and Hodges, C.C., 2008. An experimental study of flow through rigid vegetation. Journal of Geophysical Research: Earth Surface, 113(F4).

Liu, D., Diplas, P., Fairbanks, J.D. and Hodges, C.C., 2008. An experimental study of flow through rigid vegetation. Journal of Geophysical Research: Earth Surface, 113(F4).

Maduta, R., Ullrich, M. and Jakirlic, S., 2017. Reynolds stress modelling of wake interference of two cylinders in tandem: Conventional vs. eddy-resolving closure. International Journal of Heat and Fluid Flow, 67, pp.139-148.

Nepf, H., J. Sullivan, and R. Zavistoski (1997b), A model for diffusion within emergent vegetation, Limnol. Oceanogr., 42(8), 1735–1745

Nepf, H.M., 1999. Drag, turbulence, and diffusion in flow through emergent vegetation. Water resources research, 35(2), pp.479-489.

Nepf, H.M., Mugnier, C.G. and Zavistoski, R.A., (1997a). The effects of vegetation on longitudinal dispersion. Estuarine, Coastal and Shelf Science, 44(6), pp.675-684.

Ostanek, J. K., & Thole, K. A. (2012). Wake development in staggered short cylinder arrays within a channel. DOI: 10.1007/s00348-012-1313-5

Palkin, E., Hadžiabdić, M. and Hanjalić, K., 2016, October. High-frequency rotary oscillations control of flow around cylinder at Re= 1.4× 105. In Journal of Physics: Conference Series (Vol. 754, No. 6, p. 062006). IOP Publishing.

Parrondo, J., de Pedro, B., Fernández-Oro, J. and Blanco-Marigorta, E., 2018. A CFD study on the fluctuating flow field across a parallel triangular array with one tube oscillating transversely. Journal of Fluids and Structures, 76, pp.411-430.

Paul, P.H., Rehm, J.E. and Arnold, D.W., Eksigent Technologies LLC, 2008. Precision flow control system. U.S. Patent 7,465,382.

Paul, S.S., Ormiston, S.J. and Tachie, M.F., 2008. Experimental and numerical investigation of turbulent cross-flow in a staggered tube bundle. International Journal of Heat and Fluid Flow, 29(2), pp.387-414.

Pinar, E., Ozkan, G.M., Durhasan, T., Aksoy, M.M., Akilli, H. and Sahin, B., 2015. Flow structure around perforated cylinders in shallow water. Journal of Fluids and Structures, 55, pp.52-63

Price, S.J., Sumner, D., Smith, J.G., Leong, K. and Paidoussis, M.P., 2002. Flow visualization around a circular cylinder near to a plane wall. Journal of Fluids and Structures, 16(2), pp.175-191.

Rayleigh, L., 1896. L. Theoretical considerations respecting the separation of gases by diffusion and similar processes. The London, Edinburgh, and Dublin Philosophical Magazine and Journal of Science, 42(259), pp.493-498.

Ricardo, A.M., Grigoriadis, D.G. and Ferreira, R.M., 2018. Numerical simulations of turbulent flows within an infinite array of randomly placed cylinders. Journal of Fluids and Structures, 80, pp.245-261.

Roache, P.J., 1998. Verification of codes and calculations. AIAA journal, 36(5), pp.696-702.

Rodríguez, I., Lehmkuhl, O., Chiva, J., Borrell, R. and Oliva, A., 2015. On the flow past a circular cylinder from critical to super-critical Reynolds numbers: Wake topology and vortex shedding. International Journal of Heat and Fluid Flow, 55, pp.91-103.

Rutherford, J.C., 1994. River mixing. John Wiley & Son Ltd.

Rutherford, J.C., 1994. River mixing. John Wiley &amp; Son Ltd.

Sagaut, P., 2006. Large eddy simulation for incompressible flows: an introduction. Springer Science & Business Media.

Saggiori S (2010) CFD Modelling of Solute Transport in Vegetated Flow. Master’s thesis, University of Sheffield, Sheffield, UK.

Serra, T., H. J. Fernando, and R. V. Rodr————————ıguez (2004), Effects of emergent vegetation on lateral diffusion in wetlands, Water Res., 38(1), 139–147.

Shilton, A. (2000), Potential application of computational fluid dynamics to pond design, Water Sci. Technol., 42(10), 327–334.

Shucksmith, J., Boxall, J. and Guymer, I., 2007. Importance of advective zone in longitudinal mixing experiments. Acta Geophysica, 55(1), pp.95-103.

Shucksmith, J., J. Boxall, and I. Guymer (2010), Effects of emergent and submerged natural vegetation on longitudinal mixing in open channel flow, Water Resour. Res., 46, W04504, doi:10.1029/2008WR007657.

Shukla, N. and Henthorn, K.H., 2009. Effect of relative particle size on large particle detachment from a microchannel. Microfluidics and nanofluidics, 6(4), pp.521-527.

Solaimani, N., Amini, A., Banejad, H. and Taherei Ghazvinei, P., 2017. The effect of pile spacing and arrangement on bed formation and scour hole dimensions in pile groups. International Journal of River Basin Management, 15(2), pp.219-225.

Sonnenwald F, Stovin V and Guymer I (2016) Feasibility of the porous zone approach to modelling vegetation in CFD. In Hydrodynamic and Mass Transport at Freshwater Aquatic Interfaces (Rowiń ski P and Marion A (eds)). Springer, Cham, Switzerland, pp. 63–75.

Sonnenwald, F., J. R. Hart, P. West, V. R. Stovin, and I. Guymer (2017), Transverse and longitudinal mixing in real emergent vegetation at low velocities, Water Resour. Res., 53, doi:10.1002/2016WR019937.

Stoesser, T., Kim, S.J. and Diplas, P., 2010. Turbulent flow through idealized emergent vegetation. Journal of Hydraulic Engineering, 136(12), pp.1003-1017.

Sumner, D., 2010. Two circular cylinders in cross-flow: a review. Journal of Fluids and Structures, 26(6), pp.849-899.

Sumner, D., Price, S.J. and Paidoussis, M.P., 2000. Flow-pattern identification for two staggered circular cylinders in cross-flow. Journal of Fluid Mechanics, 411, pp.263-303.

Tanino, Y. and Nepf, H.M., 2008a. Laboratory investigation of mean drag in a random array of rigid, emergent cylinders. Journal of Hydraulic Engineering, 134(1), pp.34-41.

Tanino, Y. and Nepf, H.M., 2008b. Laboratory investigation of lateral dispersion within dense arrays of randomly distributed cylinders at transitional Reynolds number. Physics of Fluids, 21(4), p.046603.

Tanino, Y., 2008. Flow and solute transport in random cylinder arrays: a model for emergent aquatic plant canopies (Doctoral dissertation, Massachusetts Institute of Technology).

Taylor, G.I., 1921. Experiments with rotating fluids. Proc. R. Soc. Lond. A, 100(703), pp.114-121.

Taylor, G.I., 1953. Dispersion of soluble matter in solvent flowing slowly through a tube. Proc. R. Soc. Lond. A, 219(1137), pp.186-203.

Taylor, G.I., 1954. The dispersion of matter in turbulent flow through a pipe. Proc. R. Soc. Lond. A, 223(1155), pp.446-468.

Tennekes, H., and Lumley, J.L., 1972. A first course in turbulence. MIT press.

Tsavdaris A, Mitchell S and Williams JB (2014) Computational fluid dynamics modelling of different detention pond configurations in the interest of sustainable flow regimes and gravity sedimentation potential. Water and Environment Journal 29(1): 129–139

Van Dyke, M., An album of fluid motion,(1982). Parabolic, Palo Alto (Calif.). Versteeg, H.K. and Malalasekera, W., 2007. An introduction to computational fluid dynamics: the finite volume method. Pearson Education.

Wadzuk, B. M., and E. Burke (2006), A diffusion model for low Reynolds number flows through a constructed stormwater wetland, in Proceedings of the 7th International Conference on HydroScience and Engineering, Philadelphia, Pa.

Wang, X.K., Gong, K., Liu, H., Zhang, J.X. and Tan, S.K., 2013. Flow around four cylinders arranged in a square configuration. Journal of Fluids and Structures, 43, pp.179-199.

Webel, G. and Schatzmann, M., 1984. Transverse mixing in open channel flow. Journal of Hydraulic Engineering, 110(4), pp.423-435.

Weihong Li, Jing Ren, Jiang Hongde, Yigang Luan & Phillip Ligrani (2016) Assessment of six turbulence models for modeling and predicting narrow passage flows, part 2: Pin fin arrays, Numerical Heat Transfer, Part A: Applications, 69:5, 445-463

White, B.L. and Nepf, H.M., (2003). Scalar transport in random cylinder arrays at moderate Reynolds number. Journal of Fluid Mechanics, 487, pp.43-79

Yayla, S. and Teksin, S., (2018). Flow measurement around a cylindrical body by attaching flexible plate: A PIV approach. Flow Measurement and Instrumentation, 62, pp.56-65.

Zdravkovich, M.M., 1997. Flow around circular cylinders. Fundamentals, vol. 1. Oxford University Press, New York, 3, pp.133-198.

Zdravkovich, M.M., 1997. Flow around Circular Cylinders: Volume 2: Applications (Vol. 2). Oxford university press.

# 7 APPENDICES

# APPENDIX A, COMPUTER CODES

## MATLAB code for generating randomly distributed cylinder array geometries

The original code has been written for a general condition and can be used to build geometries with different sections, each section including a separate distribution of cylinders

```
%
% This script is for generating random cylinder patterns to represent
% vegetation, i.e., for generating patterns of artificial vegetation.
It is
% designed to produce either CSV output, e.g., for a CNC machine or
output
% for Ansys DesignModeler. This script is capable of generating
multiple
% 'plates' of vegetation of a given sizes. This is not needed for CFD.
%
% There are several configuration settings at the start of this file.
It is
% not recommended to change the code that occurs after this. The end
of the
% configuration section is clearly marked.

% Reset the workspace
clear
%clc

for count=2%:10

% Re-load results from a previous run? If blank, no, otherwise load
the
% given .mat file to restore a previous workspace and skip generating
stem
% patterns, useful for re-plotting, etc..
loadfile = '';
% loadfile = 'plate_final.mat';

% Output workspace to a MAT file
matoutput = '';
% matoutput = sprintf('test_%i.mat', count);
matoutput = sprintf('phi=0.025 d=0.008', count);
% Output stem information as a CSV file
csvoutput = '';
 csvoutput = 'phi=0.025 d=0.008.csv';

% Output stems to a JavaScript file for import into Ansys
DesignModeler
cfdoutput = '';
 cfdoutput = 'phi=0.025 d=0.008';

% In the plot, label each plate
platelabel = 0;
% platelabel = 1;

% Plot histogram of stem diamter and spacing statistics
dohist = 0;
```

```
% dohist = 1; % plot both
% dohist = 2; % plot stem diamter distribution only
% dohist = 3; % plot stem spacing distribution only

% How many plates to design. For CFD work this should be 1
numplates = 1;
% numplates = 3;

% Size of the vegetation plates. For CFD this is the size of the
vegetated
% area.
% xmax = 0.6;
% ymax = 0.2;
% xmax = 1.2;
% ymax = 0.6;
xmax = 2.2;
ymax = 0.7;

% Do not place stems closer than this to the edge of the plate. This
% probably will not need to be changed
% xedgeexclusion = 0.005; % (longitudinal)
% yedgeexclusion = 0.005; % (transverse)
% xedgeexclusion = 0;
% yedgeexclusion = 0;
% xedgeexclusion = 0.001;
% yedgeexclusion = 0.001;
xedgeexclusion = 0.005;
yedgeexclusion = 0.002;

% Desired solid volume fraction
% targetphi = 0.005; % (low-density artificial vegetation)
% targetphi = 0.02; % (high-density artificial vegetation)
% targetphi = 0.05;
% targetphi = 0.1;
% targetphi = 0.2;
targetphi = 0.025;
% targetphi = 0.4;

% Stem diameters to use for the artificial vegetation, in meters
% drange = [4 8 12 15 20]/1000; % use 5 different stem diameters
drange = 8/1000; % use a single stem diameter
% Relative frequency of each stem diameter, this array must match
drange in dimension!
% ddist = [ 2 4 2 1 1 ]; % the first stem appears 2 out of 10 times,
etc.
ddist = 1; % the single stem appears all of the time

% Multiple of d to nearest stem lower limit (e.g. 1d, 2d, etc.,
between
% stems). Note that stem holes are already excluded, so this is
addition to
% that.
% dspace = 0;
% dspace = 1;
% dspace = 2;
% dspace = 0.5;
% dspace = 0.001/drange; % ensure 1 mm spacing
% dspace = 0.0005/drange;
dspace = 0.0002/drange;
% dspace = 0.0001/drange;

% Should stem positions be fixed to a grid of holes?
gridres = 0; % No
```

```
% gridres = 0.005; % Every 5 mm
% gridres = 0.01; % Every 1 cm


% exclude a location for dye injection
% exclusionx = 0.05;
% exclusiony = 0.15;
% exclusiond = 0.01; % exclusion zone diameter
% exclusiond = drange;

exclusiony = 0.4:0.02:(ymax-0.4);
% exclusiony = [0.10];
exclusionx = ones(size(exclusiony))*0.10;
exclusiond = ones(size(exclusiony))*drange;


%%%%%%%%%%%%%%%%%%%%%%%%%%%%%%%%%%%%%%%%
%%%%     CONFIGURATION ENDS HERE    %%%%
%%%% DO NOT CHANGE BELOW THIS POINT %%%%
%%%%%%%%%%%%%%%%%%%%%%%%%%%%%%%%%%%%%%%%

% number of stems per .js file for workbench
perfile = 1500;

% cumulative distribution of stem diameters
ddistc = cumsum(ddist)/sum(ddist);
% radius of stems
r = drange ./ 2;

% a circle for plotting the stems
ang = 0:(pi/12):2*pi;
cang = cos(ang);
sang = sin(ang);
xp=cang'*r;
yp=sang'*r;


% store all output in this matrix
output = cell(1, numplates);

% estimate number of stems/plate
m = round(xmax*ymax*targetphi/(pi*mean(drange)^2/4));

% set up plotting
colors = colormap('lines');
figure(1)
clf
hold on

% generate the distribution of stems
if length(loadfile) == 0
    fprintf('Calculating')
    for ii=1:numplates % generate for each plate

        % plug injection exclusion
%         line((ii-1)*xmax+exclusionx+cos(ang)'.*(exclusiond/2),
exclusiony+sin(ang)'.*(exclusiond/2), 'Color', [1 0 0])
        caed = cos(ang)'*(exclusiond/2);
        saed = sin(ang)'*(exclusiond/2);
        line(repmat((ii-1)*xmax+exclusionx, size(caed, 1), 1)+caed,
repmat(exclusiony, size(saed, 1), 1)+saed, 'Color', [1 0 0])

        % array storing stem information for this plate
```

```
        % index 1 - x-coordinate
        % index 2 - y-coordinate
        % index 3 - stem diameter index
        % index 4 - minimum distance to nearest stem index
        % index 5 - nearest stem
        % index 6 - plate number
        stems = zeros(0,6);

        phi = 0; % the current solid volume fraction
        fails = 0; % the ammount of times a stem could not be placed
        while phi < targetphi % add more stems until the target phi is
reached
            di = find(rand() < ddistc, 1); % randomly pick a stem size
            si = find(rand() < ddistc, 1); % randomly pick a minimum
spacing bewteen stems

            numtries = 0;
            dist = -inf;
            while dist < 0 && numtries < 500
                % pick a stem location
                x = rand() * xmax;
                y = rand() * ymax;
                if gridres ~= 0
                    x = round(x / gridres) * gridres;
                    y = round(y / gridres) * gridres;
                end

                % get the stems from all panels
                ss = size(stems,1);
                for kk=1:ii-1
                    ss = ss + size(output{kk},1);
                end
                distl = zeros(ss+4,1); % the distance from this stem
to all others
                if size(stems,1) > 0
                    distl(1:size(stems,1)) = sqrt((stems(:,1)-x).^2 +
(stems(:,2)-y).^2) - reshape(r(stems(:,3)),length(stems(:,3)),1) -
r(di) - drange(si)*dspace;
                end
                % the distance from this stem to the edge of the
plates
                distl(size(stems,1)+1) = sqrt((0-x).^2) - r(di) -
xedgeexclusion;
                distl(size(stems,1)+2) = sqrt((0-y).^2) - r(di) -
yedgeexclusion;
                distl(size(stems,1)+3) = sqrt((xmax-x).^2) - r(di) -
xedgeexclusion;
                distl(size(stems,1)+4) = sqrt((ymax-y).^2) - r(di) -
yedgeexclusion;

                % take into account the edges of adjacent panels
                at = size(stems,1)+4+1;
                for kk=1:ii-1
                    distl(at:(at+size(output{kk},1)-1)) =
sqrt(((output{kk}(:,1)+(kk-1)*xmax)-(x+(ii-1)*xmax)).^2 +
(output{kk}(:,2)-y).^2) -
reshape(r(output{kk}(:,3)),length(output{kk}(:,3)),1) - r(di) -
drange(si)*dspace;
                    at = at + size(output{kk},1);
                end

                % the closest stem to this one if it is too close we
try
```

```
                % this all again
                dist = min(distl);

                % check for injection exclusion
                disti = sqrt((exclusionx-x).^2 + (exclusiony-y).^2) -
r(di) - exclusiond./2 - drange(si)*dspace;
                if min(disti) < dist
                    dist = min(disti);
                end

                numtries = numtries + 1;
            end

            if numtries < 500 % we successfully placed the stem so add
it to the array
                stems(end+1,1) = x; %#ok<SAGROW>
                stems(end,2) = y;
                stems(end,3) = di;
                stems(end,4) = si;
                stems(end,5) = dist;
                stems(end,6) = ii;

                % plot the stem
                fill((ii-1)*xmax+x+xp(:,di), y+yp(:,di), colors(di,:),
'EdgeColor', 'none')

                % re-calculate phi
                phi = sum(drange(stems(:,3)).^2*pi/4)/(xmax*ymax);
                if mod(size(stems,1), round(m/10)) == 0
                    % update the progress indicator and plot
                    fprintf('.')
                    drawnow
                end
            else % we could not place the stem
                fails = fails + 1;
                if fails == 10 % if we couldn't place the stem a lot
of times, it's a problem
                    error('Un-able to create the required plate, the
density is likely too high...')
                end
            end
        end

        % store the configuration for this plate in the array of all
plates
        output{ii} = stems;
        drawnow

    end
else
    fprintf('Reading in from file...\nNote that this the currently
specified solid volume fraction, etc.\n')
    t1 = csvoutput;
    t1b = cfdoutput;
    t1c = matoutput;
    t2 = dohist;
    t3 = platelabel;
    load(loadfile);
    % Plot the loaded data
    for ii=1:numplates
        for jj=1:size(output{ii},1)
```

```
            fill((ii-1)*xmax+output{ii}(jj,1)+xp(:,output{ii}(jj,3)),
output{ii}(jj,2)+yp(:,output{ii}(jj,3)), colors(output{ii}(jj,3),:),
'EdgeColor', 'none')
        end
    end
    csvoutput = t1;
    cfdoutput = t1b;
    matoutput = t1c;
    dohist = t2;
    platelabel = t3;
end



% Calculate the distance to closest stem for all stems
for ii=1:numplates
    oi = ii-1:ii+1;
    oi = oi(oi > 0 & oi <= length(output));
    stems = vertcat(output{oi}); % neighbouring plates
    stems(:,1) = stems(:,1) + (stems(:,6)-1) * xmax;
    for jj=1:size(output{ii},1)
        distl = zeros(size(stems,1)+2,1);
        % copied from above, distance from current stem to every other
        distl(1:size(stems,1)) = sqrt((stems(:,1)-(output{ii}(jj,1) +
(output{ii}(jj,6)-1) * xmax)).^2 + (stems(:,2)-output{ii}(jj,2)).^2) -
reshape(r(stems(:,3)),length(stems(:,3)),1) - r(output{ii}(jj,3));
        % gaps to channel walls
        distl(size(stems,1)+1) = sqrt((0-output{ii}(jj,2)).^2) -
r(output{ii}(jj,3));
        distl(size(stems,1)+2) = sqrt((ymax-output{ii}(jj,2)).^2) -
r(output{ii}(jj,3));

        output{ii}(jj,5) = min(distl(distl >= 0));
    end
end

% Mean statistics
allstems = vertcat(output{:});
d = mean(drange(allstems(:,3)));
s = std(drange(allstems(:,3)));
d2 = mean(allstems(:,5));
s2 = std(allstems(:,5));
a = sum(drange(allstems(:,3)))/(xmax*ymax*numplates);

fprintf('\n')

% draw the line sperating plates
for ii=2:numplates
    h = line([1 1]*(ii-1)*xmax, [0 ymax]);
    set(h, 'Color', [0.7 0.7 0.7])
end

% tidy up the plot
hold off
axis image
xlim([0 xmax*numplates])
ylim([0 ymax])
box on
% plate numbers
if platelabel == 1
    for ii=1:numplates
        text((ii-1)*xmax+xmax*0.01,ymax,sprintf('Plate
%i',ii),'HorizontalAlignment','left','VerticalAlignment','top')
```

```
    end
end
% xtickformat('%0.1f')
% ytickformat('%0.2f')


% plot histograms if requested
if dohist > 0
    figure(2)
    clf
    if dohist == 1 || dohist == 2
        % histogram of stem diameters
        if dohist == 1
            subplot(2,1,1)
        end
        h = hist(allstems(:,3), 1:length(ddist));
        h = bar([h./length(allstems); ddist./sum(ddist)]', 1);
        set(h(1), 'FaceColor', [1 1 1])
        if length(h) == 2
            set(h(2), 'FaceColor', [0.9 0.9 0.9])
        end
        xlim([0.25 length(ddist)+0.75])
        ylabel('Fraction of stems')
        title(sprintf('Distribution of stem diameters d=%0.3f\\pm%0.3f
m', d, s))
        % labels for x tick marks
        labels = cell(size(drange));
        for ii=1:length(labels)
            labels{ii} = sprintf('%0.3f', drange(ii));
        end
        set(gca, 'XTickLabel', labels)
        legend('Random Distribution', 'Target Distribution')
        xlabel('Stem size (m)')
        ytickformat('%0.1f')
    end

    if dohist == 1 || dohist == 3
        % histogram of stem spacings (edge to edge)
        if dohist == 1
            subplot(2,1,2)
        end
        [h, n] = hist(allstems(:,5),60);
        h = bar(n, h./sum(h), 1);
        set(h, 'FaceColor', [1 1 1])
        title(sprintf('Distribution of distance to nearest stem
s=%0.3f\\pm%0.3f m', d2, s2))
        xlabel('(m)')
        ylabel('Fraction of stems')
        xtickformat('%0.3f')
        ytickformat('%0.2f')
    end
end


figure(1)
xlabel('Longitudinal position (m)')
ylabel('Transverse position (m)')

title(sprintf('\\phi=%0.2f, a=%0.2f m^{-1}d=%0.3f m, sn=%0.6f m,
d/sn=%0.6f', targetphi, a, d, d2,d/d2))
% set(gcf, 'Renderer', 'painters')
% print('-dsvg', sprintf('test.svg'))
```

```
phi = sum(drange(allstems(:,3)).^2*pi/4)/(xmax*ymax*numplates);


%% information in the console
fprintf('phi: %0.3f (actual: %0.3f)\n', targetphi, phi)
fprintf('mean stem diameter: %0.3f m\n', d)
fprintf('standard deviation: %0.3f m\n', s)
fprintf('mean stem spacing, %0.3f m\n', d2);
fprintf('standard deviation, %0.3f m\n', s2);
fprintf('frontal facing area: %0.2f m\n', a)
fprintf('a from phi d: %0.2f m\n', targetphi / (d * pi / 4))

fprintf('d/s, %0.3f\n', d/d2);
%fprintf('d/sna, %0.3f\n', snc(phi));

%% save to a mat file if requested
if ~strcmp(matoutput, '')
    fprintf('Writing MAT output...\n');
    if exist(matoutput, 'file') ~= 0
        warning('Overwriting existing file %s! Waiting 5 seconds...',
csvoutput)
        pause(5)
        fprintf('Overwriting existing file...\n')
    end
    save(matoutput)
end

% do csv output
if ~strcmp(csvoutput, '')
    fprintf('Writing CSV output...\n');
    if exist(csvoutput, 'file') ~= 0
        warning('Overwriting existing file %s! Waiting 5 seconds...',
csvoutput)
        pause(5)
        fprintf('Overwriting existing file...\n')
    end
    fid = fopen(csvoutput, 'w');
    fprintf(fid, 'phi, %0.3f, actual, %0.3f\n', targetphi, phi);
    fprintf(fid, 'mean stem diameter, %0.3f m\n', d);
    fprintf(fid, 'standard deviation, %0.3f m\n', s);
    fprintf(fid, 'mean stem spacing, %0.3f m\n', d2);
    fprintf(fid, 'standard deviation, %0.3f m\n', s2);
    fprintf(fid, 'frontal facing area, %0.2f m\n', a);
    fprintf(fid, 'a from phi d, %0.2f m\n', targetphi / (d * pi / 4));

    for i=1:numplates
        fprintf(fid, 'plate number:, %i\n', i);
        fprintf(fid, 'x (m), y (m), d (mm)\n');
        for j=1:size(output{i},1)
            fprintf(fid, '%0.3f, %0.3f, %i\n', output{i}(j,1),
output{i}(j,2), drange(output{i}(j,3))*1000);
        end
    end
    fclose(fid);
end

%% do cfd output
if ~strcmp(cfdoutput, '')
    fprintf('Writing CFD output...\n');

    nfiles = ceil(size(allstems,1)/perfile);

    for ii=1:nfiles
```

```
        cfdoutput2 = sprintf([cfdoutput '_%i.js'], count, ii);
        if exist(cfdoutput2, 'file') ~= 0
            warning('Overwriting existing file %s! Waiting 5 
seconds...', cfdoutput2)
            pause(5)
            fprintf('Overwriting existing file...\n')
        end
        fid = fopen(cfdoutput2, 'w');
        fprintf(fid, 'function stems (p)\n');
        fprintf(fid, '{\n');
        fprintf(fid, '    p.Plane  = agb.GetActivePlane();\n');
        fprintf(fid, '\n');
        fprintf(fid, '    //Sketch\n');
        fprintf(fid, '    p.Sk2 = p.Plane.NewSketch();\n');
        fprintf(fid, '    p.Sk2.Name = "stems_%i";\n', ii);
        fprintf(fid, '    p.MyStems = [];\n');
        fprintf(fid, '\n');
        fprintf(fid, '    //Edges\n');
        fprintf(fid, '    with (p.Sk2)\n');
        fprintf(fid, '    {\n');
        fprintf(fid, '        var at = 0;\n');

%          for i=1:numplates
%              for j=1:size(output{i},1)
%                  fprintf(fid, '        p.MyStems[at++] = 
Circle(%0.5f, %0.5f, %0.5f);\n', output{i}(j,1), output{i}(j,2), 
drange(output{i}(j,3))/2); % needs radius, not diameter!
%              end
%          end
        goto = min([ii*perfile size(allstems,1)]);
        for j=(ii-1)*perfile+1:goto
            fprintf(fid, '        p.MyStems[at++] = Circle(%0.5f, 
%0.5f, %0.5f);\n', allstems(j,1), allstems(j,2), 
drange(allstems(j,3))/2); % needs radius, not diameter!
        end

        fprintf(fid, '    }\n');
        fprintf(fid, '\n');
        fprintf(fid, '    return p;\n');
        fprintf(fid, '}\n');
        fprintf(fid, '\n');
        fprintf(fid, 'var ps2 = stems (new Object());\n');
        fprintf(fid, 'agb.Regen();\n');
        fprintf(fid, '\n');

        % create surface from sketch
        fprintf(fid, 'ag.selectedFeature = 
ag.gui.TreeviewFeature(ps2.Sk2.Name, 0);\n');
        fprintf(fid, 'var SSk1=ag.gui.CreateSurfSk();  // 
IAnsFSurfSk\n');
        fprintf(fid, 'SSk1.Name="stems_%i_sk";\n', ii);
        fprintf(fid, 'SSk1.Operation=ag.c.Frozen;\n');
        fprintf(fid, 'SSk1.WithPlaneNormal=ag.c.Yes;\n');
        fprintf(fid, 'agb.Regen();\n');
        fprintf(fid, '\n');

        fclose(fid);
    end
end

end % for count
```

```
filename=['d',num2str(d),'phi', num2str(targetphi),'Geometry.png'];
 %saveas(gcf, filename, 'png');
  %saveas(gcf, filename)

print('-dpng', '-r600', '0.008phi0.025.png')

  testtt=[targetphi;phi;d;s;d2;s2;a];
filename=['d',num2str(d),'phi', num2str(targetphi),'Geometry.xlsx'];
xlswrite('d=0.008phi=0.025.xlsx',testtt);
save(filename);
```

## MATLAB codes for estimating $D_x$ and $D_y$

The codes used for Scalar Transport computations are presented in this section.

### The main code for reading 2D concentration outputs from FLUENT

```
% Main code for reading 2D concentration outputs from FLUENT

phi=0.025;
Re=100;
reach=1;
d=0.008;
up=Re*1e-6/d;


 folder='out90';
 diameter=0.008; %in m
 dt=0.01;   %second
 y = 0.0:0.001:0.7;  %in m
 dist=1.00;   %distance between two recording lines in m

%-----------------------Reading the Data---------------------------
 files = dir(folder);
 files = {files.name};
 files = files(3:end);
 files2 = nan(size(files));
for ii=1:length(files)
    files2(ii) = str2double(files{ii}(1:end-3));
end
[~, k] = sort(files2);
files = files(k);
alldata = cell(1,length(files));
%------------------------------------------------------------------
 for i=1:length(files)
    alldata{i} = readxy4b(sprintf('%s%s%s', folder, filesep,
files{i}), y);
    window1(:,i) = alldata{i}{1}(:,2);
    window2(:,i) = alldata{i}{2}(:,2);
 end
window1(isnan(window1)) = 0;
window2(isnan(window2)) = 0;
time = (1:length(alldata)) * dt;
cmax = max(window1(:));
%------------------------------------------------------------------
%==================================================================
%=========================longitudinal Mode=======================
%mode = 'longitudinal';
timect = time';
usct = mean(window1)';
dsct = mean(window2)';
```

```
dsct = dsct ./ sum(usct);
usct = usct ./ sum(usct);
Longitudinal
%==========================Transverse Mode=========================
%mode = 'transverse';
y2 = y';
uscy = mean(window1,2);
dscy = mean(window2,2);
 dscy = dscy ./ sum(uscy);
 uscy = uscy ./ sum(uscy);
xlswrite('upsCYmsblncd',uscy)
xlswrite('dnsCYmsblncd',dscy)
TransverseNew
save('d8phi025Re100Reach1');
```

## Longitudinal Optimization code

```
%-----Print the output title on the screen----------------
   fprintf('Dx,u,Dx/(ud),R_t^2\n');
% upstream centroids
usctcntr = timect(find(cumsum(usct)/sum(usct) >= 0.5, 1));
% downstream centroids
dsctcntr = timect(find(cumsum(dsct)/sum(dsct) >= 0.5, 1));
%---------------------------------------------------------
    u = dist/(dsctcntr - usctcntr);
    Dx = abs(dispersionfromvariance_ct(timect, usct, dsct, dist));
%#ok<*NASGU>
    ADEct = @(x,xdata)longitudinalADE(timect, xdata, dist/x(2), x(1),
mean(diff(timect)), x(2), 0);
    OUTPUT0ct = [Dx u];
    % R_t^2 function
    rt2 = @(original, new)(1 - sum(sum((original-new).^2)) /
sum(sum(original.^2)));
    OPTIONS_INNER = optimset('Display', 'none', 'TolFun', 1e-10,
'TolX', 1e-10, 'MaxFunEvals', 1e3);
    RT2ct = @(x)-rt2(dsct, ADEct(x,usct));
    OUTPUTct = fmincon(RT2ct,  OUTPUT0ct, [], [], [], [], [0 -0.1], [1
0.1], [], OPTIONS_INNER);
    Dx = OUTPUTct(1);
    u = OUTPUTct(2);
fprintf('%0.4e,%0.4f,%0.4e,%0.4f\n', Dx, u, Dx/(u*diameter), -
RT2ct([Dx u]));
    % downstream predictions
predct = ADEct([Dx u], usct);
```

## Longitudinal ADE

```
% Make an ade prediction
%
%     out = ade(time, data, tbar, D, dt, v, [cutoff])
%
% time: matrix of times
% data: upstream data
% tbar: travel time
%    D: dispersion coeffecient
%   dt: timestep
%    v: velocity
% (optional) cutoff: don't bother to route points lower than this
value

function out = longitudinalADE(time, data, tbar, D, dt, v, varargin)

    if nargin == 6
```

```
        cutoff = 1e-4;
    elseif nargin == 7
        cutoff = varargin{1};
    end

    out = zeros(size(data));
    fDb = 4 * D * tbar;
    vspf = v / sqrt(pi * fDb);
    v2 = v ^ 2;
    iii=0;
    for t=1:length(data)

        if data(t) > cutoff

            out = out + data(t) .* vspf .* exp(-(v2 * (tbar + time(t)
- time) .^ 2) / fDb) * dt;

        end
    end
```

## Transverse Optimization code

```
%-----Print the output title on the screen----------------
   fprintf('Dy,u,v,Dy/(Ud),R_t^2\n');
%---------------------------------------------------------
% upstream centroids
uscycntr = y2(find(cumsum(uscy)/sum(uscy) >= 0.5, 1));
% downstream centroids
dscycntr = y2(find(cumsum(dscy)/sum(dscy) >= 0.5, 1));
%---------------------------------------------------------
        v = (uscycntr-dscycntr)/(dist/u);
        Dy = abs(dispersionfromvariance_cy(y2, uscy, dscy, dist));
        ADEcy = @(x,xdata)transverseADE(y2, xdata, dist/u, x(1),
mean(diff(y2)), x(2), 0);
        OUTPUT0cy = [Dy v];
    % R_t^2 function
    rt2 = @(original, new)(1 - sum(sum((original-new).^2)) /
sum(sum(original.^2)));
    OPTIONS_INNER = optimset('Display', 'none', 'TolFun', 1e-10,
'TolX', 1e-10, 'MaxFunEvals', 1e3);
    RT2cy = @(x)-rt2(dscy, ADEcy(x,uscy));
    OUTPUTcy = fmincon(RT2cy, OUTPUT0cy, [], [], [], [], [0 -0.1], [1
0.1], [], OPTIONS_INNER);
    Dy = OUTPUTcy(1);
    v = OUTPUTcy(2);
        fprintf('%0.4e,%0.4f,%0.4f,%0.4e,%0.4f\n', Dy, u, v,
Dy/(u*diameter), -RT2cy([Dy v]));
    % downstream predictions
    predcy = ADEcy([Dy v], uscy);
```

## Transverse ADE

```
% Make a transverse ade prediction
%
%     out = xade3(xpos, data, tbar, D, dx, v, [cutoff])
%
% xpos: matrix of transverse position
% data: upstream data
% tbar: travel time
%    D: dispersion coeffecient
```

```
%   dx: spatial resolution
%    v: transverse velocity
% (optional) cutoff: don't bother to route points lower than this
value

function out = transverseADE(xpos, data, tbar, D, dx, v, varargin)

    if nargin == 6
        cutoff = 1e-4;
    elseif nargin == 7
        cutoff = varargin{1};
    end

    out = zeros(size(data));
    fDb = 4 * D * tbar;
    vspf = dx / sqrt(pi * fDb);
    vt = v * tbar;

    for i=1:length(data)
%          if data(i) > cutoff
             out = out + data(i) .* vspf .* exp( -(xpos(i) - xpos -
vt).^2 / fDb);
%          end
    end
%     disp('done')
```

## User defined function for scalar transport in C

```
#include "udf.h"



/* constants */

#define Sct 1.0

#define Dw 1.766e-9



/* the scalar UDS index of the dye */

#define TRACER 0



/* the cell center of the injection point should be in this range */

#define XPOS_INJ_X 0.1

#define XPOS_INJ_Y 0.35

#define XPOS_INJ_Z 0.075

#define INJ_RADIUS 0.001

#define LINE_SOURCE 0
```

```
/* The upstream and downstream boundaries of the channel */

#define XPOS_START_X1 0.05

#define XPOS_START_Y1 0

#define XPOS_START_X2 0.05

#define XPOS_START_Y2 1

#define XPOS_END_X1 2.15

#define XPOS_END_Y1 0

#define XPOS_END_X2 2.15

#define XPOS_END_Y2 1


DEFINE_SOURCE(tracer_inj, c, t, dS, eqn)

{

  real pos[ND_ND];


  C_CENTROID(pos, c, t);

  dS[eqn] = 0.0;


  /* the injection */

#if RP_2D || LINE_SOURCE

  if ((SQR(pos[0] - XPOS_INJ_X) + SQR(pos[1] - XPOS_INJ_Y)) < INJ_RADIUS*INJ_RADIUS)
{

#elif RP_3D

  if ((SQR(pos[0] - XPOS_INJ_X) + SQR(pos[1] - XPOS_INJ_Y) + SQR(pos[2] - XPOS_INJ_Z))
< INJ_RADIUS*INJ_RADIUS) {

#endif

    return (double)1.0;

  }

  return (double)0.0;

}
```

```
DEFINE_SOURCE(tracer_remv, c, t, dS, eqn)
{
   real pos[ND_ND];
   real start_direction;
   real end_direction;

   C_CENTROID(pos, c, t);
   dS[eqn] = 0.0;

   start_direction = (XPOS_START_X2 - XPOS_START_X1) * (pos[1] - XPOS_START_Y1) -
(XPOS_START_Y2 - XPOS_START_Y1) * (pos[0] - XPOS_START_X1);
   end_direction = (XPOS_END_X2 - XPOS_END_X1) * (pos[1] - XPOS_END_Y1) -
(XPOS_END_Y2 - XPOS_END_Y1) * (pos[0] -  XPOS_END_X1);

   /* remove the dye */
   if (start_direction > 0 || end_direction < 0) {
      if (C_UDSI(c,t,TRACER) > 0) {
         dS[eqn] = -50000.0;
         return -C_UDSI(c,t,TRACER) * 50000.0;
      }
   }
   return (double)0.0;
}

DEFINE_DIFFUSIVITY(scalar_udf,c,t,i) {
   return C_R(c,t) * Dw + C_MU_T(c,t) / Sct;
}
```